

An Electronic Structure Approach to Charge Transfer and Transport in Molecular Building Blocks for Organic Optoelectronics

by

Heidi Phillips Hendrickson

A dissertation submitted in partial fulfillment
of the requirements for the degree of
Doctor of Philosophy
(Chemistry)
in The University of Michigan
2015

Doctoral Committee:

Professor Eitan Geva, Co-Chair
Assistant Professor Barry D. Dunietz, Co-Chair
Assistant Professor Leah A. Bricker
Professor Theodore G. Goodson III
Associate Professor Jennifer P. Ogilvie

© Heidi P. Hendrickson 2015

All Rights Reserved

For my parents

ACKNOWLEDGEMENTS

First and foremost, I would like to acknowledge my research advisors Prof. Barry D. Dunietz and Prof. Eitan Geva, who have provided continual guidance and support throughout the length of my Ph.D. I cannot thank them enough for all the knowledge and expertise they have shared with me in the past six years. They have each taught me so much about chemical theory and computation, scientific practice, life in general, and most importantly, coffee.

I would also like to acknowledge my committee members, Prof. Jennifer Ogilvie, Prof. Theodore Goodson III, and Prof. Leah Bricker, for the wisdom and support they have offered during my Ph.D. I look up to each of them as role models who think deeply and creatively about scientific problems in their respective fields. I am grateful for their influence on my work and my development as a scientist.

Next I would like to acknowledge the past and present members of the Dunietz and Geva research groups, Dr. Surma Talapatra, Dr. Alex Prociuk, Dr. Shaohui Zheng, Dr. Zilong Zheng, Dr. Myeong Lee, Dr. Arun Manna, Dr. Partha Pal, Dr. Nicolai Sergueev, Dr. Kijeong Kwac, Dr. Porscha McRobbie, Dr. Xiang Sun, Dr. Frank Vazquez, Christina Franzese, Aaron White, Kyle Williams, Alex Hyla, and Francis DeVine, for their scientific perspectives and for their overall encouragement throughout my PhD. I am ever grateful to Dr. Alex Prociuk and Dr. Shaohui Zheng, who were fantastic mentors as I began my graduate research. I also would like to acknowledge those involved with the chemical education portion of this dissertation including Prof. Brian Coppola, Prof. Anne Vazquez, Dr. Jeremy Feldblyum, Eric

Chen, Alex Sapick, Aaron Goodman, Daniel Cummins, Kari Chen, Michael Gysin, Daphne Porat, and Sarah Choi. Additionally, I would like to thank the members of the Brooks group, Zimmerman group, and Zgid groups, who all contribute to a positive and cooperative computational lab environment. I especially want to thank Jessica Gagnon and Dr. Surma Talapatra, who have been amazing friends throughout my dissertation work.

I also would like to acknowledge the scientists who inspired me to pursue graduate research. I would like to thank my undergraduate research advisor, Prof. Matthew Young, as well as other Hillsdale College faculty including Prof. Lee Baron, Prof. Christopher Hamilton, Prof. Mark Nussbaum, Prof. Christopher VanOrman, Prof. Ken Hayes, Prof. Jim Peters, Prof. Cyril Slezak, Prof. Adam Smith, and Mrs. Judith Schellhammer. I would also like to thank my high school chemistry teacher, Mr. Michael Spitz, for giving me the opportunity to work as a lab assistant, which sparked my initial interest in chemistry.

Finally, I would like to thank all of my family and friends, who have always encouraged and supported me, and without whom I would not have accomplished this work. I especially want to thank my dad, my mom, my stepdad, my mother and father-in-law, and all of my brothers and sisters. At last, I would like to thank my husband Zach Hendrickson, who has supported me in everything and is a source of joy and strength.

TABLE OF CONTENTS

DEDICATION	ii
ACKNOWLEDGEMENTS	iii
LIST OF FIGURES	viii
LIST OF TABLES	xv
LIST OF APPENDICES	xix
LIST OF ABBREVIATIONS	xx
ABSTRACT	xxii
CHAPTER	
I. Introduction	1
1.1 Organic Optoelectronic Applications	2
1.1.1 Contributing to Organic Optoelectronic Design via Computational Approaches	5
1.2 Density Functional Theory and Time-Dependent Density Func- tional Theory	7
1.2.1 Density Functional Theory (DFT)	9
1.2.2 Time-Dependent Density Functional Theory (TDDFT)	17
1.2.3 Range-Separated Hybrid Functionals as Solutions to DFT Limitations	23
II. Benchmarking Novel Range Separated Hybrid Density Func- tionals for Ground and Excited State Properties	28
2.1 Orbital Gap Predictions for Rational Design of Organic Pho- tovoltaic Materials	28
2.1.1 Introduction	28
2.1.2 Computational Methods	30

2.1.3	Results and Discussion	32
2.1.4	Conclusions	41
2.2	Calculating Off-Site Excitations in Symmetric Donor-Acceptor Systems via Time-Dependent Density Functional Theory with Range-Separated Density Functionals	41
2.2.1	Introduction	42
2.2.2	Computational Methods	45
2.2.3	Results and Discussion	47
2.2.4	Conclusions	58
 III. Application of Range Separated Hybrid Density Functionals to Promising Organic Photovoltaic Systems		60
3.1	Ab Initio Calculation of the Electronic Absorption of Functionalized Octahedral Silsesquioxanes via Time-Dependent Density Functional Theory with Range-Separated Hybrid Functionals	60
3.1.1	Introduction	60
3.1.2	Computational Methods	62
3.1.3	Results and Discussion	64
3.1.4	Conclusions	81
3.2	Ab Initio Study of the Emissive Charge-Transfer States of Solvated Chromophore-Functionalized Silsesquioxanes	82
3.2.1	Introduction	82
3.2.2	Computational Methods	83
3.2.3	Results and Discussion	84
3.2.4	Conclusions	95
3.3	Future Directions: Selectively Tuning Charge Transfer Pathways via Chromophore-Functionalized Silsesquioxanes	95
 IV. Time-Dependent Electron Transport Through Model Molecular Junctions		98
4.1	Introduction	98
4.1.1	Theoretical Background	101
4.2	Modeling transient aspects of coherence-driven electron transport	109
4.2.1	Computational Model	109
4.2.2	Results and Discussion	111
4.2.3	Conclusions	118
4.3	Bias effects on the electronic spectrum of a molecular bridge	119
4.3.1	Computational Model	119
4.3.2	Results	123
4.3.3	Conclusions	128

V. Using Student Generated Explanations of Quantum Chemistry Concepts and a Peer-Review Process to Explore Student Conceptual Understanding	129
5.1 Introduction	129
5.2 Background on Design and Implementation	132
5.3 Method	136
5.3.1 Participants	136
5.3.2 Data Collection and Analysis	137
5.4 Results and Discussion	140
5.4.1 Persistent Inaccuracies	140
5.4.2 Effects of the Peer Review Process	142
5.4.3 Effect of the Extended Peer Review Process	146
5.5 Concluding Remarks	149
VI. Conclusions and Outlook	151
6.1 Summary	151
6.2 Outlook	154
APPENDICES	156
BIBLIOGRAPHY	181

LIST OF FIGURES

Figure

1.1	Simple schematic illustrating the relation of light absorption and emission processes in OPV and OLED devices.	2
1.2	Simple schematic illustrating the charge transfer process within a solar cell. The first panel shows the solar cell material in the dark. Exciton generation due to light absorption is shown in the second panel. The third panel indicates exciton diffusion to the donor-acceptor interface, and the fourth panel shows exciton dissociation at that material interface. The fifth panel indicates diffusion of the separated charges away from the interface.	3
1.3	Diagram illustrating the charge separation processes in a flat donor-acceptor interface, compared to those in a bulk heterojunction, where donor and acceptor materials are mixed.	4
1.4	The energy should be piecewise linear dependent on the electronic occupation number in the grand canonical ensemble.[1] Here this behavior is illustrated using the experimental gas phase IP and EA of carbon (green solid curve). [Data are taken from the National Institute of Standards and Technology web book at (http://webbook.nist.gov).] At integer electron numbers, the chemical potential exhibits a discontinuity. Widely-used implementations of DFT do not possess this discontinuity, compensating for the change in chemical potential via curvature (shown schematically here as the gray dashed curve).[2, 3]	15
2.1	OT-BNL and B3LYP $-\varepsilon_H$ calculated at the gas-phase compared to experimental IP measured in gas and condensed phase. Absolute errors between <i>gas phase</i> calculated and experimental energies are given by $\Delta\varepsilon_H = \varepsilon_H^{calc} - \varepsilon_H^{exp} $ (eV)	33

2.2	OT-BNL and B3LYP $-\varepsilon_L$ calculated at the gas-phase compared to experimental EA measured in gas and condensed phase. Absolute errors between gas phase calculated and experimental energies are given by $\Delta\varepsilon_L = \varepsilon_L^{calc} - \varepsilon_L^{exp} $ (eV)	36
2.3	Calculated OT-BNL and B3LYP IP^{PCM} and ε'_H compared to the measured thin film IP. Absolute errors between <i>condensed phase</i> calculated and experimental energies are shown in the lower panels and are given by $\Delta x = x^{calc} - x^{exp} $ (eV)	39
2.4	Calculated OT-BNL and B3LYP EA^{PCM} and ε'_L compared to the measured thin film EA. Absolute errors between calculated and experimental energies are shown in the lower panels and are given by $\Delta x = x^{calc} - x^{exp} $ (eV)	40
2.5	The four possible $\pi - \pi^*$ excitations of the ethene dimer. The two <i>on-site</i> excitations and two <i>off-site</i> excitations are shown in the top and bottom panels, respectively. Orbital degeneracy in symmetric dimers allows the excitations to be written also as linear combinations of the individual <i>off-site</i> excitations pictured above, which can conceal the underlying CT nature evidenced in the localized MO representation.	44
2.6	Top: Ethene dimer orbital energies (eV) for symmetric (purple), symmetry broken by electric field (0.1V) (red), and symmetry broken by bond stretching (0.102 Å from equilibrium) (blue). The results shown were obtained for a dimer where the ethenes are 15 Å apart, using the HF approximation. Bottom: Pictorial description of dimer separation and symmetry breaking schemes.	46
2.7	B3LYP excitation energies (eV) as the bond of one ethene is increasingly stretched at a dimer separation of 15 Å. A schematic illustrating the orbital shift induced by the bond stretching is included to clarify the changes in excitation energies.	48
2.8	(a) Excitation energies (eV) when symmetry is broken by bond stretching (0.102 Å from equilibrium) with increasing dimer separation. <i>Off-site</i> energies are compared to Equation 2.8. (b) Excitation energies (eV) when symmetry is broken by applying a constant electric field with increasing dimer separation. The field ($E_f = 0.1$ V/Å) is applied at each separation value. <i>Off-site</i> energies are compared to Equation 2.10. For both plots, the <i>off-site</i> energies are compared to Equation 2.9 the long-range electrostatic interaction limit where experimental IP and EA values are used. <i>On-site</i> energies for the 15 Å separation are included for comparison (Note: HF and B3LYP <i>on-site</i> state energies overlap).	50

2.9	Excitation energies (eV) of the symmetric system. <i>Off-site</i> energies are compared to Equation 2.8 and to Equation 2.9 the long-range electrostatic interaction limit, where experimental IP and EA values are used. <i>On-site</i> energies for the 15 Å separation are included for comparison (Note: HF and B3LYP <i>on-site</i> state energies overlap).	53
2.10	(a) Perpendicular 2-vinylstilbene-OHSQ, (b) Parallel 2-vinylstilbene-OHSQ (top: side view, bottom: overhead view).	55
2.11	Detachment and attachment densities corresponding to <i>on-site</i> and <i>off-site</i> excitations for 2-vinylstilbene-OHSQ in the perpendicular and parallel geometries. The non-degenerate <i>off-site</i> excitations are localized on a single vinylstilbene in the perpendicular geometry and involve net CT. The degenerate <i>off-site</i> excitations are delocalized on both vinylstilbenes in the parallel geometry and involve significantly smaller net CT.	56
2.12	Orbital pictures and energies (eV) for 2-vinylstilbene-OHSQ structures. Top: Perpendicular; non-degenerate orbitals are localized on each vinylstilbene. Bottom: Parallel; degenerate orbitals are delocalized over both vinylstilbenes.	57
2.13	Excitation energies (eV) obtained for 2-vinylstilbene-OHSQ in the parallel and perpendicular geometries via TDDFT with B3LYP and BNL. Results obtained using the 6-31G* (left) and 6-31+G* (right) basis sets are shown.	58
3.1	Molecular models of the systems studied: OHSQ, 1vinyl-OHSQ, OVSQ, ortho, meta and para isomers of 2vinyl-OHSQ.	65
3.2	HOMO and LUMO energies for OHSQ, ethylene, 1Vinyl-OHSQ, ortho, meta, and para isomers of 2Vinyl-OHSQ and OVSQ as obtained using B3LYP (orange) and BNL (purple). The BNL parameter values that were used are: $\gamma=0.47$ a.u. (OHSQ), $\gamma=0.40$ a.u. (ethylene), $\gamma=0.30$ a.u. (vinyl-OHSQ).	67
3.3	Attachment (blue) and detachment (pink) densities for the transitions with the largest oscillator strength in the first excitation band for ethylene, 1Vinyl-OHSQ and OVSQ molecules.	70

3.4	The effect on the oscillator strength by multiple ligand functionalization. Shown on the right are the oscillator strengths for vinylstilbene, 2-vinylstilbene OHSQ (para, meta and ortho isomers), 4-vinylstilbene OHSQ (the isomer shown). Shown on the left are the oscillator strengths of the of the ligand arrangements obtained after removing the OHSQ.	71
3.5	(a) Top: The molecular building blocks of the systems considered in this paper, namely OHSQ, styrene and vinylstilbene. Bottom: Different ligand-functionalized OHSQs, including different substitutions of the ligands by EDGs or EWGs. (b) Molecular models of the systems studied in this paper.	74
3.6	A correlation plot of the calculated vs. experimental absorption excitation energies. Perfect agreement corresponds to the black line. Shown are calculated results obtained for both R_s -Styrenyl-OHSQ and R_v -Vinylstilbene-OHSQ by using BNL (purple), B3LYP (orange) and LRC- ω PBEh (green). The root mean square deviation of the calculated values from the measured excitation energy is provided in the legend.	75
3.7	Detachment (pink) and attachment (blue) densities associated with transitions that have the strongest oscillator strengths in the first excitation band, for 1-Styrenyl-OHSQ, 1-CH3O-Styrenyl-OHSQ, 1-Vinylstilbene-OHSQ, 1-NH2-Vinylstilbene-OHSQ and 1-NO2-Vinylstilbene-OHSQ molecules.	77
3.8	HOMO and LUMO energies calculated for OHSQ, R_s -Styrene, R_s -Styrenyl-OHSQ; $R_{v,w}$ -Vinylstilbene, $R_{v,w}$ -Vinylstilbene-OHSQ using B3LYP (orange), BNL (purple) and LRC- ω PBEh (green).	78
3.9	The effect of ligation on the HOMO and LUMO energies given by difference in the orbital energies between the ligated OHSQ and the free ligands (in eV).	79
3.10	Illustrated picture of the behavior of chromophore-functionalized OHSQ. Absorption of functionalized OHSQ resembles that of the chromophore, but emission is red-shifted compared to chromophore emission due an expected charge transfer state.	83
3.11	SQ fully functionalized with 8 stilbene ligands (left). Molecular models of 1-stilbene-OHSQ and 2-stilbene-OHSQ (right).	85

3.12	Gas phase vertical electronic excitation energies for 2-stilbene-OHSQ at the solvated (within PCM) ground state geometry, as obtained via TDA with BNL and B3LYP functionals.	87
3.13	The CT1 and CT2 detachment and attachment electronic densities.	89
3.14	Solvated electronic excitation energies (eV), accounting for intramolecular reorganization. G_0 is the ground electronic state energy. Molecular geometries- Ground: solvated ground state geometry; CT(1,2): solvated CT(1,2) with TDA partial-charge constraints; CT(1,2)c: solvated CT(1,2) with complete electron transfer constraints.	91
3.15	Orbital energies for benzene, stilbene, OHSQ, phenyl-OHSQ, and stilbene-OHSQ (eV)	97
3.16	Calculated $\pi - \pi^*$ and CT1 (chromophore-to-SQ) excitation energies at the equilibrium geometry (optimized using a PCM). (eV)	97
4.1	The Keldysh time contour includes three branches defined in the complex plane: forward and backward real time and, extended into the imaginary axis at t_0 , the thermal lifetime. The forward and backward branches along the real axis are vertically shifted for purposes of illustration.	102
4.2	Schematic diagram of the model system. (a) Localized/atomic orbital representation where the strong coupling of the device state to the wires are indicated. (b) Diagonalized molecular orbital representation. (c) Broadened electronic density of states.	110
4.3	The transient current under the effect of a slowly varying potential. The corresponding current density is provided (band structure at the ground state). Note that the right axis corresponds to the current curve while the left axis corresponds to the energy distribution variable.	112
4.4	TD currents which differ in the rate of the potential turn off. The three TD bias curves are provided to the right.	113
4.5	TD current distributions projected on a color map ($I(t)$) are provided in 4.4). (a) fastest turn off rate, (b) medium turn off rate, (c) slowest turn off rate.	114
4.6	Effect of the coupling strength: (a) The density of states (b) TD current under and AC tuned to the original coupling strength.	114

4.7	The current band structure corresponding to the AC tuned to the energy difference of the two energy levels under the effect of varying the coupling strength (see Figure 4.6). (a) initial coupling, (b) stronger coupling, (c) weaker coupling.	116
4.8	Effects of an existing DC bias on: (a) Electronic spectra of the bias system. (b-d) Coherence driven conductance.	117
4.9	The current distributions of the cases with different applied DC biases. (a) 0 eV, (b) 0.01 eV, (c) 0.05 eV, (d) 0.10 eV.	118
4.10	The effect of coupling to electrodes and bias is illustrated. (a) The electronic spectra of the uncoupled molecule are resolved (only HOMO-LUMO transition is implied). (b) The spectral peak of the molecular bridge is broadened due to the coupling to electrodes. (c) The bias may enable or disable electronic transitions. (d) Mechanical symmetry breaking may lead to stronger coupling to the source or drain electrode.	120
4.11	Schematic diagram representing device region. Effect of potential bias is implied as well as the shift of carbons toward source and drain electrode	121
4.12	(a) The electronic DOS under increasing broadening factor. (b) The electronic spectra corresponding to increasing broadening factor.	124
4.13	(a) The electronic DOS under carbon shifting toward an electrode at equilibrium. (b) The electronic spectra under the carbon shifting. The HOMO-Virt2 transition is enabled by the symmetry breaking.	125
4.14	Molecular orbital diagrams for non-shifted case (a) and shift of 0.38 Å (b) toward source (c) and drain. Relevant bond lengths and energies are included.	125
4.15	Spectral dependence on increasing potential bias for geometrically symmetric junction. (Insert) Bias dependence for small device region indicates cause of Au-Au interaction.	126
4.16	The spectral dependence on increasing bias under carbon shift toward (a) source electrode and (b) drain electrode.	127
5.1	The number of inaccuracies identified per student in each year.	141

5.2	The fraction of inaccuracies of each type identified in the second draft (2D) for each year. The inaccuracies identified in the first draft via peer review (PR) and extended peer review (EPR) are also presented.	142
5.3	The number of inaccuracies of each type identified in the second draft (2D) for each year. The inaccuracies identified in the first draft via peer review (PR) and extended peer review (EPR) are also presented.	144
B.1	Left: HOMO and LUMO energies for the ethene dimer (separated by 15Å) calculated using the 6-31+G* basis set. The energies do not depend on orbital localization; Center: Dimer-delocalized orbitals; Right: Monomer-localized orbitals.	164
C.1	Correlation plot between <i>off-site</i> excitation energies and corresponding orbital gaps of all ethene dimer systems considered in this study. <i>Off-site</i> excitations of LDA and PBE functionals are shown to correspond to the orbital gap, and those of B3LYP depend slightly on the Coulomb interaction but remain similar to the orbital gap. The BNL RSH and HF <i>off-site</i> excitations are not correlated with the orbital gap however, and instead the excitation energies are higher than the orbital gap due to the effect of Coulomb interaction.	168
D.1	Attachment/detachment densities of the transition with the strongest oscillator strength in first excitation band for Styrene, 1Styrenyl-OHSQ, 1CH ₃ -Styrenyl-OHSQ, and 1CH ₃ O-Styrenyl-OHSQ molecules. Attachment: blue; Detachment: pink.	173
D.2	Attachment/detachment densities of the absorbing transition for vinylstilbene and <i>R_{v,w}</i> -Vinylstilbene-OHSQ molecules. Attachment: blue; Detachment: pink.	174
D.3	Attachment/detachment densities of the absorbing transition for 1Br-Vinylstilbene-OHSQ, 1COOH-Vinylstilbene-OHSQ, and 1NO ₂ -Vinylstilbene-OHSQ molecules. Attachment: blue; Detachment: pink.	175

LIST OF TABLES

Table

2.1	MAE and standard deviation of gas phase ε_H ($\Delta\varepsilon_H$) and ε_L ($\Delta\varepsilon_L$) [eV]	35
2.2	MAE and standard deviation between thin film experimental and calculated IP and EA (values in parenthesis exclude pyrazine and pyridine values) [eV]	39
2.3	Excitation energy and corresponding orbital gap for isolated ethene (eV)	49
3.1	Absorption excitation energies (in eV) of OHSQ, 1-vinyl-OHSQ and ethylene as obtained using B3LYP and BNL with different types of basis sets. The same value of the BNL parameter was used in all cases: $\gamma=0.50$ a.u. The bold font indicate basis sets for which converged results were obtained.	66
3.2	Excitation energies (in eV) for transitions that correspond to the absorbing states of ethylene and various vinyl-OHSQs. The absorption maximum (λ_{max}) is provided by the oscillator-strength-weighted average of excitation energies. The values of the BNL parameter used are: $\gamma=0.400$ a.u. (ethylene), $\gamma=0.300$ a.u. (vinyl-OHSQ).	69
3.3	Excitation energies (in eV) for transitions that correspond to the absorbing states of vinylstilbene and vinylstilbene-OHSQs. 2-vinylstilbene-OHSQ isomers and 4-vinylstilbene-OHSQ are compared to the same ligand arrangement after removing the OHSQ. The absorption maximum (λ_{max}) is provided by the oscillator-strength-weighted average of excitation energies.	72
3.4	Absorption excitation energies, in eV, and oscillator strengths of R_w -Vinylstilbene-OHSQ as obtained using B3LYP and BNL	80

3.5	The BNL HOMO and LUMO energy (eV). (The subscript 's' refers to stilbene and the subscript 'o' to the OHSQ cage).	86
3.6	The modeled relaxation energies (eV) of the electronic CT states and their difference from the excitonic $\pi - \pi^*$ energy at the ground state geometry (ΔE_0 , a negative sign means a higher energy). The sum of the relaxation energy and the ΔE_0 defines the overall emission spectra shift (ΔE). In the parenthesis we specify the charge on the donor designated chromophore used in the corresponding C-DFT calculations.	93
5.1	Activities included in each CHEM 260H exploration cycle. (Grading is incorporated into first week of the following cycle.)	134
5.2	Design considerations at each implementation of CHEM 260H. WTT: Writing-To-Teach, CTools: Online Course Tools, EPR: Extended peer review, PRI: Peer review instruction.	135
5.3	Fraction of each type of inaccuracy identified in each exploration draft. Summary statistics for 2D exploration inaccuracies are provided.	143
A.1	Calculated solvent parameters for PCM calculations	158
A.2	Experimental gas phase and thin-film ionization potentials and electron affinities reported as orbital energies. (eV)	159
A.3	Calculated gas phase orbital energies (eV)	160
A.4	BNL orbital energies calculated as IP/EA^{PCM} and $\Delta\epsilon'_{H/L}$ (eV)	161
A.5	B3LYP orbital energies calculated as IP/EA^{PCM} and $\Delta\epsilon'_{H/L}$ (eV)	162
B.1	The <i>off-site</i> excitation energies (eV), orbital contributions, and net CT observed for different MO basis set choices.	164
C.1	The BNL γ parameter (a.u.), calculated according to Eq. 1.74 for the ethene dimer system (symmetric, symmetry-broken by electric field and bond stretching) at each dimer separation distance, and the 2-vinylstilbene-SQ system.	166

C.2	Symmetry-breaking effect on the HOMO and LUMO* energies (eV) for the 15Å separated dimer. [*The orbital gap that corresponds to the $\pi - \pi^*$ excitation actually consists of the HOMO (1b1u) and LUMO+4 (1b2g) orbitals for the HF and BNL functionals. The reported values in this table correspond to the LUMO+4 orbitals instead of the LUMO for HF and BNL. This trend is also explained in footnotes (iii) and (iv) in Chapter 2.2.]	167
C.3	Comparison of ground state energies (a.u.) for parallel and perpendicular 2-vinylstilbene-SQ structures indicates both are thermally populated at room temperature.	167
D.1	Comparison of optimized geometry with experiment	169
D.2	Si-Si diagonal length comparison in vinyl-OHSQ models. The number in parenthesis is the degeneracy having the same length. (Å)	170
D.3	HOMO and LUMO gap for model systems (OHSQ coupled with vinyl). BNL parameter: OHSQ $\gamma=0.47$ a.u.; ethylene $\gamma=0.40$ a.u.; vinyl-OHSQ $\gamma=0.30$ a.u. (eV)	170
D.4	Comparison of B3LYP, BNL and LRC- ω PBEh absorption energies to experiment [4] for both $1R_s$ -Styrenyl-OHSQ ($R_s = \text{H, CH}_3, \text{CH}_3\text{O}$) and $1R_v$ -Vinylstilbene-OHSQ ($R_v = \text{H, CH}_3, \text{CH}_3\text{O, NH}_2$). For each styrene substituted OHSQ molecule, two absorption transitions are listed along with oscillator strength-weighted averaged energy and two-state summation of oscillator strength. BNL parameter $\gamma=0.27/0.24$ a.u. (R_s -styrene/ $1R_s$ -styrene-OHSQ), $\gamma=0.21/0.20$ a.u. (R_v -vinylstilbene/ $1R_v$ -vinylstilbene-OHSQ) (eV).	171
D.5	Gas phase and PCM solvent model ground state energy comparison of Styrene, 1Styrene-OHSQ, Vinylstilbene, and 1Vinylstilbene-OHSQ. (eV).	171
D.6	Attachment/Detachment density analysis of the selected strong absorption of styrene, vinylstilbene, $1R_s$ -Styrenyl-OHSQ ($R_s = \text{H, CH}_3, \text{CH}_3\text{O}$) and $1R_v$ -Vinylstilbene-OHSQ ($R_v = \text{H, CH}_3, \text{CH}_3\text{O, NH}_2$).	172
D.7	HOMO and LUMO energies and band gaps of the R_s -Styrenyl-OHSQ, R_v -Vinylstilbene-OHSQ and R_w -Vinylstilbene-OHSQ series. (eV)	172
E.1	Excitation energies of ethylene and 1Vinyl-OHSQ from Table 3.2, emphasizing the HOMO-LUMO excitation in boldface	177

E.2	Excitation energies of ethylene for different levels of theory, emphasizing the HOMO-LUMO excitation in boldface	177
F.1	Gas phase vertical electronic excitation energies (eV) for 2-stilbene-OHSQ at the solvated (within PCM) ground state geometry, as obtained via TD-DFT with the Tamm-Dancoff approximation with BNL and B3LYP functionals. (These energies correspond to Figure 3.12.) For comparison we provide the corresponding TD-DFT energies in the lower part of the table.	178
F.2	Electronic excitation energies (eV) of the charge transfer states at the ground and the corresponding excited state optimized geometry. Energies are relative to the ground state energy at the PCM optimized ground state geometry, whereas solvation energies are in absolute values. The geometry optimizations of solvated states are obtained with PCM and by constrained-DFT for CT states. Solvation energies are obtained from the difference between the C-DFT//PCM energy and the gas phase C-DFT energy <i>at the same molecular geometry</i> . The ground state gas phase reorganization energy is denoted by λ_g . (This table corresponds to Figure 3.14.)	179
F.3	The same information as in Table F.2, where the C-DFT optimization corresponds to a complete electron transfer. (This table corresponds to the CT1c and CT2c states in Figure 3.14.)	180
F.4	Ground state energy of ground and C-DFT B3LYP/PCM optimized structures	180

LIST OF APPENDICES

Appendix

- A. Supporting Information - Orbital Gap Predictions for Rational Design of Organic Photovoltaic Materials 157
- B. Supporting Information - Relation between Molecular Orbital Basis and Net Charge Transfer 163
- C. Supporting Information - Calculating Off-Site Excitations in Symmetric Donor-Acceptor Systems via Time-Dependent Density Functional Theory with Range-Separated Density Functionals 165
- D. Supporting Information - Ab Initio Calculation of the Electronic Absorption of Functionalized Octahedral Silsesquioxanes via Time-Dependent Density Functional Theory with Range-Separated Hybrid Functionals 169
- E. Supporting Information - Ethylene Absorption 176
- F. Supporting Information - Ab Initio Study of the Emissive Charge-Transfer States of Solvated Chromophore-Functionalized Silsesquioxanes 178

LIST OF ABBREVIATIONS

- CHEM 260: Chemical principles course
CHEM 260H: CHEM 260 honors studio
CI: Conceptual inaccuracy
CT: Charge transfer
DFT: Density functional theory
GSF: Graduate student facilitator
HK: Hohenberg-Kohn
HOMO: Highest occupied molecular orbital
KS: Kohn-Sham
LUMO: Lowest unoccupied molecular orbital
OHSQ: Octahedral silsesquioxane
OLED: Organic light emitting diode
OPV: Organic photovoltaic
OSC: Organic semiconducting
PCM: Polarizable continuum model
PT: Perturbation theory
RSH: Range-separated hybrid
SPL: Studio peer leader
SQ: Silsesquioxane
TI: Technical inaccuracy
TD: Time-dependent

TDDFT: Time-dependent density functional theory

WQI: Writing quality inaccuracy

XC: Exchange-correlation

ABSTRACT

An Electronic Structure Approach to Charge Transfer and Transport in Molecular Building Blocks for Organic Optoelectronics

by

Heidi P. Hendrickson

Co-Chairs: Eitan Geva, Barry Dunietz

A fundamental understanding of charge separation in organic materials is necessary for the rational design of optoelectronic devices suited for renewable energy applications and requires a combination of theoretical, computational, and experimental methods.

Density functional theory (DFT) and time-dependent (TD)DFT are cost effective ab-initio approaches for calculating fundamental properties of large molecular systems, however conventional DFT methods have been known to fail in accurately characterizing frontier orbital gaps and charge transfer states in molecular systems. In this dissertation, these shortcomings are addressed by implementing an optimally-tuned range-separated hybrid (OT-RSH) functional approach within DFT and TDDFT.

The first part of this thesis presents the way in which RSH-DFT addresses the shortcomings in conventional DFT. Environmentally-corrected RSH-DFT frontier orbital energies are shown to correspond to thin film measurements for a set of organic semiconducting molecules. Likewise, the improved RSH-TDDFT description of charge transfer excitations is benchmarked using a model ethene dimer and

silsesquioxane molecules.

In the second part of this thesis, RSH-DFT is applied to chromophore-functionalized silsesquioxanes, which are currently investigated as candidates for building blocks in optoelectronic applications. RSH-DFT provides insight into the nature of absorptive and emissive states in silsesquioxanes. While absorption primarily involves transitions localized on one chromophore, charge transfer between chromophores and between chromophore and silsesquioxane cage have been identified. The RSH-DFT approach, including a protocol accounting for complex environmental effects on charge transfer energies, was tested and validated against experimental measurements.

The third part of this thesis addresses quantum transport through nano-scale junctions. The ability to quantify a molecular junction via spectroscopic methods is crucial to their technological design and development. Time dependent perturbation theory, employed by non-equilibrium Greens function formalism, is utilized to study the effect of quantum coherences on electron transport and the effect of symmetry breaking on the electronic spectra of model molecular junctions.

The fourth part of this thesis presents the design of a physical chemistry course based on a pedagogical approach called Writing-to-Teach. The nature of inaccuracies expressed in student-generated explanations of quantum chemistry topics, and the ability of a peer review process to engage these inaccuracies, is explored within this context.

CHAPTER I

Introduction

As global energy demands increase, fossil fuels remain the dominant energy source worldwide despite their negative ecological impacts.[5] Though policy makers in several countries aim to improve energy efficiency, the world is still failing to produce sustainable energy solutions that will limit climate change in an effective way.ⁱ Creating a sustainable future in global energy requires the simultaneous effort in many areas including improving the way energy from fossil fuels is used, as well as investing in other plausible energy sources. For example, solar energy provides an important, though mostly untapped, renewable resource. The amount of energy from the sun that reaches the earth in one day is more than enough to meet global energy demands for one year, however capturing and using this energy remains a significant challenge for scientists and engineers.[6, 7]

A cost-effective approach to energy solutions lies in organic optoelectronic devices, which can be used to capture solar energy via photovoltaic applications, or can be used to increase efficiency of energy usage, for example as light-emitting diodes in lighting applications. Designing organic optoelectronic devices suited for energy applications requires a fundamental understanding of the charge transfer and transport processes that can occur within the organic semiconducting materials (OSC) used to create these devices. Combining insights gained via both experimental and computational

ⁱThe current goal is to limit total global temperature increase to only 2°C

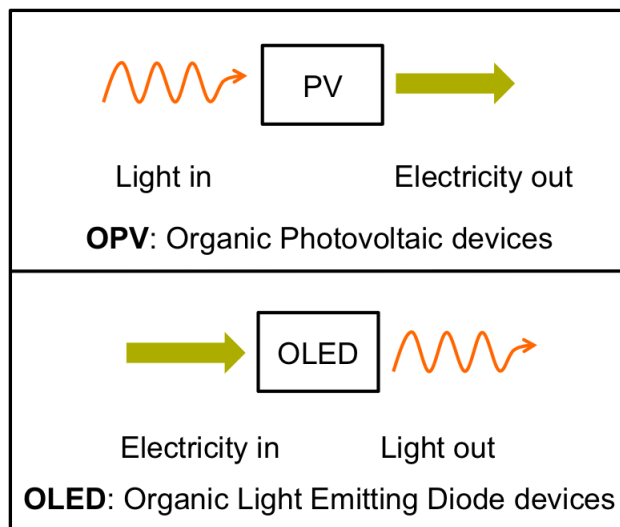


Figure 1.1: Simple schematic illustrating the relation of light absorption and emission processes in OPV and OLED devices.

approaches provides the opportunity to achieve a molecular-level understanding of such processes. This work aims to use computational chemistry to gain insight into charge transfer and transport properties of both model and experimentally relevant systems that serve as molecular building blocks for OSC materials.

1.1 Organic Optoelectronic Applications

OSC materials offer viable, low-cost alternatives to crystalline semiconductors in optoelectronic applications, such as organic photovoltaic (OPV) and light emitting diode (OLED) devices. In general, organic materials are cost effective due to the low-cost in synthesis and processing, as well as their versatility across a wide range of applications (e.g., lightweight, flexible materials).[8–14] In this work, molecular building blocks for OSC materials for use in OPV and OLED applications are investigated. Figure 1.1 provides a simplified picture of the general processes that occur within these types of devices, emphasizing their reverse relationship to one another. While OPV devices absorb light, converting it into electric current, OLED devices require electric current to drive the emission of light. While it is true that the ideal

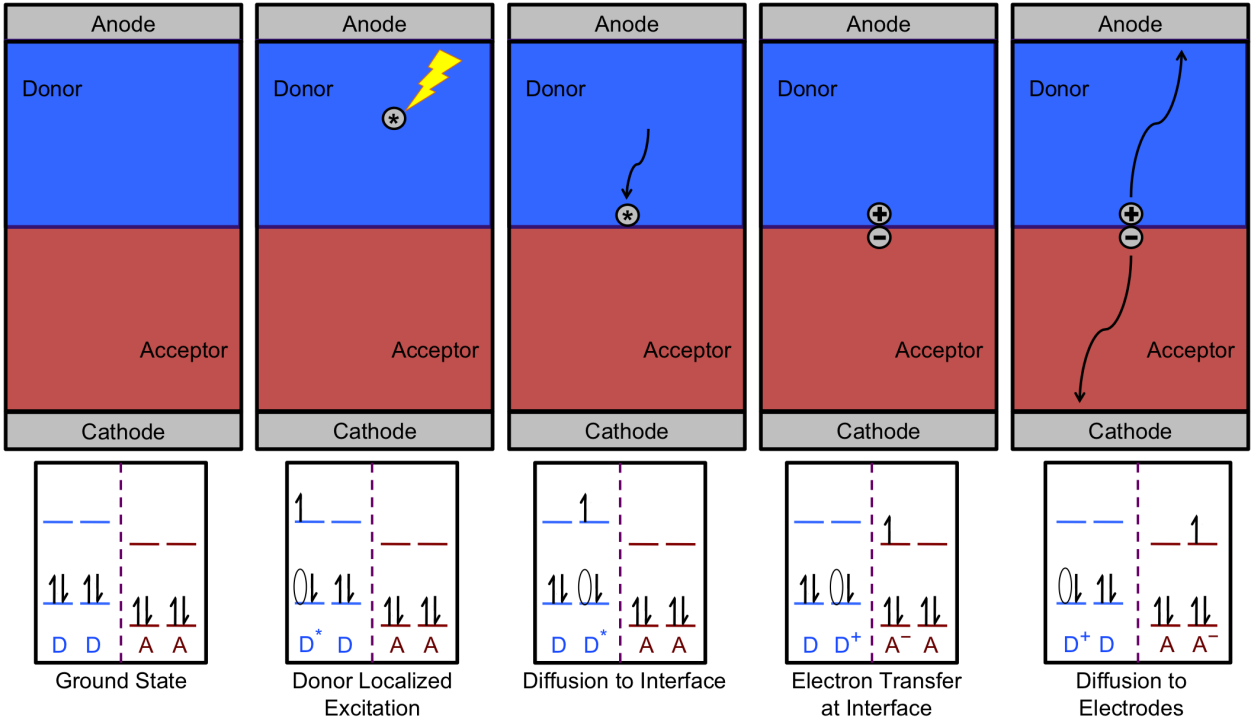


Figure 1.2: Simple schematic illustrating the charge transfer process within a solar cell. The first panel shows the solar cell material in the dark. Exciton generation due to light absorption is shown in the second panel. The third panel indicates exciton diffusion to the donor-acceptor interface, and the fourth panel shows exciton dissociation at that material interface. The fifth panel indicates diffusion of the separated charges away from the interface.

conditions for each of these processes are fundamentally different, OSC materials can be utilized in both types of devices.

A more detailed (though still over-simplified) example of the charge transfer processes within a solar cell is provided in Figure 1.2. An electron is excited in the donor material via absorption of light. The excitation typically involves the transition of an electron from the highest occupied molecular orbital (HOMO) to the lowest unoccupied molecular orbital (LUMO) in the material, as indicated in Figure 1.2. The excitation produces a localized exciton (i.e., an electron-hole pair). The exciton then diffuses through the donor material to the material interface. At the interface between donor and acceptor materials, the excited electron can be transferred from the donor

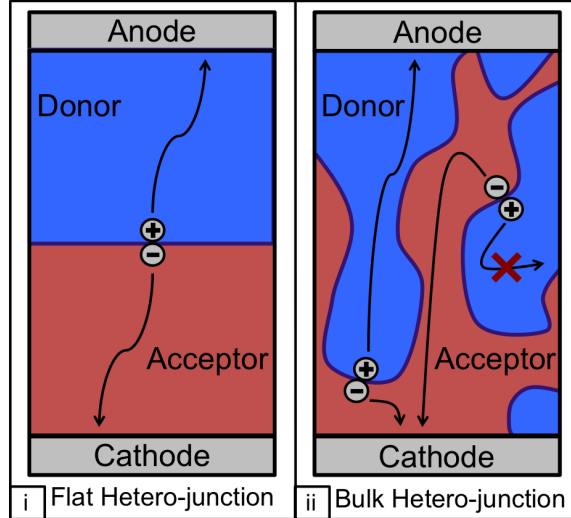


Figure 1.3: Diagram illustrating the charge separation processes in a flat donor-acceptor interface, compared to those in a bulk heterojunction, where donor and acceptor materials are mixed.

material to the acceptor material. This transfer is possible due to the energy level difference between these materials, as shown in the bottom of Figure 1.2. Ideally these separated charges will diffuse away from the interface toward the electrodes, generating a current in the cell.

While this picture illustrates the ideal function in a solar cell device, practical considerations can limit the power that can be achieved in a real OPV cell. For example, since the exciton may not initially form at the donor-acceptor interface, it must diffuse through the donor material without recombining. In many OSC materials, the distance the exciton may travel unimpeded through the material is limited, which means that not all excitons will necessarily reach the material interface.[14] Bulk heterojunction devices, as illustrated schematically in Figure 1.3, provide an approach for minimizing the distance an exciton must travel before reaching the material interface.[15] In such devices, the donor and acceptor materials are mixed, thereby increasing the interface and, as a result, charge separation in the cell. However, these devices also introduce challenges associated with controlling interface morphology and recombination, as indicated in Figure 1.3.[14]

The power conversion efficiency of a solar cell is given by the ratio of the maximum output power to the input power from the incident light source:[14]

$$\eta = \frac{P_{max}}{P_{in}} \quad (1.1)$$

The output power is a product of the photocurrent and the potential, $P = J \cdot V$, and for a given cell, there is a corresponding J_{max} and V_{max} that produce the maximum power the cell can achieve. These values are contained in the Fill Factor for device,

$$FF = \frac{J_{max}V_{max}}{J_{SC}V_{OC}} \quad (1.2)$$

which can be determined by considering the short-circuit current, J_{SC} and the open-circuit voltage, V_{OC} . The J_{SC} is the photocurrent in the system (and is called the short circuit current because it occurs under no applied bias). The V_{OC} is the forward bias that can be applied to compensate the photocurrent, until the current goes to zero, as in an open circuit. In other words, the V_{OC} is the potential difference in the HOMO energy of the donor and the LUMO energy of the acceptor, as shown in Figure 1.2. Therefore the maximum power conversion efficiency is given by,

$$\eta = \frac{J_{SC}V_{OC}FF}{P_{in}} \quad (1.3)$$

and it can be optimized via mutual optimization of the FF, J_{SC} , and V_{OC} .

1.1.1 Contributing to Organic Optoelectronic Design via Computational Approaches

Designing optoelectronic devices suited for energy applications requires fundamental understanding of the charge transfer and transport processes in organic materials outlined above.[10] Device efficiency relies on several factors, some that can be con-

trolled via rational design (i.e., the energy levels of materials within the device to optimize the V_{OC}), and some that can be difficult or even impossible to predict prior to fabrication (i.e., micro-structural device morphology that can affect various aspects of FF, J_{SC} , and V_{OC}).[7] An increased understanding of the molecular properties that contribute to these factors is necessary to inform the development of new design strategies.

Significant computational efforts have been recently focused on developing design principles for OPV and OLED materials.[7, 8, 16–45] Ideally, computational modeling intended to contribute effectively to rational design of optoelectronic applications should be explanatory and predictive. As a result, insights gained from *first principles* approaches would provide the most accurate and detailed description of OSC materials. Since it is not possible to solve the exact Schrödinger equation for OPV and OLED materials, approximate methods must be utilized in order to gain molecular-level insights.

Density functional theory (DFT) provides a cost-effective computational approach for calculating optoelectronic properties in relatively large molecular systems. Furthermore, DFT provides an exact, formal treatment of molecular systems, where the energy of the system depends on the density of the system, instead of the molecular wavefunction.[46, 47] Electron interactions are fully taken into account by the exact exchange-correlation functional, although unfortunately, this exact functional remains unknown. Therefore, DFT calculations treat electron interactions according to approximate exchange-correlation functionals that are either developed on the basis of theoretical or experimental considerations (or both). Time-dependent (TD) DFT provides a corresponding density-based approach for calculating excited state properties of a system, and has become a widely used tool for characterizing excited electronic states.[48–52] The benefits and limitations in using these methods for OSC molecular systems are discussed below.

1.2 Density Functional Theory and Time-Dependent Density Functional Theory

The electronic structure problem for molecular systems involves calculating the energies of all the electrons in the system of interest. An *ab initio* approach to solving this problem begins with the Schrödinger equation that describes these systems:[53]

$$\hat{H}(\{r\})\Psi(\{r\}) = E\Psi(\{r\}) \quad (1.4)$$

where E is the electronic energy, and $\Psi(\{r\})$ is the wavefunction for N electrons with a set of spatial coordinates $\{r\}$. The Hamiltonian, $\hat{H}(\{r\})$, is composed of (in atomic units) kinetic energy, \hat{T} ,

$$\hat{T}(\{r\}) = -\frac{1}{2} \sum_i^N \nabla_i^2 \quad (1.5)$$

the Coulomb interaction between electrons, V_{ee} ,

$$\hat{V}_{ee}(\{r\}) = \sum_{i<j}^N \frac{1}{|r_i - r_j|} \quad (1.6)$$

and the external potential acting on the system, which is typically the Coulomb interaction between electrons and nuclei, V_{ne} ,

$$\hat{V}_{ne}(\{r\}) = \sum_i^N \sum_v^{N_n} \frac{Z_v}{|r_i - R_v|} \quad (1.7)$$

where Z_v and R_v refer to the charge and position of the N_n nuclei in the system. Other external potentials, such as an applied electric field, can be incorporated as well. The eigenvalues of the Hamiltonian can be taken to form a complete, orthonormal set:

$$\int d\{x\} \Psi_k^*(\{x\}) \Psi_l(\{x\}) = \langle \Psi_k | \Psi_l \rangle = \delta_{kl}. \quad (1.8)$$

The Schrödinger equation can only be solved exactly for the most simple cases, and so in general, electronic structure methods are based on determining solutions to the Hamiltonian of a molecular system that best approximate the true energy of the system. The variation principle proves that it is possible to approximate the ground state energy using any well-behaved trial wavefunction. In order to show that a trial wavefunction, $\tilde{\Psi}\{r\}$ satisfying $\langle\tilde{\Psi}|\tilde{\Psi}\rangle = 1$ gives an upper bound to the exact ground state energy,

$$\langle\tilde{\Psi}|\hat{H}|\tilde{\Psi}\rangle \geq E_0, \quad (1.9)$$

the trial function can be expanded in the basis of eigenfunctions of the Hamiltonian operator, $\Psi_k\{r\}$, where c_k are the expansion coefficients according to

$$|\tilde{\Psi}\rangle = \sum_k c_k |\Psi_k\rangle. \quad (1.10)$$

Accordingly,

$$\langle\tilde{\Psi}|\tilde{\Psi}\rangle = 1 = \langle\tilde{\Psi}|\tilde{\Psi}\rangle = \sum_k \langle\tilde{\Psi}|\Psi_k\rangle \langle\Psi_k|\tilde{\Psi}\rangle = \sum_k |\langle\Psi_k|\tilde{\Psi}\rangle|^2 = \sum_k |c_k|^2. \quad (1.11)$$

Then the expectation value of the Hamiltonian for the trial wavefunction is given by,

$$\langle\tilde{\Psi}|\hat{H}|\tilde{\Psi}\rangle = \sum_{ij} \langle\tilde{\Psi}|\Psi_i\rangle \langle\Psi_i|\hat{H}|\Psi_j\rangle \langle\Psi_j|\tilde{\Psi}\rangle = \sum_i E_i |c_i|^2. \quad (1.12)$$

Since $E_i \geq E_0$, the expectation value is always greater than or equal to the ground state energy,

$$\langle\tilde{\Psi}|\hat{H}|\tilde{\Psi}\rangle = \sum_i E_i |c_i|^2 \geq E_0 \sum_i |c_i|^2 = E_0. \quad (1.13)$$

The variation principle, which can be expressed as an Euler equation,

$$E = \frac{\delta\langle\tilde{\Psi}|\hat{H}|\tilde{\Psi}\rangle}{\delta\langle\tilde{\Psi}|\tilde{\Psi}\rangle}. \quad (1.14)$$

provides a way to approximate the ground state energy of a system by varying the expansion coefficients, c_k , to minimize the expectation value of the Hamiltonian.

1.2.1 Density Functional Theory (DFT)

DFT is based on the Hohenberg Kohn (HK) theorems I and II.[46] HK Theorem I states that the ground state energy can be expressed in terms of the charge density of a system. Specifically, the HK theorem shows that the ground state density of a given system determines the external potential, v (up to an additive constant), and the electron number, N , and as a result, all other ground state properties.[54] The ground state energy can be written as a functional of the density,

$$E_v[\rho] = F_{HK}[\rho] + \int dr \rho(r)v(r), \quad (1.15)$$

where the HK density functional includes the kinetic energy, and electron-electron interactions,

$$F_{HK}[\rho] = T[\rho] + V_{ee}[\rho]. \quad (1.16)$$

The HK Theorem II asserts that the variational principle applies to trial densities. For a trial density satisfying

$$\tilde{\rho}(r) \geq 0 \quad (1.17)$$

$$\int dr \tilde{\rho}(r) = N \quad (1.18)$$

the resulting energy is an upper bound for the true ground state energy

$$\langle \tilde{\Psi} | \hat{H} | \tilde{\Psi} \rangle = F_{HK}[\tilde{\rho}] + \int dr \tilde{\rho}(r)v(r) = E_v[\tilde{\rho}] \geq E_v[\rho]. \quad (1.19)$$

The ground state density must also satisfy the stationary principle, assuming $E_v[\rho]$ is differentiable, and so a Lagrange multiplier, μ , is included to assure minimization

with respect to the constraint on the density

$$\delta \left\{ E_v[\rho] - \mu \left[\int dr \rho(r) - N \right] \right\} = 0 \quad (1.20)$$

This results in an Euler equation, which could be solved explicitly if the exact density functional $F_{HK}[\rho]$ was known,

$$\mu = \frac{\delta E_v[\rho]}{\delta \rho(r)} = v(r) + \frac{\delta F_{HK}[\rho]}{\delta \rho(r)}. \quad (1.21)$$

Here it is important to note the Lagrange multiplier, μ , has physical significance as the chemical potential.[54]

Determining the ground state density from a trial density involves minimizing the energy according to Equation 1.19. The constrained-search approach can be used to achieve this minimization by first searching over all wavefunctions that integrate to the ground state density to find the minimum expectation value for kinetic and electron interaction energies,ⁱⁱ $\langle \Psi | \hat{\rho}(r) | \Psi \rangle = \rho(r)$, and then out of those, searching over the densities that yield the total number of electrons, $\int dr \rho(r) = N$: [54–56]

$$E_0[\rho] = \min_{\rho \rightarrow N} \left[\min_{\Psi \rightarrow \rho} \left[\langle \Psi | \hat{T} + \hat{U} | \Psi \rangle \right] + \int dr \rho(r) v(r) \right]. \quad (1.22)$$

The Kohn-Sham (KS) formalism is a practical implementation of DFT.[47] This approach is analogous to the Hartree-Fock (HF) approximation to the Schrödinger equation, and can provide the "chemical intuition" typically sought in theoretical investigations. In the KS method, the real system is mapped to a fictitious non-interacting system with the same ground state density as the real system, which can be represented by a single Slater determinant. This allows the non-interacting kinetic

ⁱⁱNot all trial densities that integrate to the ground state density can be represented as the wavefunction for a Hamiltonian that includes an external potential $v(r)$, and this procedure first includes N-representable densities that are represented by *some* asymmetric wavefunction, thereby mitigating the initial problem.

energy, T_s to be solved exactly, while the remaining difference between the interacting and non-interacting kinetic energy is taken into account in the exchange-correlation functional. As in Equation 1.15, the total energy $E[\rho]$ can be written as a functional of the density,

$$E[\rho] = F_{KS}[\rho] + \int dr \rho(r)v(r), \quad (1.23)$$

where $v(r)$ is the external potential and $F_{KS}[\rho] = T_s[\rho] + E_H[\rho] + E_{xc}[\rho]$, where $T_s[\rho]$ is the non-interacting kinetic energy, and $E_H[\rho]$ is the classical Coulomb electron repulsion energy. The exchange-correlation energy, $E_{xc}[\rho]$, accounts for non-classical electron interactions and must be approximated in practice since the exact form of the functional is unknown. The exchange-correlation energy is defined as

$$E_{xc}[\rho] = T[\rho] - T_s[\rho] + V_{ee}[\rho] - E_H[\rho]. \quad (1.24)$$

Separating out the non-interacting kinetic energy leads to a new Euler equation defining the chemical potential

$$\mu = v_{eff}(r) + \frac{\delta T_s[\rho]}{\delta \rho(r)}, \quad (1.25)$$

where the effective KS potential is the functional derivative of the energy with respect to the density, and is given by

$$\begin{aligned} v_{eff}(r) &= v(r) + \frac{\delta E_H[\rho]}{\delta \rho(r)} + \frac{\delta E_{xc}[\rho]}{\delta \rho(r)} \\ &= v(r) + \int dr' \frac{\rho(r')}{|r - r'|} + v_{xc}(r). \end{aligned} \quad (1.26)$$

Again, here the chemical potential is equal to the variation of energy with respect to the density.

The self-consistent KS equations provide a practical procedure for finding the ground state energy in terms of the one-electron spin orbitals $\{\psi_i(r, s)\}$. The approach

requires defining an effective one-electron Hamiltonian

$$\hat{h}_{\text{eff}}\psi_i = \left[-\frac{1}{2}\nabla^2 + v_{\text{eff}}(r) \right] \psi_i = \varepsilon_i\psi_i, \quad (1.27)$$

where ε_i are the orbital energies, and the electron density is given by

$$\rho(r) = \sum_i^N \sum_s |\psi_i(r, s)|^2. \quad (1.28)$$

Then the total energy is determined by the density according to:

$$E = \sum_i^N \varepsilon_i - \frac{1}{2} \int dr dr' \frac{\rho(r)\rho(r')}{|r - r'|} + E_{xc}[\rho] - \int dr v_{xc}(r)\rho(r). \quad (1.29)$$

1.2.1.1 Limitations in DFT: Underestimated Frontier Orbital Gap

This section provides a brief formal discussion on the relationship between DFT frontier orbital energies and the ionization potential (IP) and electron affinity (EA), which are used to calculate the fundamental transport gap, E_g , in OSC molecular systems. For an N -electron system, the IP is equal to the energy required to remove an electron from the system, and the EA is equal to the energy gained when an electron is added to the system as follows:

$$IP(N) = E(N - 1) - E(N) \quad (1.30)$$

$$EA(N) = E(N) - E(N + 1), \quad (1.31)$$

where $E(x)$ refers to the ground state energy of the x electron system. Accordingly, $IP(N + 1) = EA(N)$. The fundamental gap is then given by

$$E_g(N) = IP(N) - EA(N). \quad (1.32)$$

The fundamental gap in OSC molecular systems can be measured experimentally, as discussed in Dandrade, et al., and Djurovich, et al.[16, 17], and can also be calculated from ground state energy differences as in Equation 1.32.

The physical significance of orbital energies in DFT derives from two important relations to the chemical potential, Janak’s theorem and the piecewise-linearity property.[1, 57–63] According to Janak’s theorem, the orbital energy is equal to the change in total energy with respect to occupation of that orbital,[57]

$$\frac{\partial E[\rho]}{\partial n_i} = \varepsilon_i \quad (1.33)$$

where n_i is the fractional occupation number ($0 \leq n_i \leq 1$) of orbital ψ_i , and $\rho(r) = \sum_i^N n_i \sum_s |\psi_i(r, s)|^2$. The orbital energy therefore corresponds to the chemical potential (μ) that is understood to depend on the overall electron number. However, the energy required for removing an electron from the highest occupied molecular orbital (HOMO) of the x electron system is also expressed in Equation 1.30, resulting in correspondence between the HOMO energy, ε_H^x , and the IP energy known as the IP theorem:[1]

$$\mu(x) = \begin{cases} \varepsilon_H^N = -IP(N), & N - 1 < x < N \\ \varepsilon_H^{N+1} = -IP(N + 1), & N < x < N + 1. \end{cases} \quad (1.34)$$

In OSC materials, the $IP(N)$ is different than the $IP(N + 1)$, indicating that the chemical potential is piecewise-linear from $N - 1$ to $N + 1$, changing at integer electron occupation number, N . Indeed, it has been shown that for the exact DFT functional, the total energy is piecewise-linear with respect to the change in electron number, as illustrated by the solid line in Figure 1.4, where the slope is equal to the chemical potential.[1] While these relations hold for the exact DFT energy functional, widely-used approximations (*e.g.* the LDA, GGA, or hybrid functionals) do not exhibit

the piecewise-linearity property, leading to calculated gas phase orbital energies that speciously produce condensed phase results.

The physical significance of the HOMO energies leads us to consider the relation between the fundamental gap in Equation 1.32 and the DFT HOMO-LUMO gap, $E_g^{HL}(N) = \varepsilon_L^N - \varepsilon_H^N$, where ε_L^N is the LUMO energy. We point out that the HOMO-LUMO gap is a N electron quantity, while the fundamental gap requires consideration of the $N - 1$ and $N + 1$ electron systems as well. Combining Equations 1.32 and 1.34 reveals that the fundamental and HOMO-LUMO gaps are related by the difference between the HOMO of the $N + 1$ electron system and the LUMO of the N electron system[1, 2]

$$\begin{aligned} E_g(N) - E_g^{HL}(N) &= (\varepsilon_H^{N+1} - \varepsilon_H^N) - (\varepsilon_L^N - \varepsilon_H^N) \\ &= \varepsilon_H^{N+1} - \varepsilon_L^N. \end{aligned} \tag{1.35}$$

In other words, the energy of the LUMO in the N electron system when it is empty is different than when it is occupied by a fractional charge ($x = N + f$; $0 < f < 1$).[64] This difference in LUMO energy is reflected by the change in the chemical potential that occurs at integer electron number.[1–3, 59, 64–66] As Figure 1.4 and Equation 1.39 (below) indicate, the jump in chemical potential also requires that the exact DFT potential must jump by a constant referred to as the derivative discontinuity, Δ_{xc} , where[59, 60]

$$\Delta_{xc} = v_{xc}^+(r) - v_{xc}^-(r). \tag{1.36}$$

The LUMO energy of the $N + f$ electron system at the limit $f \rightarrow 0$ is determined by the potential $v_{xc}^+(r)$ resulting in $\varepsilon_L^+ = -EA$. However, when determined by the potential $v_{xc}^-(r)$ corresponding to the $N - f$ electron system (i.e. the potential at which $\varepsilon_H^N = -IP(N)$), the LUMO differs from the $-EA$ by a constant: $\varepsilon_L^- = -EA - \Delta_{xc}$. [64] Accordingly, the difference between the HOMO-LUMO gap and fundamental gap in

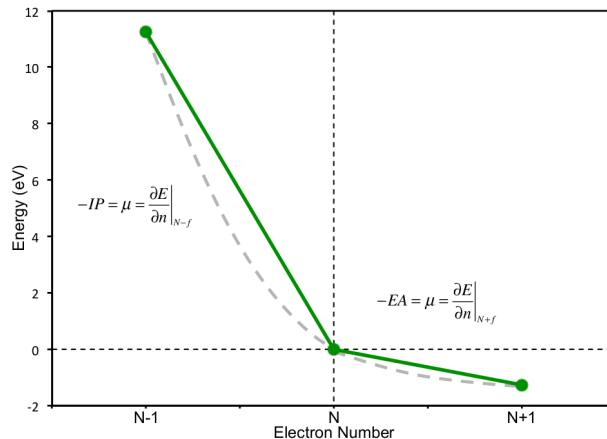


Figure 1.4: The energy should be piecewise linear dependent on the electronic occupation number in the grand canonical ensemble.[1] Here this behavior is illustrated using the experimental gas phase IP and EA of carbon (green solid curve). [Data are taken from the National Institute of Standards and Technology web book at (<http://webbook.nist.gov>).] At integer electron numbers, the chemical potential exhibits a discontinuity. Widely-used implementations of DFT do not possess this discontinuity, compensating for the change in chemical potential via curvature (shown schematically here as the gray dashed curve).[2, 3]

Equation 1.35 is equal to the derivative discontinuity:.[2, 3, 64, 67]

$$\begin{aligned}
 E_g(N) - E_g^{HL}(N) &= IP(N) - EA(N) - (\varepsilon_L^N - \varepsilon_H^N) \\
 &= \Delta_{xc}
 \end{aligned}
 \tag{1.37}$$

In general, the derivative discontinuity arises when we consider an x electron system, where $x = N \pm f$ and $0 < f < 1$. The chemical potential of an x electron system is given by Eq. 1.34, according to which the chemical potential exhibits a discontinuity at integer electron number (i.e., $x = N$), as shown in Figure 1.4.[1] According to Eq. 1.25, the difference in the chemical potential at the limit $f \rightarrow 0$ for

$N \pm f$ is given by

$$\begin{aligned}\Delta\mu &= \lim_{f \rightarrow 0} \{\mu(N+f) - \mu(N-f)\} \\ &= \lim_{f \rightarrow 0} \left\{ \left[v_{eff}(r) + \frac{\delta T_s[\rho]}{\delta \rho(r)} \right] \Big|_{N+f} - \left[v_{eff}(r) + \frac{\delta T_s[\rho]}{\delta \rho(r)} \right] \Big|_{N-f} \right\}.\end{aligned}\quad (1.38)$$

The external potential and classical Coulomb potential are continuous with respect to the density, and so do not contribute to the discontinuity at integer particle number.[2, 64–68] Therefore the change in chemical potential is related to the kinetic energy and exchange correlation potential, so that Eq. 1.38 becomes

$$\Delta\mu = \lim_{f \rightarrow 0} \left[\frac{\delta T_s[\rho]}{\delta \rho(r)} \Big|_{N+f} - \frac{\delta T_s[\rho]}{\delta \rho(r)} \Big|_{N-f} + \frac{\delta E_{xc}[\rho]}{\delta \rho(r)} \Big|_{N+f} - \frac{\delta E_{xc}[\rho]}{\delta \rho(r)} \Big|_{N-f} \right]. \quad (1.39)$$

It has been shown that the difference in kinetic energy terms in Eq. 1.39 are equal to the DFT orbital energies, so that the change in chemical potential is due to the difference in orbital energies plus the derivative discontinuity, Δ_{xc} , [60, 67]

$$\begin{aligned}\Delta\mu &= \varepsilon_L^N - \varepsilon_H^N + v_{xc}^+(r) - v_{xc}^-(r) \\ &= \varepsilon_L^N - \varepsilon_H^N + \Delta_{xc}.\end{aligned}\quad (1.40)$$

The difference in chemical potential at the limit $f \rightarrow 0$ for $N \pm f$ is also given by the fundamental gap. according to Eq. 1.34.

$$\begin{aligned}\Delta\mu &= -IP(N+1) - (-IP(N)) \\ &= IP(N) - EA(N) \\ &= E_g\end{aligned}\quad (1.41)$$

Equating $\Delta\mu$ and E_g also leads to Eq. 1.37, where the difference in the fundamental gap and the HOMO-LUMO gap is given by the Δ_{xc} .

While the exact DFT energy functional must possess a discontinuity in the chemical potential, conventional approximate DFT functionals are analytical and therefore do not possess the required derivative discontinuity.ⁱⁱⁱ[69] Instead, the approximate potentials compensate for the missing Δ_{xc} , exhibiting curvature at integer particle number instead of piecewise-linear behavior as illustrated by the dashed curve in Figure 1.4.[2, 64, 68] As a result, the v_{xc}^- underestimates and v_{xc}^+ overestimates the chemical potential at the limit where $f \rightarrow 0$. This behavior results in $-\varepsilon_H$ ($-\varepsilon_L$) values that are lower (higher) than the experimental *IP* (*EA*). Namely, within approximate DFT, the HOMO-LUMO gap underestimates the fundamental gap.

1.2.2 Time-Dependent Density Functional Theory (TDDFT)

Analogous to the HK theorems, TDDFT is based on the Runge-Gross (RG) theorems, which state that the time-dependent external potential, up to a spatially constant, time dependent function, and the the time dependent wavefunction, up to a phase factor, are determined by the exact time dependent electron density of the system.[48] The RG theorems also include a variational principle based on the action instead of on the total energy. We consider a wavefunction that is the solution to the time-dependent Schrödinger equation

$$i \frac{\partial}{\partial t} \Psi(r, t) = \hat{H}(r, t) \Psi(r, t) = [\hat{T}(r) + \hat{V}_{ee}(r) + \hat{V}_{ne}(r) + \hat{V}(t)] \Psi(r, t) \quad (1.42)$$

where the external time-dependent potential is the sum of one-electron time dependent potentials

$$\hat{V}(t) = \sum_i^N \hat{v}(r_i t) \quad (1.43)$$

ⁱⁱⁱIt was recently shown that within an ensemble DFT approach, conventional functionals such as the LDA can in fact possess a derivative discontinuity.[69] However, these discontinuities do not affect standard calculations which do not follow the ensemble approach.

and the density is given by

$$\rho(r, t) = \int dr |\Psi(r, t)|^2. \quad (1.44)$$

Then the action, which is given by,

$$A[\rho] = \int_{t_0}^{t_1} dt \langle \Psi[\rho](r, t) | i \frac{\partial}{\partial t} - \hat{H}(rt) | \Psi[\rho](r, t) \rangle \quad (1.45)$$

should be stationary with respect to variations of the density,

$$\frac{\delta A[\rho]}{\delta \rho(r, t)} = 0. \quad (1.46)$$

Similar to ground state DFT, the KS approach can be applied to provide a practical way to minimize the action with respect to the density. The Hamiltonian can be separated into an internal Hamiltonian independent of the external potential and an external part that does depend on the potential, and so the action can likewise be separated in terms of a universal action, $B[\rho]$, independent of the external potential for a given number of electrons.

$$A[\rho] = B[\rho] - \int_{t_0}^{t_1} dt dr \rho(r, t) v(r, t), \quad (1.47)$$

where the universal action is given by

$$B[\rho] = \int_{t_0}^{t_1} dt \langle \Psi[\rho](r, t) | i \frac{\partial}{\partial t} - \hat{T}(r) + \hat{V}_{ee}(r) | \Psi[\rho](r, t) \rangle \quad (1.48)$$

According to the KS approach, the real time-dependent system can be mapped to a fictitious non-interacting system with the same time-dependent density. The non-interacting system can be represented by a single Slater determinant composed of

single electron orbitals that are solutions to the time-dependent Schrödinger equation:

$$i\frac{\partial}{\partial t}\phi_i(r, t) = \left(-\frac{1}{2} + v(r, t) + \int dr' \frac{\rho(r', t)}{|r - r'|} + \frac{\delta A_{xc}}{\delta \rho(r, t)}\right)\phi_i(r, t) \quad (1.49)$$

where,

$$\rho(r, t) = \sum_i^N \sum_s |\psi_i(r, s, t)|^2. \quad (1.50)$$

Here the time-dependent KS potential, $v_S(r, t)$ is given by

$$v_S(r, t) = v(r, t) + \int dr' \frac{\rho(r', t)}{|r - r'|} + \frac{\delta A_{xc}}{\delta \rho(r, t)}. \quad (1.51)$$

The action of the real system can be written in terms of the universal action of the non-interacting system,

$$A[\rho] = B_S[\rho] - \int_{t_0}^{t_1} dt dr \rho(r, t) v(r, t) - \frac{1}{2} \int_{t_0}^{t_1} dt \int dr \int dr' \frac{\rho(r, t) \rho(r', t)}{|r - r'|} - A_{xc}[\rho] \quad (1.52)$$

where

$$B_S[\rho] = \int_{t_0}^{t_1} dt \langle \Psi[\rho](r, t) | i\frac{\partial}{\partial t} - \hat{T}_S(r) | \Psi[\rho](r, t) \rangle \quad (1.53)$$

and

$$A_{xc}[\rho] = B_S[\rho] - \frac{1}{2} \int_{t_0}^{t_1} dt \int dr \int dr' \frac{\rho(r, t) \rho(r', t)}{|r - r'|} - B[\rho]. \quad (1.54)$$

This gives a new Euler equation (when evaluated at the exact interacting density to preserve causality)[70, 71]

$$\frac{\delta B[\rho]}{\delta \rho(r, t)} \Big|_{\rho=\rho(r, t)} = v_S(r, t). \quad (1.55)$$

The functional derivative of the exchange-correlation action is extremely complex, and therefore the adiabatic approximation is applied so that the ground state

exchange correlation potential can be used in practice. The adiabatic approximation assumes the exchange-correlation action is local in time so that the variation of the action with respect to the time-dependent density is equivalent to the variation of the energy with respect to the density evaluated at time, t :

$$v_{xc}[\rho](r, t) = \frac{\delta A_{xc}[\rho]}{\delta \rho(r, t)} \cong \frac{\delta E_{xc}[\rho]}{\delta \rho_t(r)} = v_{xc}[\rho_t](r). \quad (1.56)$$

In order to obtain excited state properties, the time-dependent KS equations can be written in terms of linear response theory, which provides the time-dependent response of the density of the ground state system to a weak perturbing electric field. The change in the ground state density of a system in response to a small change in the external potential is given by[72]

$$\delta \rho_\sigma(r, \omega) = \sum_{\sigma'} \int dr' \chi_{\sigma\sigma'}(r, r', \omega) \delta v_{ext\sigma'}(r', \omega), \quad (1.57)$$

where $\chi(r, r', \omega)$ is the linear density response function. In terms of the KS orbitals, this function becomes

$$\delta \rho_\sigma(r, \omega) = \sum_{\sigma'} \int dr' \chi_{KS\sigma\sigma'}(r, r', \omega) \delta v_{KS\sigma'}(r', \omega), \quad (1.58)$$

where the variation in the KS potential is

$$\delta v_{KS\sigma}(r, \omega) = \delta v_{ext\sigma}(r, \omega) + \int dr' \frac{\delta \rho(r', \omega)}{|r - r'|} + \sum_{\sigma'} \int dr' f_{xc\sigma\sigma'}(r, r', \omega) \delta \rho_{\sigma'}(r', \omega) \quad (1.59)$$

where $\delta \rho = \delta \rho \uparrow + \delta \rho \downarrow$ and $f_{xc\sigma\sigma'}(r, r', \omega)$ is the Fourier transform of the exchange correlation kernel,

$$f_{[xc\sigma\sigma']}[\delta \rho \uparrow, \delta \rho \downarrow](r, r', t - t') = \frac{\delta v_{xc\sigma}[\delta \rho \uparrow, \delta \rho \downarrow](r, t)}{\delta \rho_{\sigma'}(r', t')} \quad (1.60)$$

The linear density response function is given by,

$$\chi_{KS\sigma\sigma'}(r, r', w) = \delta_{\sigma\sigma'} \sum_{jk}^{\infty} (f_{k\sigma} - f_{j\sigma}) \frac{\phi_{j\sigma}(r) \phi_{j\sigma}^*(r') \phi_{k\sigma}(r') \phi_{k\sigma}^*(r)}{\omega - (\varepsilon_{j\sigma} - \varepsilon_{k\sigma}) + i\eta}, \quad (1.61)$$

where $\phi_{j\sigma}$ and $\varepsilon_{j\sigma}$ are the KS orbitals and corresponding energies, $f_{j\sigma}$ is the orbital occupation number, and η is a positive infinitesimal. Applying algebraic manipulations and the single pole approximation, which assumes a single particle excitation between one occupied and one virtual orbital, results in the Casida equations, where the linear response is represented as an eigenvalue problem (in the random phase approximation [RPA]):[51, 52, 73, 74]

$$\begin{pmatrix} A & B \\ B^* & A^* \end{pmatrix} \begin{pmatrix} X \\ Y \end{pmatrix} = \omega \begin{pmatrix} 1 & 0 \\ 0 & -1 \end{pmatrix} \begin{pmatrix} X \\ Y \end{pmatrix} \quad (1.62)$$

Here X and Y represent the occupied-to-virtual and virtual-to-occupied contributions to the perturbation density in the molecular orbital representation, and ω is the transition frequency. The matrix elements A and B are given by

$$\begin{aligned} A_{ia\sigma, jb\sigma'} &= (i_{\sigma} a_{\sigma} | r_{12}^{-1} | j_{\sigma'} b_{\sigma'}) + (1 - c_{HF}) (i_{\sigma} a_{\sigma} | f_{\sigma\sigma'} | j_{\sigma'} b_{\sigma'}) \\ &\quad - c_{HF} \delta_{\sigma\sigma'} (i_{\sigma} j_{\sigma} | r_{12}^{-1} | a_{\sigma'} b_{\sigma'}) + \delta_{\sigma\sigma'} \delta_{ij} \delta_{ab} (\epsilon_{a\sigma} - \epsilon_{i\sigma'}) \end{aligned} \quad (1.63)$$

$$\begin{aligned} B_{ia\sigma, jb\sigma'} &= (i_{\sigma} a_{\sigma} | r_{12}^{-1} | b_{\sigma'} j_{\sigma'}) + (1 - c_{HF}) (i_{\sigma} a_{\sigma} | f_{\sigma\sigma'} | b_{\sigma'} j_{\sigma'}) \\ &\quad - c_{HF} \delta_{\sigma\sigma'} (i_{\sigma} b_{\sigma} | r_{12}^{-1} | a_{\sigma'} j_{\sigma'}) \end{aligned} \quad (1.64)$$

where i, j and a, b are indices for the ground-state occupied orbitals and virtual orbitals, respectively, σ, σ' are the spin indices, ϵ is the orbital energy, c_{HF} is the percentage of HF exchange included in a hybrid functional.

1.2.2.1 Limitations in TDDFT: Underestimated Charge Transfer Excitations

The approximate implementations of TDDFT can pose serious limitations, for example, in treating CT states.[75–80] The limitations for treating CT using TDDFT are due, in part, to the inability of conventional local exchange-correlation kernels to account for the distance-dependent exchange contributions when treating transitions between orbitals with zero spatial overlap.[80–85] This failure can be observed by considering Equations 1.63 and 1.64.

In the case of a transition between spatially separated orbitals (*off-site*), when using a pure density exchange-correlation functional ($c_{HF} = 0$), all terms in A and B vanish due to orthogonality, except for the last term in A [Equation 1.63], which corresponds to the energy difference between participating orbitals.[80] In this way, the CT excitation energies are approximated as the energy difference between the spatially separated orbitals. If these orbitals are, for example, frontier orbitals in a donor-acceptor system, such as potential building blocks for organic semiconducting materials, then the CT state energy is underestimated due to underestimated orbital energies, which result from the missing derivative discontinuity in the exchange correlation functional.[1, 57, 59, 60, 86–90] The CT state energies can be further underestimated since the electrostatic electron-hole interaction is neglected. As a result, the CT state energies lack the correct distance dependence, and are equal to the orbital energy difference regardless of the separation between the charges.

When a hybrid XC-functional is used, the exchange term in A does not vanish [third term in Equation 1.63], but depends linearly on c_{HF} , and thus partial distance dependence is captured in the excitation energy. The third term in B [Equation 1.64] will vanish however, because the spatial overlap will be zero for i, b , and j, a when the spatial overlap is non-zero for i, j and a, b . Although hybrid functionals may partially compensate for some of the discrepancy in *off-site* excitation energies, the

final result often remains significantly underestimated as a result of underestimated orbital energies.

The B terms are neglected in the Tamm-Dancoff Approximation (TDA)[91–93], and so the TDA expression for a charge transfer state becomes equivalent to the full TDDFT. Therefore, for pure CT excitations, TDDFT and TDA predict the same excitation energies.[80, 91–93] These relations are confirmed for the *off-site* excitations in the symmetric systems that are analyzed in Chapter 2.

1.2.3 Range-Separated Hybrid Functionals as Solutions to DFT Limitations

RSH functionals have been designed to overcome the limitations of conventional functionals discussed above.[88, 90, 94–106] These functionals are based on the Generalized KS (GKS) formalism, in which the KS scheme is extended to include non-local effective potentials, $v_{eff}(r, r')$. [88, 89]

The KS approach provides a way to minimize the expectation value of the Hamiltonian (see Equation 1.22), without requiring calculation of the many-body wavefunction. Instead, the wavefunction can be replaced with a Slater determinant, composed of single-particle orbitals, that refers to a non-interacting system with the same density. The GKS scheme extends this idea to interacting reference systems, where some of the electron-interactions are incorporated along with the kinetic energy.[89] In this way, the expectation value of the Hamiltonian is expected to approach the true energy of the real system, depending on the choice of reference system.

The HK functional in Equation 1.23 can be rewritten in terms of a functional of the Slater determinants corresponding to the reference system, $S[\Phi]$, and the remainder part related to electron interactions not taken into account by $S[\Phi]$, referred to as

the GKS correlation energy, E_c^{GKS} [89, 90]

$$F_{HK}[\rho] = F_S[\rho] + R_S[\rho]. \quad (1.65)$$

Then the total energy is given by

$$\begin{aligned} E_0[\rho] &= \min_{\rho \rightarrow N} \left[F_S[\rho] + E_c^{GKS}[\rho] + \int dr \rho(r)v(r) \right] \\ &= \min_{\rho \rightarrow N} \left[\min_{\Phi \rightarrow \rho} S[\Phi] + E_c^{GKS}[\rho] + \int dr \rho(r)v(r) \right] \\ &= \min_{\Phi \rightarrow N} \left[S[\Phi] + E_c^{GKS}[\rho[\Phi]] + \int dr \rho([\Phi]; r)v(r) \right] \\ &= \min_{\{\phi_i\} \rightarrow N} \left[S[\{\phi_i\}] + E_c^{GKS}[\rho[\{\phi_i\}]] + \int dr \rho([\{\phi_i\}]; r)v(r) \right]. \end{aligned} \quad (1.66)$$

The resulting GKS equations are analogous to the KS equations, however, the exchange-correlation energy is an orbital functional in the GKS approach.

$$\left(-\frac{1}{2}\nabla^2 + v(r) + v_H(r) \right) \phi_j(r) + \hat{K}_x \phi_j(r) + v_c^{GKS}(r)\phi_j(r) = \varepsilon_j \phi_j(r) \quad (1.67)$$

where

$$\hat{K}_x \phi_j(r) = \frac{\delta E_x^{GKS}}{\delta \phi_j(r)} = - \sum_i^N \phi_i(r) \int dr' \frac{\phi_k(r')\phi_k(r')}{|r - r'|} \quad (1.68)$$

and

$$v_c^{GKS}(r) = \frac{\delta E_c^{GKS}}{\delta \rho(r)}. \quad (1.69)$$

According to this approach, RSH can incorporate exact non-local exchange to accurately treat the long range Coulomb interactions. The exchange consists of two terms, one corresponding to long-range and another to short-range contributions via a range-separation parameter, γ :

$$E_{xc}^{RSH}[\{\phi_j\}] = E_x^{GKS}[\{\phi_j\}] + \int dr \varepsilon_c^\gamma(\rho(r))\rho(r) + \left[\int dr \varepsilon_x^{\gamma-HEG}(\rho(r))\rho(r) - E_x^\gamma[\{\phi_j\}] \right] \quad (1.70)$$

where $\varepsilon_x^{\gamma-HEG}$ and ε_c^γ are the exchange and correlation energies per electron (in this case, for the homogeneous electron gas), and where

$$E_x^\gamma[\{\phi_j\}] = \frac{1}{2} \int dr \int dr' \left| \sum_j \phi_j(r) \phi_j(r') \right|^2 y_\gamma(|r - r'|). \quad (1.71)$$

$E_x^\gamma[\{\phi_j\}]$ accounts for short-range, screened electron interactions via $y_\gamma(|r - r'|)$, which is often the Yukawa potential, $y_\gamma(r) = \frac{e^{-\gamma r}}{r}$, or the complimentary error function, $y_\gamma(r) = \frac{\text{erfc}(\gamma r)}{r}$

The corresponding GKS equations for the RSH approach are given by

$$\left(-\frac{1}{2}\nabla^2 + v(r) + v_H(r) + v_x^\gamma(r) + v_c^\gamma(r)\right)\phi_j(r) + \hat{K}_x^\gamma\phi_j(r) = \varepsilon_j\phi_j(r) \quad (1.72)$$

where

$$K_x^\gamma\phi_j(r) = \frac{\delta E_x^\gamma}{\delta\phi_j(r)} = -\sum_i^N \phi_i(r) \int dr \phi_k(r') \phi_k(r') \bar{y}_\gamma(|r - r'|). \quad (1.73)$$

and \bar{y}_γ is a complimentary electron interaction. The sum of the exchange interactions for adhere to the correct asymptotic decay of the potential with particle separation, which is why the complimentary switching functions between short and long range interactions are required: $\frac{1}{r} = \frac{\text{erfc}(\gamma r)}{r} + \frac{\text{erf}(\gamma r)}{r}$. [90]

1.2.3.1 Solutions to DFT Limitations

RSH functionals can provide a practical means to address the underestimated frontier orbital gap in DFT by reducing the size of the derivative discontinuity [107] and by minimizing the curvature in $v_{\text{eff}}(r)$, thereby mimicking the correct piecewise linear behavior. [2, 3, 66, 108, 109]

First of all, it has been shown that the non-local contributions to the Δ_{xc} are included in the GKS orbital energies along with the kinetic energy terms, resulting in a larger HOMO-LUMO gap and smaller Δ_{xc} in the GKS approach than in the KS

approach.[107] Secondly, γ can be tuned to minimize the difference in IP and $-\varepsilon_H$ of the neutral (N) and anionic ($N + 1$) electron systems, and thereby minimize the curvature in $v_{eff}(r)$. [86] In this scheme, the parameter is determined by minimizing $J^2(\gamma)$, [86]

$$J^2(\gamma) = \sum_{x=N,N+1} [IP^\gamma(x) + \varepsilon_H^\gamma(x)]^2. \quad (1.74)$$

This optimal tuning procedure minimizes the curvature of the chemical potential at integer electron number, reducing the underestimation of the $-\varepsilon_H$ (IP) values. [2, 66, 86, 108, 110, 111] Equation 1.74 also reduces overestimation of the $-\varepsilon_L$ (EA) when the the difference in ε_L^N and ε_H^{N+1} (i.e., Δ_{xc}) is small.

RSH functionals address the limitations of TDDFT in treating transitions between spatially separated orbitals. It is the explicit non-local HF exchange in the XC-potential, $r^{-1}f_{lr}(\gamma r)$, which prevents the long-range Coulomb interaction term (third term in A [Equation 1.63]) from vanishing. [85] Therefore, when a RSH functional is employed, the matrix element for an *off-site* excitation with zero spatial overlap between orbitals i and a is given by,

$$A_{ia,jb}^{RSH}(off-site) = \delta_{\sigma\sigma'}\delta_{ij}\delta_{ab}(\epsilon_{a\sigma} - \epsilon_{i\sigma'}) - \delta_{\sigma\sigma'}(i_\sigma j_\sigma | r_{12}^{-1} f_{lr}(\gamma r_{12}) | a_{\sigma'} b_{\sigma'}) \quad (1.75)$$

The excitation energy for transitions between spatially separated orbitals is then equal to the orbital energy gap minus the distance-dependent Coulomb interaction.

While the system-dependent OT-RSH approach is an important step forward in improving the capability of DFT to reliably describe charge polarization and transfer in OSC materials, these approaches are not without limitations. For example, including an optimally-tuned range-separation parameter is known to violate size consistency. Karolewski, et al. recently reported errors related to this issue. [112] Körzdörfer, et al. have also examined the range-separation parameter within the OT-RSH approach for polymers and other OSC molecules, demonstrating the γ de-

pendence on system size and orbital character.[113, 114] These limitation does not seem to affect the quality of the OT-RSH treatment in the small to medium-sized OSC molecular building blocks considered in this thesis.

CHAPTER II

Benchmarking Novel Range Separated Hybrid Density Functionals for Ground and Excited State Properties

2.1 Orbital Gap Predictions for Rational Design of Organic Photovoltaic Materials

Contributions: Conception and design of study; acquisition, analysis, and interpretation of data; drafting and revision of final version to be published.

2.1.1 Introduction

Significant computational efforts have been recently focused on developing design principles for organic photovoltaics (OPV) and organic light emitting diodes (OLED).[8, 16–45] An important aspect of device design is understanding how fundamental properties of organic semiconducting (OSC) molecules are affected by the environment. For example, the ionization potential (IP) and electron affinity (EA) of OSCs play a vital role in electron transfer and transport processes, and these values have been shown to depend on the molecular environment in which they are measured.[16, 17, 115] Several studies investigating such environmental effects com-

pare gas phase, solution, and thin film experiments, thereby addressing the confusion in the literature related to the different types of IP and EA measurements. [16, 17] Unfortunately discrepancies still remain in the comparison between experimental and calculated properties, a particularly notable example of which is the accidental agreement between gas phase calculated orbital energies and condensed phase measured IPs and EAs.[16–19, 21, 22, 40, 41, 116]

While in general it is expected that computational modeling provides fundamental understanding of molecular systems, theoretical insights are unreliable when the underlying computational method succeeds due to an uncontrolled cancellation of errors.[18, 19, 21] Despite the benefits of using the DFT computational approach, widely-used implementations of DFT have been shown to systematically underestimate the IP, and overestimate the EA, obtained from calculated molecular orbital energies.[2, 64, 66, 69, 87, 108, 117] In fact, these values calculated at the gas phase erroneously compare quite well with condensed phase IP and EA measurements, rendering the resulting molecular level insights uncertain. [17–19, 21, 22, 40] For example, Djurovich et al. pointed out the correlation between inverse photoelectron spectroscopy EA measurements performed on thin films and calculated lowest unoccupied molecular orbital (LUMO) energies (ε_L) of single molecules in the gas phase.[17]

Clearly, gas phase calculations should not account for solid state effects, which are expected to vary across the wide range of OSC molecules. Instead, environmental effects should be carefully taken into account. Indeed, properly considering these effects in conventional DFT calculations reveals the specious agreement between gas phase orbital energies and condensed phase IP and EA measurements.

This work demonstrates the previously observed discrepancies in conventional DFT methods for predicting (gas phase) IP and EA energies of relevant OSC molecules.[1, 40, 66] Optimally-tuned range-separated hybrid (OT-RSH) DFT approaches offer improvements to gas phase IP and EA energies compared to conventional approaches.[1,

2, 40, 66, 108, 111] In particular, this study shows the improved modeling for condensed phase IP and EA properties of OSC molecules afforded by an OT-RSH DFT based approach. Specifically, we show that

1. orbital energies calculated at the gas phase using OT-RSH functionals compare well to gas phase measured IPs and EAs, thereby improving the notoriously underestimated band gap associated with conventional functionals.
2. orbital energies corrected for solid state effects using a polarizable continuum model (PCM) compare well to experimentally measured thin film IP and EA, thereby achieving reliable modeling of electron transport properties.

Thus, this study demonstrates that the OT-RSH approach achieves a predictive quality in modeling IP and EA properties and therefore can provide a theoretical foundation for developing design principles in organic optoelectronic devices.

2.1.2 Computational Methods

In this study, we analyze the IP and EA of a subset of the OSC molecules considered in Djurovich, et al., as shown in Figs. 2.1 and 2.2.[17] Molecular geometries were calculated using the B3LYP[118–121] functional. IP and EA were calculated from the orbital energies obtained using both B3LYP functional and the OT-RSH Baer-Neuhauser-Livshits functional (BNL).[86, 102, 103] Calculations were performed using the cc-pVTZ basis set, except for the CuPc molecule, for which calculations utilized the LANL2DZ effective core potential for the metal atom and 6-311+G(d,p) basis set for all other atoms. All calculations were performed using the Q-Chem version 4.1 software package.[122]

To approximate thin film effects on the RSH-BNL IP and EA values,[18, 19, 21] we also obtained the IPs and EAs using total energy differences of the neutral and ionic species (also known as the Δ SCF method[123]) at both the gas phase

and using the switching gaussian conductor-like screening model (SWIG-COSMO) PCM.[124–126] The PCM calculation for each molecule was carried out using the corresponding dielectric constant of that molecule. The dielectric constants were calculated according to the Clausius-Mossotti equation, which expresses the dielectric constant of a material by:

$$\epsilon = \left(1 + \frac{8\pi\alpha}{3V}\right) \left(1 - \frac{4\pi\alpha}{3V}\right)^{-1} \quad (2.1)$$

where ϵ is the dielectric constant, α is the isotropic polarizability, and V is the molecular volume. The isotropic polarizability was calculated using the B3LYP functional. The molecular volume was approximated based on the molecular surface area determined from the van der Waals surface generated during the PCM calculation.[18, 19, 21] The molecular volume was defined as the volume contained within a sphere having a surface area equivalent to the calculated molecular surface area. The calculated solvent parameters are provided in Appendix A.

The thin film IPs and EAs were determined by a direct calculation of the total energy using PCM, as well as by applying a PCM-based correction to the gas phase orbital energies. The environment-affected orbital energies are determined by adding the PCM effect on the IP and EA to the gas phase orbital energies:

$$\epsilon'_H = \epsilon_H + [IP^{\text{gas-phase}} - IP^{\text{PCM}}] \quad (2.2)$$

$$\epsilon'_L = \epsilon_L + [EA^{\text{gas-phase}} - EA^{\text{PCM}}] \quad (2.3)$$

The $IP^{\text{gas-phase}}$ and $EA^{\text{gas-phase}}$ are defined in Eqs. 2.4 and 2.5:

$$IP(N)^{\text{gas-phase}} = E(N-1)^{\text{gas-phase}} - E(N)^{\text{gas-phase}} \quad (2.4)$$

$$EA(N)^{\text{gas-phase}} = E(N)^{\text{gas-phase}} - E(N+1)^{\text{gas-phase}}. \quad (2.5)$$

where $E(x)$ refers to the ground state energy of the x electron system. The IP^{PCM} and EA^{PCM} are the total PCM energy differences (ΔSCF) between the neutral, anion, and cation energies expressed as:

$$IP^{\text{PCM}} = E^{\text{PCM}}(N - 1) - E^{\text{PCM}}(N) \quad (2.6)$$

$$EA^{\text{PCM}} = E^{\text{PCM}}(N) - E^{\text{PCM}}(N + 1) \quad (2.7)$$

In all OT-RSH PCM calculations, the optimization parameter (γ) is set to the corresponding gas phase value according to Equation 1.74.[111] This approximation is valid when the condensed phase environment (e.g. thin film) corresponds to a relatively weak polarizing dielectric resulting with little effect on the electronic densities of neutral molecule, as is the case for the molecules in this study. We point out that the PCM model is appropriate to represent the electrostatic environment effects, though more direct solid-state (periodic) calculations are another option that has been pursued.[111, 127]

2.1.3 Results and Discussion

We begin by comparing our computational results to gas phase measurements of the IP and EA for a benchmark set of small molecular OSC materials. The experimental gas phase energies used for comparison in this study were obtained from the NIST database,ⁱ except for those of phthalocyanines for which we used values reported by Berkowitz.ⁱⁱ[131] Figure 2.1 provides a comparison between the experimen-

ⁱData are taken from the National Institute of Standards and Technology web book at [<http://webbook.nist.gov>]. The given values are the averages of the different experimental gas-phase vertical ionization potentials and electron affinities reported in the web book.

ⁱⁱThe values reported in the NIST database by Eley, et. al.[128] for H₂Pc and CuPc (7.36 eV and 7.37 eV, respectively) differ from values reported in later studies.[129, 130] The later studies utilized experimental gas-phase IP energies for H₂Pc and CuPc (6.41 eV and 6.38 eV, respectively) reported by Berkowitz.[131] Berkowitz acknowledges that values reported in previous work by Eley, et al. may contain artifacts from the experimental method. Furthermore, a recent GW-BSE study corroborates the Berkowitz measurement.[130] In the current study, therefore, we compare our calculated results to the experimental values reported by Berkowitz.

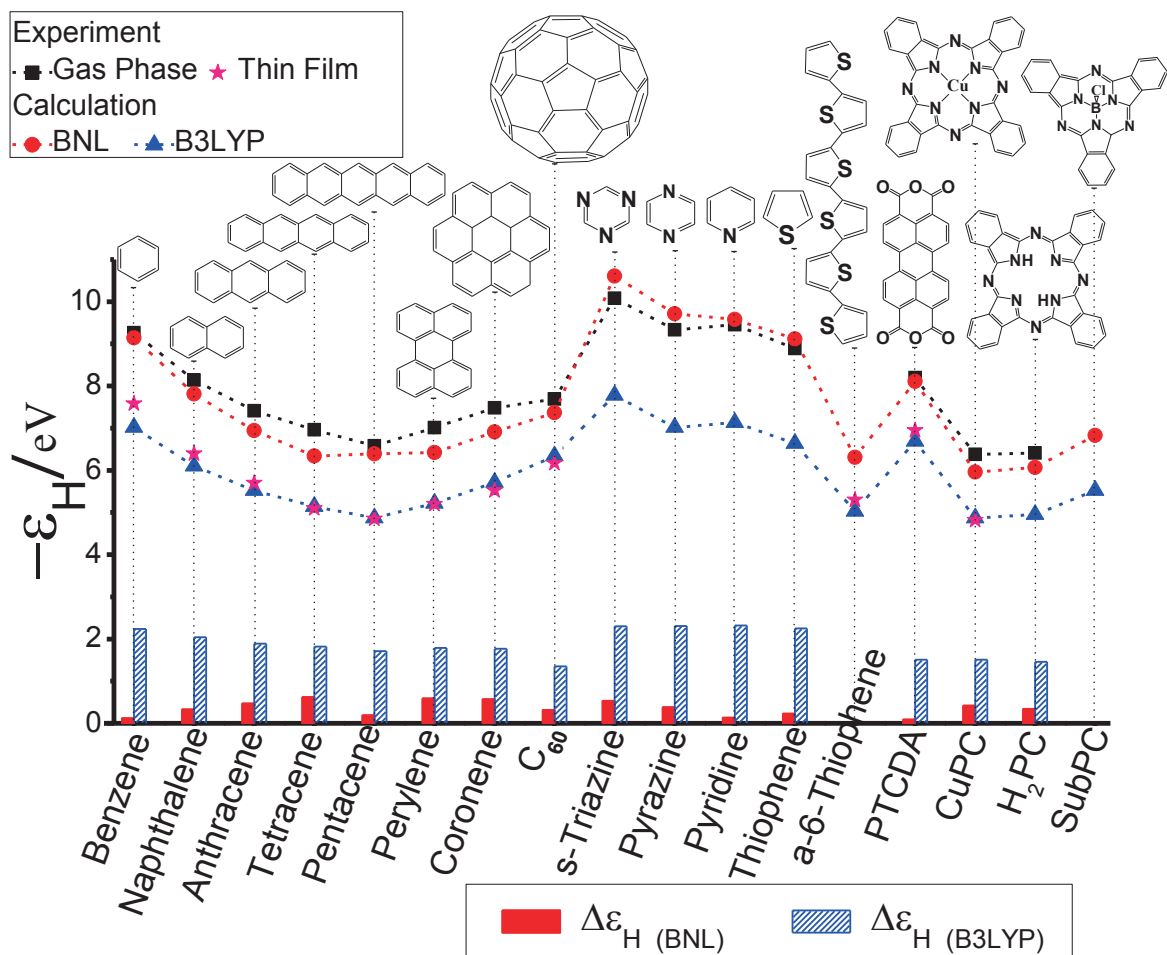


Figure 2.1: OT-BNL and B3LYP $-\epsilon_H$ calculated at the gas-phase compared to experimental IP measured in gas and condensed phase. Absolute errors between *gas phase* calculated and experimental energies are given by $\Delta\epsilon_H = |\epsilon_H^{calc} - \epsilon_H^{exp}|$ (eV)

tally measured and calculated IP values for a range of small molecules with potential applications in optoelectronic devices. As shown in Figure 2.1, the OT-RSH BNL $-\varepsilon_H$ agrees well with the experimental gas phase IP energies. The absolute errors, $\Delta\varepsilon_H$, between the gas phase experimental and calculated results are provided in the bottom of Figure 2.1. The mean absolute error (MAE) and standard deviation of $\Delta\varepsilon_H$, 0.35 eV and 0.18 eV, respectively, are provided in Table 2.1. The $\Delta\varepsilon_H$ for the set of molecules range from 0.06 eV to 0.62 eV. Similarly, the OT-BNL $-\varepsilon_L$ energies are compared to experimental EAs in Figure 2.2. The MAE and standard deviation of $\Delta\varepsilon_L$, 0.56 eV and 0.26 eV, respectively, are also provided in Table 2.1. As shown in Table 2.1, the MAE and standard deviation of $\Delta\varepsilon_L$ are larger than for $\Delta\varepsilon_H$. This trend is expected, since the EA is only equal to ε_L when $\varepsilon_L(N) = \varepsilon_H(N + 1)$, according to Equation 1.34.

In all cases, the OT-BNL functional predicts orbital energies in better agreement with gas phase experimental values than the conventional B3LYP functional. Table 2.1 points out that the MAE of 1.92 eV between gas phase B3LYP $-\varepsilon_H$ and experimental IP energies is substantially higher than the BNL value of 0.35 eV. Likewise, the MAE between calculated and experimental EA energies for B3LYP, 1.32 eV, is also greater than that for BNL, 0.56 eV. While the standard deviations of $\Delta\varepsilon_{H/L}$ are similar in magnitude for BNL and B3LYP, the approaches exhibit opposite trends regarding the variation of $\Delta\varepsilon_H$ compared to $\Delta\varepsilon_L$. For B3LYP, the standard deviation is greater for $\Delta\varepsilon_H$ than $\Delta\varepsilon_L$. This could be attributed to the fairly homogenous subset of molecules with experimental EAs considered in this study (e.g., mostly acenes), though as mentioned previously, we would typically expect the trend found for the BNL functional. A greater variation in $\Delta\varepsilon_L$ than $\Delta\varepsilon_H$ is expected to result from the more accurate association between IP and $-\varepsilon_H$, as well as the derivative discontinuity that may distinguish EA from $-\varepsilon_L$. It is also important to note that the absolute error does not reflect a constant shift from the experimental values. Instead, we stress

	B3LYP		BNL	
	MAE	Std. Dev.	MAE	Std. Dev.
$\Delta\varepsilon_H$	1.92	0.37	0.35	0.18
$\Delta\varepsilon_L$	1.32	0.11	0.56	0.26

Table 2.1: MAE and standard deviation of gas phase ε_H ($\Delta\varepsilon_H$) and ε_L ($\Delta\varepsilon_L$) [eV]

that the calculated EAs and IPs depend on the electron density for each molecule, resulting with a molecule-dependent absolute error. Indeed, a simple shifting of the gas-phase B3LYP frontier orbital gaps by a system-independent constant value would not achieve the detailed molecular insight sought from *ab-initio* calculations.

Next we proceed to consider the IP/EA of the OSC materials at the solid phase. Experimental IP and EA values of thin films measured using ultraviolet photoelectron spectroscopy and inverse photoelectron spectroscopy, reported by Djurovich, et al., provide the solid state $-\varepsilon_{H/L}$ energies used to compare with calculated results.[17] The difference shown here between the gas phase and thin film IPs illustrates the dependence of these energies on the molecular environment.[16–19, 21, 22] Furthermore, it was recently shown that the various dipolar environments in condensed phases can significantly affect molecular properties such as IP.[115] On the other hand, the comparisons in Figs.2.1 and 2.2 indicate that the gas phase B3LYP orbital energies misleadingly appear to reproduce the solid state experimental measurements. Such findings reiterate that orbital energies calculated for single molecules should be treated with caution, as they may not provide molecular insight into condensed phase properties.

The OT-RSH approach substantially improves the description of gas phase molecular properties, where the frontier orbital energies correspond better to IP and EA. As explained above, this success is essentially achieved by assuring the correspondence of the frontier molecular orbital energies to the fundamental gap properties

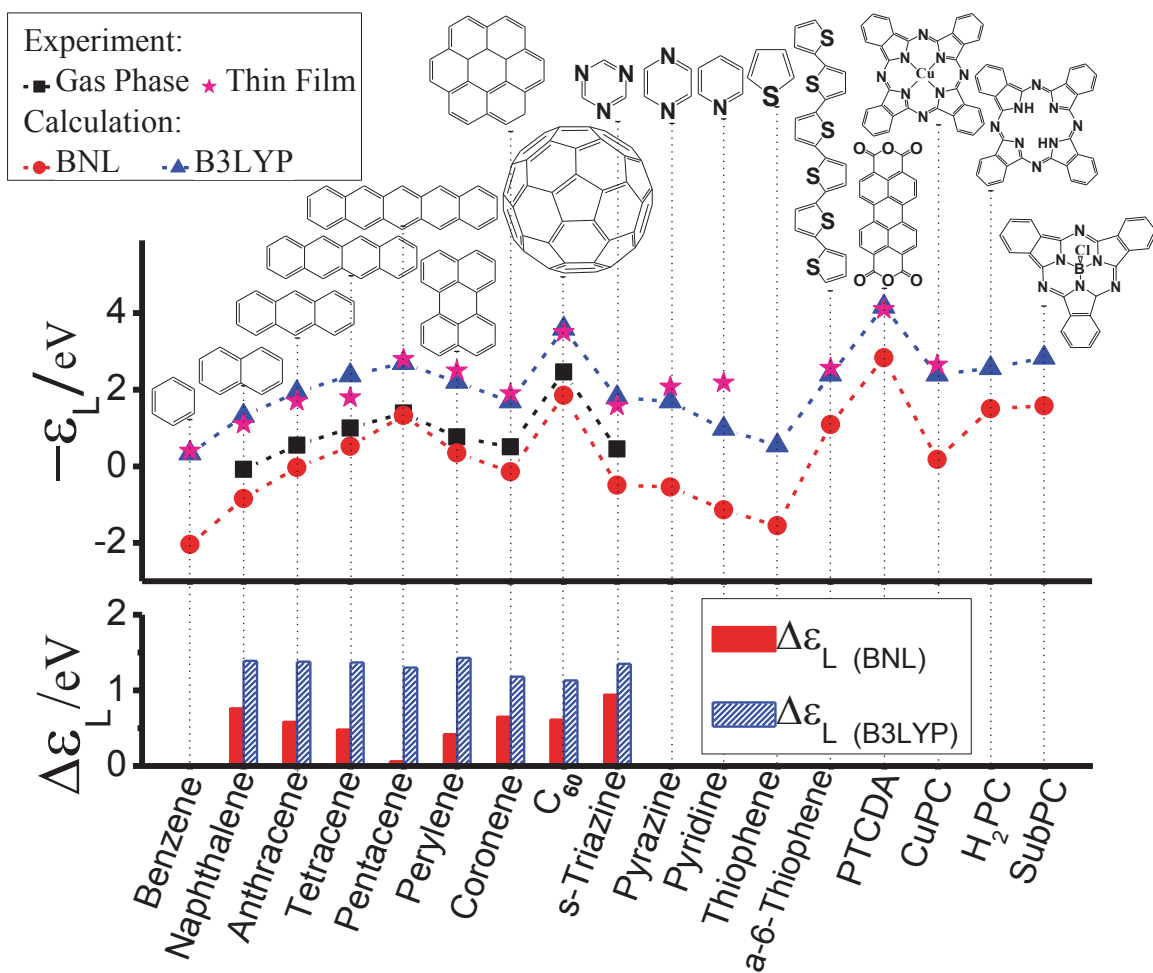


Figure 2.2: OT-BNL and B3LYP $-\varepsilon_L$ calculated at the gas-phase compared to experimental EA measured in gas and condensed phase. Absolute errors between gas phase calculated and experimental energies are given by $\Delta\varepsilon_L = |\varepsilon_L^{calc} - \varepsilon_L^{exp}|$ (eV)

(IP and EA values). We next address extending the RSH approach to treat condensed phase effects. Before proceeding, however, we point out that Δ SCF IP and EA values calculated with conventional functionals in combination with PCM can reproduce measured values quite well.[18, 19, 21] However, we are concerned of the use of densities within functionals that do not provide a consistent value for IPs and EAs when comparing with the corresponding frontier molecular orbital energies. In such cases, the success of the Δ SCF cannot be extended to provide predictive quality in modeling optoelectronic properties. On the other hand, as shown below our approach provides consistent Δ SCF and orbital energies and therefore provides for a reliable platform to model molecular level optoelectronic properties affected by an extended electrostatic environment.

Indeed, an important advantage of OT-RSH functionals is the correspondence of the IP/EA and orbital energies in the gas phase. This correspondence is also observed for the condensed-phase adjusted models. Figures 2.3 and 2.4 provide a comparison between experimental thin film and calculated IP and EA energies. Namely, we compare experimental values to calculated $IP(EA)^{PCM}$ [Eqs. 2.6 and 2.7] and corrected orbital energies [Eqs. 2.2 and 2.3]. As shown in Figure 2.3, the electrostatic environment effect calculated using the OT-BNL functional leads to environment-affected orbital energies ε'_H that remain consistent with IP^{PCM} values.

The correspondence between IP^{PCM} and ε'_H , as expected, is not confirmed for the B3LYP orbital energies. The B3LYP environment-affected orbital energies underestimate the experimentally measured values, even though the B3LYP IP^{PCM} energies agree with the BNL IP^{PCM} energies. The mean and standard deviation of the absolute error in condensed phase IP (ΔIP^{PCM}) and orbital energies ($\Delta \varepsilon'_H$) are given in Table 2.2. Importantly, the MAE for BNL $\Delta \varepsilon'_H$, 0.25 eV, is substantially lower than the corresponding B3LYP value of 1.17 eV. Indeed, the B3LYP $\Delta \varepsilon'_H$ and ΔIP^{PCM} differ substantially in contrast to BNL calculations, even though the standard deviations

are similar for all calculations. Therefore, while B3LYP can predict the solid state corrections using Δ SCF energies with relative accuracy, the orbital energies remain significantly underestimated as in the gas phase calculations, leading to unreliable condensed phase IP and EA values.

Similarly, when solid state effects on the EA energies are considered, BNL EA^{PCM} and $-\varepsilon'_L$ energies remain more consistent than compared to the conventional functional. Both B3LYP and BNL approaches seem to provide comparable EA^{PCM} energies, though they slightly underestimate the experimental EA. On the other hand, the B3LYP $-\varepsilon'_L$, as observed in the Figure 2.4 trend, is inconsistent with the other calculated values and overestimates the EA. Therefore, while Table 2.2 indicates that the MAE in $-\varepsilon'_L$ is similar between BNL and B3LYP functionals, only the BNL $-\varepsilon'_L$ features the correct trend between the calculated EA^{PCM} and orbital energy values.

We point out that the similarity in MAE results from the discrepancies between calculations for two molecules in this study: pyridine and pyrazine. Indeed, while the experimental trend suggests that the EA becomes larger for the triazine, pyrazine, and pyridine molecular series, all the calculated trends predict the EA to decrease instead. This failure to reproduce the trend seems to reflect limitations in the PCM to capture the specific solid state effects for these molecules. Clearly, a continuum model cannot account for differences in dipolar contributions arising from varied crystal structures, which have been confirmed to affect measured IPs.[115] When the pyrazine and pyridine values are excluded from the MAE calculations [values included in parenthesis in Table 2.2], clearly the BNL $-\varepsilon'_L$ is in better agreement with experimental data than the B3LYP $-\varepsilon'_L$, with a MAE of 0.76 eV compared to 1.06 eV.

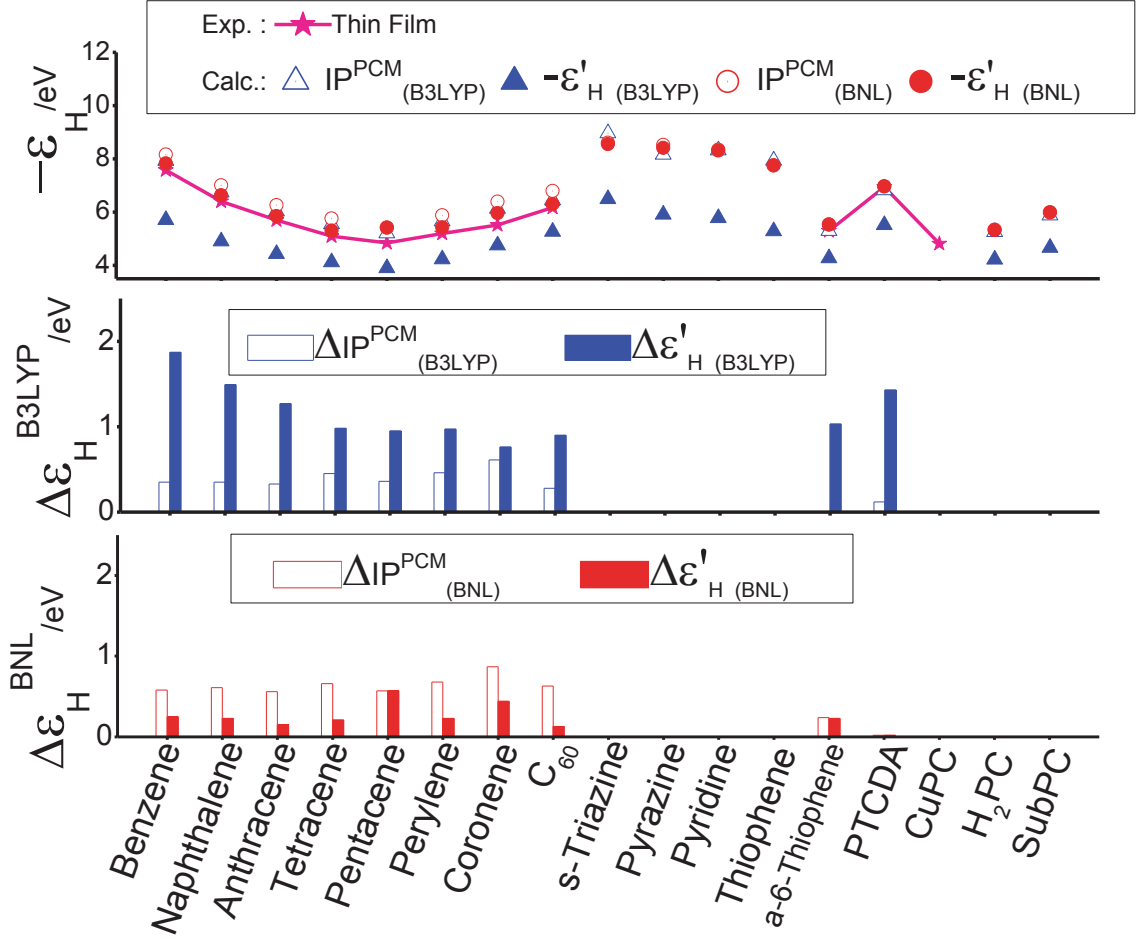


Figure 2.3: Calculated OT-BNL and B3LYP IP^{PCM} and ε'_H compared to the measured thin film IP. Absolute errors between *condensed phase* calculated and experimental energies are shown in the lower panels and are given by $\Delta x = |x^{\text{calc}} - x^{\text{exp}}|$ (eV)

	B3LYP		BNL	
	MAE	Std. Dev.	MAE	Std. Dev.
ΔIP^{PCM}	0.33	0.17	0.54	0.24
ΔEA^{PCM}	0.68 (0.50)	0.51 (0.22)	0.69 (0.52)	0.47 (0.21)
$\Delta \varepsilon'_H$	1.17	0.34	0.25	0.16
$\Delta \varepsilon'_L$	0.96 (1.06)	0.43 (0.36)	0.90 (0.76)	0.45 (0.28)

Table 2.2: MAE and standard deviation between thin film experimental and calculated IP and EA (values in parenthesis exclude pyrazine and pyridine values) [eV]

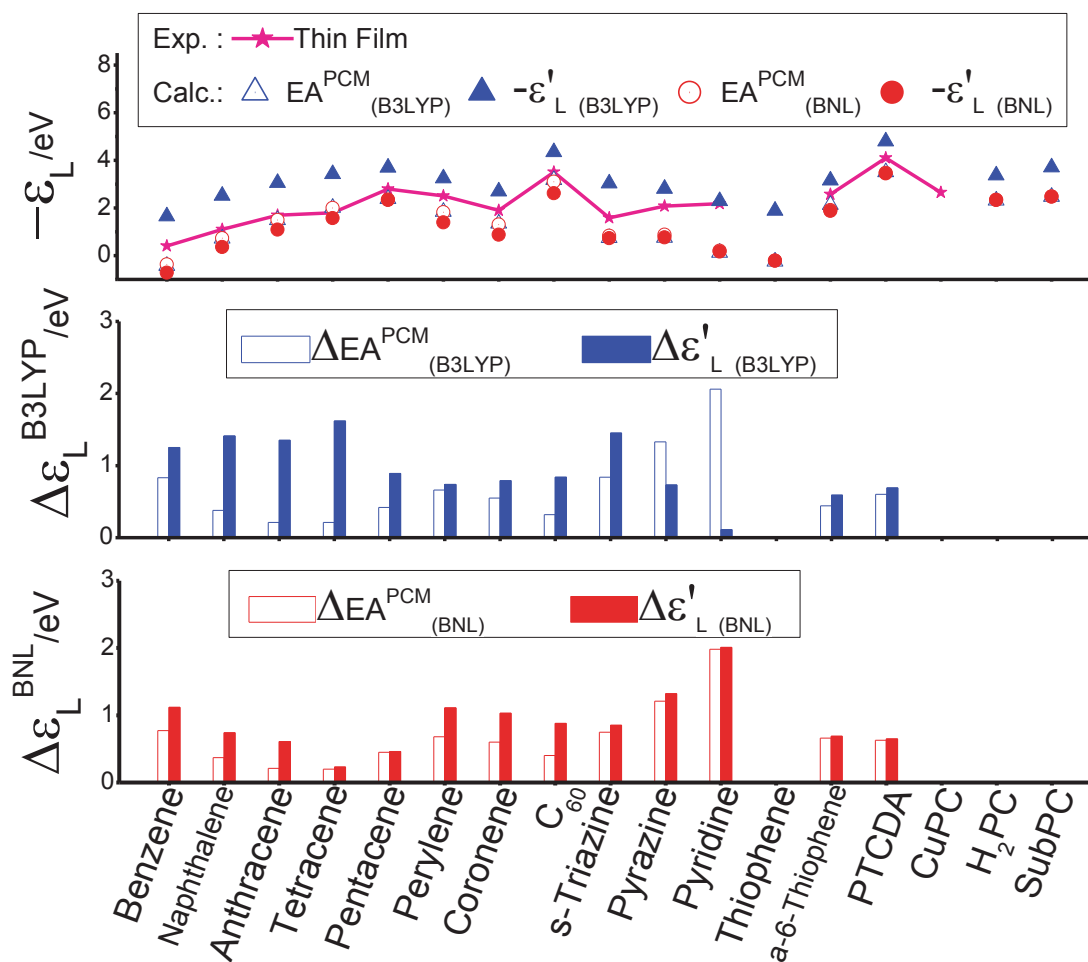


Figure 2.4: Calculated OT-BNL and B3LYP EA^{PCM} and ε'_L compared to the measured thin film EA. Absolute errors between calculated and experimental energies are shown in the lower panels and are given by $\Delta x = |x^{\text{calc}} - x^{\text{exp}}|$ (eV)

2.1.4 Conclusions

This study highlights the importance in accounting for the molecular environment when considering optoelectronic properties of OSC materials. Specifically, we revisit the well known orbital gap issue in DFT, demonstrating the disparity between gas phase experimental IP and EA measurements and gas phase orbital energies calculated using conventional functionals. We then proceed to consider IPs and EAs measured in thin film environments relevant for optoelectronic applications. Unfortunately, the specious agreement between gas phase orbital energies and condensed phase IP and EA measurements weakens the theoretical insight that can be reliably gained from such calculations. Modern OT-RSH functionals offer a solution to the orbital gap problem in the gas phase, and can be combined with a polarizable continuum model (PCM) to address the condensed phase effects on the IP and EA. The success of the OT-RSH/PCM approach provided in this study also agrees with a recent study where screened-RSH functionals were shown to capture the effects of a solid state environment on the $\varepsilon_{H/L}$ energies.[111] These findings also indicate the importance in properly accounting for environmental effects to achieve predictive modeling of optoelectronic properties. Overall, this study illustrates the success of the combined OT-RSH/PCM scheme to gain insight into fundamental molecular properties affected by electrostatic environments.

2.2 Calculating Off-Site Excitations in Symmetric Donor-Acceptor Systems via Time-Dependent Density Functional Theory with Range-Separated Density Functionals

Contributions: Conception and design of study; acquisition, analysis, and interpretation of data; drafting and revision of final version to be published.

2.2.1 Introduction

Systematically improving the performance and efficiency of OPV devices calls for detailed molecular understanding of the underlying charge separated states and charge transfer (CT) processes within these devices. Since a purely experimental characterization of these states and processes is difficult, it is beneficial to use theoretical modeling and *ab-initio* calculations for this purpose. TDDFT is a cost-effective approach to calculating electronic excited states, however serious limitations can affect the reliability of this approach for OSC systems, where CT excitations are of interest.[75–80] The failure of these methods can appear more pronounced in model systems, such as those considered in this study.

Previously, conventional TDDFT was shown to underestimate *off-site* excitation energies even when no net transfer of charge is involved.[81–83] For instance, a previous study considered the low-lying $\pi - \pi^*$ excitations in a symmetric ethene (C_2H_4) dimer system, which correspond to the transition between the monomer highest occupied and lowest unoccupied molecular orbitals, HOMO and LUMO respectively.[81–83] Four excitations were observed: Two *on-site* excitations, which were localized on each monomer, and two *off-site* excitations, which each involves CT from the HOMO of one ethene to the LUMOⁱⁱⁱ of the other (see 2.5). In this case, the CT due to the *off-site* excitations is vanishing when the two states are assigned equal weights. The two states are degenerate due to the system symmetry. We point out that the MO representation is arbitrary and can be chosen to be localized on each monomer (as shown in 2.5), or delocalized over the dimer, that is, written as symmetrical and anti-symmetrical linear combinations with equal weights for the monomer-localized orbitals.[85] We emphasize that in either two possible MO representations, localized

ⁱⁱⁱThe $\pi - \pi^*$ excitation corresponds to the 1b1u to 1b2g orbital transition for all functionals considered in this study. In the Hartree-Fock approximation, the 1b1u orbital is the HOMO, however the 1b2g orbital is the LUMO+4 instead of the LUMO (which has 4 Ag symmetry). This is a basis set effect, and does not occur when a smaller basis is employed, such as 6-31G*. For the conventional functionals in this study, the LUMO does possess 1b2g symmetry

and delocalized, we obtain pairs of equivalent excited states (further discussed in the Supporting Information provided in Appendix B). In the delocalized representation, each of the two states are of non-CT character, whereas in the localized representation, each of the states exhibit CT character and are mirror images of each other. Though the degenerate *off-site* excitations in a symmetric dimer possess zero net CT, due to the inherent CT nature of the individual *off-site* excitations, their energies are poorly described by conventional TDDFT.

This study demonstrates the ability of RSH functionals to correctly treat *off-site* CT excitations. The aim is two-fold:

1. Demonstrate that the shortcomings of conventional functionals in treating *off-site* CT excitations[81] can be more severe in symmetric systems, characterized by zero net CT. More specifically, we show that a qualitatively correct ordering of the excited electronic energy levels may be accidentally achieved as a result of symmetry-breaking. Thus, conventional functionals may fail in cases involving zero net CT, while they may appear qualitatively correct in cases involving non-zero net CT.
2. Demonstrate that the Baer-Neuhauser-Livshitz (BNL) RSH functional is able to accurately predict the *off-site* excitation energies in both the symmetrical and symmetry-broken cases, via applications to the spatially separated model ethene dimer and experimentally relevant dye-functionalized silsesquioxane (SQ). In a previous study, the BNL functional was shown to successfully capture *off-site* excitations between strongly coupled orbitals in oligoacenes.[85] Here we use modes in spatially separated dimer model systems to follow the effect of symmetry breaking on the *off-site* states' energies.

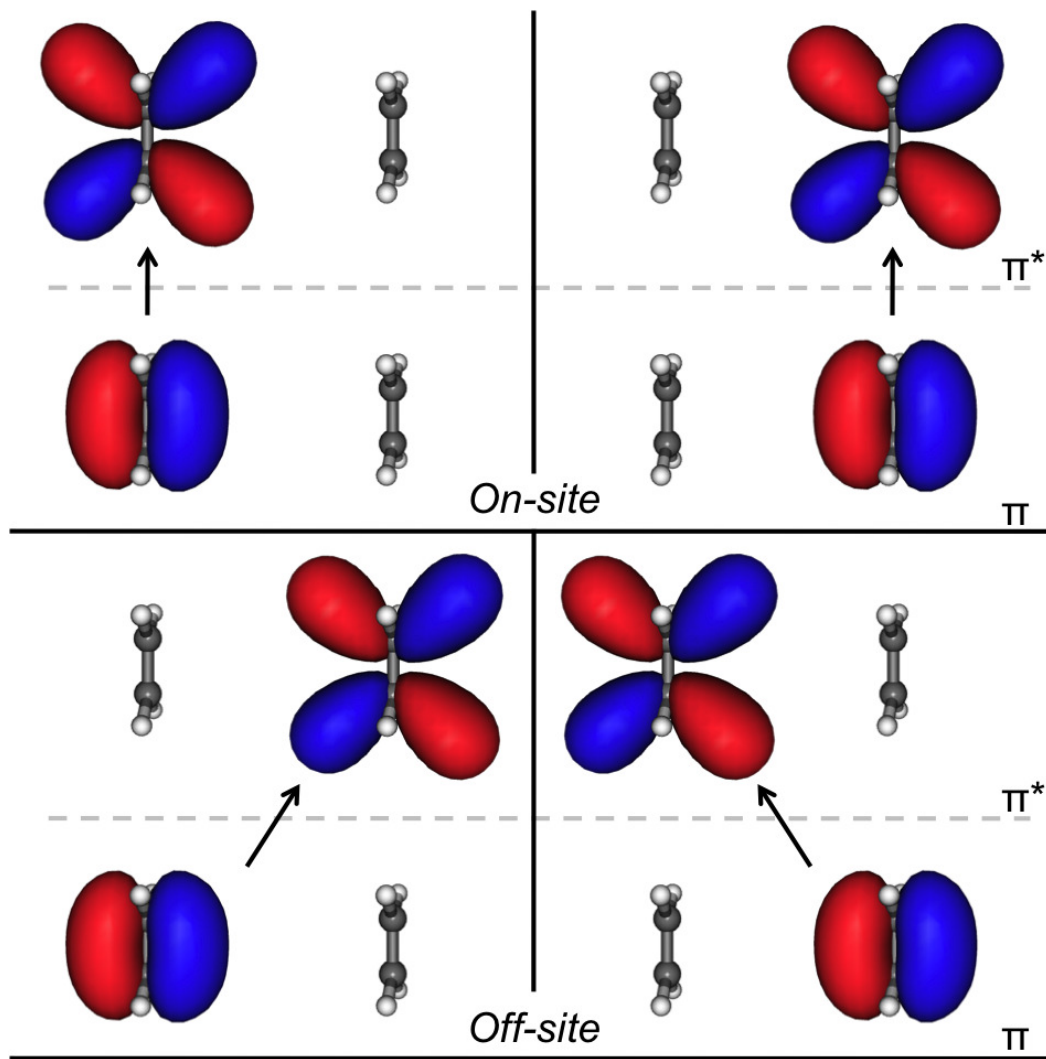


Figure 2.5: The four possible $\pi - \pi^*$ excitations of the ethene dimer. The two *on-site* excitations and two *off-site* excitations are shown in the top and bottom panels, respectively. Orbital degeneracy in symmetric dimers allows the excitations to be written also as linear combinations of the individual *off-site* excitations pictured above, which can conceal the underlying CT nature evidenced in the localized MO representation.

2.2.2 Computational Methods

We begin our analysis by considering the ethene dimer model system previously used to demonstrate the shortcomings of the standard functionals in symmetric systems.[81] We then extend the analysis to the case of functionalized SQs. It should be noted that chromophore-functionalized SQs have recently drawn attention due to the ability to tune their optoelectronic properties by the choice of chromophores.[4, 35, 132, 133]

Two types of excitations are considered in our study: the *on-site* low-lying excitations, which are transitions between occupied and unoccupied orbitals localized on the same species, and the corresponding *off-site* excitations, which are transitions between an occupied orbital localized on one species and an unoccupied orbital localized on the other (see Figure 2.5). At sufficiently large dimer separation, the *on-site* excitations coincide with those of the isolated molecules. In the case of symmetric dimers, the *off-site* excitations have no preference for CT due to orbital degeneracy. We therefore also examine the effect of systematic symmetry breaking, which removes the degeneracy to reveal the CT nature of these excitations.

In the ethene dimer model, we consider two symmetry-breaking schemes. In one scheme, an electric field is applied, and in the other scheme, the bond of one ethene is stretched while that of the other ethene remains unchanged. The qualitative effect of these two symmetry breaking schemes on the orbital gap energies is illustrated in Figure 2.6. In the case where an electric field is applied, both orbital energies are shifted (i.e. gated) by a similar amount, thereby maintaining almost the same orbital gap. In the case of the bond stretching, the HOMO energy of the stretched ethene increases while the LUMO energy decreases to reduce the orbital gap.

All calculations were carried out using a developer version of the Q-Chem Program Package version 4.0.[122] The molecular geometry of the ethene monomer was optimized at the B3LYP//cc-pVTZ level of theory. TDDFT calculations on the monomer

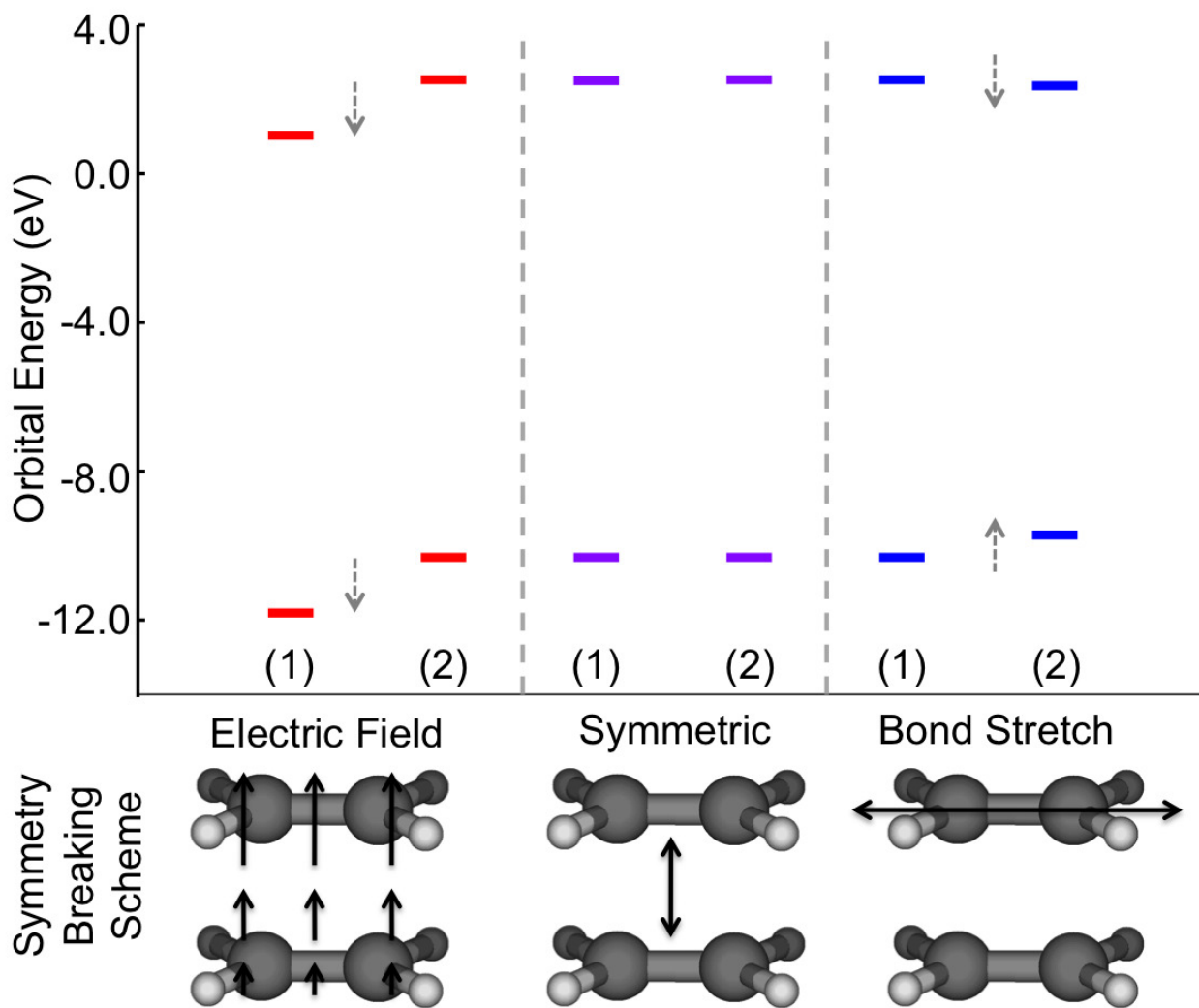


Figure 2.6: Top: Ethene dimer orbital energies (eV) for symmetric (purple), symmetry broken by electric field (0.1V) (red), and symmetry broken by bond stretching (0.102 Å from equilibrium) (blue). The results shown were obtained for a dimer where the ethenes are 15 Å apart, using the HF approximation. Bottom: Pictorial description of dimer separation and symmetry breaking schemes.

and dimer systems were performed using the aug-cc-pVTZ basis set, with the Slater-Dirac (LDA),^[134] PBE (GGA),^[135] B3LYP (hybrid),^[118–121] and BNL (RSH)^[102, 103] functionals, and the HF approximation. The BNL is a recently developed RSH functional that has been used to successfully treat CT state energies.^[37, 85, 136–138] The range-separation parameter (γ) for the BNL functional was independently determined for each system according to 1.74. The parameter values for the ethene dimer system were centered around 0.40 a.u., and values for the vinylstilbene-SQ systems were 0.20 a.u. All values are listed in Appendix C. All orbitals and densities were visualized using the Molekel program.^[139]

2.2.3 Results and Discussion

In this study, we consider the lowest singlet valence excitations corresponding to $\pi - \pi^*$ transitions^[81]. The excitation energies and corresponding orbital gaps for the *ethene monomer* predicted by each functional are listed in Table 2.3. Importantly, the BNL corresponding orbital gap,^{iv} of 12.4 eV, differs by only 0.1 eV from the fundamental gap, 12.3 eV, which was determined using the experimental IP (10.5 eV) and EA (-1.8 eV) values.^[140] The excitation energy predicted by both HF and B3LYP is 7.46 eV. The B3LYP orbital gap of 5.45 eV is lower than that predicted by HF and BNL. The PBE and LDA functionals both predict lower excitation energies and orbital gaps than HF and BNL. The orbital gap for the BNL functional is found to be slightly lower than the HF orbital gap, however the BNL excitation energy is slightly higher.

To examine *off-site* excitations, we consider dimers where the ethenes are separated by 4 Å to 15 Å. First, we confirm that at the largest separation distance, 15 Å,

^{iv}For BNL, as for HF, the 1b1u orbital is the HOMO, and the 1b2g orbital is the LUMO+4, where the LUMO has 4 Ag symmetry. We compare the corresponding (1b1u-1b2g) orbital gap of the $\pi - \pi^*$ excitation to the fundamental gap, due to the significance of the IP and EA in transfer of an electron between ethene monomers. For reference, the BNL HOMO-LUMO gap, 11.2 eV, differs only 1.1 eV from the fundamental gap, outperforming the conventional functionals considered in this study

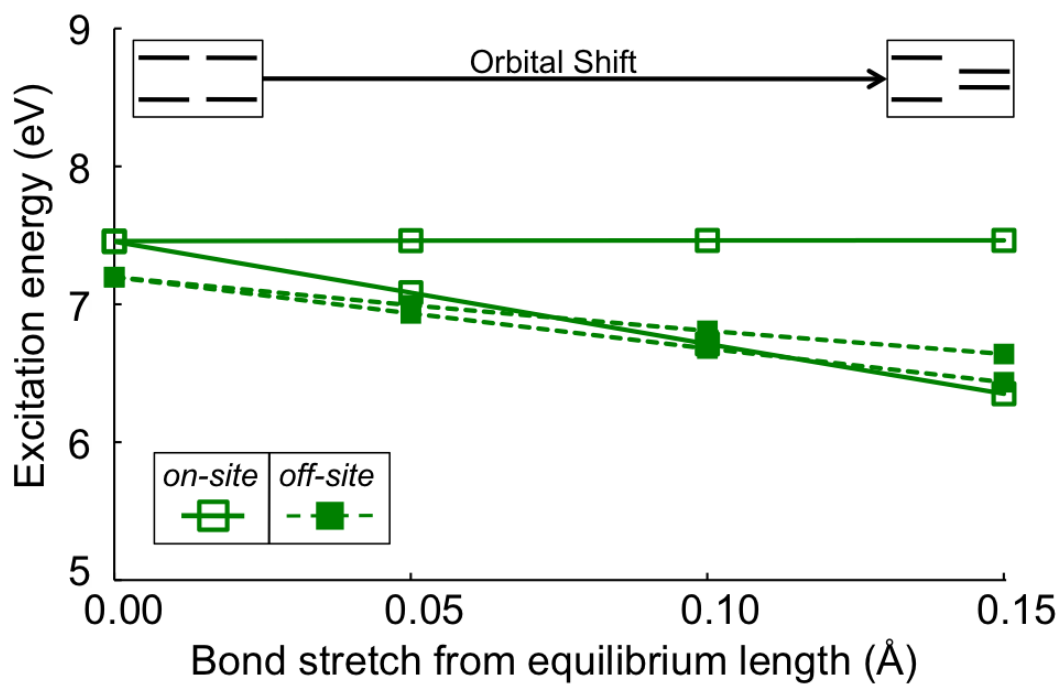


Figure 2.7: B3LYP excitation energies (eV) as the bond of one ethene is increasingly stretched at a dimer separation of 15 Å. A schematic illustrating the orbital shift induced by the bond stretching is included to clarify the changes in excitation energies.

XC-functional	Excitation Energy	Orbital Gap
HF	7.46	12.82
BNL	7.59	12.41
B3LYP	7.46	7.37
PBE	6.97	5.58
LDA	7.18	5.63

Table 2.3: Excitation energy and corresponding orbital gap for isolated ethene (eV)

the excitation energies and orbital gaps are the same as the corresponding energies of the isolated molecule (orbital energies are included in Appendix C). We then illustrate the limitations of TDDFT with conventional XC-functionals in Figure 2.7. In this case we consider the ordering of the *on-site* and *off-site* excitation energies as a function of stretching the C=C bond in one of the ethene molecules. Indeed, as local functionals cannot account for the energy required to separate the electron-hole pair, TDDFT B3LYP underestimates the *off-site* excitation energies in the symmetric case. The symmetry breaking induced by stretching the bond in one of the ethenes stabilizes the *off-site* states and even more so the corresponding *on-site* state (see Figure 2.7). These trends result in an accidental correct ordering of the *off-site* excitation energies above the *on-site* energy for a sufficiently symmetry-broken system.

Importantly, in symmetric systems, the CT nature of *off-site* excitations can be hidden due to orbital degeneracy. However, these excitation energies remain underestimated within B3LYP. Likewise, in the symmetry-broken dimer, the *off-site* excitations are obviously CT in nature, but the failure of B3LYP can be hidden by the accidental correct ordering of the excitation energies due to the extent in which the orbital degeneracy is broken. The problem is enhanced as the electronic structure becomes more complex. For example, though the *on-site* and *off-site* excitations are clearly designated in the ethene dimer, the assignment is much more difficult in systems such as fully-functionalized 8-vinylstilbene-OHSQ.

In the next step, we show that the RSH BNL functional correctly handles *off-*

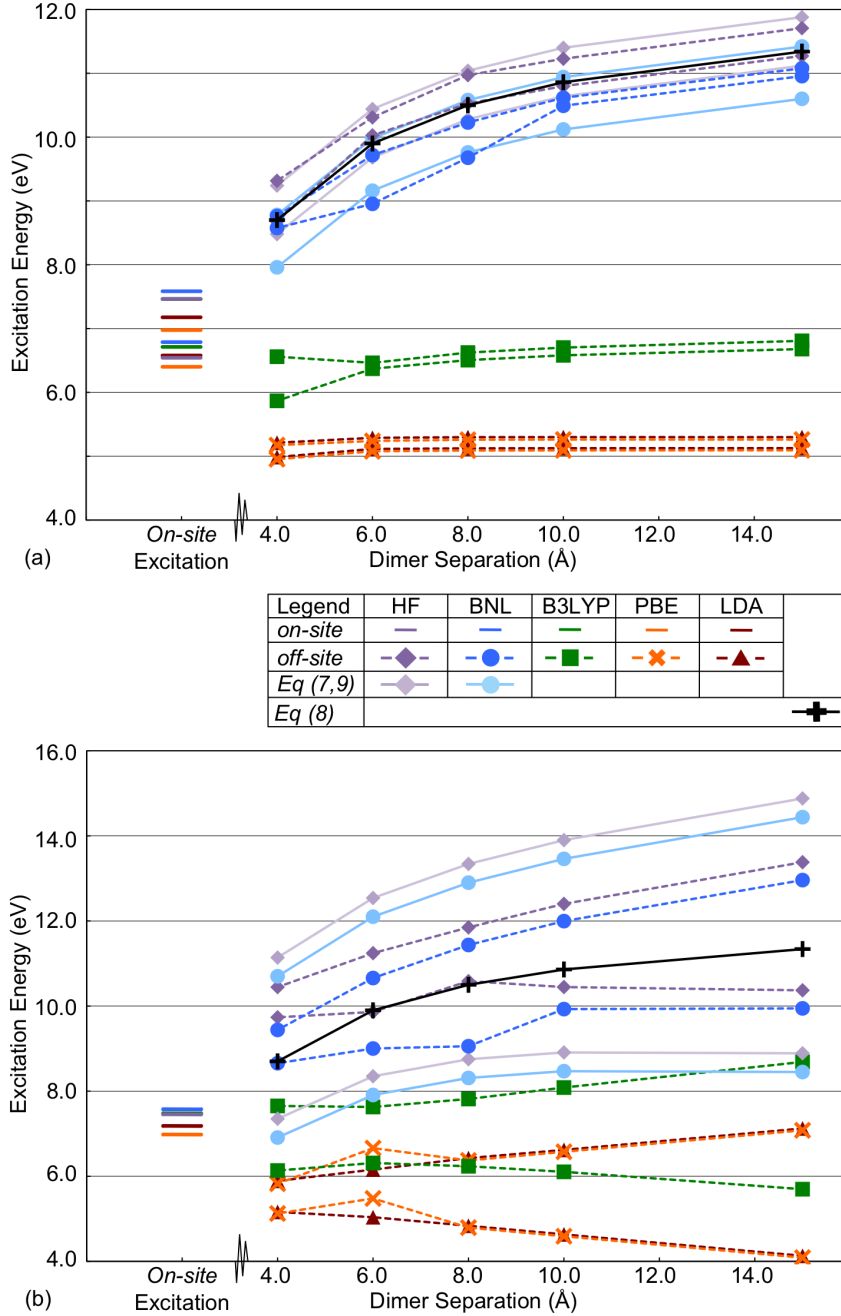


Figure 2.8: (a) Excitation energies (eV) when symmetry is broken by bond stretching (0.102 \AA from equilibrium) with increasing dimer separation. *Off-site* energies are compared to Equation 2.8. (b) Excitation energies (eV) when symmetry is broken by applying a constant electric field with increasing dimer separation. The field ($E_f = 0.1 \text{ V/ \AA}$) is applied at each separation value. *Off-site* energies are compared to Equation 2.10. For both plots, the *off-site* energies are compared to Equation 2.9 the long-range electrostatic interaction limit where experimental IP and EA values are used. *On-site* energies for the 15 \AA separation are included for comparison (Note: HF and B3LYP *on-site* state energies overlap).

site excitations in both the symmetric and symmetry-broken ethene dimer. Figure 2.8(a) shows both the *on-site* and *off-site* excitation energies as a function of dimer separation in a dimer where the bond of one ethene is stretched by 0.102 Å relative to equilibrium. The *on-site* excitation energies follow the same trends as those of the isolated ethene molecule. However, the *off-site* excitation energies exhibit quite different trends depending on the XC-functional/method.

The energies of the *off-site* excitations should be equal to the orbital gap plus the contribution from the XC-kernel. We compare the *off-site* excitation energies, E_{CT} , to the corresponding orbital gap, $\Delta\epsilon_{orb}$, minus the Coulomb attraction between the separated charges, $-R^{-1}$ (in atomic units)[81]

$$E_{CT} = \Delta\epsilon_{orb} - \frac{1}{R}. \quad (2.8)$$

We use the orbital gaps calculated using HF and BNL, since the value of the expression calculated using the orbital gaps of the conventional XC-functionals is much lower than the *on-site* excitation energies. The Equation 2.8 expression mirrors the long-range electrostatic interaction, where[80, 81, 83]

$$E_{CT} = IP - EA - \frac{1}{R}. \quad (2.9)$$

We present the electrostatic interactions by taking into account the fundamental gap. We use the experimentally determined IP (10.5 eV) and EA (-1.8 eV) energies[140] in order to benchmark the calculated *off-site* energies with the “experimental trend” in Equation 2.9.

We find that TDDFT PBE and LDA *off-site* excitation energies are considerably lower than the *on-site* excitation energies and do not exhibit correct dependence on the dimer separation distance. The B3LYP energies do depend on dimer separation, but only to the extent that HF exchange is included in the functional. The excitation

energy remains underestimated despite including a fraction of HF exchange. On the other hand, the TDHF and TDDFT BNL *off-site* excitation energies are much higher than the other functionals and do in fact follow the Coulomb, $-R^{-1}$, dependence. In Figure 2.8, the *off-site* excitation energies for HF and BNL are compared to energies predicted by Equation 2.8. The expression predicts that, upon breaking the symmetry through bond stretching, the two *off-site* energies remain quite similar. The TDHF and the TDDFT BNL energies are shown to be only slightly offset from the values predicted by Equation 2.8. The other functionals greatly underestimate the *off-site* energies when compared to Equation 2.8. Similarly, the BNL energies closely coincide with the Equation 2.9 expression, where the differences between them are attributed to the symmetry-breaking effects on the BNL energies.

We also present the calculated energies upon symmetry breaking by a constant electric field of $0.1\text{V}/\text{\AA}$ applied perpendicular to the planes of the two parallel ethene molecules (see Figure 2.6[left]). The energy due to the electric field ($\pm E_f r$) is now added to the Equation 2.8 expression, leading to

$$E_{CT} = \Delta\epsilon_{orb} - \frac{1}{R} \pm E_f r. \quad (2.10)$$

Accordingly, one *off-site* excitation is stabilized and the other is destabilized by the field. We find that the LDA, PBE and B3LYP *off-site* energies are again underestimated in comparison to Equation 2.10. We also find that the *off-site* energy following the field direction is stabilized with increasing distance. This results from applying the same field over a larger distance, which amounts to an overall larger potential bias. The plotted Equation 2.10 energies show that the Coulomb term (R^{-1}) is larger than the field term ($\pm E_f r$) at small dimer separation, and therefore dominates. At large dimer separation, the ($\pm E_f r$) term becomes dominant. The *off-site* energies of the pure density functionals are shown only to depend on the field term, as ex-

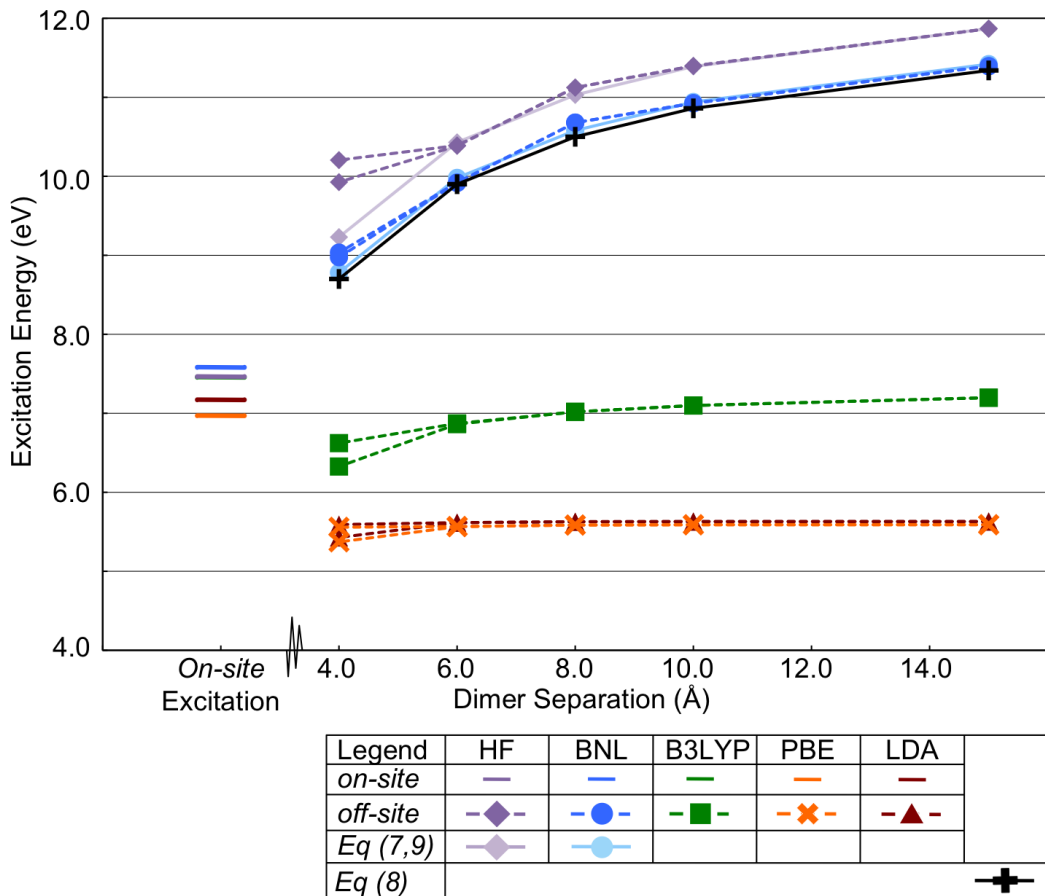


Figure 2.9: Excitation energies (eV) of the symmetric system. *Off-site* energies are compared to Equation 2.8 and to Equation 2.9 the long-range electrostatic interaction limit, where experimental IP and EA values are used. *On-site* energies for the 15 Å separation are included for comparison (Note: HF and B3LYP *on-site* state energies overlap).

pected. Likewise, initially the B3LYP hybrid functional energies partially depend on the Coulomb term, however the field term becomes dominant too quickly with increasing dimer separation. This spurious trend is eliminated in the case of the BNL functional, for which the evaluated *off-site* energies lie between both the formal expression in Equation 2.10 and the electrostatic interaction expression in Equation 2.9, which includes the experimental IP and EA.

In the symmetric limit of the dimer system, the *off-site* excitations exhibit no net CT. At this limit, the B3LYP functional was shown above to fail (Figure 2.7).

Indeed, conventional functionals greatly underestimate the *off-site* excitation energies, predicting energies lower than those of the *on-site* excitations (shown in Figure 2.9). A comparison between *off-site* excitation energies and corresponding orbital gaps also confirms the failure of the conventional functionals to incorporate the Coulomb distance dependence (shown in Appendix C). The HF and BNL *off-site* excitation energies are much higher than the *on-site* excitations, and they follow Equation 2.8 until the dimer separation becomes small (also illustrated in Appendix C). TDHF fails at short dimer separations, as HF theory does not treat correlation effects. The BNL functional, on the other hand, treats both the correlation effects at the short range and the Coulomb dependence at long range. It is important to note that both Equation 2.8 and the *off-site* excitation energies for the BNL functional follow Equation 2.9, essentially reproducing the "experimental trend". Therefore, the BNL functional is shown to produce accurate *off-site* excitation energies.

We next consider the vinylstilbene functionalized octahedral silsesquioxanes (2-vinylstilbene-OHSQ) shown in Figure 2.10. Recent experiments suggest the existence of CT (*off-site*) excitations in this system between the vinylstilbenes.[4, 132] Although we have recently reported the importance of considering solvation effects on the CT state energy in such systems, here we only consider the *off-site* excitation energies in the gas phase. [37]

We consider two geometries of the 2-vinylstilbene-OHSQ molecule, where the vinylstilbene ligands are aligned either perpendicular (symmetry-broken) or parallel (symmetric) to each other, as illustrated in Figure 2.10. We used the B3LYP//6-31G* level of theory for geometry optimizations. For the TDDFT calculations, we used the 6-31G* and 6-31+G* basis sets, with the BNL and B3LYP functionals. It should be noted that the importance of including diffuse functions has previously been shown.[35] The ground state energies of the two structures differ by less than $k_B T$ at room temperature, indicating that both are thermally populated at the ground state

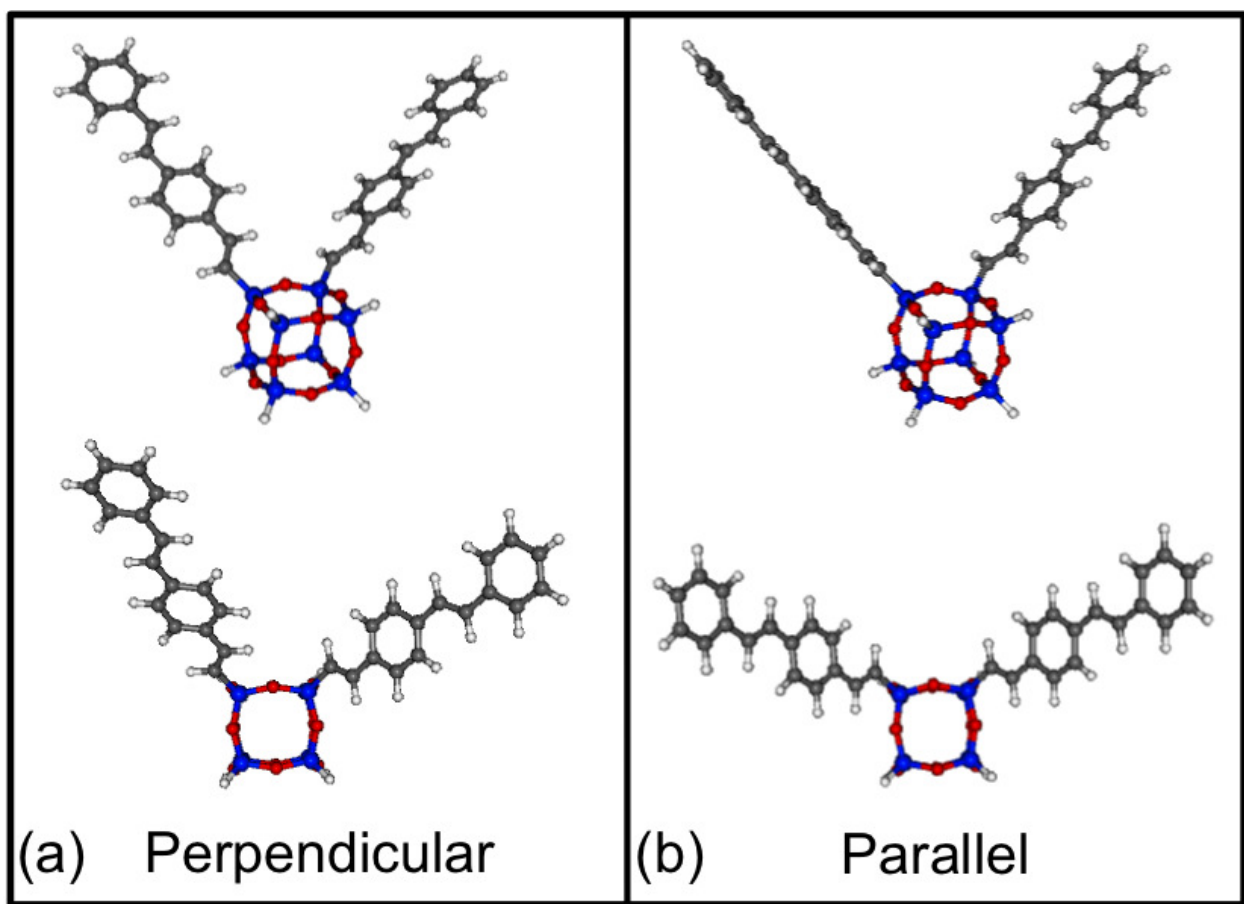


Figure 2.10: (a) Perpendicular 2-vinylstilbene-OHSQ, (b) Parallel 2-vinylstilbene-OHSQ (top: side view, bottom: overhead view).

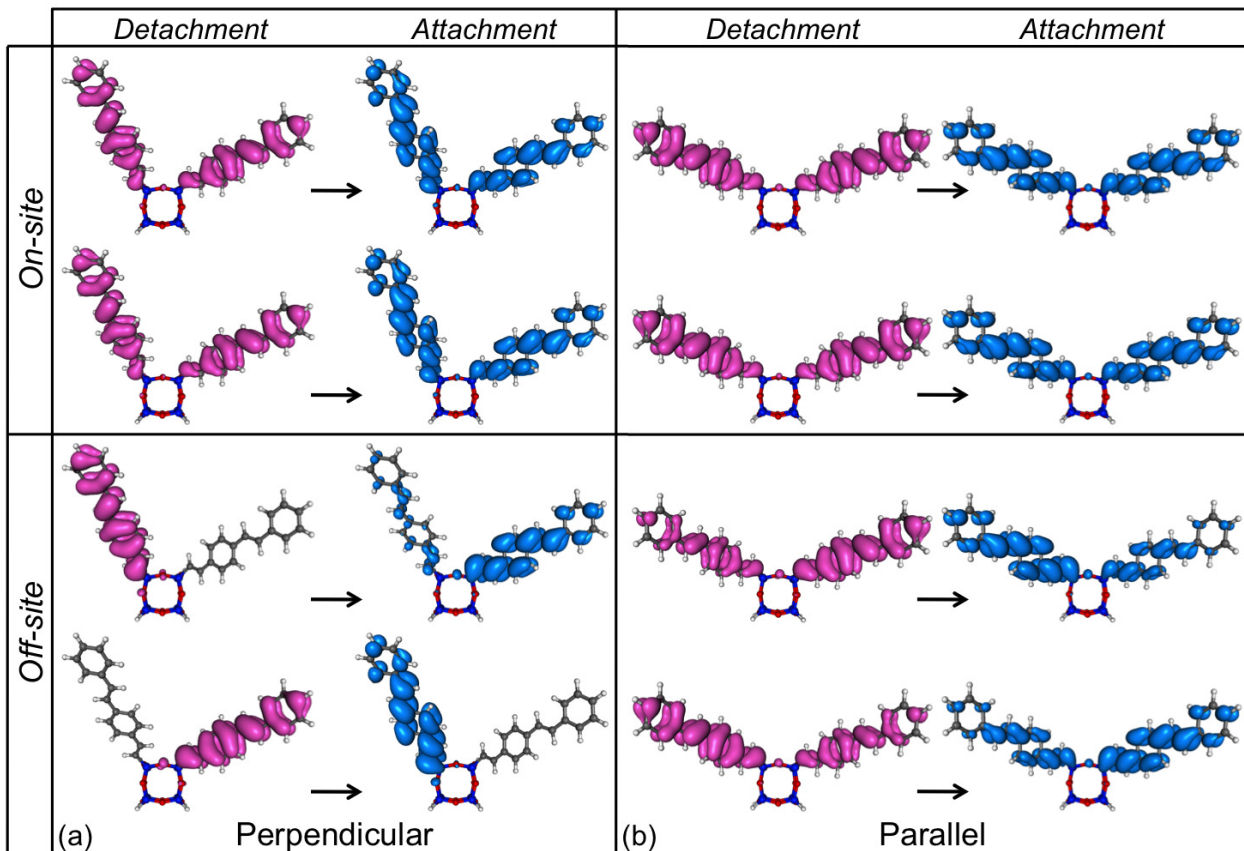


Figure 2.11: Detachment and attachment densities corresponding to *on-site* and *off-site* excitations for 2-vinylstilbene-OHSQ in the perpendicular and parallel geometries. The non-degenerate *off-site* excitations are localized on a single vinylstilbene in the perpendicular geometry and involve net CT. The degenerate *off-site* excitations are delocalized on both vinylstilbenes in the parallel geometry and involve significantly smaller net CT.

(ground state energies are provided in Appendix C). Similar to the ethene dimer, the low-lying excitations are *on-site* and *off-site* $\pi - \pi^*$ transitions.

We compare the parallel and perpendicular geometries in order to demonstrate the effect of symmetry breaking on the *off-site* excitation energies in the SQ-functionalized system. Figure 2.11 illustrates the detachment and attachment densities[141] corresponding to the *on-site* and *off-site* excitations. In the parallel (symmetric) geometry, the HOMO and LUMO orbitals are degenerate, and therefore can be represented in the canonical MO basis as delocalized over both vinylstilbenes in the molecule, as

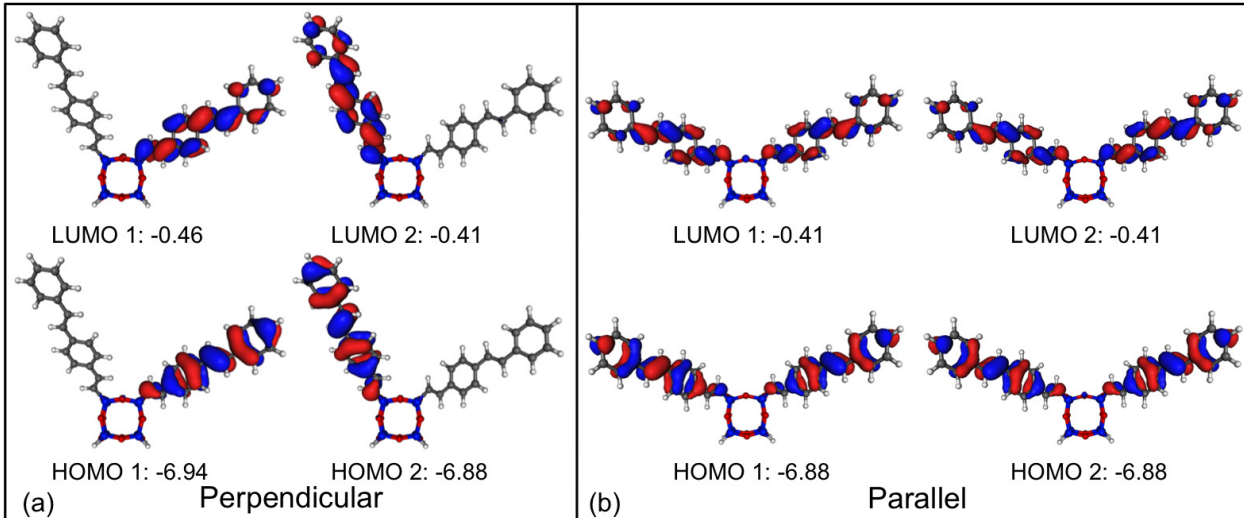


Figure 2.12: Orbital pictures and energies (eV) for 2-vinylstilbene-OHSQ structures. Top: Perpendicular; non-degenerate orbitals are localized on each vinylstilbene. Bottom: Parallel; degenerate orbitals are delocalized over both vinylstilbenes.

shown in Figure 2.12. In the perpendicular (symmetry-broken) geometry, the orbital degeneracy is broken and each orbital is localized on a single vinylstilbene in the canonical MO basis. The orbital symmetry breaking also affects the net CT observed in the *off-site* excitations of 2-vinylstilbene-OHSQ. For instance, the *off-site* transitions exhibit minimal net CT in the parallel geometry and significant CT in the perpendicular geometry, as illustrated in Figure 2.11.

The $\pi - \pi^*$ excitation energies calculated using B3LYP and BNL are compared in Figure 2.13. Results obtained using both the 6-31G* and 6-31+G* basis sets are shown. The BNL *on-site* energies are slightly higher than the B3LYP energies, and more so for the 6-31+G* basis set. The *off-site* excitations are less basis set dependent than the *on-site* excitations for the B3LYP functional. The B3LYP functional greatly underestimates the *off-site* excitation energies in accord with the TDDFT limitations discussed above. The RSH BNL functional correctly predicts the *off-site* excitation energies by correctly accounting for the electron-hole interaction and orbital gap.

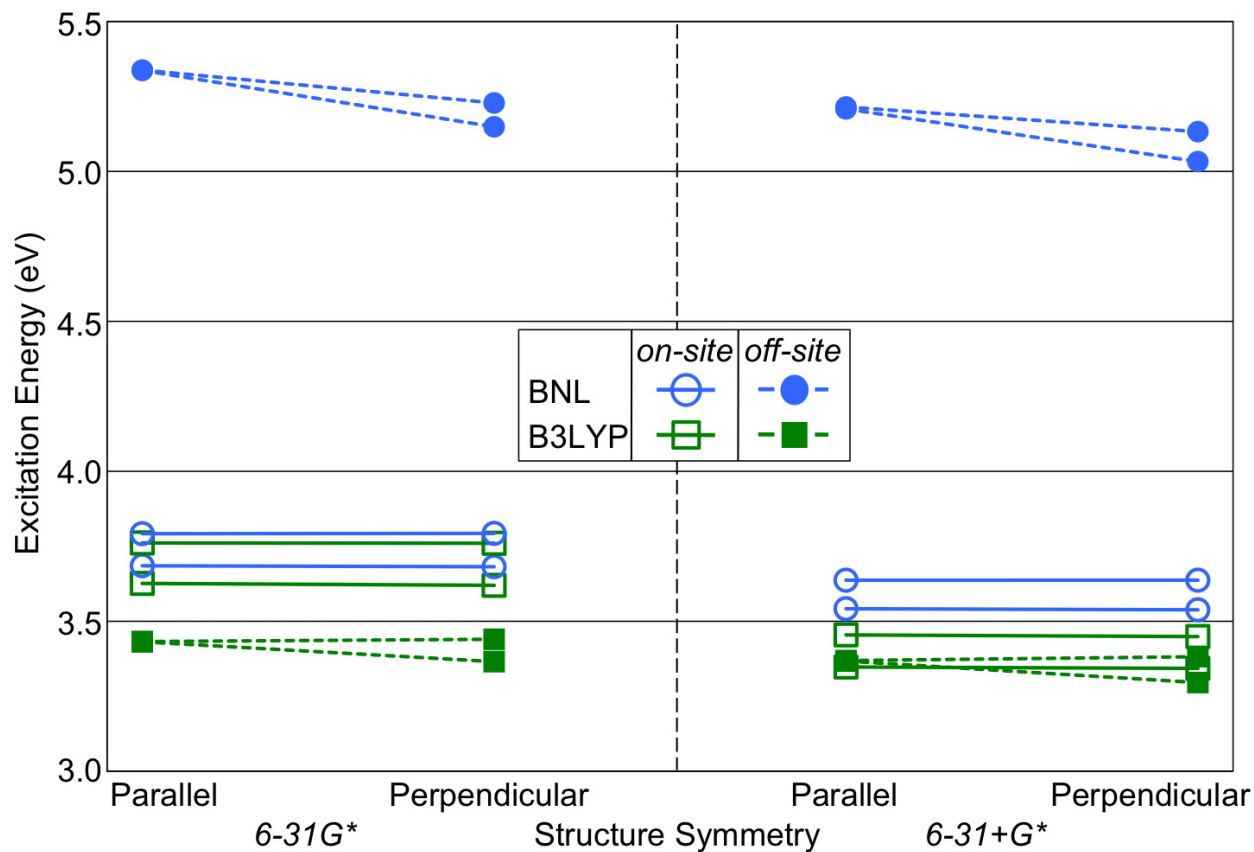


Figure 2.13: Excitation energies (eV) obtained for 2-vinylstilbene-OHSQ in the parallel and perpendicular geometries via TDDFT with B3LYP and BNL. Results obtained using the 6-31G* (left) and 6-31+G* (right) basis sets are shown.

Importantly, even in the symmetric parallel case where there is minimal net CT, the BNL functional correctly identifies the *off-site* excitations as linear combinations of CT-type excitations.

2.2.4 Conclusions

Electronic states involving *off-site* excitations are not always characterized by net CT when the system is symmetrical. Nevertheless, standard DFT functionals such as B3LYP are still unable to account for the energies of such states. Furthermore, breaking the symmetry, and thereby giving rise to net CT, may improve the ability of

the standard functionals to account for the energies of these states due to accidental cancellation of errors. In this study, we demonstrate the accuracy and robustness of the BNL RSH functional for obtaining *off-site* excitations in both symmetric systems with zero net CT and asymmetric systems with net CT. We utilized a systematic symmetry breaking scheme to determine the success of the BNL in treating *off-site* excitations in spatially separated dimer systems.

Indeed, the correct characterization of orbital gaps and CT character is particularly important in applications to OPV and OLED materials. In such systems, as exemplified by 2-vinylstilbene-OHSQ, multiple geometries with various symmetries can be populated at thermal equilibrium. Thus, robustness and accuracy of the BNL functional across geometries and symmetries makes it particularly suitable for understanding CT in these systems.

CHAPTER III

Application of Range Separated Hybrid Density Functionals to Promising Organic Photovoltaic Systems

3.1 Ab Initio Calculation of the Electronic Absorption of Functionalized Octahedral Silsesquioxanes via Time-Dependent Density Functional Theory with Range-Separated Hybrid Functionals

Contributions: Design of study; acquisition, analysis, and interpretation of data; drafting and revision of final version to be published.

3.1.1 Introduction

Ever since the oligomeric silsesquioxane (SQ), $(\text{CH}_3\text{SiO}_{1.5})_n$, was first isolated by Scott et al. in 1946,[142] these compounds have been studied extensively both experimentally and computationally.[4, 132, 133, 142–169] , More recently, the ability to tune the electronic and photonic properties of these SQs by functionalizing them with different ligands has also turned them into attractive candidates for photovoltaic and optical applications.[4, 132, 133, 150, 167–169] The electronic structure and reactiv-

ity of octahedral SQ (OHSQ) and its derivatives have been studied extensively over the last two decades at varying levels of theory ranging from molecular mechanics to first-principles model studies.[133, 147–149, 151, 152, 154, 156, 159–165, 167] Xiang et al. studied the electronic structure of OHSQs of different cage sizes using density functional theory (DFT).[147] The electronic spectra of mono- and multi-phenyl functionalized OHSQs were calculated using plane-wave DFT by Lin et al.[152] The optical properties of methyl-functionalized OHSQ were modeled by Shen et al. via time-dependent DFT (TDDFT).[154] Kieffer and coworkers have recently calculated excitation and intramolecular reorganization energies of several OHSQs functionalized with variety of electron-withdrawing groups (EWG) and electron-donating groups (EDG) via DFT and TDDFT.[133] It is widely accepted that TDDFT can provide a reliable description of electronic excited states of molecular systems.[51, 90] TDDFT is particularly advantageous in the case of large systems, where other higher-level treatments are prohibitively expensive. However, TDDFT based on conventional density functionals is also known to suffer from well-documented limitations. For example, B3LYP-based TDDFT calculations are known to underestimate electronic excited state energies involving charge transfer character.[90, 102, 103, 136, 137, 170–172] This discrepancy can be traced back to density discontinuities and the electronic self-interactions introduced at the level of ground state DFT.[2, 64, 68, 90] Charge-transfer excitations are known to be sensitive to the asymptotic long-range behavior of the exchange-correlation functional, which is often not treated accurately in widely used functionals such as B3LYP.[80–85, 90] Range separated hybrid (RSH) functionals have been recently proposed by several groups as a way of overcoming these limitations.[85, 90, 102, 103, 136, 137, 170–172] The new RSH functionals have been shown to be reliable in predicting ionization potentials, excitation energies, and oscillator strengths in several benchmark charge transfer systems.[90, 103, 136, 172] Our purpose in this paper is twofold:

1. To test and benchmark (against experiment) TDDFT-calculated absorption excitation energies of functionalized OHSQs using RSH functionals and different basis sets and compare them to those obtained via the B3LYP functional.
2. To study the effect of different ligation schemes on the electronic absorption spectra, including the effect of multiple ligands and the presence of EWGs and EDGs.

3.1.2 Computational Methods

The electronic absorption spectra of functionalized OHSQs are dominated by excitations with large oscillator strength that take place between the ground state and excited singlet states at the equilibrium ground state geometry. The calculation of the excitation energies reported in this study were carried out via the Q-Chem program package version 4.0.[173] Mattori et al. have previously demonstrated the reliability of B3LYP in describing the ground state geometry of OHSQs.[148] In this study, all ground state geometry optimizations following the benchmarking were performed using the B3LYP functional together with the 6-311+G** basis set. The pairing of DFT functional and basis set for the excited state calculations was systematically studied in the case of vinyl-functionalized OHSQs. To this end, the excited state energies of ethylene and of 1Vinyl-OHSQ (i.e., OHSQ functionalized by a single vinyl, see Figure ??) were calculated using TDDFT with three different functionals, namely:

1. The B3LYP functional. [118–121]
2. The RSH functional recently introduced by Baer, Neuhasuer and Livshits (BNL).[102, 103]
3. The long range corrected (LRC- ω PBEh) RSH functional, also recently developed by Herbert and co-workers. [171, 172]

Convergence of the calculated excited state energies with respect to the following basis sets was considered: The all-electron 6-31G, 6-311G, 6-31G*, 6-31G**, 6-311G*, 6-311G**, 6-31+G, 6-31+G*, 6-31+G**, 6-311+G*, 6-311+G**, 6-311++G**, aug-cc-pVTZ basis sets, and the effective core potential (ECP) basis set for the silicon atoms, LANL2DZ, combined with 6-311G**, 6-311+G**, 6-311++G** basis sets. In all cases we used the same basis set for the geometry optimization and the excited states evaluation. The BNL functional involves a system-dependent parameter (γ), [85, 136] which is determined by minimizing the function $J(\gamma)$ as shown in , which minimizes the differences between the absolute values of the highest occupied molecular orbital (HOMO) energy and the ionization potential, IP:ⁱ

$$J(\gamma) = (\epsilon_{(N,HOMO)} + IP(N)) + (\epsilon_{(N+1,HOMO)} + IP(N + 1)), \quad (3.1)$$

where $\epsilon_{(HOMO)}$ is the highest occupied molecular orbital energy, IP the ionization potential, and N and $N + 1$ are the number of electrons referring respectively to the neutral and anion forms. The orbital and ionization energies are parametrically dependent on γ . We used vinyl-OHSQs to benchmark the convergence of the TDDFT calculations with respect to the basis set, using a fixed parameter value of $\gamma=0.5$ a.u.[103] In all other calculations, system specific values of γ were used. More specifically, the evaluated γ values were 0.30 a.u. for 1vinyl-OHSQ, 0.22 a.u. for 1styrene-OHSQ, and 0.20 a.u. for 1vinylstilbene-OHSQ. These values are slightly smaller than the corresponding free molecule value (0.40 a.u., 0.27 a.u., and 0.21 a.u. for ethylene, styrene, and vinylstilbene molecules, respectively). It should also be noted that γ is slightly reduced upon increased conjugation length of the chromophore, but remains relatively constant upon adding ligands of the same type. For example, the values of γ for 1Vinyl-OHSQ and 2Vinyl-OHSQ (para isomer [see Figure 3.1]) were found

ⁱNote that in this study, $J(\gamma)$ depends on the difference between HOMO and IP for the systems, instead of the square of these values as in 1.74. The current study was completed prior to wide acceptance of the $J^2(\gamma)$ scheme.

to be quite similar (2Vinyl-OHSQ parameter is slightly larger). Finally, the value of γ for the unfunctionalized OHSQ molecule was found to be 0.47 a.u. The nature of the transition was analyzed by considering the underlying changes in charge densities upon excitation.[51, 141] The density change upon an electronic excitation is reflected in the corresponding attachment/detachment densities, which are derived from the one-electron difference density matrix between the ground state and excited state.[141] The detachment density describes the charge density that is removed upon excitation, i.e. the hole created in the electronic density. The attachment density describes the charge density created upon excitation. The densities are visualized using the Molekel program package.[139] Finally, we used the polarizable continuum model (PCM) in order to account for solvent shifts in the case of styrene and vinylstilbene dissolved in tetrahydrofuran (THF).[174–176] To this end, we evaluated the solvation energy for the molecules described at the B3LYP/6-311+G**//B3LYP/6-311+G** and B3LYP/6-311+G**//BNL/6-311+G** levels of theory.

3.1.3 Results and Discussion

3.1.3.1 Vinyl-OHSQ

In this section we report the results of benchmarking our approach on vinyl-functionalized OHSQs. The calculated excitation energies of ethylene and 1Vinyl-OHSQ (see Figure 3.1), using several combinations of functionals (B3LYP and BNL) and basis sets (all-electron and involving electron core potentials [ECP]) are shown in Table 3.1. Overall, the vinyl-OHSQ excitation energies obtained with B3LYP are significantly lower than those obtained using BNL. In contrast, the B3LYP and BNL calculated excitations energies are similar in the case of ethylene.

In the next step, we consider the convergence with respect to basis set type and size (as shown in Table 3.1). The addition of diffuse functions slightly decreases the excitation energies in most cases. The addition of polarization functions increases

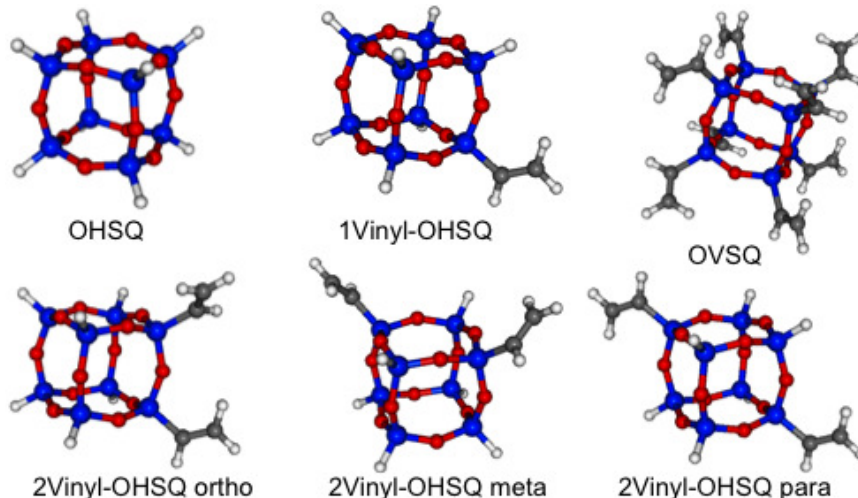


Figure 3.1: Molecular models of the systems studied: OHSQ, 1vinyl-OHSQ, OVSQ, ortho, meta and para isomers of 2vinyl-OHSQ.

the B3LYP energies and decreases the BNL excitation energies, and also reduces the difference in the excitation energies between the two functionals. We note that adding diffuse and polarization basis functions on the hydrogen atoms does not impact the excitation energies. In addition, we find that the use of ECP for Si atoms reproduces the corresponding all-electron basis set results quite well. We find that the 6-31+G* basis set offers converged results in terms of the basis set size. Below we use the larger 6-311+G** basis set for vinyl-OHSQ and mono-ligated styrene and vinylstilbene derivatives of OHSQ, and 6-31+G* is used in the case of multi-ligated vinylstilbene derivatives of OHSQ.

The optimized geometry (bond angles and bond lengths) of OHSQ at the B3LYP/6-311+G** level agrees very well with the experimental X-ray diffraction resolved structures (provided in Appendix D).[177] The calculated Si-O bond length is only slightly overestimated by 0.02 Å and the bond angles deviate from experimental values by less than 2%. These deviations reflect the geometric distortions due to solid state packing and the overall tendency of DFT to overestimate bond lengths (as a general trend, hybrid functionals slightly reduce the overestimation of bond lengths featured

Basis Set	1Vinyl-OHSQ		Ethylene Only	
	B3LYP	BNL	B3LYP	BNL
6-31G	7.3125	8.3935	9.1743	9.1289
6-311G	7.3291	8.2755	8.8774	8.8250
6-31G*	7.7282	8.2847	9.0562	9.0295
6-31G**	7.7126	8.2725	9.0422	9.0052
6-311G*	7.6242	8.1270	8.7402	8.7091
6-311G**	7.6016	8.1102	8.7248	8.6782
6-31+G	7.1001	7.9349	7.9375	8.1264
6-31+G*	7.3849	7.8153	7.8463	8.0552
6-31+G**	7.3684	7.7943	7.8361	8.0332
6-311+G*	7.4131	7.8376	7.9078	8.0958
6-311+G**	7.3894	7.8151	7.8960	8.0652
6-311++G**	7.3888	7.7906	7.8958	8.0645
aug-ccP-VTZ	7.3351	7.7657	7.8219	8.0167
LANL2DZ with 6-311G**	7.4854	8.1912	8.7248	8.6782
LANL2DZ with 6-311+G**	7.3116	7.8840	7.8960	8.0652
LANL2DZ with 6-311++G**	7.3103	7.8686	7.8958	8.0645

Table 3.1: Absorption excitation energies (in eV) of OHSQ, 1-vinyl-OHSQ and ethylene as obtained using B3LYP and BNL with different types of basis sets. The same value of the BNL parameter was used in all cases: $\gamma=0.50$ a.u. The bold font indicate basis sets for which converged results were obtained.

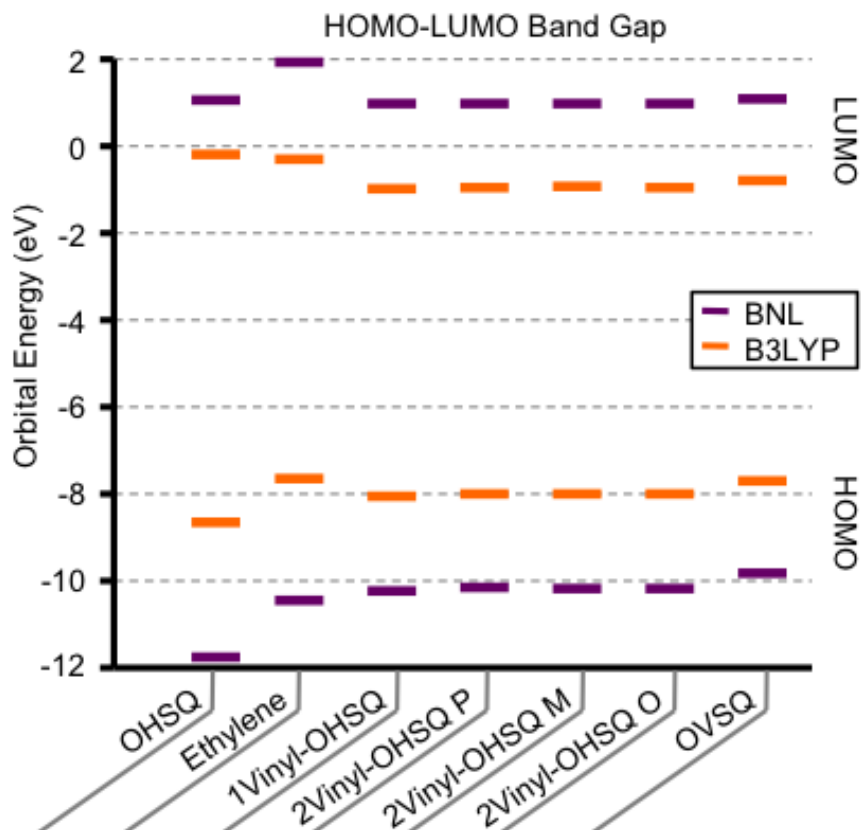


Figure 3.2: HOMO and LUMO energies for OHSQ, ethylene, 1Vinyl-OHSQ, ortho, meta, and para isomers of 2Vinyl-OHSQ and OVSQ as obtained using B3LYP (orange) and BNL (purple). The BNL parameter values that were used are: $\gamma=0.47$ a.u. (OHSQ), $\gamma=0.40$ a.u. (ethylene), $\gamma=0.30$ a.u. (vinyl-OHSQ).

by GGA functionals).

In Figure 3.2 we provide the HOMO-LUMO energies of the vinyl-substituted systems. In this figure, the BNL results were generated using system-specific values of γ . Energy gaps calculated via BNL are significantly larger than those calculated via B3LYP, with the BNL LUMO energy higher, and the HOMO energy lower than the corresponding B3LYP values. The excitation energies corresponding to the lowest absorption transitions of ethylene, 1Vinyl-OHSQ, the ortho, meta, and para isomers of 2Vinyl-OHSQ, and 8Vinyl-OHSQ (OVSQ) are shown in Table 3.2. In the case of BNL, the results reported in this table were obtained using the system-specific

values of γ . The electronic absorption spectrum of free ethylene has been measured extensively[86, 178–180] and the comparison with the corresponding calculated value is discussed further in the Appendix E.

The vinyl substituted OHSQs are found to have two absorption excitation bands that correspond to the two excitations of the ethylene molecule but are shifted in energy. The vinyl-OHSQ system is unique as it exhibits strong mixing between the ethylene and OHSQ molecular orbitals. The mixing is reflected in the detachment and attachment densities corresponding to the excitations with largest oscillator strength of ethylene, 1Vinyl-OHSQ and OVSQ as provided in Figure 3.3. For example, in the case of 1Vinyl-OHSQ the excitation includes the OHSQ oxygen 2p lone-pair orbitals, in addition to the dominant vinyl π and π^* replacements. We also find that the ordering of the two excitations is switched by the BNL functional, compared to B3LYP, where the HOMO-LUMO dominated excitation is the first excited state (see Appendix D).

3.1.3.2 Multi-Chromophore effect on the absorption cross section

In this section, we analyze the effect of multiple ligands. We start out by considering 1Vinyl-OHSQ, 2Vinyl-OHSQ isomers and OVSQ. Figure 3.1 shows the molecular structures of these compounds, Figure 3.2 provides the corresponding HOMO-LUMO energy gaps and Table 3.2 lists the corresponding excitation energies and oscillator strengths. We find that the diagonal Si-Si distances are not affected by the addition of ligands, which implies that ligation does not affect the ground state structure of the OHSQ (more information is provided in Appendix D). HOMO-LUMO energies of the multiply-ligated OHSQs remain quite similar to those of 1Vinyl-OHSQ, where the energy gap decreases only slightly with the addition of a second ligand (as shown in Appendix D). The addition of a second ligand is also observed to double the overall oscillator strength, which is consistent with the view that the ligands are weakly

Molecule	BNL		B3LYP	
	Energy	Strength	Energy	Strength
Ethylene	7.566	0.155	7.187	0.123
	7.601	0.371	7.481	0.338
	Average	7.583	0.526	7.334
1Vinyl-OHSQ	7.210	0.043	7.079	0.032
	7.230	0.453	7.105	0.448
	Average	7.220	0.495	7.092
2Vinyl-OHSQ ortho	7.175	0.063	7.033	0.064
	7.184	0.020	7.051	0.060
	7.202	0.236	7.069	0.154
	7.256	0.650	7.122	0.606
	Average	7.204	0.969	7.069
2Vinyl-OHSQ meta	7.189	0.007	7.064	0.013
	7.192	0.020	7.065	0.015
	7.212	0.500	7.092	0.464
	7.250	0.474	7.139	0.453
	Average	7.211	1.001	7.090
2Vinyl-OHSQ para	7.196	0.084	7.068	0.065
	7.198	0.000	7.074	0.000
	7.215	0.914	7.104	0.888
	7.241	0.000	7.131	0.000
	Average	7.213	0.998	7.094
OVSQ	7.0742	0.000	6.885	0.000
	7.0796	0.062	6.907	0.055
	7.0801	0.062	6.908	0.056
	7.0854	0.000	6.934	0.000
	7.0872	0.008	6.947	0.000
	7.0876	0.011	6.966	0.000
	7.0925	0.000	6.966	0.000
	7.0930	0.000	6.967	0.003
	7.1624	0.001	7.035	0.000
	7.1659	0.000	7.047	0.000
	7.1673	0.000	7.051	0.000
	7.1820	0.000	7.086	0.000
	7.2023	1.999	7.094	1.678
	7.2123	0.826	7.120	0.672
	7.2134	0.827	7.121	0.677
7.3471	0.000	7.219	0.000	
Average	7.146	3.795	7.016	3.140

Table 3.2: Excitation energies (in eV) for transitions that correspond to the absorbing states of ethylene and various vinyl-OHSQs. The absorption maximum (λ_{max}) is provided by the oscillator-strength-weighted average of excitation energies. The values of the BNL parameter used are: $\gamma=0.400$ a.u. (ethylene), $\gamma=0.300$ a.u. (vinyl-OHSQ).

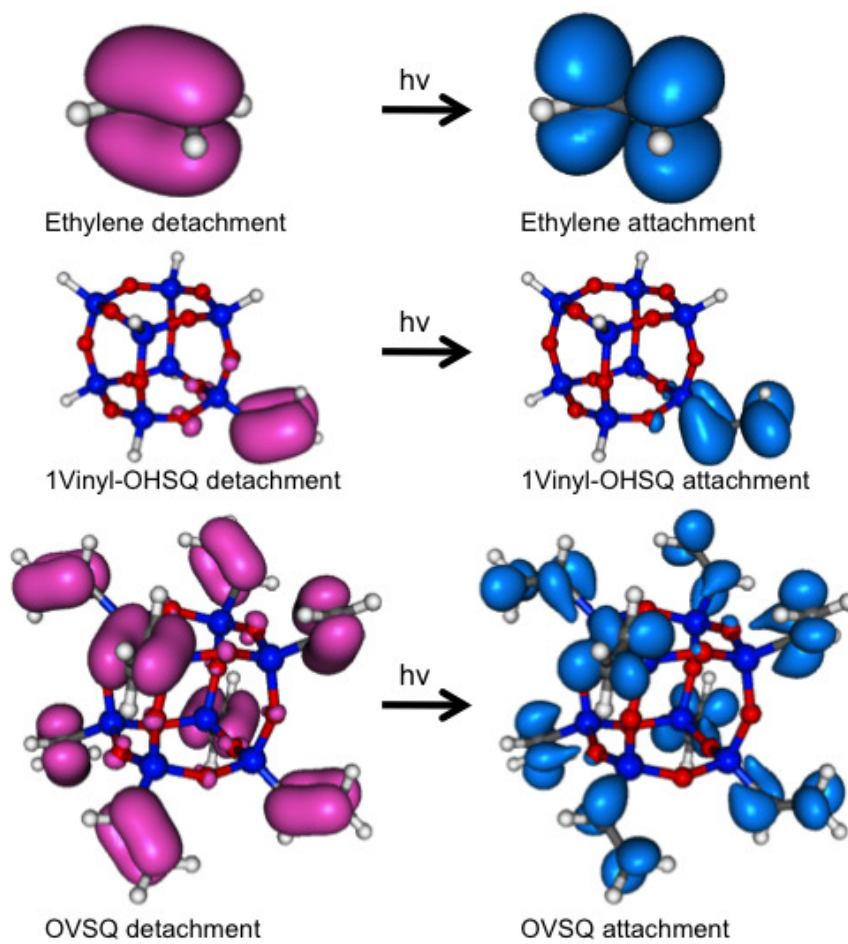


Figure 3.3: Attachment (blue) and detachment (pink) densities for the transitions with the largest oscillator strength in the first excitation band for ethylene, 1Vinyl-OHSQ and OVSQ molecules.

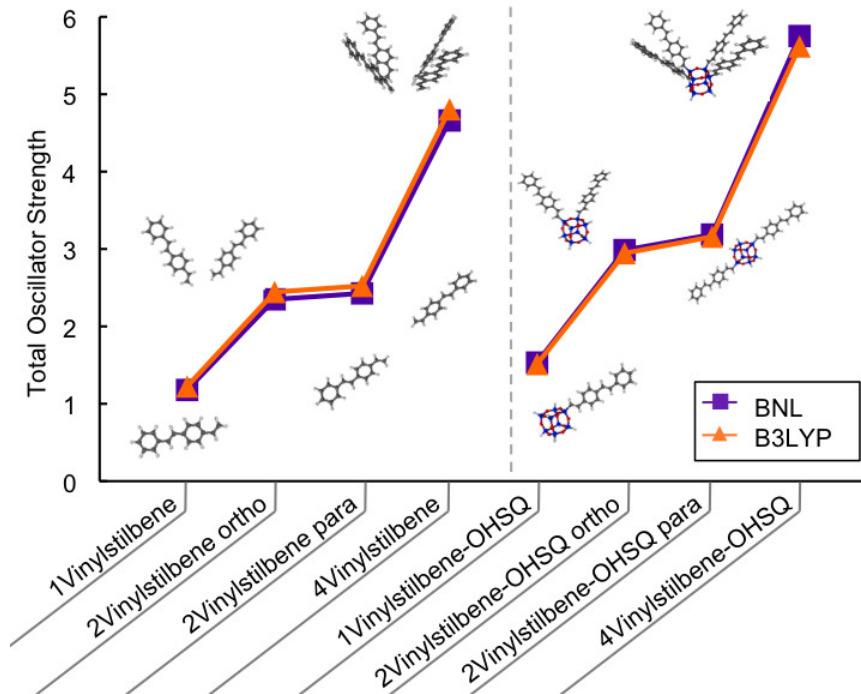


Figure 3.4: The effect on the oscillator strength by multiple ligand functionalization. Shown on the right are the oscillator strengths for vinylstilbene, 2-vinylstilbene OHSQ (para, meta and ortho isomers), 4-vinylstilbene OHSQ (the isomer shown). Shown on the left are the oscillator strengths of the of the ligand arrangements obtained after removing the OHSQ.

coupled. Overall, the oscillator strengths predicted by both functionals are quite similar, however the differences are greater in the case of the smaller ligand. In the case of OVSQ, the oscillator strength, as obtained via BNL, is close to eight times that of the 1Vinyl-OHSQ, whereas for the B3LYP the strength is seen to be smaller. The corresponding OVSQ detachment-attachment plots in Figure 3.3 suggest that the excitation involves mixing between vinyl and OHSQ orbitals, as in the case of 1Vinyl-OHSQ.

The linear increase of the oscillator strength with the number of ligands was observed to persist even when across shift from the relatively small vinyl ligand to larger ligands, such as styrene and vinylstilbene. For example, the overall oscillator strength as a function of the number of vinylstilbene ligands is shown in Figure 3.4. We also compared the increase of the oscillator strength with the number of ligands

Molecule	BNL		B3LYP	
	Energy	Strength	Energy	Strength
Vinylstilbene	3.709	1.179	3.488	1.224
2Vinylstilbene ortho	3.601	0.802	3.426	0.824
	3.685	1.548	3.518	1.621
Average (λ_{\max})	3.657	2.350	3.487	2.444
2Vinylstilbene meta	3.820	1.178	3.470	0.974
	3.877	1.800	3.522	1.458
Average (λ_{\max})	3.855	2.978	3.501	2.431
2Vinylstilbene para	3.632	2.427	3.460	2.523
	3.663	0.000	3.494	0.000
Average (λ_{\max})	3.632	2.427	3.460	2.523
4Vinylstilbene	3.576	0.002	3.406	0.001
	3.612	1.011	3.449	0.974
	3.624	1.555	3.464	1.600
	3.744	2.093	3.613	2.230
Average (λ_{\max})	3.675	4.661	3.530	4.805
1Vinylstilbene-OHSQ	3.589	1.533	3.395	1.513
2Vinylstilbene-OHSQ ortho	3.539	1.009	3.343	0.972
	3.638	1.978	3.449	1.974
Average (λ_{\max})	3.604	2.986	3.414	2.946
2Vinylstilbene-OHSQ meta	3.577	1.302	3.377	1.239
	3.647	1.710	3.452	1.694
Average (λ_{\max})	3.617	3.012	3.420	2.933
2Vinylstilbene-OHSQ para	3.564	3.187	3.370	3.159
	3.620	0.000	3.429	0.000
Average (λ_{\max})	3.564	3.187	3.370	3.159
4Vinylstilbene-OHSQ	3.523	0.003	3.359	1.006
	3.552	1.312	3.368	0.662
	3.565	1.923	3.380	1.354
	3.714	2.514	3.539	2.597
Average (λ_{\max})	3.627	5.752	3.449	5.618

Table 3.3: Excitation energies (in eV) for transitions that correspond to the absorbing states of vinylstilbene and vinylstilbene-OHSQs. 2-vinylstilbene-OHSQ isomers and 4-vinylstilbene-OHSQ are compared to the same ligand arrangement after removing the OHSQ. The absorption maximum (λ_{\max}) is provided by the oscillator-strength-weighted average of excitation energies.

in the presence of the OHSQ to that in its absence. More specifically, we removed the OHSQ from the structure and calculated the oscillator strength of the resulting OHSQ-free arrangement of ligands (which remains the same as it was in the presence of the OHSQ). We found that the presence of the OHSQ gave rise to a modest increase of the oscillator strength. For example, the oscillator strength increased from 1.2 to 1.5 for 1Vinylstilbene-OHSQ (Table 3.3). Additional examples are discussed below.

3.1.3.3 Vinylstilbene-OHSQ and Styrenyl-OHSQ

In this section, we focus on the ligands for which there are available experimental data to compare with. We model the absorptive excitations of vinylstilbene- and styrene-functionalized OHSQ and compare them to available spectroscopic data.[4, 132, 169] Importantly, the vinylstilbene and styrene ligands feature a HOMO-LUMO energy gap that is significantly smaller relative to that of the bare OHSQ, thereby leading to significantly less mixing between the two subsystems in comparison to the vinyl-OHSQ system. The calculated excitation energies and oscillator strengths for these systems are listed in Appendix D.

We also considered a series of EDG-substituted styrene and vinylstilbene as the ligands. Specifically, we model the absorption spectra of octa- R_s -styrene-SQ ($R_s = \text{H, CH}_3, \text{CH}_3\text{O}$) and octa- R_v -vinylstilbene-SQ ($R_v = \text{H, CH}_3, \text{CH}_3\text{O, NH}_2$) (see Figure 3.5). The absorption and emission spectra of these molecules have recently been measured experimentally and the absorption band was observed to be centered around 260nm for the styrene series and 330nm for the vinylstilbene series.?? We also consider the effect of EWG substitutions that have not been considered experimentally (see Figure 3.5).

A correlation plot of the calculated vs. experimental excitation energies of the EDG-functionalized molecules is shown in Figure 3.6 (the values of the excitation energies and the corresponding oscillator strengths are included in Appendix D). For the styrene series, the plotted excitation energy is given by the oscillator-strength-weighted average of the two excited states in the lowest absorption band. In general, the ligation lowers the excitation energies relative to the free ligands. This ligation effect is even greater when the ligands are functionalized by an EDG.

We also found that the excitation energy decreases with increasing EDG strength for both R_s -Styrenyl-OHSQ and R_v -Vinylstilbene-OHSQ series, with a larger EDG-induced shift observed for the smaller styrene chromophore. As expected, the B3LYP

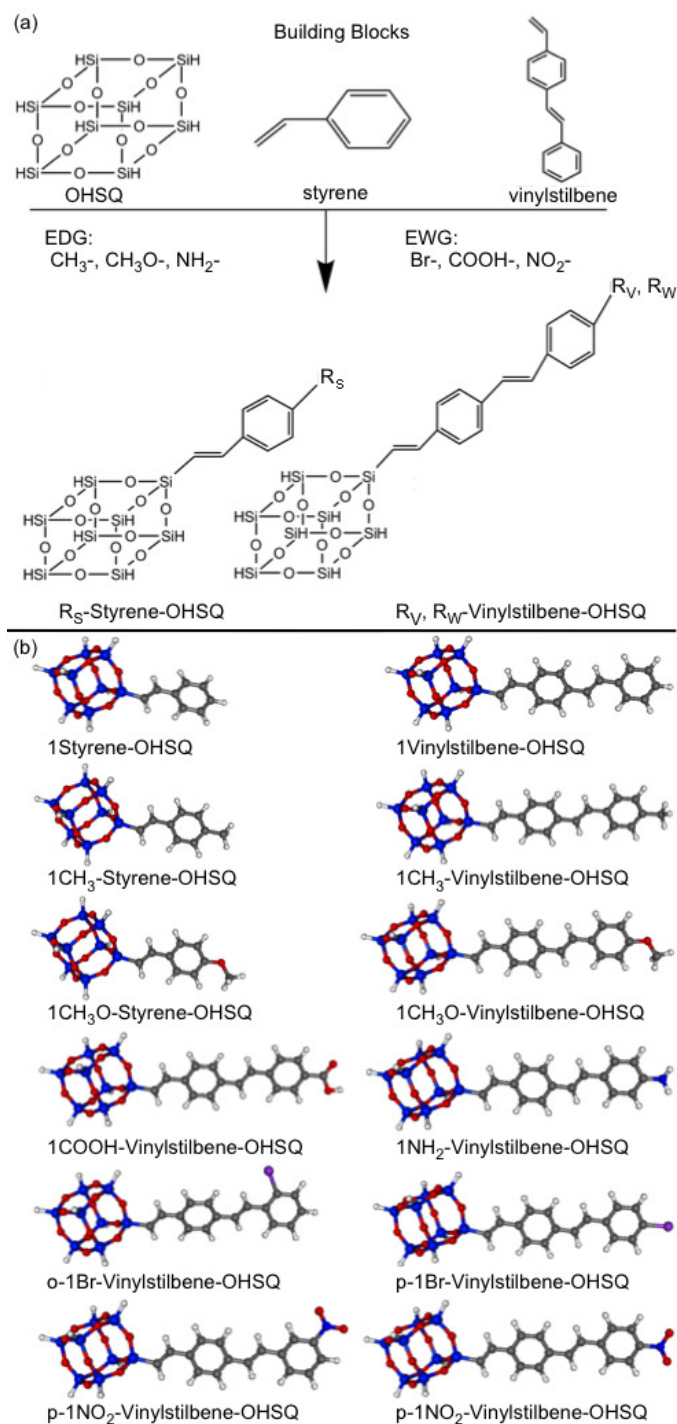


Figure 3.5: (a) Top: The molecular building blocks of the systems considered in this paper, namely OHSQ, styrene and vinylstilbene. Bottom: Different ligand-functionalized OHSQs, including different substitutions of the ligands by EDGs or EWGs. (b) Molecular models of the systems studied in this paper.

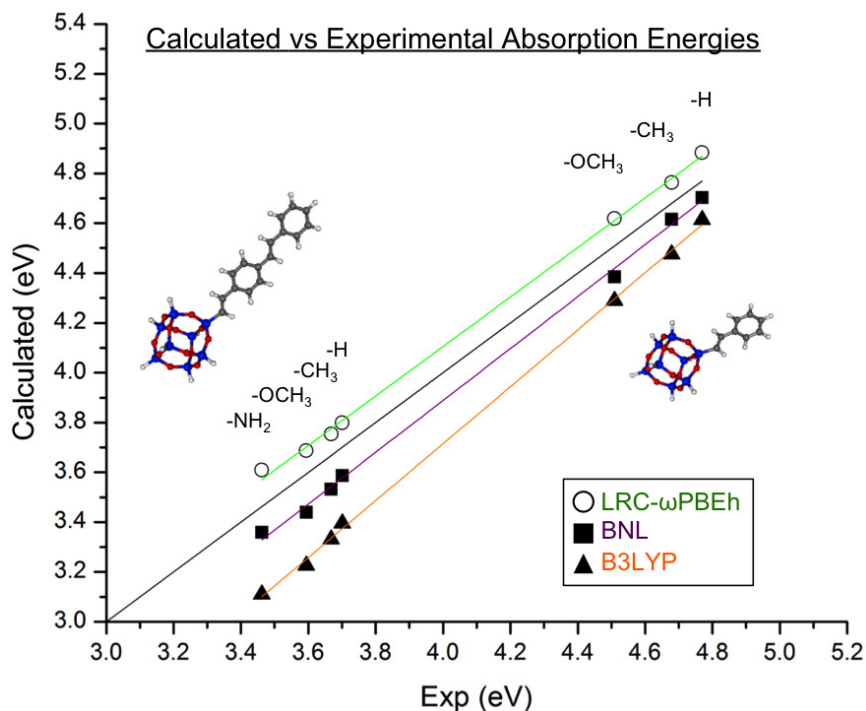


Figure 3.6: A correlation plot of the calculated vs. experimental absorption excitation energies. Perfect agreement corresponds to the black line. Shown are calculated results obtained for both R_s -Styrenyl-OHSQ and R_v -Vinylstilbene-OHSQ by using BNL (purple), B3LYP (orange) and LRC- ω PBEh (green). The root mean square deviation of the calculated values from the measured excitation energy is provided in the legend.

functional underestimates the excitation energies by as much as 0.3 eV root mean square deviation (RMSD) in comparison to the experimental values. At the same time, the BNL functional underestimates the excitation energies by as little as 0.1 eV RMSD, while the LRC- ω PBEh functional overestimates the excitation energies by a similar amount (0.1 eV RMSD).

We also note the ligation effect on the absorption oscillator strength (Appendix D). Upon ligation, the oscillator strength becomes approximately 1.8 and 1.3 times higher relative to the free ligand, in 1Styrenyl-OHSQ and 1Vinylstilbene-OHSQ, respectively. This trend of increased oscillator strength upon ligation is confirmed for all functionals. In addition, the RSH functionals show a trend of slightly increasing oscillator strengths with EDG substitution, while for the B3LYP functional the

oscillator strength decreases with increasing EDG strength.

The experimental spectra are measured in tetrahydrofuran (THF) solvent.[4] We used a polarizable continuum model[174, 175] to estimate solvation effects on the absorption. We have found that with BNL, the solvation energies for the styrene and vinylstilbene are 0.17 eV and 0.32 eV, respectively (Appendix D). Solvent stabilization is increased by approximately 0.1 eV upon chromophore ligation to the OHSQ, where 1styrenyl-OHSQ and 1vinylstilbene-OHSQ solvation energies are 0.30 eV and 0.44 eV, respectively. The B3LYP functional predicts the same trends as BNL, with solvation energies that are slightly smaller by 0.1 eV.

Excited state detachment and attachment densities for some of the styrene- and vinylstilbene-functionalized systems are provided in Figure 3.7. The excitations are observed to involve transitions from the ligand’s π bonding orbital into the ligand’s π^* anti-bonding orbital, with no significant charge transfer to or from the OHSQ. The largest eigenvalues of the different detachment/attachment density matrices are listed in Appendix D. Additional density plots are also provided in Appendix D.

The HOMO-LUMO energy gaps for the R_s -Styrenyl-OHSQ and R_o -Vinylstilbene-OHSQ systems are shown in Figure 3.8 and are listed in Appendix D. Both the HOMO and LUMO are dominated by the chromophore-localized π bonding and π^* anti-bonding MOs, respectively. The BNL and LRC- ω PBEh functionals predict significantly higher HOMO-LUMO energy gaps than B3LYP. Both the HOMO and LUMO energies are reduced when the ligand is substituted with an EDG, and are increasingly reduced as the electron-donating strength of the EDG increases (from CH3 to NH2). Our results are consistent with these of Ronchi et al. who performed ground state electronic structure analyses on [RSiO1.5]₈ (R = H, F, HO, NH2, alkyl) compounds and reported decreasing HOMO-LUMO energy gap with increasing EDG strength.[132]

Ligation to OHSQ is observed to lower both the HOMO and LUMO energies

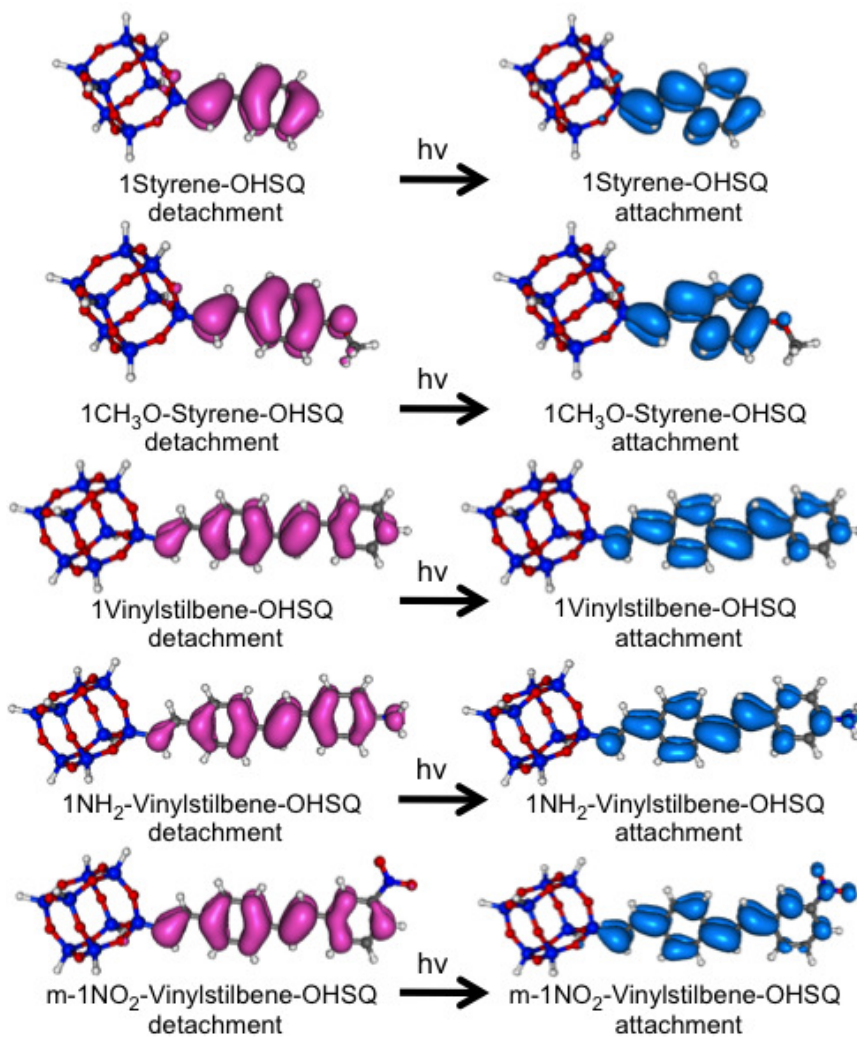


Figure 3.7: Detachment (pink) and attachment (blue) densities associated with transitions that have the strongest oscillator strengths in the first excitation band, for 1-Styrenyl-OHSQ, 1-CH₃O-Styrenyl-OHSQ, 1-Vinylstilbene-OHSQ, 1-NH₂-Vinylstilbene-OHSQ and 1-NO₂-Vinylstilbene-OHSQ molecules.

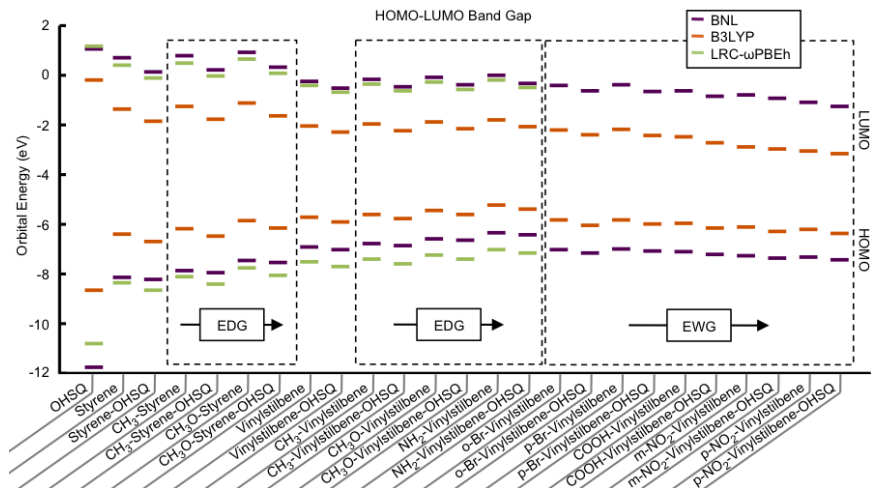


Figure 3.8: HOMO and LUMO energies calculated for OHSQ, R_s -Styrene, R_s -Styrenyl-OHSQ; $R_{v,w}$ -Vinylstilbene, $R_{v,w}$ -Vinylstilbene-OHSQ using B3LYP (orange), BNL (purple) and LRC- ω PBEh (green).

relative to the free ligand, as shown in Figure 3.8. The effect of ligation on the orbital energies is demonstrated in Figure 3.9, which shows the difference between the ligated-OHSQ orbital energy and the free ligand orbital energy. The LUMO energy is stabilized by ligation more so than the HOMO, which is consistent with a similar finding reported in Ref. [133]. Interestingly, the LUMO stabilization in the styrene series is greater than that in the vinylstilbene series. The larger stabilization in the styrene series is likely due to the greater proximity between the LUMO energies of free styrene and free OHSQ, which leads to more mixing and thereby enhanced stabilization of the R_s -Styrene-OHSQ LUMO orbitals. The same reasoning can be applied to the HOMO energies. For instance the BNL functional, when compared to the other functionals, predicts the smallest energy difference between the free styrene and free OHSQ LUMOs and the largest energy difference between the corresponding HOMOs. As a result, BNL predicts the largest stabilization of the LUMO and the smallest stabilization of the HOMO for R_s -Styrene-OHSQ.

We also considered the effect of electron withdrawing groups (EWG), which has not been experimentally measured yet. We modeled the spectra of R_w -Vinylstilbene-

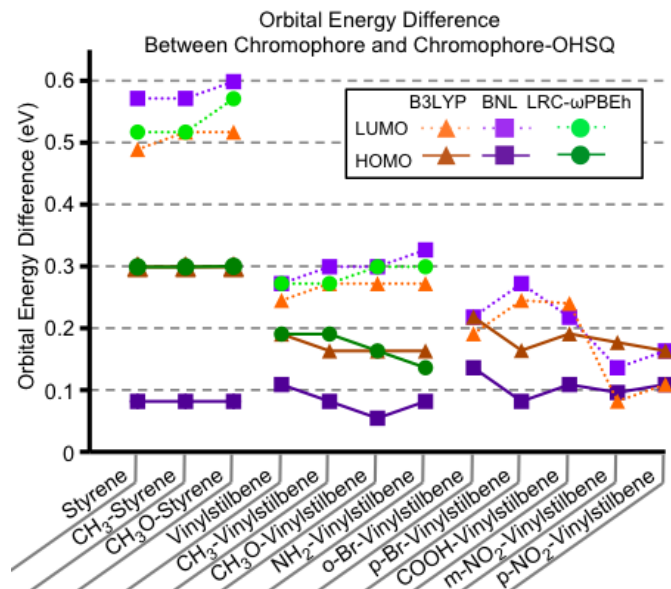


Figure 3.9: The effect of ligation on the HOMO and LUMO energies given by difference in the orbital energies between the ligated OHSQ and the free ligands (in eV).

OHSQ ($R_w = \text{NO}_2$ [strong EWG], COOH [moderate EWG] and Br [weak EWG]). The Br and NO_2 EWG are also considered in the experimentally relevant ortho and meta positions, respectively, as shown in Figure 3.5. The HOMO-LUMO energies and band gaps are plotted in Figure 3.8 with the values listed in Appendix D. The calculated excitation energies of this molecular series are listed in Table 3.4. As is the case of the EDGs, when the ligand is substituted with EWGs the HOMO and LUMO are dominated by the ligand's π bonding and $|\pi^*$ anti-bonding orbitals, respectively. We find, in general, that the HOMO-LUMO energy gap and the corresponding excitation energies decrease with increasing EWG strength. Unlike the trends observed with EDG-functionalized ligands however, the excitation energies of the EWG-functionalized ligands are less affected by ligation to OHSQ than the excitation energies of the unfunctionalized ligand. Therefore, EWG-functionalization lessens the ligation effect on the excitation energies, while EDG-functionalization increases it.

Similar to the trends observed for the EDG series, the LUMO energy is stabilized

Molecule	BNL		B3LYP	
	Energy	Strength	Energy	Strength
o-Br-Vinylstilbene	3.42	1.14	3.61	1.11
o-1Br-Vinylstilbene-OHSQ	3.40	1.40	3.59	1.42
p-Br-Vinylstilbene	3.45	1.40	3.67	1.37
p-1Br-Vinylstilbene-OHSQ	3.34	1.66	3.54	1.68
COOH-Vinylstilbene	3.31	1.35	3.59	1.42
1COOH-Vinylstilbene-OHSQ	3.27	1.71	3.49	1.73
m-NO ₂ -Vinylstilbene	3.51	1.22	3.62	0.72
m-1NO ₂ -Vinylstilbene-OHSQ	3.46	1.55	3.57	1.24
p-NO ₂ -Vinylstilbene	2.96	0.94	3.46	1.33
p-1NO ₂ -Vinylstilbene-OHSQ	3.00	1.24	3.42	1.65

Table 3.4: Absorption excitation energies, in eV, and oscillator strengths of R_w -Vinylstilbene-OHSQ as obtained using B3LYP and BNL

more so than the HOMO energy when the ligand is substituted with an EWG. However, the LUMO stabilization decreases as the electron-withdrawing strength of the EWG increases, while the HOMO is further stabilized by increasing EWG strength. These trends are opposite to those observed for the EDG series, though as discussed above, they can be attributed to the energy difference between free ligand and OHSQ orbitals. More specifically, the ligand’s LUMO energy becomes much lower than the OHSQ LUMO energy as the EWG strength increases, which reduces the stabilization achieved from mixing the molecular orbitals (see Figure 3.8). Likewise, the chromophore HOMO energy becomes closer to that of OHSQ as EWG strength increases, thereby enabling greater mixing between the molecular orbitals.

We note that the detachment-attachment analysis demonstrates that a C=N or C=C double bond forms during the excitation process for the COOH and p-NO₂ functionalized ligands (shown in Figure 3.7 and in Appendix D). No double bond can be formed in the case of the Br functional group. Thus, the decrease of the excitation energy upon increasing EWG strength seems to be associated with an electronic resonance effect that results in the formation of a double bond.

Finally, we point out that the success of the RSH functional in reproducing the measured absorption spectra results from the improved ground state treatment. With the RSH treatment, the HOMO and LUMO energies are closer to the experimental IP and EA energies. Indeed, Stein et al. have shown that the RSH functional reduces the difference between the fundamental gap (IP-EA) and the (HOMO-LUMO) gap.[86] The difference in these gaps, the derivative discontinuity, affects the description of the electron and hole mobility, which are key properties in photovoltaic applications.

3.1.4 Conclusions

The absorption excitation energies of functionalized OHSQs have been investigated computationally via TDDFT, using B3LYP and RSH (BNL and LRC- ω PBEh) functionals. We find that pairing the RSH functionals with basis sets that include diffuse and polarized basis functions is required to obtain converged results. The calculated excitation energies at the RSH/6-311+G**//B3LYP/6-311+G** level for vinylstilbene- and styrenyl-functionalized OHSQ are found to be in better agreement with the available experimental data than the B3LYP results, which significantly underestimate the excitation energies. Functionalization of these ligands by EDG and EWG decreases the excitation energies, in agreement with available experimental data. The excitations are mainly localized on the ligands, with the exception of vinyl, where mixing between vinyl and OHSQ was observed. We present the success of the RSH functional to improve the description of the HOMO and LUMO energies and of the excited state energies as compared to the experimental data. The LUMO (HOMO) mediates the photo induced electron (hole) transport in photovoltaic applications. The demonstrated success to eliminate the derivative discontinuity error provides promise for the prospect of using RSH functionals for modeling materials used in photovoltaic applications.

3.2 Ab Initio Study of the Emissive Charge-Transfer States of Solvated Chromophore-Functionalized Silsesquioxanes

Contributions: Design of study; interpretation of data; drafting and revision of final version to be published.

3.2.1 Introduction

The ability to tune the electronic and photonic properties of silsesquioxanes (SQ) by functionalizing them with different ligands has recently turned them into attractive candidates for photovoltaic and optical applications. [4, 132, 133, 150, 167, 168, 181]. These compounds have also been studied computationally at various levels of theory ranging from molecular mechanics to first-principles model studies.[133, 147, 148, 150–152, 154, 159–165, 167, 168, 182] One of the most striking spectroscopic observations pertaining to these compounds is the significant increase in the red-shift of the emission spectrum, relative to the absorption spectrum, that occurs upon ligation.[4, 132] For example, whereas the red shift in stilbene is ~ 0.3 eV, that of stilbene-functionalized octahedral SQ is $\sim 0.8–0.9$ eV.[132] The emission spectrum of the SQ-coupled chromophores is strongly red-shifted, while the absorption spectrum remains similar to that of the isolated stilbene. This suggests that while the absorption spectrum is dominated by excitations which are localized on the ligand, the increase in the red-shift is associated with the emergence of low lying emissive states that extend beyond a single ligand. The fact that the red-shift increases with increasing polarizability of the solvent[183, 184] also suggests that these emissive states involve extensive charge-transfer (CT) character. Figure 3.10 provides an illustration of the expected behavior of the charge transfer states according to these observations.

Our goal in this study is to elucidate the nature of the emissive CT states in

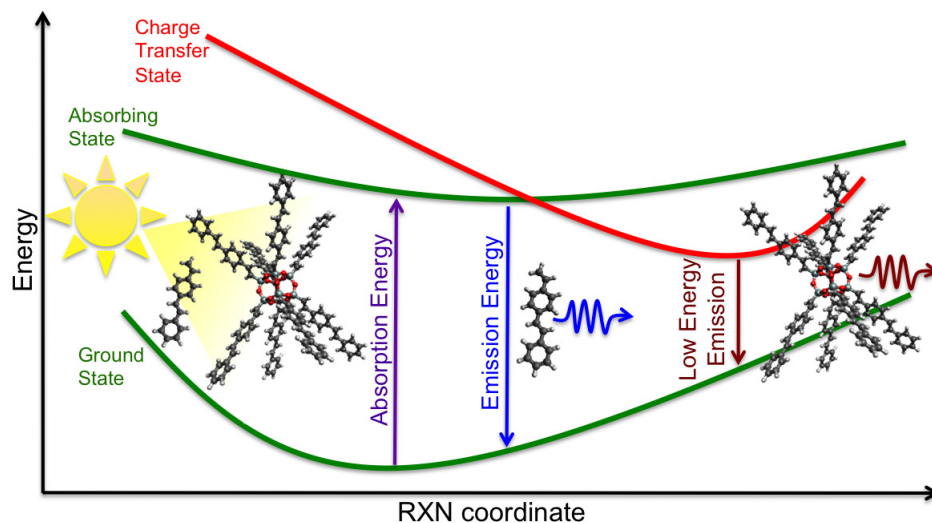


Figure 3.10: Illustrated picture of the behavior of chromophore-functionalized OHSQ. Absorption of functionalized OHSQ resembles that of the chromophore, but emission is red-shifted compared to chromophore emission due an expected charge transfer state.

functionalized SQs with the help of state-of-the-art density functional theory (DFT) techniques. To this end, we employed time-dependent DFT (TD-DFT) and the Tamm-Dancoff approximation (TDA)[91–93] with the recently developed range separated hybrid (RSH) functional of Baer-Neuhauser-Livshits (BNL).[102, 103, 136] We present a state-of-the-art approach to address the solvation effects on the charge transfer states. We combine charge-constrained DFT (C-DFT)[185–188] optimizations with novel polarizable continuum models (PCM)[174, 175] implementing switching/Gaussian (SWIG)[125, 126] PCMs. We successfully benchmark our scheme against the experimental emission spectrum.

3.2.2 Computational Methods

All the calculations reported here were carried out within version 4.0 of the Q-Chem program package[122] and using the 6-31G* basis set. We use the B3LYP functional[118–121] for all the geometry optimizations described below. In calculating the BNL γ parameter, we use the $J(\gamma)$ [85, 136] scheme that has been previously

introduced:

$$J(\gamma) = (\epsilon_{(N,HOMO)} + IP(N))^2 + (\epsilon_{(N+1,HOMO)} + IP(N + 1))^2, \quad (3.2)$$

where $\epsilon_{(HOMO)}$ is the highest occupied molecular orbital energy, IP the ionization potential, and N and $N + 1$ are the number of electrons referring respectively to the neutral and anion forms. The PCM dielectric constant was set equal to that of tetrahydrofuran (THF)[$7.42\epsilon_0$], which is the solvent used in the experiment.[132]

3.2.3 Results and Discussion

The ground state trends reflected in the molecular orbital energies are essential for understanding the electronic spectra and the roles of the SQ and chromophore as an electron acceptor and donor, respectively. In particular, the highest occupied and lowest unoccupied molecular orbital (HOMO-LUMO) gaps must correspond to the fundamental gap[80, 87] (the difference between the ionization potential and the electron affinity), which is taken into account by obtaining the correct BNL γ parameter. Indeed, Section 3.1 points out that TD-DFT with the BNL functional provides excellent agreement with the experimental absorption spectra for a wide range of functionalized OHSQs.[189] We also found that for the system under study here, the absorptive excitations are localized on the stilbene ligands. In the present study, we address the significantly more challenging problem of identifying the emissive CT state and quantitatively predicting its energy relative to the absorptive state.

We demonstrate that the combined RSH-CDFT-PCM scheme as implemented in this report yields predictions related to CT processes which are in excellent agreement with experiment. This is contrasted with the results obtained using more traditional functional choices, such as B3LYP, which are known to significantly underestimate the energy of CT states. In general, we have found that TDA provides a slightly

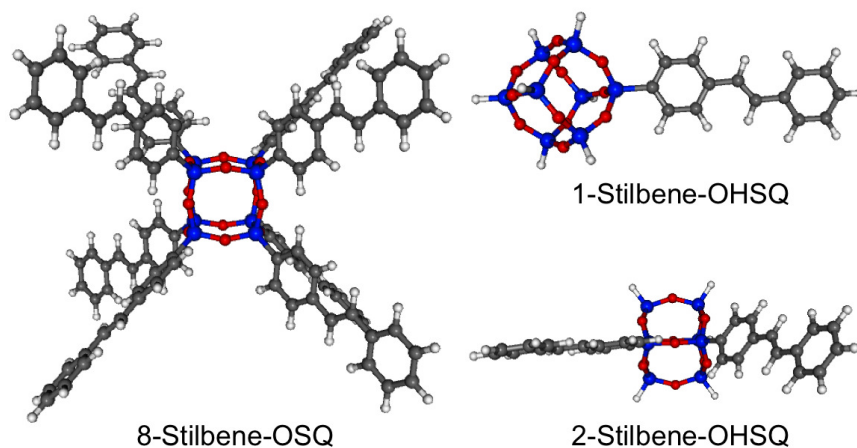


Figure 3.11: SQ fully functionalized with 8 stilbene ligands (left). Molecular models of 1-stilbene-OHSQ and 2-stilbene-OHSQ (right).

better agreement with experiment in reproducing the absorption spectra with about 0.2 eV higher excitation energies than TD-DFT. For completeness both the TDA and TD-DFT excitation energies are listed in the Appendix Table F.1. This comparison between TDA and the full TD-DFT is indicated in other previous studies as well.[52, 190, 191] We therefore continue below with the TDA and note that the CT excited state energies are found to have even smaller difference between the TDA and the full TD-DFT energies.[52, 91–93, 190–194]

The current study is focused on octahedral silsesquioxane (OHSQ) functionalized with trans-stilbene that has been shown to result in the large shift of the emission spectrum of up to 0.9 eV.[132] The systems studied via experimental methods are assumed to be fully functionalized by eight chromophores, as shown in Figure 3.11[left].[4, 132] Two charge transfer pathways may explain the red-shift in the emission spectrum. The first involves charge transfer from the chromophore to the SQ core, and the second is solvent-mediated charge transfer between chromophores. The CT between chromophores can be intramolecular, involving chromophores attached on the same SQ molecule, or intermolecular, within aggregates of the functionalized SQs. However, it remains unclear which of these pathways is relevant to the

	HOMO _s	LUMO _s	HOMO _o	LUMO _o
Trans-stilbene	-6.67	0.71	—	—
OHSQ	—	—	-9.42	2.10
1-stilbene-OHSQ	-6.86	0.35	-9.14	2.07
2-stilbene-OHSQ	-6.78	0.33	-8.95	2.10

Table 3.5: The BNL HOMO and LUMO energy (eV). (The subscript 's' refers to stilbene and the subscript 'o' to the OHSQ cage).

red-shifted emission.

In order to answer this open question concerning the charge transfer, we use one and two trans-stilbene functionalized OHSQ as models. The corresponding models are illustrated in Figure 3.11[right] and are referred to as 1-stilbene-OHSQ and 2-stilbene-OHSQ respectively. In the 2-stilbene-OHSQ, the chromophores are added at two nearest neighbor Si sites, where the strongest coupling is expected. The energies of the HOMOs and LUMOs of the OHSQ, stilbene, 1-stilbene-OHSQ and 2-stilbene-OHSQ are listed in Table 3.5. Importantly, we find that the chromophore gap is substantially lower than the OHSQ, with a 1.4 eV lower LUMO energy. We also point out that the chromophore-localized LUMO in the functionalized-SQ system is stabilized by 0.3 eV, however the orbital localized on the SQ, the LUMO of OHSQ, remains at a higher energy.

We begin by considering the *gas phase* vertical electronic excitation energies for stilbene-OHSQ at the solvated ground state geometry (i.e. the optimized ground state structure obtained within PCM at the B3LYP level). The excitation energies obtained via TDA using the BNL and the B3LYP functionals are shown in Figure 3.12. A tabulated list of the TDA excited states energies is provided in the Supporting Information [Table F.1].

The excitations can be classified into three different types: (1) $\pi - \pi^*$ excitations which are localized on the stilbene ligands; (2) Type CT1 excitations that involve CT between stilbene and OHSQ; (3) Type CT2 excitations that involve CT from

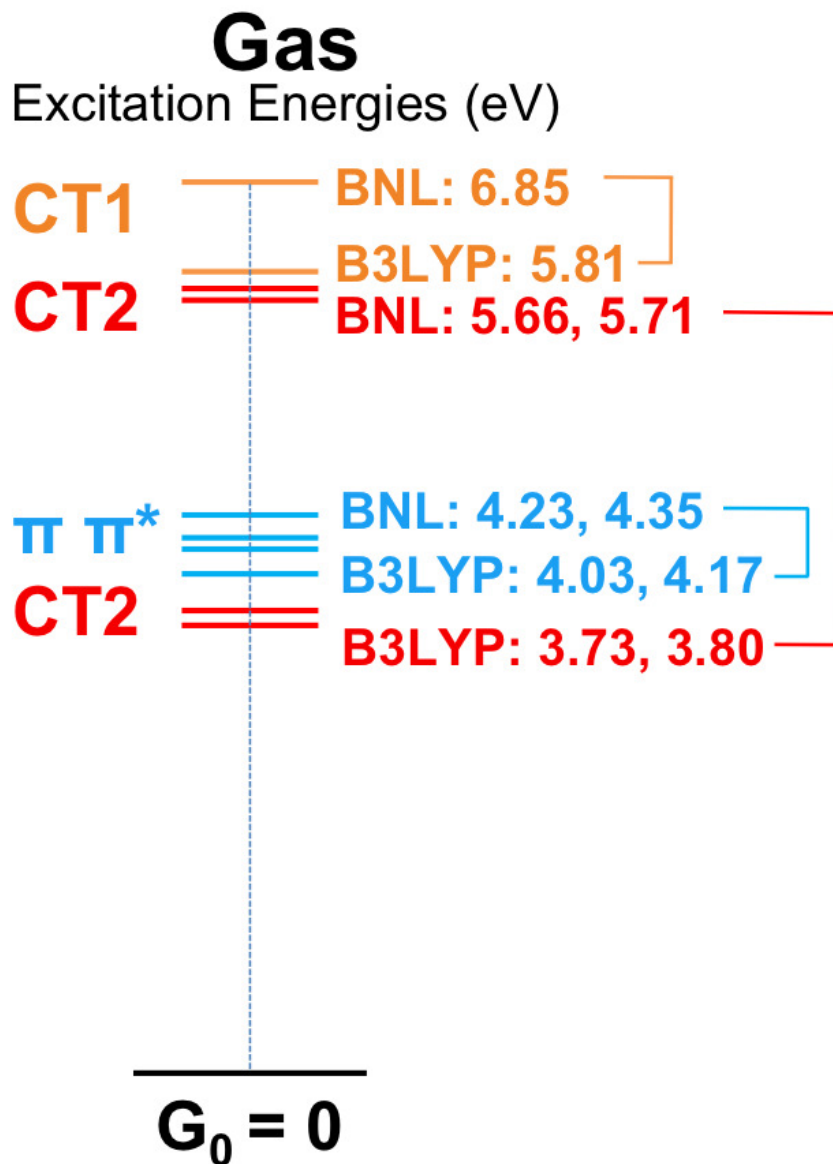


Figure 3.12: Gas phase vertical electronic excitation energies for 2-stilbene-OHSQ at the solvated (within PCM) ground state geometry, as obtained via TDA with BNL and B3LYP functionals.

one stilbene to another stilbene. We report the CT1 energies calculated with the 1-stilbene-OHSQ model and CT2 energies calculated with the 2-stilbene-OHSQ model (See Figure 3.11). We find that the two CT1 energies calculated using the 2-stilbene-OHSQ model are in good agreement with the CT1 energy of the 1-stilbene-OHSQ model. In our current study, the 2-stilbene-OHSQ model directly represents CT2 excitations between chromophores on the same SQ molecule and CT between chromophores within aggregates of functionalized SQs. The energetics of the CT states is expected to remain qualitatively the same with models that explicitly address the possibility of aggregates.

The $\pi - \pi^*$ excitations with the larger oscillator strengths dominate the absorption spectra and have been studied extensively recently.[189] The BNL energies of these absorbing states are 0.2 eV higher than the B3LYP values.[189] The CT states are characterized by oscillator strengths which are significantly smaller than the oscillator strength of the $\pi - \pi^*$ transitions. The CT excited states are classified as either CT1 or CT2 based on the corresponding attachment and detachment densities, as shown in Figure 3.13.[141] The $\pi - \pi^*$ excitations are identified with HOMO to LUMO replacements occurring on the same chromophore unit. The CT2 state involves mainly HOMO to LUMO replacements where the orbitals are related to different chromophores. Finally, the CT1 state is dominated by the replacement of the chromophore HOMO by the SQ-LUMO.

Both CT1 and CT2 excited state energies obtained via BNL are significantly higher than those obtained via B3LYP. This is consistent with the well documented tendency of B3LYP to over-stabilize CT states.[80, 195–199] The gas phase CT1 energies obtained with both BNL and B3LYP functionals are observed to be significantly higher than the corresponding $\pi - \pi^*$ excited state energy. This implies that the CT1 state does not affect the emission spectrum following the $\pi - \pi^*$ excitations. The situation is quite different for the CT2 state, however.

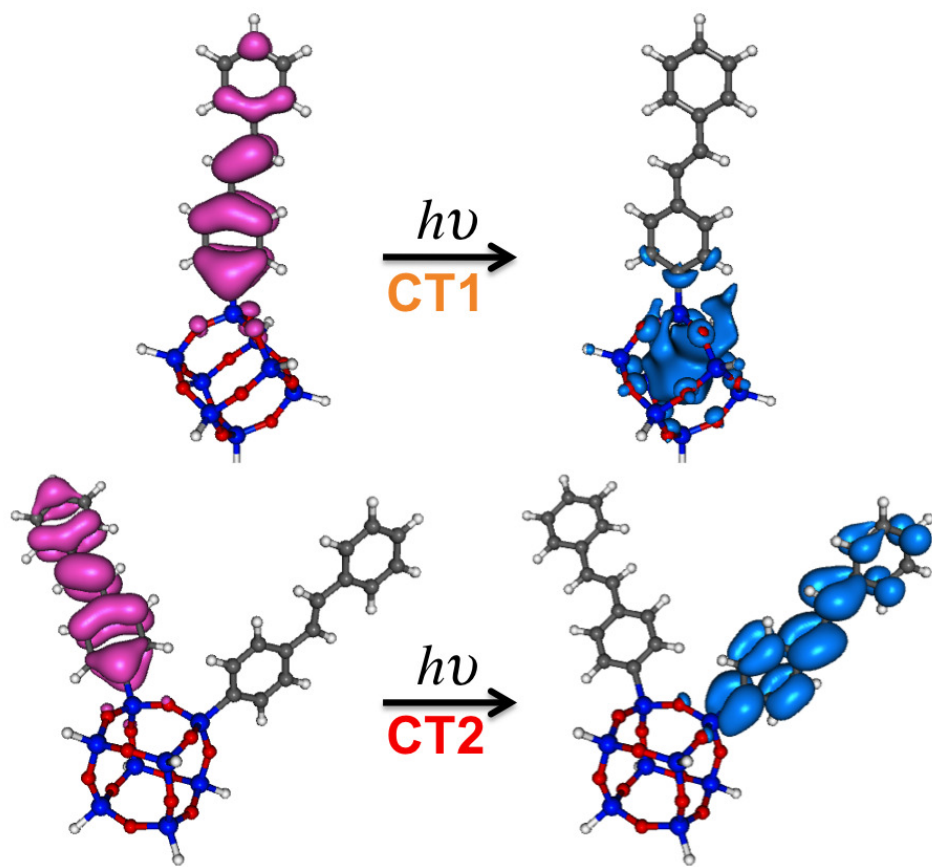


Figure 3.13: The CT1 and CT2 detachment and attachment electronic densities.

The B3LYP functional indicates that the CT2 state affects the emission spectrum, where the CT2 energy lies below the corresponding $\pi - \pi^*$ energy. However B3LYP is known to underestimate the energies of CT states, and therefore the low CT2 energy observation cannot be used to conclusively indicate the CT2 state as the low lying emissive state. Indeed, the CT2 states at the gas phase are indicated to lie significantly above the $\pi - \pi^*$ by BNL. We therefore proceed with only BNL, which is expected to be more reliable for CT states. In the next step, we consider solvation that strongly affects the CT state energies.

The relatively strong dependence of the emission spectrum on solvent polarity[4] indicates that the emissive state energies are strongly influenced by solvation. We consider the solvation effect on the excited states by starting with the vertical excitations at the solvated ground state geometry, then allowing for solvated geometry relaxation using C-DFT. We evaluate the CT state solvation energies from the difference between the C-DFT/PCM energy and the gas phase C-DFT energy *at the same solvated molecular geometry* (particular to each CT type):

$$E_{\text{solvation}}^{CT} = E(CDFT_{PCM}) - E(CDFT_{GAS}). \quad (3.3)$$

The C-DFT relaxations use charge constraints ranging from the subunit partial charges at the gas-phase TDA level to the limit where a whole electron is transferred. The TDA charges correspond to the Mulliken atomic populations. We find that the donor chromophore in the CT1 and CT2 at the ground state geometry is charged 0.84 and 0.95 respectively, where 1.0 indicates the complete electron transfer limit. For CT1 we consider the fragment charges of the chromophore (donor) and the SQ unit (acceptor) and for CT2 we define the constraints to apply on the sum of the atomic charges of the two chromophores, designating one as the donor and the other as the acceptor.

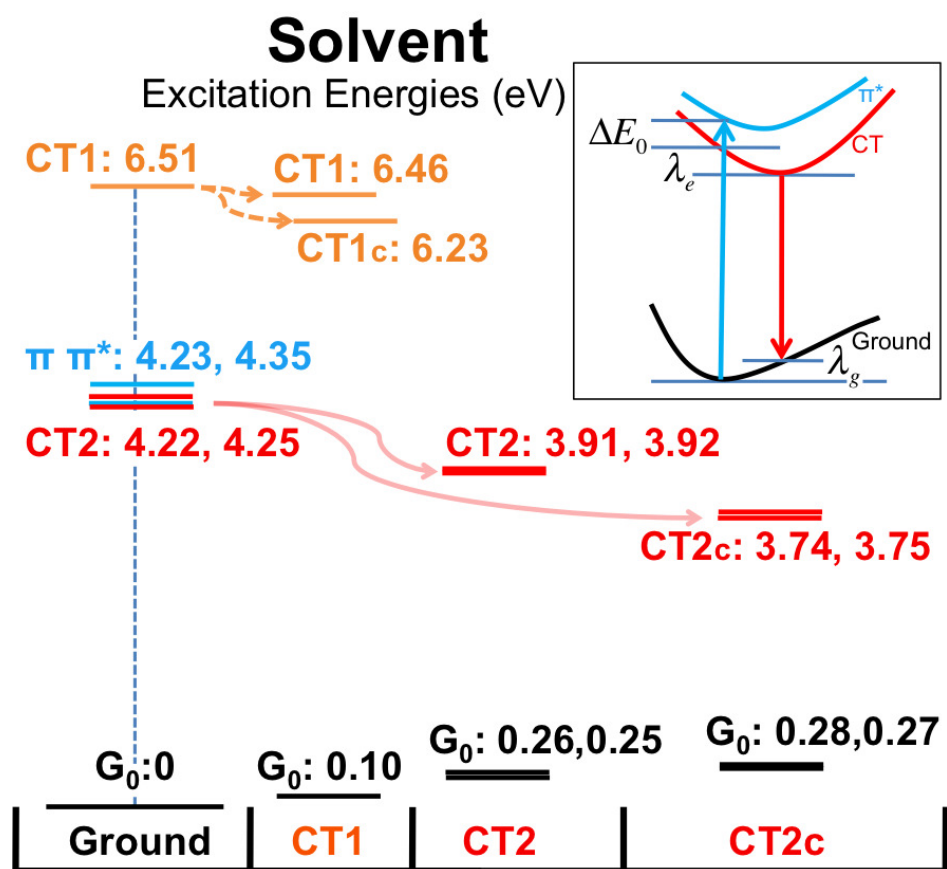


Figure 3.14: Solvated electronic excitation energies (eV), accounting for intramolecular reorganization. G_0 is the ground electronic state energy. Molecular geometries- Ground: solvated ground state geometry; CT(1,2): solvated CT(1,2) with TDA partial-charge constraints; CT(1,2)c: solvated CT(1,2) with complete electron transfer constraints.

The solvated excited state energies are shown in Figure 3.14. A list of the corresponding energies is provided in the Appendix Table F.2. We first consider the solvated excited state energies at the solvated ground state geometry. As expected, solvation gives rise to significant stabilization of both CT1 and CT2 states. However, even with this extra stabilization, the CT1 energy remains significantly higher than that of the non-CT $\pi - \pi^*$ state. At the same time, the solvation lowers the CT2 state energy below that of the $\pi - \pi^*$ state by up to 0.1 eV at the solvated ground state geometry, which suggests that CT2 is the emissive state, rather than CT1.

We focus next on the relaxation processes following the electronic excitation that result in an even larger red-shift between absorption and emission. The different types of energy contributions to the relaxation are illustrated in the insert in Figure 3.14. The intramolecular reorganization energies affecting the emission spectrum include the stabilization of the excited state (λ_e) and destabilization at the ground electronic level (λ_g). An additional third term, ΔE_0 , is the energy difference between the absorbing excited state and the emitting excited state. Here the energy difference is between the vertical excited states at the solvated and unrelaxed ground state geometry. The overall red-shift of the emission spectra, therefore, becomes:

$$\Delta E = \lambda_g + \lambda_e + \Delta E_0. \quad (3.4)$$

The solvated electronic state energies at the CT state optimized structures are also illustrated in Figure 3.14 and in Appendix F. For the CT2 case, we consider the two possible transfer directions (CT to and from each chromophore), where the symmetry breaking effect due to SQ binding results with the slightly different energies for the two possible CT2 processes. Therefore, geometry optimization for each CT2 state was performed separately.

We consider the intramolecular reorganization energies for the CT states, where

Electronic states	Relaxation Energy		ΔE_0	ΔE
	λ_e	λ_g		
$\pi - \pi^*$	0.10	0.17	0.00	0.27
	0.06	0.12	0.00	0.18
CT1(0.84)	0.05	0.10	-2.16	—
CT2(0.95)	0.31	0.26	0.13	0.70
	0.33	0.25	-0.02	0.56
CT2(1)	0.48	0.28	0.13	0.89
	0.50	0.27	-0.02	0.75

Table 3.6: The modeled relaxation energies (eV) of the electronic CT states and their difference from the excitonic $\pi - \pi^*$ energy at the ground state geometry (ΔE_0 , a negative sign means a higher energy). The sum of the relaxation energy and the ΔE_0 defines the overall emission spectra shift (ΔE). In the parenthesis we specify the charge on the donor designated chromophore used in the corresponding C-DFT calculations.

the geometry optimization was carried out only with respect to the ligands while keeping the OHSQ in its ground state geometry. We do so because full optimization leads to a distortion of the SQ unit, which we believe to be a nonphysical artifact of using a continuum model for solvation. More specifically, the attraction between the positively and negatively charged ligands tends to bring them together more than they would be in a molecular liquid, where the solvent molecules would keep them further apart. As a result, the SQ unit is distorted more than it would have in a molecular liquid. However, it is important to note that even when full optimization is carried out, the CT1 state energy remains substantially higher than the absorbing state energy. On the other hand, we find that the intramolecular reorganization associated with the CT2 states lowers the energy by 0.3 eV.

Another contribution to the emission spectral shift is the corresponding destabilization of the ground electronic state, which is close to 0.3 eV for either of the CT2 optimized geometries. Interestingly the relaxation terms are effectively the same for the two CT2 states. The contribution to the spectral red-shift due to excited state

energy differences (ΔE_0) is 0.1 eV for the first state and almost vanishing for the second state. The 0.1 eV energy split emerges from the difference between the two low lying $\pi - \pi^*$ excitations, where the SQ binding induces the symmetry breaking in the absorption energies.

The solvation due to using the partial charges from the BNL TDA gas-phase calculation as C-DFT constraints already indicates significant stabilization. However as summarized in Table 3.6 the predicted shift still does not account for the experimentally observed red-shift in the emission spectrum. Indeed, the solvation may stabilize the transfer of a whole electron, therefore we consider the electronic CT2 state upon a complete electron transfer. We assign the charge constraints 1.0 and -1.0 for the donor and acceptor, respectively. We denote this state as CT2c and illustrate the corresponding energy levels to the right side of Figure 3.14. (A list of the corresponding energies is provided in the Appendix F). The solvation energies corresponding to the complete electron transfer increase for either of the CT states by 0.2 eV. The destabilization of the ground state at the new geometry, however, remains almost unchanged. We therefore find that the stabilization of the CT2c state is twice the destabilization of the ground state energy.

The resulting red-shift between absorption and emission spectra for the CT2 state represented by the CT2c model adds up to 0.8 eV and 0.9 eV which is in excellent agreement with the experimental values of 0.8 eV and 0.9 eV[132]. This suggests that the polarizable nature of the solvent increases the partial charges in solution beyond their values as obtained from the gas phase calculation, thereby leading to further stabilization of the CT states. We list the different energy contributions to the spectral shift in Table 3.6. We include for comparison the relaxation energies of the CT1 state, but emphasize again that only CT2 is indicated to be lowered enough by the solvent to potentially play the role of the emissive state in the relaxation process of the $\pi - \pi^*$ state.

3.2.4 Conclusions

To summarize, we have been able to *quantitatively* reproduce the enhanced red-shift between the absorption and emission spectra of stilbene-functionalized OHSQs using a strategy that combines TD-DFT/TDA with the BNL range-separated hybrid functional, and accounts for solvation effects via C-DFT and PCM. We have been able to identify the emissive states as *ligand-to-ligand* (CT2) as opposed to *ligand-to-silsesquioxane* (CT1) CT states. Our results demonstrate the importance of using range-separated hybrid functionals, and of accounting for solvent effects in modeling the unique spectroscopic properties of this multi-chromophoric system.

3.3 Future Directions: Selectively Tuning Charge Transfer Pathways via Chromophore-Functionalized Silsesquioxanes

In the previous studies discussed in this chapter, accurate characterization of the excitations in chromophore-functionalized SQ was achieved. It was found that charge transfer between chromophores (CT2) is more energetically favorable and is therefore more likely to play a role in the excited state relaxation of stilbene-functionalized OHSQ. However additional investigations into excited state relaxation processes in functionalized SQ molecules suggest multiple emissive states that may depend on the spatial orientation of the chromophores.[200] Furthermore, the lifetime of an excitation in functionalized SQs has been shown to depend on the presence and size of the SQ cage.[200] While the results presented in this work provide explanations for the red-shifted emission spectra in these molecules based on chromophore interactions, for example, as expected in molecular aggregates,[201], a more detailed description of the role of the SQ core in excited state relaxation is required.

Current effort is focused on understanding the solvent stabilization that can occur

for the chromophore to SQ cage (CT1) charge transfer state in more detail. Preliminary calculations according to the methods presented in Chapter 3.2 are presented here. We seek to understand the interaction between the SQ cage and ligated chromophores by comparing the behavior for chromophores weakly coupled to the SQ core to those more strongly coupled to the SQ core.

According to the findings presented in Chapter 3.1, the proximity between molecular orbitals of the SQ core and the free ligand plays a role in determining the mixing between these molecular components in functionalized-SQs.[35] Figure 3.15 highlights the proximity of free chromophore molecular orbital energies to those of the SQ core. The HOMO and LUMO energies for free benzene are only slightly higher in energy than those of the OHSQ, and therefore can achieve better mixing with the SQ core than the stilbene HOMO and LUMO, also shown in the figure. Therefore, current studies investigate the relaxation of CT1 in phenyl-functionalized SQ cages (including octahedral (T8 or OHSQ), decahedral (T10) and dodecahedral (T12) SQ cages).

Following the first step in calculating the solvent stabilization, structural optimization using a polarizable continuum model and RSH-DFT was performed as outlined in Chapter 3.2. Figure 3.16 indicates similar behavior for CT1 in phenyl-SQ systems as was observed for CT2 in stilbene-SQ systems. The solvent stabilization of the CT1 state may suggest that this type of charge transfer is energetically favorable in phenyl-SQ systems, which prompts deeper investigation into the relaxation of the CT1 state in these systems. Current and future work will be pursued in this direction.

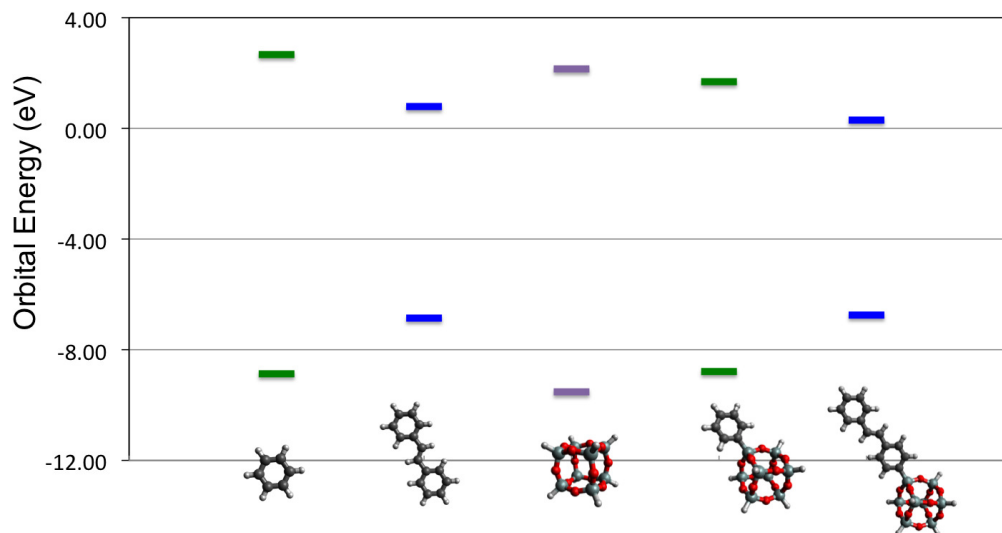


Figure 3.15: Orbital energies for benzene, stilbene, OHSQ, phenyl-OHSQ, and stilbene-OHSQ (eV)

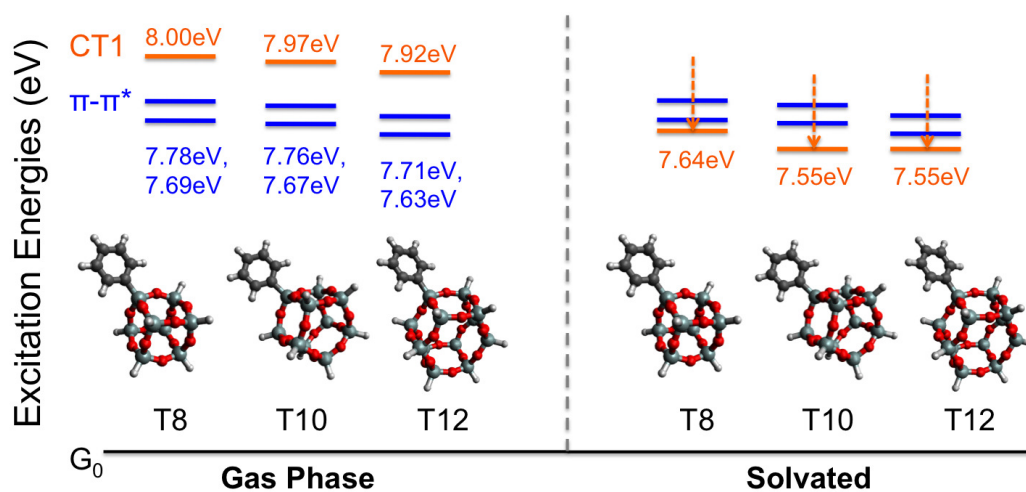


Figure 3.16: Calculated $\pi - \pi^*$ and CT1 (chromophore-to-SQ) excitation energies at the equilibrium geometry (optimized using a PCM). (eV)

CHAPTER IV

Time-Dependent Electron Transport Through Model Molecular Junctions

4.1 Introduction

The study of electron and energy transport through molecular and nanoscale systems has recently drawn wide research attention. [202–242] The appeal stems mainly from prospects associated with nanotechnology and requires understanding of the complex physics of electron transport (ET) processes at the atomic and electronic structure levels.[218, 219, 243–253] A wide range of experimental schemes[202, 203, 210, 211, 214–216, 223, 231, 233, 238, 241] are used to fabricate molecular transport junctions, where typically large statistical sampling and elaborate control schemes are required. It therefore remains a challenge to identify a robust, controllable, and reproducible molecular junction fabrication scheme. Recent technological advances are also promising to shift the focus of electron transfer studies from steady state to non-equilibrium phenomena.[254, 255]

A promising prospect for enhancing characterization of molecular junctions under bias is offered by combining spectroscopy and current measurements. The charging of a small molecular bridge during the conductance process is coupled with changes in nuclear configuration. These geometric changes underlie the strong dependence

of electron transport (ET) on vibrational degrees of freedom. Experimentally, the vibrational spectra of single molecules are obtained by inelastic electron tunneling spectroscopy (IETS).[256–258] This procedure has been accompanied by substantial progress in modeling phonon-assisted conduction.[259–263] Other experimental developments combine optical spectroscopy with transport studies,[264–268] whereby conductance enhancement of the junction is correlated with changes of the *in situ* measured Raman spectra.

Computational transport modeling through molecular systems has the potential to address this difficulty and has indeed demonstrated strong conductance dependence on geometric aspects related to the bonding at the interface.[269, 270] Proper characterization of bulk-coupled molecular systems is crucial for establishing a meaningful comparison between modeled and measured conductance. Therefore, accurate modeling of the temporal resolution of electron transport becomes essential for obtaining fundamental insight.[271–278]

In general, resolution of the time-dependent (TD) conductance is necessary in systems where quantum interferences affect the electron transport, This includes the study of transient conductance, where the system still evolves to a steady state. TD studies revealed interesting quantum effects associated with photo-assisted conductances in mesoscopic systems, such as absolute negative conductance, Coulomb blockade, and Kondo effects driven by alternating-current (AC) fields.[245–247, 252, 253, 279] Other studies highlight the importance of transient effects, where the non-equilibrium nature of electron transport determines the switching rate and efficiency of the transport.

The dynamics of electron transport is greatly complicated by inherent dissipative aspects. The complexity of the electron transport due to quantum dephasing is reflected even for model systems of non-interacting electrons in bulk-coupled systems driven by TD potentials.[278, 280–289] Recent TD computational studies that analyze

currents under TD applied potentials include approaches based on TDDFT,[271–273, 290–296] density matrix equations with Floquet representation or quantum master equations,[278, 297–301] Floquet scattering matrix approach,[302, 303] and Keldysh non-equilibrium formalism.[274, 278, 304–308] Keldysh Green’s function (GF)-based expansions[309–313] provide for a rigorous route to treat electron dynamics in biased systems[304] and are utilized in the following studies to analyze quantum interferences affecting the transient transport, and bias-induced non-equilibrium effects on the electronic spectra of model systems.

Specifically, we implement a dynamical approach based on Keldysh formalism to study electron transport. The coupling between a molecular junction and the bulk electrodes broadens and shifts the electronic density of states, resulting with an energy distribution of the electronic density matrix ($\rho(E)$). This may involve broadened states that can couple the two leads, thereby providing an efficient transport channel. The Keldysh non-equilibrium Green’s function (GF) formalism relates a coupled electronic system experiencing a TD perturbation to its thermally equilibrated initial state. In this approach, by expressing the electronic equations of motion on a time ordered contour, the bulk-coupling induced non-Hermiticity in the Hamiltonian is addressed. Broadening effects due to the electrode coupling are treated consistently, where the bulk-induced manifolds of junction states are directly propagated. The electronic density of the coupled system can be extracted from these equations.

Most descriptions of dynamic transport that are GFs-based formalisms follow the seminal work of Jauho et al.,[304] where system partitioning for the unperturbed state is employed. In this picture the system’s components are each kept in thermal isolation up to switching on the perturbation. Initial state designation, as reflected from model-partitioning, however, may affect the evolution of the system to steady state. Transient effects, therefore, can reliably be treated only by a non-partitioning scheme, which is fully and consistently equilibrated. The following studies employ

the more consistent approach within the Keldysh formalism, where the full equilibration of the unperturbed device with the electron baths is included.[314] The importance of the partition-free approach was highlighted in several recent real time-based propagations.[271, 272, 278]

4.1.1 Theoretical Background

The approach for evaluating the evolving electronic density that is used to derive the electronic properties of a molecular junction under bias conditions is described here. We solve the electronic equations of motion using Keldysh formalism, in which electron dynamics is represented by the lesser Green's function (GF),

$$G^<(xt, x't') \equiv i \frac{\text{Tr}[\hat{U}(t_0 - i\beta, t_0) \hat{\Psi}_H^\dagger(x't') \hat{\Psi}_H(xt)]}{\text{Tr}[\hat{U}(t_0 - i\beta, t_0)]}. \quad (4.1)$$

where $\hat{U}(t_0 - i\beta, t_0)$ is the grand canonical density operator,

$$\hat{U}(t_0 - i\beta, t_0) = e^{-\beta(\hat{H}_0 - \mu\hat{N})} \quad (4.2)$$

and can be viewed as a propagator of the time independent Hamiltonian, $\hat{H}_0 = \int h(xt_0) \hat{\Psi}_H^\dagger(xt_0) \hat{\Psi}_H(xt_0) dx$, offset by the electron number operator, $\hat{N} = \int \hat{\Psi}_H^\dagger(xt_0) \hat{\Psi}_H(xt_0) dx$, at equilibrium conditions designated by a given initial chemical potential μ and temperature $\beta \equiv (k_B T)^{-1}$. This propagator then acts over the complex time interval $[t_0, t_0 - i\beta]$. The traces in Eq. (4.1) are taken over states of all possible energies and electron numbers. The field operator, $\hat{\Psi}_H^\dagger(x't')$ ($\hat{\Psi}_H(xt)$) is a sum of single electron creation (annihilation) operators weighted by corresponding single electron states in the Heisenberg picture. For example,

$$\hat{\Psi}_H(xt) = \hat{U}(t_0, t) \left[\sum_j \psi_j(x) \hat{a}_j \right] \hat{U}(t, t_0) \quad (4.3)$$

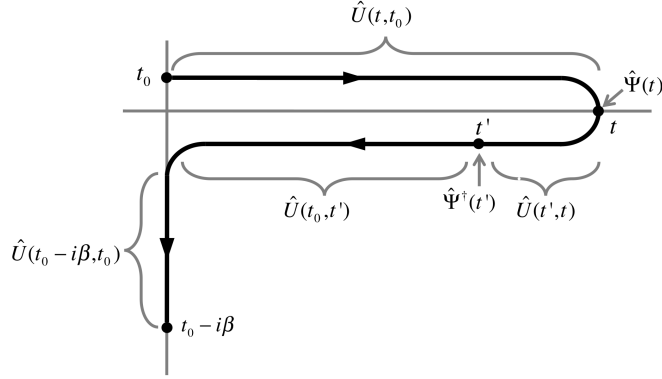


Figure 4.1: The Keldysh time contour includes three branches defined in the complex plane: forward and backward real time and, extended into the imaginary axis at t_0 , the thermal lifetime. The forward and backward branches along the real axis are vertically shifted for purposes of illustration.

where $\hat{U}(t, t')$ propagates the full time dependent Hamiltonian, $\hat{H}_0 + \hat{V}(t) - \mu\hat{N} = \int h(xt)\hat{\Psi}_H^\dagger(xt_0)\hat{\Psi}_H(xt_0)dx$, over the *real* time interval $[t', t]$. Note that we have chosen to absorb μ into $h(xt)$. This convention will be followed from this point forward. The numerator in Eq. (4.1) can be viewed as containing a sequence of propagators and field operators. This sequence defines the Keldysh contour (Figure 4.1).

In the absence of explicit electron correlation and exchange terms (i.e., for non-interacting electrons) the lesser GF solves the equation of motion:

$$\left[i\frac{\partial}{\partial t} - h(xt) \right] G^<(xt, x't') = 0 \quad (4.4)$$

$$[G^<(xt, x't')]^* = -G^<(x't', xt). \quad (4.5)$$

where $h(xt)$ is the one-body hamiltonian describing the system. Here, we use the variable x to represent a vector of the spatial coordinates and use atomic units, where $\hbar \equiv 1$. We express operators in a localized diadic basis representation, where, for example, the propagated $G^<$ becomes

$$G^<(xt, x't') = \sum_{i,j} G_{i,j}^<(t, t') \phi_i(x) \phi_j(x'), \quad (4.6)$$

and $h_{i,j}(t) = \int dx \phi_i(x) h(xt) \phi_j(x)$. Note that a localized non-orthogonal basis set, such as the gaussian basis sets typically used in electronic structure theory, can be rotated to a localized orthogonal basis set. Therefore, without loss of generality, Eqs. (4.4) and (4.5) become

$$\left[i\mathbf{1} \frac{\partial}{\partial t} - \mathbf{h}(t) \right] \mathbf{G}^<(t, t') = 0, \quad (4.7)$$

$$[\mathbf{G}^<(t, t')]^\dagger = -\mathbf{G}^<(t', t). \quad (4.8)$$

The complete one body Hamiltonian takes the following form

$$\mathbf{h}(\mathbf{t}) = \mathbf{h}_0 + \mathbf{v}(t), \quad (4.9)$$

where \mathbf{h}_0 represents the electron kinetic energy and electron-nuclear attractions, which are defined by the model system, and the TD component $v(t)$ is the external potential acting on the electrons. We combine the Equations 4.7 and 4.8, and rewrite in terms of the time variables: $\bar{t} \equiv \frac{t+t'}{2}$ and $\Delta t \equiv t - t'$ to obtain:

$$\frac{\partial}{\partial \bar{t}} \mathbf{G}^<(\bar{t}, \Delta t) = i \left[\mathbf{G}^<(\bar{t}, \Delta t) \mathbf{h}(\bar{t} - \frac{\Delta t}{2}) - \mathbf{h}(\bar{t} + \frac{\Delta t}{2}) \mathbf{G}^<(\bar{t}, \Delta t) \right]. \quad (4.10)$$

The two-time variable GF is the correlation function of an electronic system coupled to electron reservoirs as expressed on the Keldysh contour.[311, 313] The dynamical electronic density ($\rho(E, t)$ in Eq. 4.32) can be extracted from this GF by Fourier trans-

forming from the Δt domain to the frequency ($\bar{\omega}$) or energy ($E = \hbar\bar{\omega}$) domain[277]:

$$\rho(E, \bar{t}) = -i \int_{-\infty}^{\infty} d(\Delta t) e^{iE \Delta t} \mathbf{G}^<(\bar{t}, \Delta t). \quad (4.11)$$

The first transformation over Δt results directly with the desired evolving electronic distribution. The bulk projection is based on using the electrode's self-energy expressed by Σ 's.ⁱ The corresponding $G^<$ electronic Kadanoff-Baym equations of motion[311, 313] are written asⁱⁱ

$$\begin{aligned} i \frac{\partial}{\partial \bar{t}} \Delta \mathbf{G}^<(\bar{t}, \bar{\omega}) &= [\mathbf{h}_0 + \mathbf{v}_0, \Delta \mathbf{G}^<(\bar{t}, \bar{\omega})] + \int d\omega' [\mathbf{v}(\bar{t}, \omega') \mathbf{G}^<(\bar{t}, \bar{\omega} - \omega') - \mathbf{G}^<(\bar{t}, \bar{\omega} + \omega') \mathbf{v}(\bar{t}, \omega')] \\ &+ \int_{-\infty}^{\infty} dt' [\Sigma^{\mathbf{R}}(\bar{t} - t') \Delta \mathbf{G}^<(t', \bar{\omega}) e^{-i\mathbf{h}_0(\bar{t}-t')} - e^{i\mathbf{h}_0(\bar{t}-t')} \Delta \mathbf{G}^<(t', \bar{\omega}) \Sigma^{\mathbf{A}}(t' - \bar{t})]. \end{aligned} \quad (4.12)$$

The self energy (Σ) terms above introduce the effects of the electrodes by projecting the GFs for the time independent electrode hamiltonian, $\mathbf{g}^{\mathbf{R}}_i(t)$, onto the device,

$$\Sigma^{\mathbf{R}}(t) = \sum_i \mathbf{h}_{0i} \mathbf{g}^{\mathbf{R}}_i(t) \mathbf{h}_{0i}^\dagger. \quad (4.13)$$

Here \mathbf{h}_{0i} is the electrode-device hopping term for the i -th electrode in the time independent hamiltonian. Several methods exist for calculating $\mathbf{g}^{\mathbf{R}}$. We use a decimation technique that, in effect, iteratively renormalizes the tight-binding hamiltonian for a periodic semi-infinite electrode.[315, 316]

The $G^<$ of the bridging system written in the mixed time-frequency representation,

ⁱPure time-domain representations require using sufficiently large clusters to reliably treat conductance through a device region. In the frequency domain on the other hand self-energy expressions can use a cluster model to effectively represent an open system. Frequency domain bulk-self energy models can be used to represent the dissipative effect of coupling to the electrodes.

ⁱⁱThe full derivation of Eq. (4.12) is provided in Ref. [277].

can be separated into time dependent and independent components:

$$\mathbf{G}^<(\bar{t}, \bar{\omega}) = \mathbf{G}_{v_0}^{0,<}(\bar{\omega}) + \Delta \mathbf{G}^<(\bar{t}, \bar{\omega}). \quad (4.14)$$

In this picture, the $\Delta \mathbf{G}^<(\bar{t}, \bar{\omega})$ is defined to be the difference between the total lesser GF, $\mathbf{G}^<(\bar{t}, \bar{\omega})$, and the steady state lesser GF, $\mathbf{G}_{v_0}^{0,<}(\bar{\omega})$, under the effect of a constant bias (\mathbf{v}_0). At steady state, the electronic density reduces to an energy distribution that results from coupling to electrodes. The electronic density distribution can be extracted from the lesser GF, where $G^<(t_1, t_2) \rightarrow G^<(t_1 - t_2)$ and, therefore, $\rho(E, \bar{t}) \rightarrow \rho(E)$, which is an appropriate form for a perturbation theory (PT) treatment.

We re-express the GFs using Fourier transforms and solve for the response of the system to a TD perturbation $v(t)$ using PT. In this approach, the excitation spectrum of the biased system is obtained from the first order electronic response to the instantaneously impulsive perturbing potential (see Eq. 4.33). As reference for the PT treatment we use the simplified equation of motion under steady biasing conditions ($G_{v_0}^{0,<}(\bar{\omega})$).ⁱⁱⁱ The energy distribution, $\mathbf{v}(\bar{t}, \bar{\omega})$, of the TD perturbation acting on the electrode-coupled system, $\mathbf{v}(t)$, is given in terms of the perturbation's Fourier transform, $\tilde{\mathbf{v}}(2\bar{\omega})$:

$$\mathbf{v}(\bar{t}, \bar{\omega}) = \frac{1}{\pi} e^{-i2\bar{\omega}\bar{t}} \int_{-\infty}^{\infty} dt e^{i(2\bar{\omega})t} \mathbf{v}(t) = \frac{1}{\pi} e^{-i2\bar{\omega}\bar{t}} \tilde{\mathbf{v}}(2\bar{\omega}). \quad (4.15)$$

In calculating $\mathbf{G}_{v_0}^{0,<}(\bar{\omega})$, we use the relationship between $\mathbf{G}^<(\bar{\omega})$ and the retarded GF, $\mathbf{G}^R(\bar{\omega})$, which entails calculating the Fermi-matrix.[277]

In the full frequency representation, where $\mathbf{G}^<(\Delta\omega, \bar{\omega}) \equiv \int_{-\infty}^{\infty} d\bar{t} e^{i\Delta\omega\bar{t}} \mathbf{G}^<(\bar{t}, \bar{\omega})$, the application of the TD-PT treatment becomes more effective than in the mixed

ⁱⁱⁱThe effect of \mathbf{v}_0 enters explicitly into the Hamiltonian super operator (Eq. 4.17) and the initial lesser GF $G^{0,<}$. The constant perturbation cannot be simply added to the Hamiltonian for calculating the initial lesser Green function $G^{0,<}(\bar{\omega})$ for proper description of existing non-equilibrium conditions. The effect of a source-drain bias on an initially decoherent electronic charge density cannot be modeled by a simple field asymmetry embedded within the Hamiltonian.

representation. In the PT expansion expressed in the frequency domain the bulk self energies are written exactly; for example, without using the wide band approximation. The equation of motion takes the following form[317]

$$\begin{aligned} \sum_{k,l} \mathcal{H}_{ijkl}(\Delta\omega) \Delta G_{kl}^<(\Delta\omega, \bar{\omega}) &= B^{(1)}(\Delta\omega, \bar{\omega})_{ij} \\ &+ \frac{1}{\pi} \int d\omega' [\tilde{\mathbf{v}}(2\omega') \mathbf{\Delta G}^<(\Delta\omega - 2\omega', \bar{\omega} - \omega') - \mathbf{\Delta G}^<(\Delta\omega - 2\omega', \bar{\omega} + \omega') \tilde{\mathbf{v}}(2\omega')]_{ij}, \end{aligned} \quad (4.16)$$

where

$$\mathcal{H}_{ijkl}(\Delta\omega) \equiv (\Delta\omega + i\eta - \Delta\epsilon_{ij}) \delta_{ik} \delta_{jl} - \Gamma_{ijkl}(\Delta\omega) - (\mathbf{v}_{0ik} \delta_{lj} - \mathbf{v}_{0lj} \delta_{ik}). \quad (4.17)$$

Here

$$\mathbf{B}^{(1)}(\Delta\omega, \bar{\omega}) \equiv [\tilde{\mathbf{v}}(\Delta\omega) \mathbf{G}_{v_0}^{0,<}(\bar{\omega} - \Delta\omega/2) - \mathbf{G}_{v_0}^{0,<}(\bar{\omega} + \Delta\omega/2) \tilde{\mathbf{v}}(\Delta\omega)], \quad (4.18)$$

and $\Gamma_{ijkl}(\Delta\omega)$ is the broadening function due to coupling to the electrodes that is generalized to include dynamical effects (i.e., serves as a memory kernel) by defining

$$\Gamma_{ijkl}(\Delta\omega) \equiv \int dt e^{i\Delta\omega t} [\Sigma_{ik}^R(t) e^{i\epsilon_j t} \delta_{lj} - \Sigma_{lj}^A(-t) e^{-i\epsilon_i t} \delta_{ik}] = \Sigma_{ik}^R(\epsilon_j + \Delta\omega) \delta_{lj} - \Sigma_{lj}^A(\epsilon_i - \Delta\omega) \delta_{ik}. \quad (4.19)$$

In the above equation $\Delta\epsilon_{ij} \equiv \epsilon_i - \epsilon_j$ is the difference between the i -th and j -th eigenvalues (ϵ_i, ϵ_j) of h_0 . The bias (\mathbf{v}_0) effect is entered in the expansion treatment but also in defining the \mathcal{H} super operator. The implemented formalism includes a broadening factor (η) in defining the tensor \mathcal{H} (see Eq. 4.17). This broadening ensures that eventually (at $t \rightarrow \infty$) the system will return to its initial equilibrium configuration.^{iv}

^{iv}In practice, any finite grid method in the frequency domain requires an artificial broadening to

In Eq. (4.16), which can formally be expanded to arbitrary order in the perturbation, we express the TD electronic density in terms of the evolving occupations of the projected junction states.[317] The band structure due to the electrode-coupling is included directly in this expansion through the energy distribution variable, $\bar{\omega}$. The final result in Eq. (4.16) can be Fourier transformed back to the mixed representation to generate Wigner type information that provides important insight on the quantum mechanical effects that determine the time-dependence of the observable (*i.e.* the current operator).

Eq. (4.16) involves a tensor of rank four that is contracted with a matrix (tensor of rank two), and so tetradic notation can be employed to re-expresses matrices as vectors and rank four tensors as matrices. In this notation, a tensor equation appears as a matrix equation and all matrix operations (multiplication, inversion, diagonalization, etc.) can be applied to the reexpressed equation of motion. The convolution integral (second term in the RHS of Eq. 4.16) is dropped in the first order expansion. Using tetradic notation, the tensor \mathcal{H}_{ijkl} of rank four with n dimensionality in each index is re-expressed as a matrix with elements $\mathbf{H}_{ni+j, nk+l}$ and n^2 dimensionality in each index, likewise a matrix becomes a vector. The first order expansion of Eq. (4.16) then becomes:

$$\mathbf{H}(\Delta\omega)|\Delta\mathbf{G}^<(\Delta\omega, \bar{\omega})\rangle\rangle = |B^{(1)}(\Delta\omega, \bar{\omega})\rangle\rangle, \quad (4.20)$$

where $\mathbf{H}_{ni+j, nk+l}(\Delta\omega) \equiv \mathcal{H}_{ijkl}(\Delta\omega)$, $|\Delta\mathbf{G}^<(\Delta\omega, \bar{\omega})\rangle\rangle_{ni+j} \equiv \Delta\mathbf{G}_{ij}^<(\Delta\omega, \bar{\omega})$ and $|B^{(1)}(\Delta\omega, \bar{\omega})\rangle\rangle_{ni+j} \equiv \mathbf{B}^{(1)}_{ij}(\Delta\omega, \bar{\omega})$.

The grand canonical expectation value of any dynamical variable (following the

resolve infinitesimally narrow peaks.

KC formalism[311, 313, 318]) is given by

$$\langle \hat{J}(t_1) \rangle = -i \int_{-\infty}^{\infty} d\vec{x}_1 \lim_{x_2 \rightarrow x_1} [\mathcal{J}(\vec{x}_1) G^<(x_1, x_2)] \quad (4.21)$$

The expectation value can be expressed as a product of two matrices

$$\begin{aligned} \langle \mathbf{J}(t_1) \rangle &= -i Tr \left[\lim_{t_2 \rightarrow t_1} [\mathcal{O} \mathbf{G}^<(t_1, t_2)] \right] = -i Tr \left[\lim_{\Delta t \rightarrow 0, \bar{t} \rightarrow t_1} [\mathcal{J} \mathbf{G}^<(\bar{t}, \Delta t)] \right] = \\ &= Tr \left[\lim_{\bar{t} \rightarrow t_1} \left[\frac{-i}{2\pi} \int_{-\infty}^{\infty} d\bar{\omega} \mathcal{J} \mathbf{G}^<(\bar{t}, \bar{\omega}) \right] \right], \end{aligned} \quad (4.22)$$

where $\mathcal{J}_{ij} = \int_{-\infty}^{\infty} d\tilde{\mathbf{x}} \phi_i(\tilde{\mathbf{x}}) \mathcal{J}(\tilde{\mathbf{x}}) \phi_j(\tilde{\mathbf{x}})$.

In the specific case of the current density operator, which is given by

$$\mathcal{J}(\vec{x}) = -i \left[\vec{\nabla}_x \delta(\vec{x} - \vec{r}) + \delta(\vec{x} - \vec{r}) \vec{\nabla}_x \right] \quad (4.23)$$

or in an AO basis representation

$$\mathcal{J}_{ji}(\vec{r}) = i \left[\phi_i(\vec{r}) \vec{\nabla} \phi_j(\vec{r}) - \phi_j(\vec{r}) \vec{\nabla} \phi_i(\vec{r}) \right], \quad (4.24)$$

the electron current through a given plane is calculated by tracing $[-i \mathcal{J} \mathbf{G}^<]$.

We can apply an instantaneously impulsive potential in the dipole approximation to calculate the spectral response,

$$\mathbf{v}(t) = \mathbf{v}_a \delta(t) = \mathcal{E}_0 \delta(t) \mathbf{D}. \quad (4.25)$$

where $D_{ij} = \int dx \phi_i(x) \hat{D} \phi_j(x)$ and the dipole moment operator is given by

$$\hat{D} = e \hat{x}. \quad (4.26)$$

In the frequency domain, such a pulse is independent of frequency,

$$\tilde{\mathbf{v}}(\Delta\omega) = \mathbf{v}_a = \mathcal{E}_0\mathbf{D}. \quad (4.27)$$

We obtain the electronic density response to the perturbation to generate the time-dependence of the dipole moment:^v

$$\langle D(t) \rangle = \int dE \text{Tr} \left[\rho(E, t) \hat{D} \right]. \quad (4.28)$$

The temporal response of the dipole moment ($D(t)$) contains the excitation spectrum of the biased system, where peaks in the frequency representation ($\tilde{D}(\Delta\omega) = \int e^{i\Delta\omega t} D(t) dt$) correspond to the excitation energies.

4.2 Modeling transient aspects of coherence-driven electron transport

Contributions: Acquisition, analysis, and interpretation of data; drafting and revision of final version to be published.

4.2.1 Computational Model

In this study, the transient aspects of the resulting conductance under effects of applied direct-current and alternating current potentials. The dependence of the coherence-induced response on different aspects of the applied perturbation is resolved in time and analyzed using calculated TD distributions of the current operator.

This study concentrates on the transient current through a one dimensional wire composed of hopping sites, where interactions are included only between neighboring sites. In the considered model, the confined system includes two states which are

^vaccording to Equation 4.11

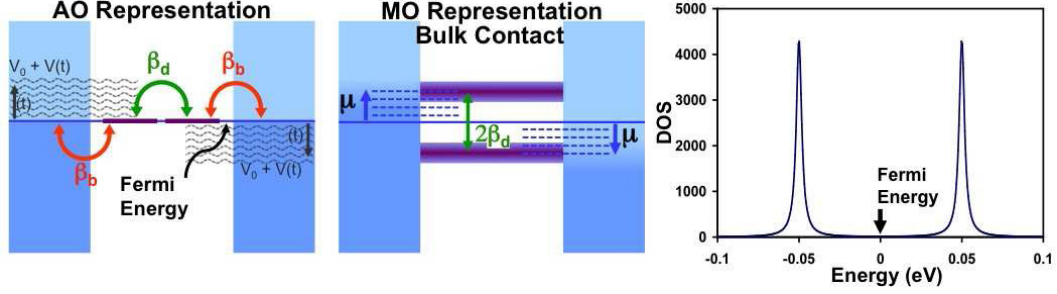


Figure 4.2: Schematic diagram of the model system. (a) Localized/atomic orbital representation where the strong coupling of the device state to the wires are indicated. (b) Diagonalized molecular orbital representation. (c) Broadened electronic density of states.

coupled strongly β_d to result with a pair of bonding and anti-bonding states separated by $2\beta_d$ ($H_{12} = H_{21} \equiv \beta_d$, where H is the electronic Hamiltonian). This energy level scheme is illustrated in Figure 4.11, where the atomic orbital representation is provided in part (a) and the corresponding MO picture reflecting the coupling is given in part (b). The two strongly inter-coupled orbitals are interfaced with electrodes to result with pair of conducting (broadened) bands of states. In the AO representation this is achieved by coupling each site of the strongly interacting pair to a different lead. The coupling to the leads is represented by the self-energies, $\Sigma = \beta_c^\dagger g_s \beta_c$. In our model, the surface GF (g_s) is an imaginary constant number that implements a wide band approximation for the electronic density of the bulk material projected on the surface site. We use $\beta = \beta_c = \beta_d = -0.05(eV)$, where the resulting density of states (DOS) is plotted in part (c).

We note that β and s are the electronic and overlap coupling terms. The diagonal terms of the model Hamiltonian are set to the initial Fermi energy of the system. Accordingly, we express the current operator with the numerical values assigned to the electronic integrals in the Hamiltonian

$$\mathbf{J} = \mathbf{i} \begin{bmatrix} 0 & \beta_d \\ -\beta_d & 0 \end{bmatrix}. \quad (4.29)$$

The traced quantity $i\mathbf{J}\mathbf{G}^<(\bar{t}, \bar{\omega})$ provide the TD band structure (energy distribution) of the current operator. In this case it describes the evolving current through the center of the model system. In all calculations reported below in the results section we set the Fermi energy to zero ($\mu_0 = 0$). This also defines the on site energies as described in the figure.

We use a sufficiently small value ($\eta_d = 0.005eV$) for the broadening factor added to the imaginary component of the Hamiltonian used to calculate the G^R used to calculate the equilibrated system. Finally, we note that in all calculations the target bias potential is set to 0.2 eV unless otherwise stated.

4.2.2 Results and Discussion

We begin by considering the effect of a direct current (DC) potential bias, where we follow the switching temporal effect on the transient current. The current following a (relatively) slow rate for switching off the bias is provided in Figure 4.3. (Note the current scale is provided to the right). We note that while the switching time is long, where an oscillatory transient response is almost absent, the transient current dips below zero before the full dissipation of the system to the zero current limit as a response to the change of the bias. We then further resolve the time-dependence of the band structure of the current operator. The figure also depicts, by a projected color map, the distribution of the current operator ($J(\bar{\omega}, \bar{t})$), where the current at any time can be extracted by integrating over the energy distribution ($\int d\bar{\omega} J(\bar{\omega}, \bar{t})$). The current is associated with contributions from the lower occupied state (ground state), where the upper portion of the band contributes to the positive current. The band structure of the current operator at the switch off is the reflection of the band at the turn on event. At turn off, the positive part of the distribution is at the energetically lower part of the band (further away from the Fermi energy). As the current continues to dissipate the band narrows.

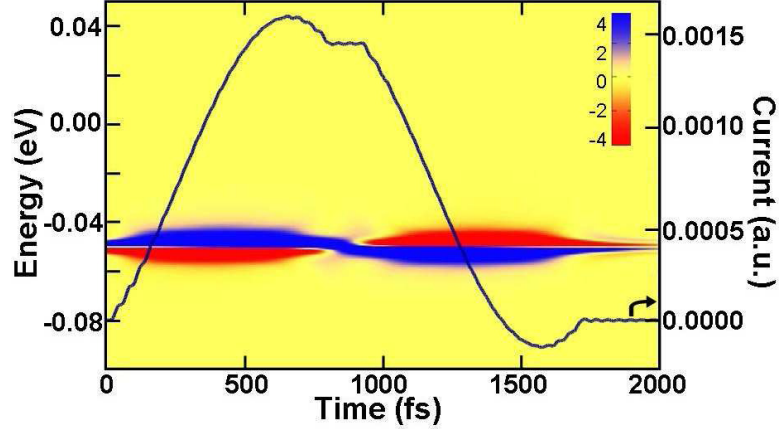


Figure 4.3: The transient current under the effect of a slowly varying potential. The corresponding current density is provided (band structure at the ground state). Note that the right axis corresponds to the current curve while the left axis corresponds to the energy distribution variable.

The current under increased rates of bias switching is considered next. In Figure 4.4 we provide the current upon varying the rate for switching off the bias. The oscillatory response of the current is shown to increase in amplitude with the rate of switching. It is also evident that the current will oscillate with a larger number of periods when the rate is increased. This is also reflected in the band structure as shown in Figure 4.5. The oscillatory response is shown to be related to the direct interference of the two states. The quicker rate of the turn off is shown to result in stronger interference due to the two states. The frequency of the oscillation depends on the present energy levels, where the amplitude of the oscillation is determined by the rate of perturbation change.

We now clarify that the temporal features of the current distribution prior to the switching off as indicated in the figure is not a violation of causality. This is related to the nature of the \bar{t} variable, and by taking the full distribution we generate information that is dependent on the observational time. Indeed, the current operator, which serves as the probe, illustrates that causality is preserved. This can also be understood as a reflection of the uncertainty principle, where Husimi transformations can

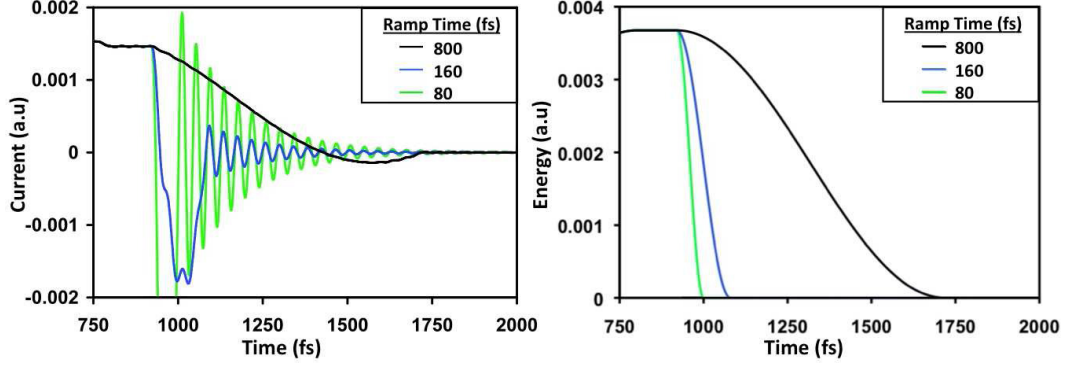


Figure 4.4: TD currents which differ in the rate of the potential turn off. The three TD bias curves are provided to the right.

be used to reflect the fundamental limitations of measurements. This highlights the importance in the current distributions expressed in Wigner form as further demonstrated below. This representation is used to analyze the underlying quantum effects leading to the oscillatory and directed response of the current.

As apparent by the current distribution due to the quick switching event, the two states can be coupled to interfere and lead to an oscillatory response of the current. Stronger coherence can clearly be achieved by a monochromatic field that is tuned to oscillate at a frequency associated to the energy separating the two energy levels. In Figure 4.6 we follow the effect of an applied and tuned driving AC bias on the current. We apply an AC pulse tuned exactly to the weakly coupled states and then apply the same AC bias on the two states where their coupling is either enhanced or decreased by 30% relative to the original value. The change in the coupling strength, as reflected in Figure 4.6a, either further separates (increased β) or diminishes the energy gap between the two states (reduced β). In either case, as shown in Figure 4.6b, the responding current oscillations are reduced. The case where the energy levels are further separated leads to a reduced time period of the response (increase of the frequency). This is expected from the nature of the coupling-induced detuning effect. We note that upon the opposite shift in β the amplitude remains slightly higher with the period slightly increasing.

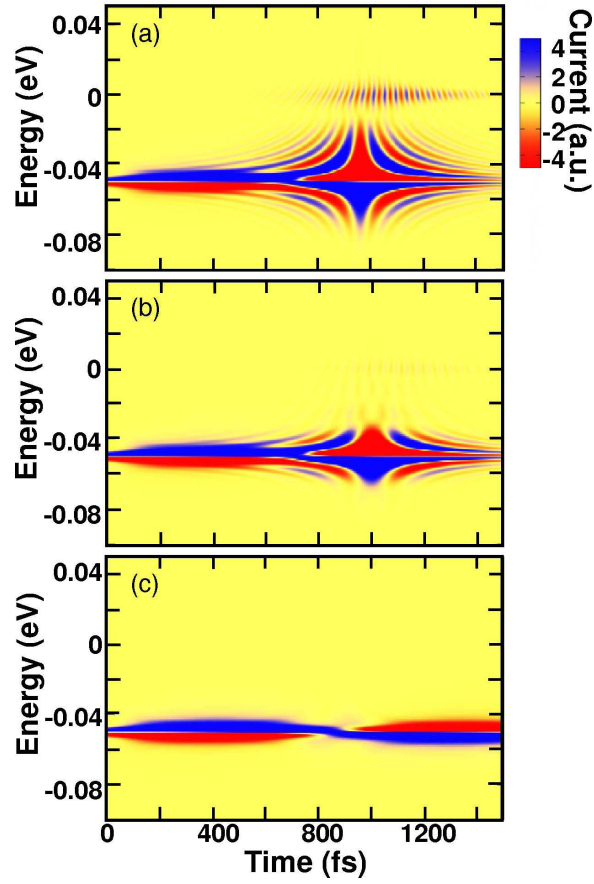


Figure 4.5: TD current distributions projected on a color map ($I(t)$) are provided in 4.4). (a) fastest turn off rate, (b) medium turn off rate, (c) slowest turn off rate.

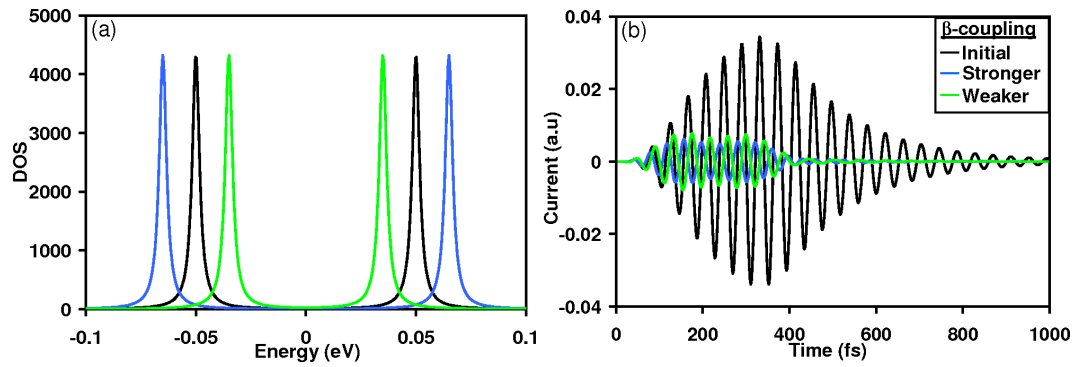


Figure 4.6: Effect of the coupling strength: (a) The density of states (b) TD current under and AC tuned to the original coupling strength.

The coherence underlying the response to an AC bias is also reflected in the band structure of the current operator. In Figure 4.7 the color maps for the current plots of Figure 4.6 are provided. We follow the effect of varying the coupling strength where the AC remains tuned exactly to the system with the original β coupling parameter. The current band structure of the perfectly tuned case (un shifted β) demonstrates the strong amplitude of the AC response by the straight (vertical) bands. These bands are slanted at the transient conditions as shown in Figure 4.7a. For the β detuned cases as shown in Figures 4.7b-c the slanting is increased and the conductance amplitudes are diminished as expected. The mini-band that appears at a shift below the populated state due to the interference with the excited state depends on the tuning. The detuning diminishes its strength and shifts its location. It is shifted below -0.1eV for the case with the stronger coupling or above that value for the second detuned case. Finally, we also point at the different features of the detuning due to the change in beta as reflected, for example, in the decay regime of the main coherence (see Figures 4.7b-c).

We next consider the effect of a DC bias on a coherent driven system, where the frequency of the applied AC bias is set exactly to the energy difference between the two levels. The effect of the DC bias to detune the response was analyzed before[277]. Here its effect to shift the electronic spectra is demonstrated in Figure 4.8(a). The electronic excitation energy is shown to increase due to the DC bias as expected. The applied DC bias also further broadens the spectral peak and diminishes its height. In Figures 4.8(b-d) we follow the TD currents with different strengths of an applied DC under the effect of an AC bias that is retuned to the DC affected energy states. The three plots focus each on different time ranges, where Figure 4.8(b) provides an overall view, Figure 4.8(c) zooms on the initial times where the existing conducting flux is evident. It is also demonstrated that the flux due to the DC bias reduces the amplitude of the oscillatory response, an effect that can be studied only by a TD

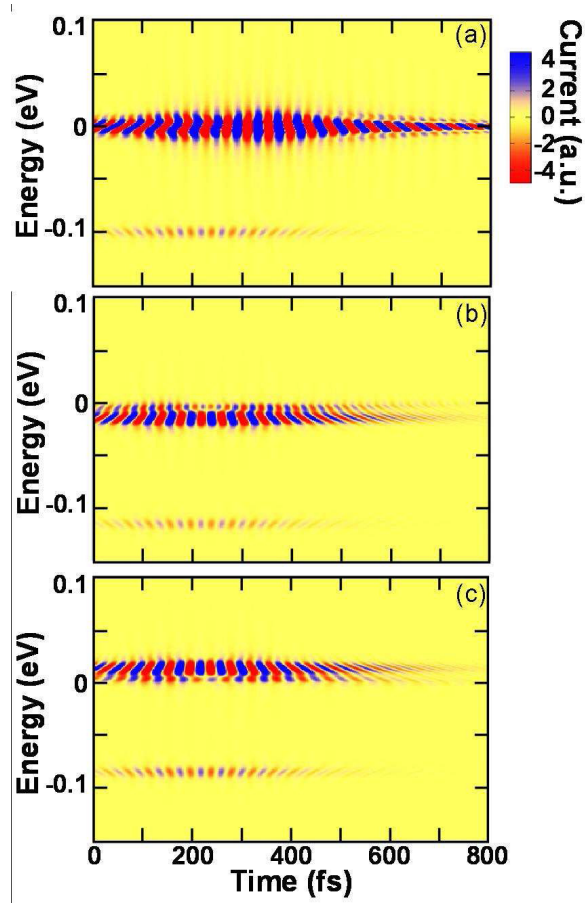


Figure 4.7: The current band structure corresponding to the AC tuned to the energy difference of the two energy levels under the effect of varying the coupling strength (see Figure 4.6). (a) initial coupling, (b) stronger coupling, (c) weaker coupling.

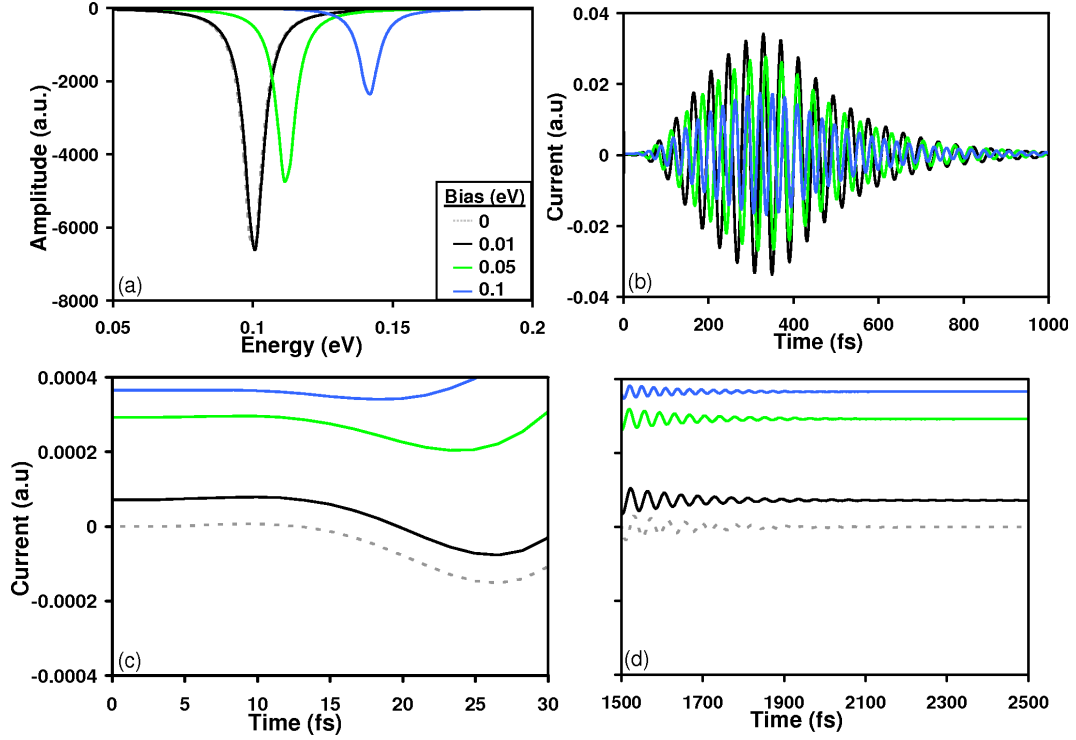


Figure 4.8: Effects of an existing DC bias on: (a) Electronic spectra of the bias system. (b-d) Coherence driven conductance.

scheme. Finally Figure 4.8(d) shows the tail, where the AC bias is turned off and the system returns to its constant biased state.

The band structure of the corresponding current operator is provided in Figure 4.9. The effect of the bias to induce constant flux is reflected in the thin band centered about the ground state energy that is enhanced by the increase of the DC bias. As expected the main coherence is obtained at the energy exactly between the two interfering states. This main coherence is shown to decrease, in spite of the retuning of the AC bias, in the presence of the DC induced flux. This is a consequence of the DC to reduce the spectral peak that corresponds to the electronic excitation as revealed above. Interestingly, the mini-band of the current operator corresponding to the shift below the ground state features an opposite trend. This mini-band is somewhat enhanced upon the application of the bias. This effect however is still not able to reverse the overall observation of the DC bias reducing the oscillatory

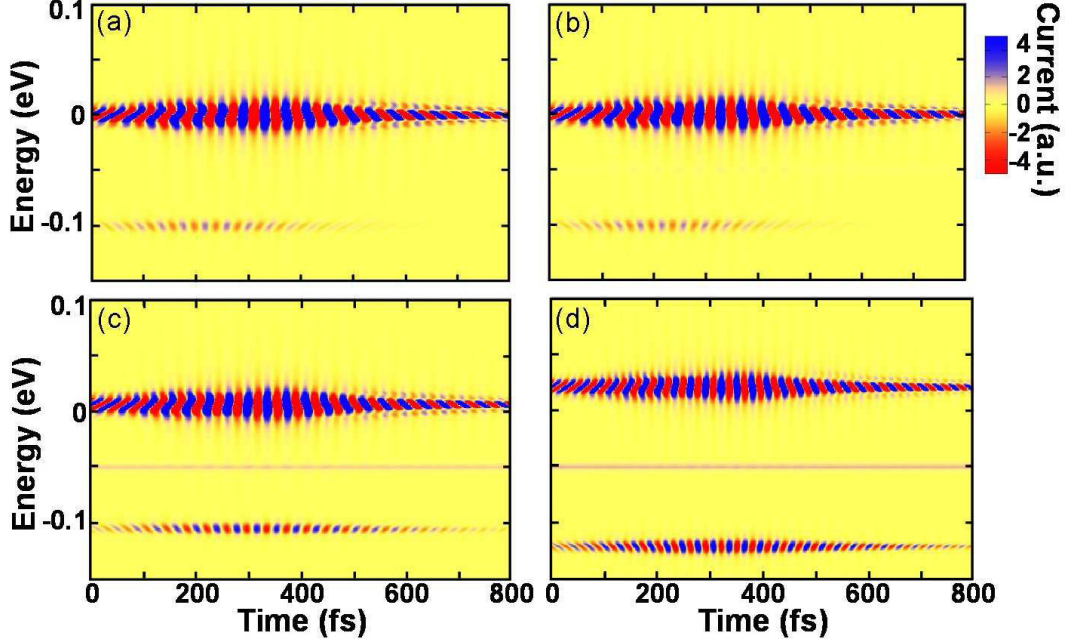


Figure 4.9: The current distributions of the cases with different applied DC biases. (a) 0 eV, (b) 0.01 eV, (c) 0.05 eV, (d) 0.10 eV.

response.

4.2.3 Conclusions

Electron transport through model electronic channels are studied by solving the electronic equations of motion of coupled and bias systems. The electronic equations of motion are represented using Keldysh formalism by Green Functions. Their solution is obtained by expressing the time dependence in the frequency domain, where in order to achieve full time resolution the GFs are defined using two independent and inverted time variables. TD perturbation theory is used to solve the equations.

The TD approach provides a rigorous treatment of the extended system. The calculations also provide a plethora of information through the resolved band structure of the evolving electronic density. This study investigates the band structure of the current operator in model electronic channels. The study considers the transient features of the transport through biased systems. The evolving current operator is

used to generate data that highlights the quantum interferences that determine the oscillatory current at transient conditions. The oscillatory component of the current that is noted at transient conditions is associated with interference of the conducting states, whereas the constant component under steady state conditions when the transient features are dissipated is determined by the broadening extent of the conducting states.

The TD approach is also used to study driven transport. In the system considered here, the oscillatory bias perturbation affects the current via the interferences between states. The relationships between DC bias and AC-inducing coherences are studied in detail. The calculated current operator is used to examine the quantum interferences affecting the current under the driving TD perturbations. As previously mentioned, recent experimental advances underscore the increased importance in the ability to analyze the possibility for current-driven phenomena via applied TD perturbations.

4.3 Bias effects on the electronic spectrum of a molecular bridge

Contributions: Acquisition, analysis, and interpretation of data; drafting and revision of final version to be published.

4.3.1 Computational Model

In this study, bias-induced non-equilibrium effects on the electronic spectra of electrode-coupled systems are analyzed at a fundamental level. The basic effect of bias on the spectrum of a molecular bridge is illustrated. The electronic density of states (DOS) of the bridge is broadened due to the projection of the electrodes DOS on the bridge. The bulk coupling, therefore, also broadens the spectral peak, as illustrated in Figure 4.10 (a) and (b). The qualitative effect of the bias on the electronic transitions

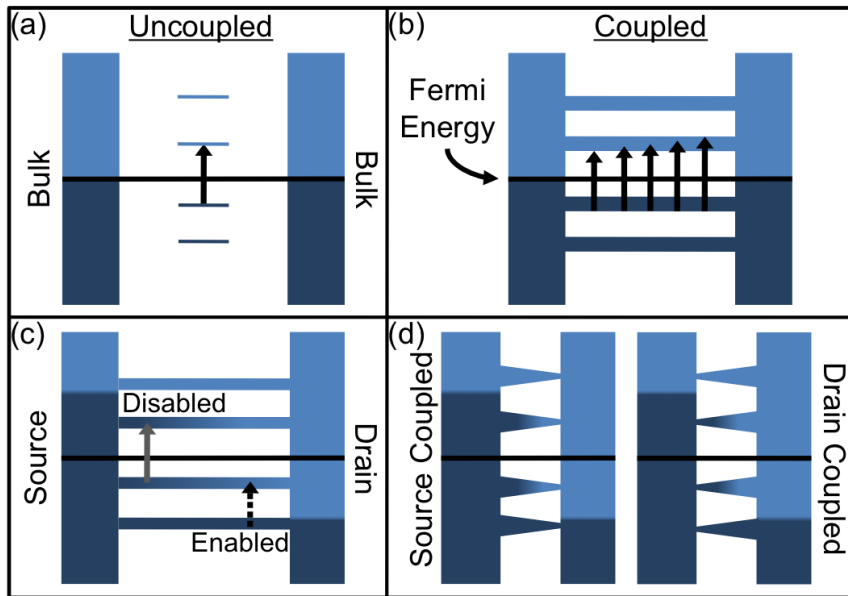


Figure 4.10: The effect of coupling to electrodes and bias is illustrated. (a) The electronic spectra of the uncoupled molecule are resolved (only HOMO-LUMO transition is implied). (b) The spectral peak of the molecular bridge is broadened due to the coupling to electrodes. (c) The bias may enable or disable electronic transitions. (d) Mechanical symmetry breaking may lead to stronger coupling to the source or drain electrode.

is also demonstrated. The electronic transitions between the molecular bands are greatly affected by the bias.[319] The applied bias leads to dynamical flux through the broadened energy levels. The dynamical electron flux disables excitations between states that differ in their occupation at the equilibrium state and which support the current under bias. Likewise, the bias enables excitations between transporting states that are equally populated at equilibrium. (See Fig. 4.10(c) for illustration of these effects of the bias on the spectra.) The disabling and enabling effect of the bias on a model molecular level are quantified, and the the bias and symmetry breaking modes of the molecular bridge are correlated to the electronic spectrum. Different coupling strengths between the bridge and the source and drain electrodes are also considered. (See Fig.4.10(d)).

The electronic spectra of biased molecular junctions are studied using the model

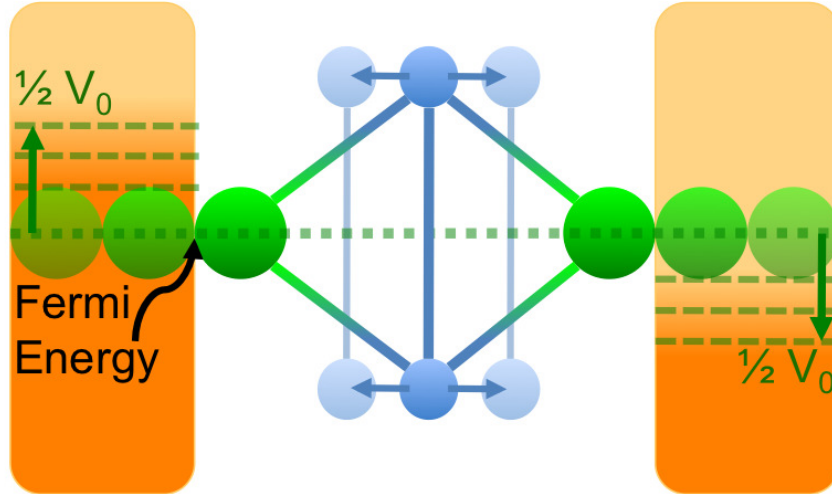


Figure 4.11: Schematic diagram representing device region. Effect of potential bias is implied as well as the shift of carbons toward source and drain electrode

system illustrated in Figure 4.11. The simple model consists of a pair of one-dimensional wires as the electrodes and two sites oriented perpendicularly to the wires as the junction. Each site is described using a single s-type gaussian basis function, which is spherically isotropic relative to the center of the site. The spherical function size is set to the electronic radius of a gold atom (for wire sites) or carbon atom (for the junction sites).

We then identify a “core” region consisting of the two carbon atoms and the two center gold atoms between which the carbons are situated. The gold atoms within the wires are spaced 2.88 \AA apart and the two core gold atoms are spaced 1.90 \AA apart. The carbon bond length is set to 3.29 \AA . In a previous study, it was found that this “diamond” like structure at the simple model Hamiltonian level provides an opportunity to probe the electronic spectrum of an electrode-coupled system affected by an applied bias.[319]

Specifically, the atomic orbital Hamiltonian matrix is parametrized based on the

ionization potential and evaluated using the following Huckel-type expressions:

$$H_{A,A} = -I_A, \quad (4.30)$$

$$H_{A,B} = -\frac{1}{2}K(I_A + I_B)S_{A,B}, \quad (4.31)$$

where $S_{A,B}$ is the atomic orbital overlap between the s-type basis functions centered on atoms A and B , I_A is the ionization potential for atom A , and K is a constant set to 1.75. The numerical values for these parameters are provided in Table I. The Hamiltonian is then orthogonalized ($\mathbf{H} \rightarrow \mathbf{S}^{-1/2}\mathbf{H}\mathbf{S}^{-1/2}$) followed by the imposition of a tight-binding condition within the electrode regions, where only on-site and nearest-neighbor hopping elements are non-zero. All site and hopping elements are maintained in the four-site region of the orthogonalized Hamiltonian that corresponds to the Au-C₂-Au region of the pre-orthogonalized Hamiltonian. In addition, this Hamiltonian is padded with electrode wires of nine gold atoms on each side of the perpendicular C₂ system to ensure that edge effects are minimized in the orthogonalization procedure.

We obtain the electronic spectrum from the dynamic electronic density of the system upon response to relevant perturbations. As described below, the inherent two-time (time-correlation) properties of the Keldysh propagators can be used to formally extract the evolving electronic energy distribution density $\rho(E, t)$, thereby providing access to the responding electronic density $\rho(t)$ of the perturbed, electrode-coupled junction:

$$\rho(t) = \int dE \rho(E, t). \quad (4.32)$$

In this representation, the energy distribution reflects the band structure of the junction coupled with the electrodes. The energy bands have finite widths that support current through scattering states that couple both electrodes. For example, a DOS peak centered at E' with a ΔE width describes the effectively infinite number of states resulting from the projection. In general, $\rho(E, t)dE$ contributes states to the

density matrix ($\rho(t)$) with energies in the range E to $E + dE$.

Below we study the effects of geometric symmetry breaking (by nuclear configuration shifts) of voltage biased systems on their electronic spectra. The steady potential bias is represented by chemical potential shifts from the Fermi energy with an opposite sign on each of the electrodes as shown in Fig. 4.11. The electronic density response to an impulsive pulse is obtained following the dipole approximation (i.e. the pulse is $\mathcal{E}_0\delta(t)\hat{D}$, where \hat{D} is the dipole operator) to generate the time-dependence of the dipole moment:

$$\langle D(t) \rangle = \int dE \text{Tr} [\rho(E, t) \hat{D}]. \quad (4.33)$$

The temporal response of the dipole moment ($D(t)$) contains the excitation spectrum of the biased system, where peaks in the frequency representation ($\tilde{D}(\Delta\omega) = \int e^{i\Delta\omega t} D(t) dt$) correspond to the excitation energies.

The electronic DOS projected on the bridging atomic region at equilibrium (zero applied-bias) are shown in Figures 4.12 and 4.13 (left). As discussed further below, the first figure considers the electronic spectrum affected by electrode-induced electronic DOS broadening, and the second figure considers geometrically-induced symmetry breaking effects. The electronic spectrum is calculated using the dipole moment oriented along the C-C bond (y-axis). In all calculations, the energy scale is shifted to set the Fermi energy to zero for convenience.

4.3.2 Results

We first study the electrode-coupling effect (i.e., the broadening of energy states) on the electronic spectrum. The electronic spectrum of the coupled system is provided in Figure 4.12 (right). We focus on the broadening effect, which can be tuned by the fundamental broadening factor in calculating the retarded GF, $\mathbf{G}^R(\bar{\omega})$, of the electrode-coupled system. The broadening of the electronic DOS leads to broadening of the main spectral peak related to the transition between the highest occupied

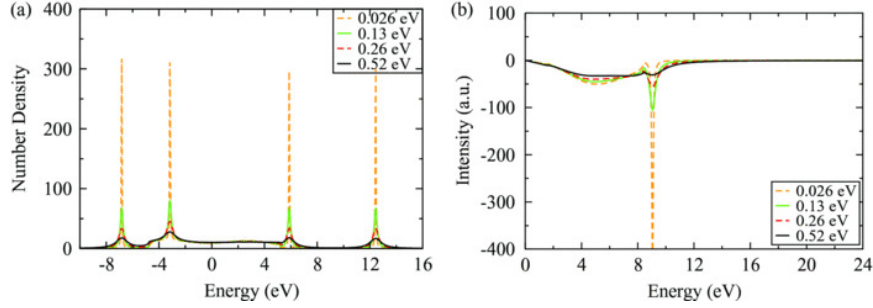


Figure 4.12: (a) The electronic DOS under increasing broadening factor. (b) The electronic spectra corresponding to increasing broadening factor.

molecular orbital (HOMO) and lowest unoccupied molecular orbital (LUMO) orbitals. An additional widely broadened peak is observed at lower spectral frequencies and is associated with the band of states in the DOS located energetically between the HOMO and LUMO peaks.

We also study the combined effect of bias and molecular scale motion on the spectrum. The carbon atoms are shifted by increments of 0.19 \AA toward either electrode, where the resulting molecular electronic DOS is provided in Figure 4.13. The two occupied states respond only slightly to the carbon shift. More substantial changes are observed for the virtual state energies, where a larger, positive shift of the higher virtual state is noted. The corresponding spectra are provided in Fig. 4.13 (right). Upon the symmetry breaking shift, the symmetry forbidden HOMO-Virt2 transition becomes allowed (Virt2 denotes the higher unoccupied state, which is the LUMO+1). The two spectral peaks are shifted to higher and lower values in energy, corresponding to the changes in the virtual state energy.

It is important to comment on the HOMO-LUMO transition, where symmetry-induced disabling effects are noted. The molecular orbital picture for the core region at equilibrium (no bias applied) is provided in Figure 4.14. The orbital energies, corresponding to Fermi energy of -8.067 eV , are provided along with the orbital assignment. The even/odd symmetry of the original orbitals is broken when the carbons are shifted toward the electrode. Clearly, at equilibrium, shifting the carbon

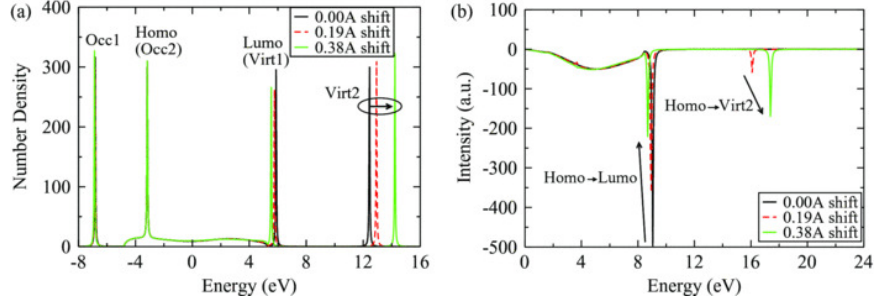


Figure 4.13: (a) The electronic DOS under carbon shifting toward an electrode at equilibrium. (b) The electronic spectra under the carbon shifting. The HOMO-Virt2 transition is enabled by the symmetry breaking.

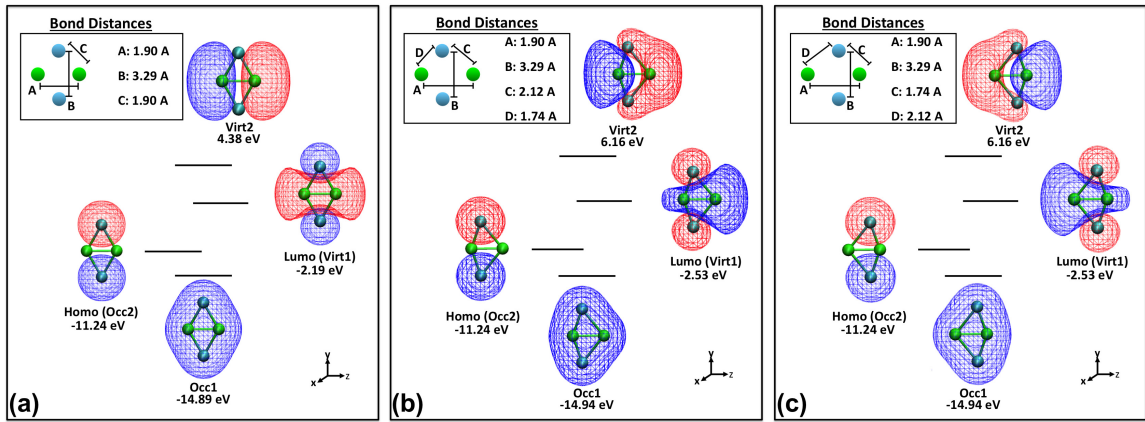


Figure 4.14: Molecular orbital diagrams for non-shifted case (a) and shift of 0.38 Å (b) toward source (c) and drain. Relevant bond lengths and energies are included.

atoms toward either electrode has the same effect on the electronic DOS and therefore on the spectrum. Next we consider the electronic spectrum under applied bias.

Potential bias is applied to the geometrically symmetric system in increments of 2V. The resulting flux populates and depopulates the virtual and occupied orbitals respectively. Specifically, the electron flux partially occupies the LUMO and partially depletes the HOMO, affecting the spectrum fundamentally. First, the spectral cross section of the corresponding allowed excitation in the unbiased system is reduced. As the bias is increased, the HOMO-LUMO transition is disabled as illustrated in Figure 4.15. The dynamical occupation of the orbitals also affects the spectrum by

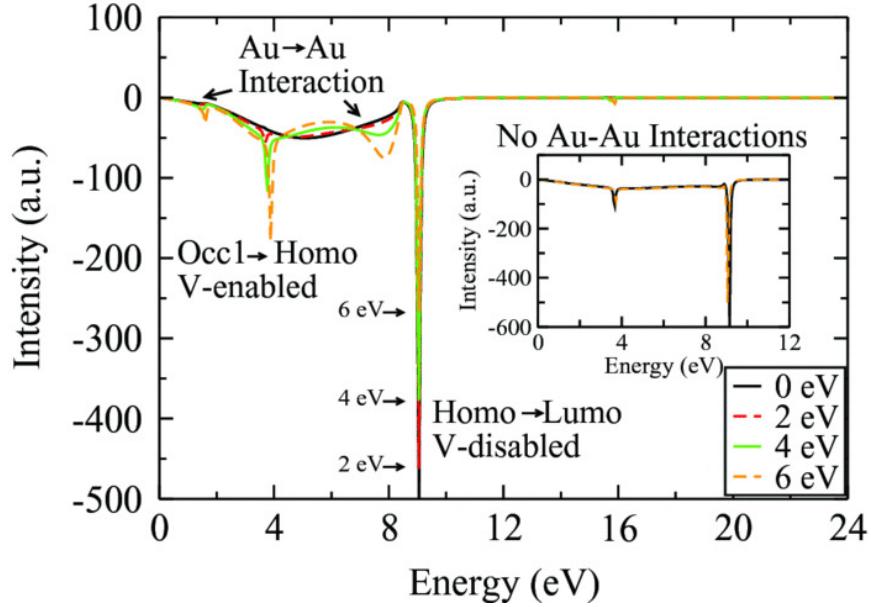


Figure 4.15: Spectral dependence on increasing potential bias for geometrically symmetric junction. (Insert) Bias dependence for small device region indicates cause of Au-Au interaction.

enabling new transitions that are otherwise absent for the unbiased system. Upon bias induced flux, the Occ1-HOMO transition becomes enabled and increases with increasing applied bias (Occ1 denotes the lower occupied, or HOMO-1 state).

On a side note, we confirm the assignment of the bias-enabled peak to the Occ1-HOMO excitations. The same peak appears in the spectrum of a model device that includes only one gold atom on each side, as shown under biases ranging from 0 to 6V (insert to Fig. 4.15). This model, while insufficient for converging the representation of electrode-coupling, confirms that the additional peaks in the low energy regime are assigned only to intra-gold wire transitions (Fig.4.15).

The application of bias potential to the shifted (symmetry broken) carbon systems is now considered. Figures 4.16(a) and (b) show the spectra when the carbons are shifted toward the source and drain electrode, respectively. We focus on the effect of potential bias on the HOMO-LUMO transition for different geometric shifts. The bias-disabling of this transition is enhanced when the carbons are shifted toward the

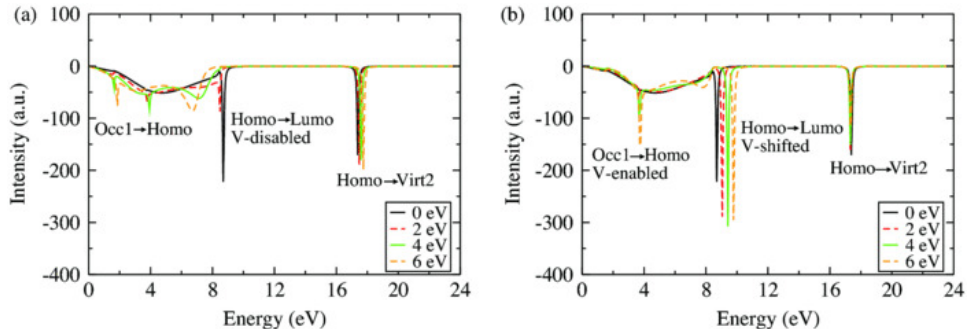


Figure 4.16: The spectral dependence on increasing bias under carbon shift toward (a) source electrode and (b) drain electrode.

source. The opposite effect occurs when the symmetry breaking involves a shift toward the drain. In this case, the bias-disabling is diminished and the spectrum features a small increase of the bias-induced peak as well as a shift to higher excitation energies.

To understand the reason for this difference, the relation of the electronic orbitals illustrated in Fig. 4.14 to applied bias can be considered. For example, we focus on the LUMO where the symmetry breaking results in a shift of the projected density to the more *distant* gold atom. The symmetry breaking-induced polarization is enhanced, therefore, by flux-induced polarization when the molecule is shifted toward the source. On the other hand, the flux negates the symmetry breaking-induced polarization of the LUMO when the carbons are shifted toward the drain. Therefore, the bias-disabling effect on the HOMO-LUMO spectral peak is enhanced when the geometric shift is oriented toward the source and is decreased when the shift is oriented toward the drain.

The symmetry breaking is more subtle in the case of the occupied orbital transitions. Unlike the LUMO, the symmetry breaking shifts the projected density toward the *closer* gold atom. This slight symmetry breaking of the occupied orbitals is reversed by bias-induced flux upon shifting the carbons toward the source and is enhanced when the carbons are shifted toward the drain. Enabling of the Occ1-HOMO transition requires that the HOMO level becomes (at least partially) unoccupied. We

find that increasing bias enhances the bias-enabled Occ1-HOMO peak for the geometric shift toward the drain. This peak appears and then is reduced with further increase in bias for the shift toward the source. The effect on the Occ1-HOMO transition can be attributed to the transmission of each orbital due to electrode-coupling. When coupled to the drain, the transport through the HOMO is decreased, allowing the Occ1-HOMO transition to occur. When coupled to the source, the transport through the HOMO increases as the bias increases, causing the orbital to remain occupied and the Occ1-HOMO transition to become disabled.

4.3.3 Conclusions

The effects of electrode-coupling and bias on the electronic spectrum of a simple molecular model system are analyzed. Fundamentally, electrode-coupling leads to broadened electronic spectral peaks. Biasing conditions can lead to further substantial changes in the electronic spectrum. Under bias, spectral peaks can be enabled by the dynamical occupation and depletion of levels due to the electron flux. The dynamical occupation therefore reduces spectral peaks that are present at equilibrium conditions but can also enable additional transitions, for example, those between equilibrium occupied levels. Finally, symmetry breaking molecular motion fundamentally affects the spectrum by enabling symmetry forbidden transitions. The bias effect on the spectrum can be negated or enhanced by this symmetry breaking of molecular orbitals. Indeed, we find, for example, that the bias-enabled transition between two occupied states is maintained in the drain-coupled case, since the electronic population of the higher occupied level depletes more effectively than in the source-coupled case.

CHAPTER V

Using Student Generated Explanations of Quantum Chemistry Concepts and a Peer-Review Process to Explore Student Conceptual Understanding

Contributions: Conception and design of study; acquisition, analysis, and interpretation of data; drafting and revision of final version to be published.

5.1 Introduction

Challenges related to incorporating student-centered learning approaches within the undergraduate chemistry curriculum have been a topic of discussion since the early 1980s.[320] Though considerable progress has been made in understanding how students construct knowledge within scientific disciplines, a recent report on undergraduate science education by the National Research Council emphasizes the need to implement this understanding in instructional practice.[321]

In this chapter, the design and implementation of an intervention called the CHEM 260H Studio that incorporates student-centered learning approaches is presented. We also present an analysis of the student-generated explanations of quantum chemistry

topics that are constructed within the CHEM 260H Studio, which reveals that while inaccurate representations of course concepts may persist within student-generated materials, there are many dimensions to what instructors would typically consider to be “wrong” within the explanations.

It is well known that as novices in the field of chemistry, undergraduate students typically exhibit misunderstandings of introductory concepts.[321] The construction of new knowledge depends on the prior knowledge that students possess, which can either contribute to or interfere with the way students incorporate new concepts into their own understanding.[321, 322] Introductory quantum chemistry concepts pose a particular challenge to the construction of new knowledge, since in many cases the abstract, probabilistic nature of the models underlying these concepts requires students to think about chemistry in a fundamentally new way.[323]

Writing activities can be incorporated into science courses to provide an avenue for instructors to engage with student misunderstandings.[321] Considerable effort has been focused on developing and refining instructional approaches and formative assessments centered around writing in science courses.[320, 324–338] In recent years, instructional approaches have also begun to incorporate scientific writing in multi-modal contexts that are applicable to wikis, podcasts, and blogging websites, where writing can be supported by other modes of expression including figures, audio, video, and other media.[339–345] In most cases, such writing activities are pursued within collaborative environments, where peer interaction and discussion of ideas supports students’ co-construction of knowledge.[346] Furthermore, it has been shown that writing with the intent to explain or teach can have a positive effect on student learning outcomes.[347, 348]

While writing can provide a way for students to reflect upon and revise their understanding, it is unclear how effective students are at identifying, reflecting upon, and revising their own misunderstandings. As mentioned above, quantum chemistry

concepts may require students to radically change the way that they think about chemistry, and students often struggle to incorporate quantum mechanical models into their pre-existing understanding of chemical phenomena.[323, 349] The “illusion of competence” that low-performing students have been shown to exhibit are an additional cause for concern, since such students typically perceive that they possess a better understanding of course topics than they actually do.[350] In this way, we suspect that students (especially low-performing students) may not always be able to identify and revise their own misunderstandings through writing.

One way to address these concerns would be for the instructor to identify and respond to misunderstandings, using student writing as formative assessments.[351] However, evaluating students’ written work for both content and clarity within large lecture courses can become a considerable challenge for instructors.[320, 352] As a solution, many large introductory chemistry courses rely on peer instruction, such as peer review and peer grading, as a way to provide feedback on student writing.[320, 327, 335, 338, 353] Recent investigations by Freeman & Parks into the accuracy of peer grading reveals that the students struggle to grade higher-order conceptual questions (e.g., according to Bloom’s taxonomy).[354] These authors suggest that the effectiveness of peer grading depends on the context of the assignment, and may work best for low-stakes assignments. Their findings rekindle our concern that student misunderstandings of quantum chemistry concepts may not be adequately addressed when the misunderstandings are expressed within the context of peer-reviewed or peer-graded writing activities.

In this study, we use the CHEM 260H Studio as a platform to investigate the inaccuracies that persist within student-generated explanations of quantum chemistry concepts. We focus on the relationship between inaccuracies that persist after a peer review process, and those that are identified during peer review. In other words, we are interested in determining whether the types of inaccuracies that persist after

the peer review differ from those that a peer review process is able to engage. Furthermore, we aim to understand whether it is possible to construct the peer review process in a way that would maximize the ability of students to identify and revise inaccuracies in student-generated explanations.

The following research questions have guided the analysis we present here:

1. What types of inaccurate representations of quantum chemistry topics are present in the final version of student-generated explanations, and in particular, what types of inaccuracies persist through a peer review process?
2. In what way does the peer review process affect the types of inaccuracies that may persist in student-generated explanations?

5.2 Background on Design and Implementation

In this study, the design of the CHEM 260H Studio itself is also investigated within the context of design-based research. Design-based research has gained popularity in educational research communities as a method to develop and refine theories of learning by designing, implementing, and studying educational artifacts.[355–357] Studying the iterative process of design and implementation provides a unique opportunity to understand aspects of learning in situ, which ensures a high degree of ecological validity.[355–357] In this respect, Collins, Joseph, & Bielaczyc liken design-based research to other design sciences such as engineering or medicine. Therefore, design-based research should not only provide design principles and strategies related to the educational intervention itself, but should also contribute to the refinement of our understanding of student learning.[355] In this way, our current analysis seeks to not only improve and build upon the principles that have contributed to the original design of the CHEM 260 Honors Studio, but also to surface inaccuracies in student-generated explanations, as well as explore avenues to address student misun-

derstandings via the peer review process.

The CHEM 260 Honors Studio was originally designed as an avenue to address the need for a textbook that covers introductory quantum chemistry topics at the appropriate level for the university's unique chemistry curriculum.[338] Unlike many universities, the chemistry coursework begins with an organic chemistry course that emphasizes general chemistry principles in the first year.[358, 359] After organic chemistry, students then take a semester of introductory physical chemistry (CHEM 260), situated at a level somewhat between that of a typical general chemistry II course and a typical upper-level physical chemistry course. Students may simultaneously enroll in other advanced courses as well, and so the overall curriculum structure provides the opportunity for students to explore a wider range of advanced chemistry topics.

The unique placement of CHEM 260 within the chemistry curriculum creates the need for a textbook suited to discuss quantum chemistry topics at the appropriate level. Currently, the course relies on excerpts from a more advanced physical chemistry textbook, as well as additional readings from quantum chemistry texts. While the combination of these resources can approach the appropriate level of the course, selection of additional resources depends on the particular instructor for the course. On the other hand, student-generated instructional material not only allows opportunities for collaborative knowledge-building, but can also provide a "textbook" resource at the exact level required for CHEM 260.[338, 346] The CHEM 260 Honors Studio was initially designed as a space in which student-generated instructional materials can be created and combined to form a textbook for the general CHEM 260 course.

The CHEM 260 Honors Studio (referred to as CHEM 260H) was designed as a two-hour, weekly, supplemental studio session during which students collaboratively construct explanations of quantum chemistry topics called "explorations", with the aim to eventually combine their explanations into a textbook for the general CHEM 260 course.[338] CHEM 260H was designed with the performance studio in mind,

Week	Activity
Week 1	Research, Proposal
Week 2	Write first draft
Week 3	Peer review of first draft
Week 4	Respond to peer review, Revise second draft
Week 5	Peer grading of second draft

Table 5.1: Activities included in each CHEM 260H exploration cycle. (Grading is incorporated into first week of the following cycle.)

where students have the opportunity to express the mastery of their skills while receiving constructive critique from their more experienced peers.[330, 360, 361] Accordingly, CHEM 260H is led by Studio Peer Leaders (SPLs) who are undergraduate students who have successfully completed CHEM 260H. Graduate Student Facilitators (GSFs) oversee CHEM 260H activities, and mostly serve in an administrative role.

The activities in CHEM 260H are based on the Writing-To-Teach (WTT) pedagogy, which incorporates meaningful learning and situated cognition theories.[322, 338, 362–364] Meaningful learning occurs when students are able to incorporate new concepts into their already existing cognitive structures. Therefore, an emphasis on prior knowledge and real-world applications can assist learning.[322] Situated learning occurs as a social process within a specific context, and therefore flourishes within collaborative environments that allow students to become practicing members of a discipline.[362–364] In WTT, these learning theories are combined with activities that support such learning within the sciences, such as writing to learn and peer teaching approaches.[325, 328, 329, 331, 333, 347, 365–367]

The semester consists of three four-week exploration cycles, outlined in Table 5.1, in which students practice authentic science writing processes. They begin by researching the topics contained in their explorations, and then they draft a proposal that outlines the information they will present in the exploration. During the second

Year	Pedagogy	Medium	Accuracy
2008	WTT	CTools	–
2009	WTT	CTools	–
2010	WTT	Wiki	?
2011	WTT	Wiki	?
2012	WTT	Wiki	EPR
2013	WTT	Wiki	EPR+PRI

Table 5.2: Design considerations at each implementation of CHEM 260H. WTT: Writing-To-Teach, CTools: Online Course Tools, EPR: Extended peer review, PRI: Peer review instruction.

week of the cycle, students work together to construct the first draft of the exploration. In the third week, the student groups peer review the explorations created by other groups. During the fourth week, students receive and formally respond to the comments and suggestions provided by their peer reviewers. During the session, they also revise their second, “final” exploration draft based on the peer review comments they received. Lastly, students grade each other’s final explorations based on its content and quality as a teaching tool.

In the initial implementation of CHEM 260H WTT pedagogy (the first iteration in Table 5.1), the student-generated instructional materials were shared as Microsoft Word documents among students in CHEM 260H, and were posted on an online course website (hosted by CTools). However, these were never shared with the students in the general course. In the Fall 2010 semester (the third iteration), we decided to extend these materials to the students in the general course via a CHEM 260H wiki site. This decision was based on the benefits of utilizing wiki sites, as well as to emphasize the actual instructional nature of the CHEM 260H activities.[341, 342, 344, 347, 368] Recently, the act of teaching itself, compared to simply preparing to teach others, has been shown to increase delayed learning outcome measures.[369] Table 5.2 outlines the design considerations that arose due to this change in exploration medium (i.e., CTools to wiki). Previously, the explorations were not actually used

for instructional purposes, and focus was on the process of creating the explorations instead of on their final accuracy. Our shift to a wiki-site format immediately brought the accuracy of the final versions of the explorations to light. While recent work highlights the benefits in learning from reviewing and discussing errors, instructors were still cautious to support the CHEM 260H wiki as a course resource for general CHEM 260 students.[370]

The instructor concerns prompted us to introduce an extended peer review (EPR) process during the fifth iteration. The EPR process requires that Studio Peer Leaders (SPLs) and Graduate Student Facilitators (GSFs) also contribute to peer review of the first exploration drafts. While the EPR comments were meant to help the course instructors feel more comfortable with the wiki site, we provided them in a way that fit with the general framework of the course. For example, SPLs generally provide students with EPR comments in the form of suggestions and questions, rather than explicit instructions. In order to emphasize the value of PR comments, the EPR comments are not provided until students have received comments from their peers.

5.3 Method

5.3.1 Participants

Participants were 43 undergraduate students at a large Midwestern university who were enrolled in an introductory physical chemistry course, CHEM 260: Chemical Principles. Overall, 22 students in Fall 2010 (19 consented to participate in the study), 8 students in Fall 2011 (all consented), and 16 students in Fall 2012 (all consented) had chosen to take part in the weekly, two-hour, supplemental Honors Studio described above. The Honors Studio option had been made available to all students enrolled in the general CHEM 260 course, not only students that were part of the Honors College. In this report, the Honors Studio is referred to as CHEM

260H.

5.3.2 Data Collection and Analysis

This study investigates the nature of inaccuracies that persist in the peer-reviewed version of student-generated explanations (called “explorations”) created in CHEM 260H, in order to understand the many dimensions to what we consider to be “wrong” in discipline-based student writing. Our study team, which consists of Studio Peer Leaders and Graduate Student Facilitators (SPLs and GSFs), collected inaccuracies from the explorations. Next, we categorized each inaccuracy according to the way that it relates to course content and the way we perceive the inaccuracy may reflect student misunderstandings of course material, as further described below.

The inaccuracies investigated in this study were collected from the peer-reviewed, second draft of the explorations that the students had posted to the CHEM 260H-wiki from the third, fourth and fifth iterations. These were considered to be “final” drafts (after week four in Table 5.2), since it was expected that students in the general course could use them as study materials. The inaccuracies in these second drafts (2D) were compared to the inaccuracies that had been pointed out during the peer review process (PR) and extended peer review process (EPR). Both the PR and EPR refer to inaccuracies identified in the first exploration drafts (1D) prepared by the students. The PR and EPR for the Fall 2012 semester are included in this report, and future work will seek to incorporate PR/EPR from additional iterations.

The inaccuracies were individually collected by each study team member. We considered each statement containing an inaccurate representation of course material to be an individual inaccuracy. The collected inaccuracies were then combined in one document (duplicates were removed) and each inaccuracy was assigned a unique identifier according to exploration topic and semester. Once the inaccuracies were collected, they were coded individually by each study team member according to

the type of understanding expected to produce such an inaccuracy and how the inaccuracy would be expected to affect the understanding of students who read the exploration.[371] The individual codes for each inaccuracy were compared during full group discussions with at least three study team members present at each meeting. During these meetings, any disagreement in individual code assignment was discussed until agreement could be achieved.

Each inaccuracy was coded according to the following scheme:

- Conceptual Inaccuracy (CI): These inaccuracies would impede a student's deeper conceptual understanding of a course topic. They reflect misconceptions or a fundamental lack of understanding of the content/concept in question.

Example: "When there is more energy in the system, it becomes favorable for electrons to use this energy to move to the anti-bonding orbital subsequently dissolving the bond between the two atoms." - Exploration Topic: Molecular Orbitals (2012)

- Technical Inaccuracy (TI): These inaccuracies would not impede a student's deeper conceptual understanding of a course topic. Those reflecting what might be simple inattention to detail or errors in numerical quantities or equations, or would indicate a lack of knowledge for concepts outside the scope of the course.

Example: "The distance that the electron jumps directly correlates with the wavelength of light needed to excite the electron that distance." - Exploration Topic: Chromophores (2011)

- Writing Quality Inaccuracy (WQI): These inaccuracies are related to the clarity/quality of the writing instead of the accuracy of the content.

Example: "The implications of the transfer from classic mechanics to quantum mechanics carries the harmonic oscillator with it, making it a simple, re-

peating function into a group of probabilities.” - Exploration Topic: Quantum Harmonic Oscillator (2010)

According to this scheme, CI and TI are mutually exclusive, and cannot refer to the same inaccuracy. However, the WQI category is not exclusive and could apply to either CI or TI inaccuracies.

The example of a conceptual inaccuracy presented above illustrates the type of misunderstanding that can underlie the presentation of course material. While the exploration describes molecular orbital representations and energies, the statement above reflects a misunderstanding of the way molecular orbitals relate to the total electron density of a molecule. Specifically, the molecular orbital only represents the state of one electron in the molecule, instead of the entire electron density. Therefore, when one electron is promoted to an anti-bonding orbital, the bond between atoms does not necessarily break. Instead, the bonding depends on the relative number of bonding and anti-bonding orbitals that are occupied, and therefore on more than one electron in the molecule. We expect that this type of inaccuracy could also hinder a student reader’s conceptual understanding of electron density and bonding within molecules, and this may prevent instructors from wanting to suggest the CHEM 260H wiki-site as a study resource for their students.

On the other hand, we do not expect that the example of a technical inaccuracy would necessarily hinder the correct understanding of a concept, even if it is somewhat misrepresented. The statement describes the electron transition between energy levels in an atom upon absorption of light, however the language does not quite convey the correct phenomenon. The term “distance” is not equivalent with “energy gap”, although the students may be referring to the typical diagram of energy gaps, where the “gap” in energy could be thought of as a “distance” separating the levels in the diagram. Therefore, while the information presented does not conform to conventional description of this process, and so could indicate some level of misunderstanding, the

overall presentation of the topic provides the correct illustration. In this way, we expect that this type of inaccuracy would not prevent a conceptual understanding of electron transitions between energy levels.

The example of a writing quality inaccuracy presents an occasion where the expression in the statement is inaccurate, due to both grammar and vocabulary, and we expect that the statement would likely prevent other students from understanding the concept. Furthermore, the statement does not indicate whether the students clearly understand the relation between the harmonic oscillator model in classical and quantum mechanics. In this case, the statement would be classified as both a WQI and CI inaccuracy.

5.4 Results and Discussion

5.4.1 Persistent Inaccuracies

The number of inaccuracies that persist in the second draft (2D) explorations identified each year varied between semesters in which CHEM 260H was implemented. Figure 5.1 presents a comparison of the total number of inaccuracies identified for each exploration draft divided by the number of student participants for the semester. According to the discrepancy in absolute number of inaccuracies found per semester in the 2D explorations ($M=1.93$, $SD=1.15$), we choose to analyze the fraction of each coded inaccuracy type observed in each draft. The fraction of inaccuracy type, F_{XI}^D , is determined by the ratio of inaccuracy type to total number of inaccuracies for a given exploration draft according to,

$$F_{XI}^D = \frac{N_{XI}^D}{\sum_X N_{XI}^D} \quad (5.1)$$

where N is the number of inaccuracies for a given type and exploration draft, XI stands for the type of inaccuracy (with X representing C , T , or WQ), and D stands

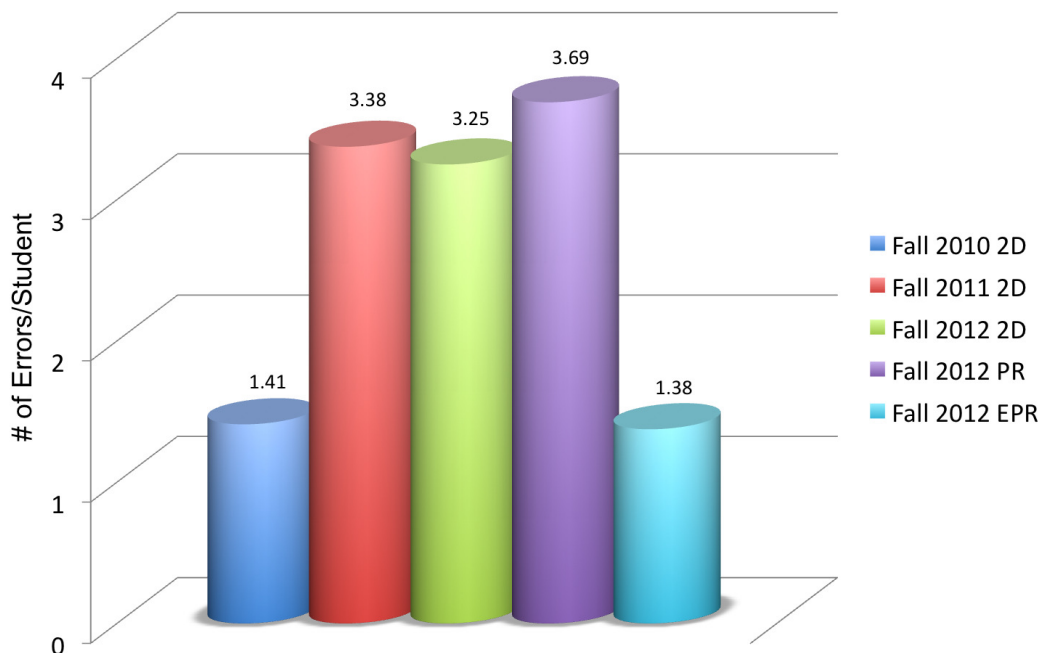


Figure 5.1: The number of inaccuracies identified per student in each year.

for the exploration draft in which the inaccuracies were identified (2D, PR, or EPR). This normalization procedure allows for direct comparison of the type of inaccuracies between years, even when the number of inaccuracies detected in each year varies.

We present the fraction of each type of inaccuracy identified in the drafts in Figure 5.2 and the values, along with summary statistics, are provided in Table 5.3. As shown in the figure, the fraction of conceptual inaccuracies (CI) identified in 2D exploration is greater than the fraction of technical (TI) and writing quality (WQI), which indicates that the students are producing generally well-written explanations of a topic, though the expression of the concepts surrounding the topic may be fundamentally inaccurate and persist despite the peer review process. This finding confirms our concern that the peer-review process is not adequately engaging with student misunderstandings.

The small sample size ($n_{obs} = 3$) prevents detailed statistical analysis of the difference in mean fraction of inaccuracies. Significance tests suggest the possibility of a

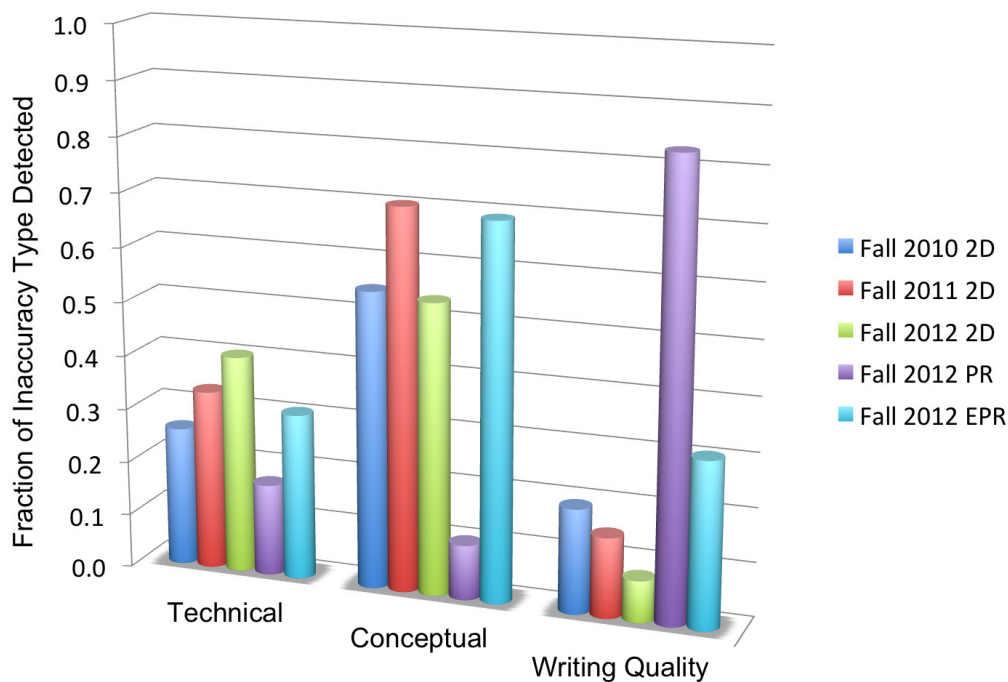


Figure 5.2: The fraction of inaccuracies of each type identified in the second draft (2D) for each year. The inaccuracies identified in the first draft via peer review (PR) and extended peer review (EPR) are also presented.

difference between fraction of CI and WQI identified in 2D explorations ($t(2)=7.22$; $p=0.016$), though investigation into this possible relationship would require larger sample sizes. In this report, we explore the qualitative relationships between these observations, with the intent to pursue detailed investigations into these relationships in the future.

5.4.2 Effects of the Peer Review Process

According to the data presented in Figure 5.2, perhaps the most striking relationship occurs between the inaccuracies identified by study team members (in 2012-2D) and student participants (in 2012-PR). While students did not identify many CIs or TIs in the first draft (1D) of their peers' explorations, they were able to identify a relatively large quantity of WQIs (the absolute number of inaccuracies identified

Year	CI	TI	WQI
2010	0.55	0.26	0.19
2011	0.70	0.33	0.15
2012	0.54	0.40	0.077
M	0.33	0.60	0.14
<i>SD</i>	0.073	0.093	0.059
2012-PR	0.10	0.17	0.83
2012-EPR	0.82	0.36	0.36

Table 5.3: Fraction of each type of inaccuracy identified in each exploration draft. Summary statistics for 2D exploration inaccuracies are provided.

are presented in Figure 5.3 for illustration, even though these vary across year and draft). Interestingly, an inverse relationship exists between the fraction of inaccuracies of each type identified in the 2012-2D explorations and the 2012-PR. Students identify a majority of WQIs in the 1D exploration, and we find fewer of these in the 2D explorations. Students do not seem to identify CIs in the 1D exploration, however we find the CIs to persist into the 2D explorations after peer review. This finding suggests that the peer-review process provides a successful approach for improving the quality of student writing within the context of quantum chemistry topics.

Importantly, the type of WQIs students are identifying during peer review are not only limited to grammar and mechanics. In fact, many comments suggest the explanation in the 1D explorations is incomplete or does not explain a topic in the best possible way. A few reviewer comments that were classified as WQI are provided below to illustrate these types of “higher-order” writing concerns.

1. “Depict more clearly the connection between what is meant by “classical perspective” and macroscopic objects.” - Exploration Topic: Heisenberg Uncertainty Principle (2012)
2. “The explanation of the math is beyond the expectation of a student in 260. Most students are not advanced mathematicians like the authors may be. It

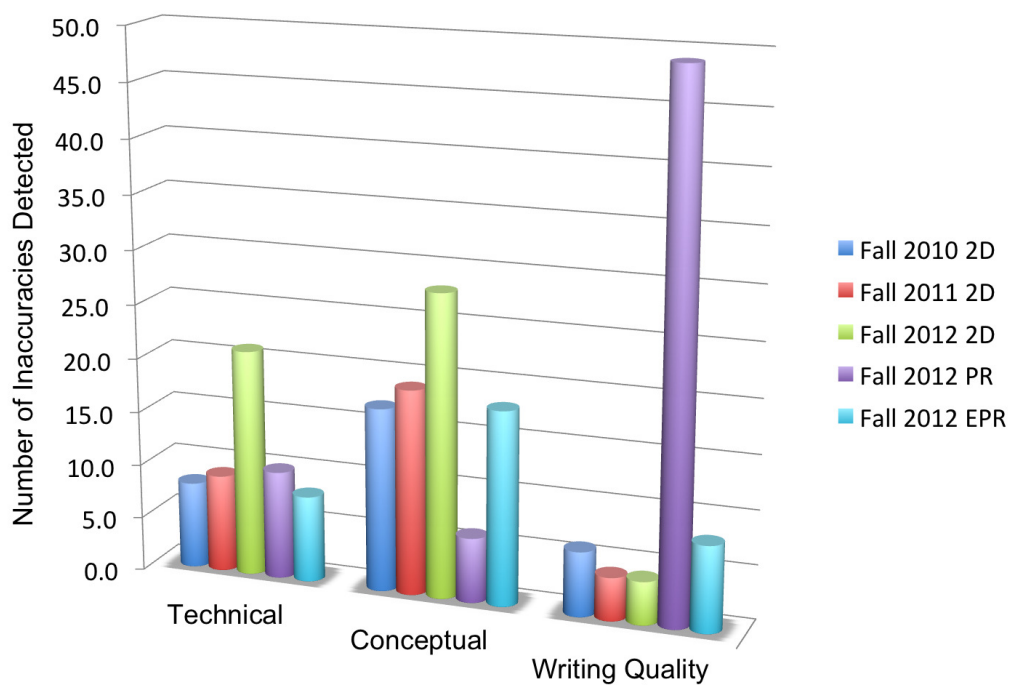


Figure 5.3: The number of inaccuracies of each type identified in the second draft (2D) for each year. The inaccuracies identified in the first draft via peer review (PR) and extended peer review (EPR) are also presented.

would be more beneficial to explain this math in simpler terms, and also to use the equation tool in Microsoft Word. Furthermore, an explanation of terms used would be useful.” - Exploration Topic: Heisenberg Uncertainty Principle (2012)

3. “In the second paragraph, the reduced mass is introduced, and how to find it, but the paper never mentions what the reduced mass is conceptually.” - Exploration Topic: The Hydrogen Atom (2012)
4. “When the authors use the term larger and smaller to describe wavelengths, the more appropriate modifier would be longer and shorter, as wavelengths are lengths.” - Exploration Topic: Vibrational and Rotational Spectroscopy (2012)

Example 1 points out issues related to flow and logical structure within the exploration. Likewise, Example 2 centers around structure, organization, and presentation, while paying attention to the role of audience. Example 3 indicates a gap in logical structure and also considers the audience’s perspective. The comment in Example 4 is more focused on scientific vocabulary and word choice, though it indicates a concern over correct representation of course material. These examples highlight that students are in fact capable of providing comments that challenge the accuracy and completeness of the exploration, as well as its quality as an instructional material. However, in a more subtle way, these findings suggest that if the CIs in the 1D drafts could be identified during the PR process in a similar way, then perhaps students would be able to revise their work based on the PR comments, thereby engaging with the CIs that persist in the 2D explorations just as they seem to engage the WQIs.

These findings prompted improvements to the design and implementation of CHEM 260H, where an additional peer review instruction (PRI) component was incorporated into the structure of the course during the sixth iteration (Fall 2013 semester), as shown in Table 5.1. In previous implementations, the PRI included examples of

authentic peer review within the context of scientific publishing. Students were introduced to actual reviewer comments and responses to those comments (which were based on GSF publications). While this level of authenticity provided an inside view of the scientific writing process, it did not give students the chance to practice this process in a legitimate, though peripheral way.[363]

Current implementations of CHEM 260H incorporate authentic practice into PRI. Students are still exposed to the peer review comments and responses from actual research articles, however we incorporate PRI by including additional exposure to previous peer review comments and responses within the context of CHEM 260H. In particular, comments addressing CIs and TIs are emphasized and discussed when peer review is introduced during week three of the first exploration cycle (see Table 5.2). After the initial discussion, students then complete an activity in which they practice constructing these types of comments as they review previous versions of CHEM 260H explorations. We expect that this practice will provide the type of instruction, modeling, and experience necessary for students to critically evaluate CIs that exist in their own 1D explorations.

5.4.3 Effect of the Extended Peer Review Process

Next, we compare the types of inaccuracies identified by SPLs and GSFs during the EPR process. EPR identified a larger fraction of CIs than any other inaccuracy type, however the total number of inaccuracies identified was less than the number identified by student participants during peer review. The differences could be due to multiple factors, one of which we discuss in more detail. Differences in PR and EPR comments could result from the different levels of experience of student participants and SPLs/GSFs with quantum chemistry topics. The students may not be familiar enough with the concepts themselves to pick out inaccuracies related to these topics.

For instance, the difference in the way SPLs/GSFs approached the discussion of

the Particle-in-a-Box model serves as an example. The 1D exploration on the Hamiltonian included the statement provided below. The discussion in this exploration section prompted the corresponding EPR and PR comments.

- “In order to satisfy the waveform requirements of quantum mechanics, the potential energy outside the box must be infinite, and inside the box must be 0”
-Exploration Topic: Hamiltonian (2012).
- EPR: “The infinite potential outside the box, and lack of potential inside the box is not due to waveform requirements. Instead, the potential energy is defined this way for the problem. We could easily have the situation where the potential is not zero inside the box, or we could have a potential outside the box that is not infinite. The solutions for the wavefunction and energies in these cases will be different due to these changes in the Hamiltonian.”
- PR: “The separation of the three models (particle in a box, the harmonic oscillator, rigid rotor) is very effective at explaining these concepts.”

The EPR comments highlight the mention of the dependence of potential on “waveform” requirements, pointing out that the potential energy is actually defined by the problem that is to be solved. The PR comment did not focus on this aspect, and instead praised the exploration authors for clearly delineating between model systems.

The EPR comments and PR comments related to the Particle-in-a-Box model indicate that these two groups may notice different aspects in the explanations depending on their experience, which is consistent with the rationale for utilizing student-generated instructional materials within CHEM 260H pedagogy.[338] Likewise, this finding agrees with current descriptions of the way expertise depends on the level of experience within a discipline.[372] The students are not as experienced with the material, and so they do not notice the problems with the Particle-in-a-Box model, and instead are able to learn from the way these models are presented. This could also

explain why students are proficient in identifying WQIs, since peer-review is typically incorporated in high school and college level writing courses (and is in fact required in first-year writing courses at the university where this study takes place). The students' familiarity with writing-centered peer review allows them to more efficiently identify problems related to writing quality.

Next, we point out that despite the fraction of CIs identified by EPR in the 1D explorations, the actual number of CIs increased between the 1D and the 2D explorations, as illustrated for Fall 2012 in Figure 5.3. In the context of this study, it appears that EPR does not minimize the CIs persisting in 2D explorations. Further investigation into the role of the EPR process are necessary, though here we will discuss some issues that prompt further study as well as suggest improvements in implementation design.

The increase in CIs identified in 2D explorations could be due to inaccuracies that arise as students address peer review comments. For example, students may introduce new inaccuracies in cases where peer review comments suggest further clarification or elaboration on topics that are not thoroughly discussed in the 1D exploration. In this way, it could be beneficial to incorporate a second review process of the 2D draft, which could provide an opportunity for students to not only reevaluate their explanations (as is the aim of writing a response to peer review comments), but also the chance to receive feedback on their revised explanations. As suggested by Sampson, Grooms, and Walker, the chance to revise a second time more accurately reflects the process for publishing a research report in scientific contexts.[373]

It could also be the case that the EPR did not identify all of the inaccuracies in the 1D documents. Practical requirements limit the amount of time SPLs and GSFs can spend on identifying inaccuracies, since the EPR takes place over one-week during the exploration cycle. On the other hand, the time that SPLs and GSFs spend searching for inaccuracies in the 2D explorations is not limited by the course itself,

and therefore it is possible that identification of inaccuracies could simply depend on the time spent searching for them. In order to test this hypothesis, equal time on task identifying inaccuracies in the 1D documents is currently pursued and will be reported in future work.

Another reason for the discrepancy in CIs identified between 1D and 2D explorations could involve the development of the conceptual understanding for SPLs and GSFs themselves. Roscoe and Chi discuss the effect of knowledge-building activities on peer tutors and suggest that reflective practices such as self-monitoring and knowledge integration can influence comprehension.[368] Earlier work by Fuchs, Fuchs, Bentz, Phillips, and Hamlett and by King also indicates that experience and training can affect the way students learn while tutoring.[366, 374] SPLs and GSFs are experienced as peer tutors, since even the least experienced SPL has spent one semester developing explorations within the context of CHEM 260H. In this way, it is not unreasonable to expect that providing comments via EPR would improve the conceptual understanding of SPLs and GSFs so that they are able to identify more inaccuracies in 2D explorations.

5.5 Concluding Remarks

This study presents a mixed-method analysis of inaccuracies in student-generated instructional materials covering introductory quantum chemistry topics. We found that inaccuracies related to conceptual understanding of course topics can persist into the final drafts of student-generated explanations, even after a peer review process, which makes it difficult for instructors to readily accept these materials as study resources for the course. More conceptual inaccuracies are found to persist than technical or writing quality inaccuracies, though the statistical significance of these relationships requires increased sampling.

Findings also indicate that while students struggle to identify conceptual inac-

curacies during the peer review process, they successfully identify and engage with writing quality issues that address higher-order concerns such as content, audience, structure, and style, rather than simply focusing on grammar and mechanics. It is expected that the amount of writing quality comments provided during peer review minimizes the amount of these inaccuracies that persist in the second exploration draft. These findings suggest that persistent conceptual inaccuracies could likewise be minimized if students were able to identify them. We suspect that incorporating authentic peer review instruction aimed at identifying and engaging with these types of inaccuracies could aid students identifying not only writing quality inaccuracies, but also technical and conceptual inaccuracies during peer review.

The extended peer review process, which incorporates studio peer leaders and graduate student facilitators, does not appear to minimize the persistent inaccuracies, though the difference between peer review and extended peer review comments could provide insight into the way students and peer tutors approach quantum chemistry topics. Overall, this study prompts further analysis into the relationships between peer review comments and persistent inaccuracies in student-generated instructional materials. By investigating the many dimensions of “wrong” contained within student-generated explanations, we hope to gain a more nuanced description of the way students construct an understanding of quantum chemistry concepts.

CHAPTER VI

Conclusions and Outlook

6.1 Summary

The work in this dissertation has focused on understanding charge transfer and transport processes in molecular systems that can serve as building blocks for materials in organic optoelectronic devices. Detailed insight at the molecular level can only be attained via the combination of experimental observations and high-level theoretical and computational approaches. Therefore, the studies presented in this work benchmark novel theoretical approaches that address limitations in current methods, as well as apply these approaches to experimentally-relevant molecular systems including chromophore-functionalized silsesquioxanes.

This work highlights the limitations in conventional approximations to density functional theory related to charge transfer processes and shows that range-separated hybrid density functionals can be used to solve these problems for molecular systems. Specifically, this work highlights two major limitations:

1. The failure of conventional density functionals to possess a derivative discontinuity, and therefore the underestimation of the ionization potential and electron affinity according to frontier orbital energies.
2. The failure of conventional density functionals to account for the electrostatic

interaction between an electron and hole pair, and therefore the inability to account for the distance dependence in charge transfer state energies. Charge transfer excitations involving frontier orbitals are further underestimated when the previous limitation is considered.

The first limitation was explored in the context of various molecular building blocks for organic semiconducting materials. While conventional frontier orbital energies calculated at the gas phase were shown to compare well with solid state experimental IP and EA, they in fact underestimated the experimental gas phase values. Likewise, when a solvent correction was applied to these calculated gas phase energies, the resulting solvent-corrected orbital energies were shown to underestimate the solid state measurements. On the other hand, gas phase frontier orbital energies calculated using RSH-DFT compared well with gas phase experimental measurements, and once a solvent correction was applied, the solvent-corrected orbital energies compared well with solid state values. These results clearly present the RSH-DFT as a solution to the first limitation in conventional DFT and also highlight the need for careful consideration of the molecular environment when comparing calculated and experimental data.

The second limitation was investigated in model and experimentally relevant systems, with careful attention paid to the role of symmetry in exacerbating the problem. The failure of a range of conventional DFT methods to accurately characterize the charge transfer excitation energies in a symmetric and symmetry broken ethene dimer system was solved by implementing a RSH-DFT approach. The RSH-DFT excitation energies were shown to agree with predicted charge transfer excitations based off of experimental IP and EA values. Charge transfer excitations were also calculated in symmetric and symmetry-broken 2-vinylstilbene-OHSQ systems. The correct theoretical treatment of charge transfer demonstrated in these systems, even when degeneracy disguises the underlying CT nature of the excitation as illustrated

in 2vinylstilbene-OHSQ systems, further validates the use of RSH-DFT when calculating charge transfer properties and processes within molecular systems.

The RSH-DFT approach was also applied to several chromophore-functionalized SQ systems in order to understand the absorption and emission in these molecules. The absorbing states for vinyl, styrenyl, stilbene, and vinylstilbene-OHSQ were determined to be $\pi - \pi^*$ in nature, and mixing between the chromophore and OHSQ molecular components was determined to depend on the proximity between the molecular orbital energies of each component. The ability to tune the orbital gap and absorption energies of functionalized-SQ systems through the addition of electron donating or withdrawing groups was accurately reproduced by RSH-DFT. Two types of charge transfer states were identified in these systems, CT1 - between the chromophore and SQ core, and CT2 - between the chromophores ligated to the SQ core. The effect of solvent stabilization on the CT states was taken into account using charge-constrained DFT, a polarizable continuum model for the solvent, and RSH-DFT. Energy transfer from the absorbing $\pi - \pi^*$ state to the CT2 state was found to be energetically favorable, and quantitative agreement between calculated CT2 state energies and the experimental emission spectrum of stilbene-OHSQ was achieved. Current work is focused on understanding the role of CT1 states in phenyl-SQ systems, where preliminary calculations suggest that the CT1 state energy approaches that of the $\pi - \pi^*$ state when solvent stabilization is taken into account.

Another aspect of this dissertation work involves high-level treatment of time-dependent electron transport in model molecular junctions. A non-equilibrium Green's function approach was utilized to study the effect of a weak perturbation on the electric current and the electronic spectra of model systems. The transient response of the current in a two-state system coupled to electrodes is shown to be a result of the coherences between the coupled states. The effect of an applied bias on the electronic spectrum of a model molecular junction is shown to depend on the nuclear config-

uration (i.e., vibrational coordinate) of the junction with respect to the electrodes. These studies provide insights into the ability to drive current in molecular junctions using time-dependent potentials, as well as the implications for using vibrational spectroscopy as a probe for characterizing molecular junctions.

6.2 Outlook

While the majority of this work clearly presents the improved treatment of ground and excited state properties that can be achieved using RSH-DFT, the practical argument could be made that these limitations in DFT are not quite as serious as they seem, especially when it comes to predicting the behavior of actual material systems. For example, relative energies predicted using conventional DFT can provide an idea of how a given material is expected to perform in a device. The work presented in this dissertation contributes to the conversation and the nuance surrounding this type of argument.

The level of theory required to treat a system of interest is generally based on the level of insight that is expected. Therefore, both the claim that conventional DFT approaches are worthwhile, and the claim that RSH-DFT should be used instead of conventional approaches, can be equally valid and depend on the situation.[26] However, recent studies have pointed out that current attempts to establish design principles for OPV materials based solely on molecular energetics may not actually provide the desired level of understanding for device development.[7] Jackson et al. point out that in most cases, improving device performance reduces to improvements in the actual fabrication and morphological structure of the device, rather than the energy levels of the composite materials. Therefore, detailed molecular-level insight into the charge transfer and transport properties of OSC materials and their components, rather than approximate relative energies, becomes crucial for predicting aspects of OPV design. Accordingly, as discussed in Chapter 2.1, it becomes more

important to include system-dependent, solid-state effects in computational studies of such materials. Identifying, describing, and predicting material interfaces and bulk properties at a high-level of theory is a considerable challenge, though the level of molecular insight required justifies pursuing a RSH treatment of such systems.

Despite the promise in RSH-DFT, this approach also provides considerable challenges itself. For example, recent work has shown that the size-consistency error resulting from the optimal tuning procedure causes this method to fail, for example, in predicting the correct binding energies of diatomic molecules, and also causes problems in calculating potential energy surfaces.[112] As a result, current efforts for improving the RSH approach, for example in treating solid state environments[111] are pursued, as well as other avenues for solving the limitations in DFT.[69] Future development in these methods, especially within application to experimentally-relevant systems, promises to provide an excellent approach for achieving fundamental understanding of charge transfer and transport in organic materials.

APPENDICES

APPENDIX A

Supporting Information - Orbital Gap Predictions for Rational Design of Organic Photovoltaic Materials

Molecule	Dielectric constant	Isotropic Polarizability	Molecular Surface Area
Benzene	2.289	188.359	123.892
Naphthalene	2.464	333.835	171.201
Anthracene	2.609	513.487	218.774
Tetracene	2.750	727.589	266.306
Pentacene	2.882	974.185	313.847
Perylene	2.698	735.658	271.723
Coronene	2.718	871.070	302.565
C60	3.04	76.661	414.442
s-Triazine	2.098	47.366	110.857
Pyrazine	2.192	53.689	115.813
Pyridine	2.241	58.041	119.700
Thiophene	2.287	57.245	116.596
a-6-thiophene	2.758	603.152	487.889
PTCDA	2.570	345.485	353.194
H ₂ Pc	2.666	640.910	519.752
SubPc	2.531	419.795	406.702

Table A.1: Calculated solvent parameters for PCM calculations

Molecule	Gas Phase (NIST)		Condensed Phase	
	ε_H	ε_L	ε_H	ε_L
Benzene	-9.26	-	-7.58	-0.40
Napthalene	-8.14	0.08	-6.40	-1.10
Anthracene	-7.41	-0.55	-5.70	-1.70
Tetracene	-6.96	-1.00	-5.10	-1.80
Pentacene	-6.58	-1.39	-4.85	-2.80
Perylene	-7.01	-0.77	-5.20	-2.50
Coronene	-7.48	-0.51	-5.52	-1.90
C60	-7.69	-2.46	-6.17	-3.50
s-Triazine	-10.08	-0.45	-	-1.58
Pyrazine	-9.33	-	-	-2.08
Pyridine	-9.45	-	-	-2.18
Thiophene	-8.89	-	-	-
a-6-thiophene	-	-	-5.30	-2.57
PTCDA	-8.20	-	-6.95	-4.10
CuPc	-6.38	-	-4.82	-2.65
H ₂ Pc	-6.41	-	-	-
SubPc	-	-	-	-

Table A.2: Experimental gas phase and thin-film ionization potentials and electron affinities reported as orbital energies. (eV)

Molecule	B3LYP				BNL			
	ε_H	ε_L	$\Delta\varepsilon_H$	$\Delta\varepsilon_L$	ε_H	ε_L	$\Delta\varepsilon_H$	$\Delta\varepsilon_L$
Benzene	-7.02	-0.33	2.24	-	-9.14	2.04	0.12	-
Napthalene	-6.10	-1.31	2.05	-1.39	-7.81	0.84	0.33	0.76
Anthracene	-5.52	-1.93	1.88	-1.38	-6.94	0.03	0.47	0.58
Tetracene	-5.14	-2.37	1.81	-1.37	-6.34	-0.52	0.62	0.48
Pentacene	-4.87	-2.69	1.71	-1.30	-6.39	-1.33	0.19	0.06
Perylene	-5.22	-2.20	1.78	-1.43	-6.42	-0.35	0.59	0.42
Coronene	-5.71	-1.69	1.76	-1.18	-6.91	0.14	0.56	0.64
C60	-6.34	-3.59	1.35	-1.13	-7.37	-1.85	0.31	0.61
s-Triazine	-7.78	-1.80	2.30	-1.35	-10.61	0.49	-0.53	0.94
Pyrazine	-7.02	-1.69	2.31	-	-9.69	0.54	-0.36	-
Pyridine	-7.13	-0.98	2.32	-	-9.58	1.14	-0.13	-
Thiophene	-6.64	-0.54	2.25	-	-9.12	1.55	-0.23	-
a-6-thiophene	-5.03	-2.39	-	-	-6.31	-1.09	-	-
PTCDA	-6.69	-4.16	1.51	-	-8.14	-2.80	0.06	-
CuPc	-4.87	-2.39	1.51	-	-5.96	-1.33	0.42	-
H ₂ Pc	-4.95	-2.56	1.46	-	-6.07	-1.50	0.34	-
SubPc	-5.52	-2.83	-	-	-6.83	-1.58	-	-

Table A.3: Calculated gas phase orbital energies (eV)

Molecule	$-IP^{PCM}$	$-EA^{PCM}$	ΔIP^{PCM}	ΔEA^{PCM}	ε'_H	ε'_L	$\Delta\varepsilon'_H$	$\Delta\varepsilon'_L$
Benzene	-8.16	0.37	0.58	0.77	-7.83	0.72	0.25	1.12
Napthalene	-7.01	-0.73	0.61	0.37	-6.63	-0.36	0.23	0.74
Anthracene	-6.26	-1.49	0.56	0.21	-5.85	-1.09	0.15	0.61
Tetracene	-5.76	-2.00	0.66	0.20	-5.31	-1.57	0.21	0.23
Pentacene	-5.42	-2.35	0.57	0.45	-5.42	-2.34	0.57	0.46
Perylene	-5.88	-1.82	0.68	0.68	-5.43	-1.39	0.23	1.11
Coronene	-6.39	-1.30	0.87	0.60	-5.96	-0.87	0.44	1.03
C60	-6.80	-3.10	0.63	0.40	-6.30	-2.62	0.13	0.88
s-Triazine	-8.60	-0.83	-	0.75	-8.55	-0.73	-	0.85
Pyrazine	-8.52	-0.87	-	1.21	-8.41	-0.76	-	1.32
Pyridine	-8.34	-0.20	-	1.98	-8.31	-0.17	-	2.01
Thiophene	-7.76	0.21	-	-	-7.75	0.21	-	-
a-6-thiophene	-5.54	-1.91	0.24	0.66	-5.53	-1.88	0.23	0.69
PTCDA	-6.97	-3.47	0.02	0.63	-6.97	-3.45	0.02	0.65
H ₂ Pc	-5.34	-2.33	-	-	-5.33	-2.33	-	-
SubPc	-5.99	-2.48	-	-	-5.99	-2.47	-	-

Table A.4: BNL orbital energies calculated as IP/EA^{PCM} and $\Delta\varepsilon'_{H/L}$ (eV)

Molecule	$-IP^{PCM}$	$-EA^{PCM}$	ΔIP^{PCM}	ΔEA^{PCM}	ε'_H	ε'_L	$\Delta\varepsilon'_H$	$\Delta\varepsilon'_L$
Benzene	-7.93	0.43	0.35	0.83	-5.71	-1.65	1.87	1.25
Napthalene	-6.75	-0.72	0.35	0.38	-4.91	-2.51	1.49	1.41
Anthracene	-6.03	-1.49	0.33	0.21	-4.43	-3.05	1.27	1.35
Tetracene	-5.55	-2.01	0.45	0.21	-4.12	-3.42	0.98	1.62
Pentacene	-5.21	-2.38	0.36	0.42	-3.90	-3.69	0.95	0.89
Perylene	-5.66	-1.84	0.46	0.66	-4.23	-3.24	0.97	0.74
Coronene	-6.13	-1.35	0.61	0.55	-4.76	-2.69	0.76	0.79
C60	-6.45	-3.18	0.28	0.32	-5.27	-4.34	0.90	0.84
s-Triazine	-8.97	-0.74	-	0.84	-6.49	-3.03	-	1.45
Pyrazine	-8.16	-0.75	-	1.33	-5.91	-2.81	-	0.73
Pyridine	-8.32	-0.12	-	2.06	-5.78	-2.29	-	0.11
Thiophene	-7.94	0.25	-	-	-5.29	-1.89	-	-
a-6-thiophene	-5.30	-2.13	0.00	0.44	-4.27	-3.16	1.03	0.59
PTCDA	-6.83	-3.50	0.12	0.60	-5.52	-4.79	1.43	0.69
H ₂ Pc	-5.26	-2.31	-	-	-4.22	-3.37	-	-
SubPc	-5.88	-2.47	-	-	-4.67	-3.70	-	-

Table A.5: B3LYP orbital energies calculated as IP/EA^{PCM} and $\Delta\varepsilon'_{H/L}$ (eV)

APPENDIX B

Supporting Information - Relation between Molecular Orbital Basis and Net Charge Transfer

In a symmetric dimer there are *on-site* and *off-site* degenerate pairs of excitations. The molecular orbitals can be chosen to be localized on each monomer, as illustrated in B.1[right], or to be delocalized over the dimer as symmetrical and anti-symmetrical linear combinations with equal weights for the monomer-localized orbitals (B.1[center]). We compare the effect of using both sets of MOs in TDDFT calculations. We confirm that the ground state energies are the same for both representations, where the numerical differences are 6×10^{-10} hartree. The orbital energies are also included in B.1[left]. The excitation energies are not affected by choice of MO basis. The orbital contributions to the *off-site* excitations and the CT for each are given in B.1. We find that the CT character of the *off-site* excitations is evidenced in the localized representation, where the *off-site* states are mirror images of each other.

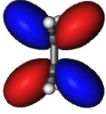
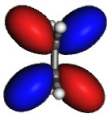
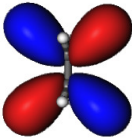

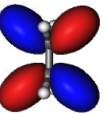
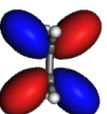

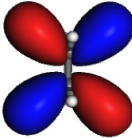
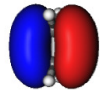
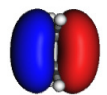
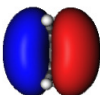

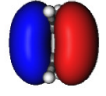
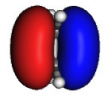

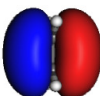
<u>LUMO 2</u> 2.10eV				
<u>LUMO 1</u> 2.10eV				
<u>HOMO 2</u> -10.37eV				
<u>HOMO 1</u> -10.37eV				

Figure B.1: Left: HOMO and LUMO energies for the ethene dimer (separated by 15Å) calculated using the 6-31+G* basis set. The energies do not depend on orbital localization; Center: Dimer-delocalized orbitals; Right: Monomer-localized orbitals.

MO localization	<i>Off-site</i> excitation energy	Orbital contributions	Net CT
Dimer-delocalized			
State 1	11.48	H1 - i L1	0
		(-) H2 - i L2	
State 2	11.48	(-) H1 - i L2	0
		H2 - i L1	
Monomer-localized			
State 1	11.48	H1 - i L2	1.0
State 2	11.48	H2 - i L1	-1.0

Table B.1: The *off-site* excitation energies (eV), orbital contributions, and net CT observed for different MO basis set choices.

APPENDIX C

Supporting Information - Calculating Off-Site Excitations in Symmetric Donor-Acceptor Systems via Time-Dependent Density Functional Theory with Range-Separated Density Functionals

System	γ (a.u.)
Symmetric	
15 Å	0.398
10 Å	0.398
8 Å	0.396
6 Å	0.386
4 Å	0.360
0.1 V Electric Field	
15 Å	0.408
10 Å	0.403
8 Å	0.398
6 Å	0.400
4 Å	0.361
0.102 Å Bond-Stretch	
15 Å	0.402
10 Å	0.409
8 Å	0.404
6 Å	0.402
4 Å	0.368
2-vinylstilbene-SQ	
Parallel	0.20
Perpendicular	0.20

Table C.1: The BNL γ parameter (a.u.), calculated according to Eq. 1.74 for the ethene dimer system (symmetric, symmetry-broken by electric field and bond stretching) at each dimer separation distance, and the 2-vinylstilbene-SQ system.

Functional	Symmetric	0.1 V Electric Field	0.102 Å Bond-Stretch
HF			
HOMO	-10.31	-11.81	-9.47
LUMO*	2.53	1.03	2.37
BNL			
HOMO	-10.48	-12.00	-10.01
LUMO*	1.91	0.41	1.55
B3LYP			
HOMO	-7.67	-9.17	-7.29
LUMO	-0.30	-1.80	-0.82
PBE			
HOMO	-5.88	-7.37	-5.55
LUMO	-0.30	-1.80	-0.79
LDA			
HOMO	-5.80	-7.18	-5.47
LUMO	-0.16	-1.66	-0.65

Table C.2: Symmetry-breaking effect on the HOMO and LUMO* energies (eV) for the 15Å separated dimer. [*The orbital gap that corresponds to the $\pi - \pi^*$ excitation actually consists of the HOMO (1b1u) and LUMO+4 (1b2g) orbitals for the HF and BNL functionals. The reported values in this table correspond to the LUMO+4 orbitals instead of the LUMO for HF and BNL. This trend is also explained in footnotes (iii) and (iv) in Chapter 2.2.]

System	Ground State Energy (a. u.)	
	6-31G*	6-31+G*
BNL		
Parallel	-4384.7037	-4384.8426
Perpendicular	-4384.7044	-4384.8434
B3LYP		
Parallel	-4458.5182	-4458.6064
Perpendicular	-4458.5188	-4458.6069

Table C.3: Comparison of ground state energies (a.u.) for parallel and perpendicular 2-vinylstilbene-SQ structures indicates both are thermally populated at room temperature.

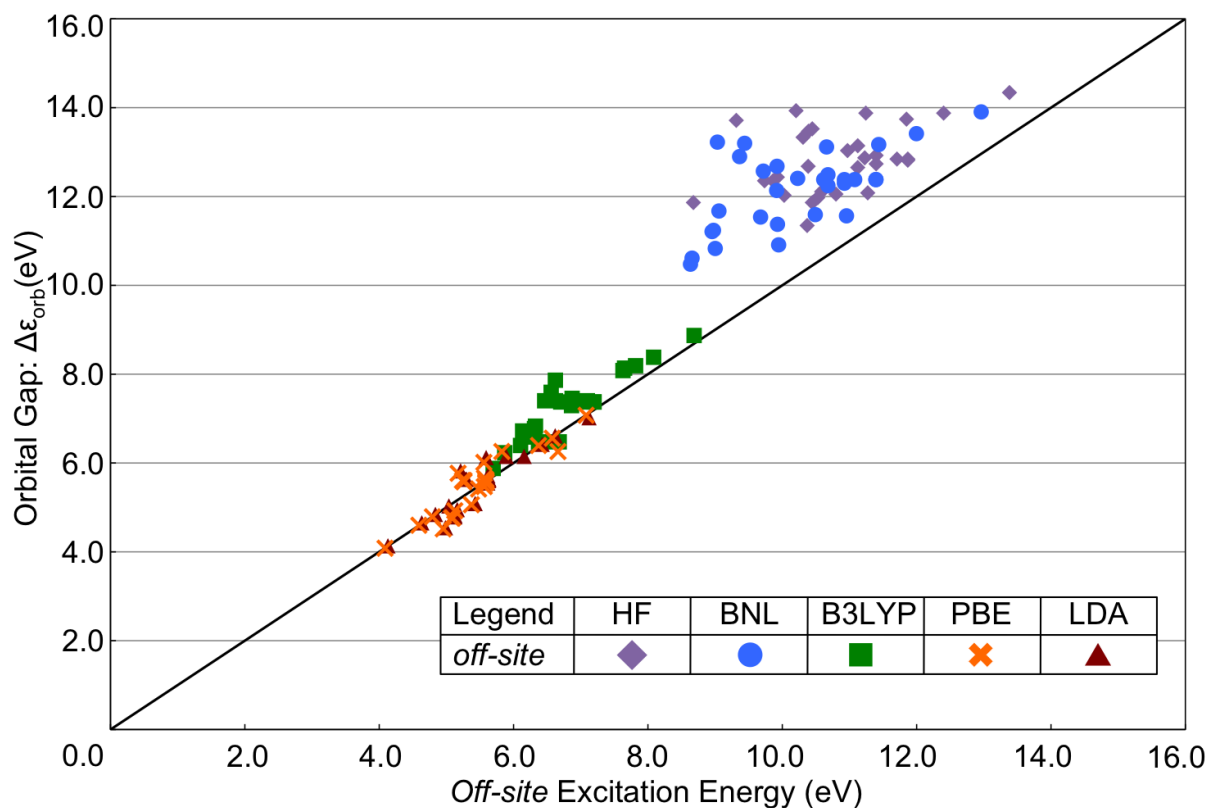


Figure C.1: Correlation plot between *off-site* excitation energies and corresponding orbital gaps of all ethene dimer systems considered in this study. *Off-site* excitations of LDA and PBE functionals are shown to correspond to the orbital gap, and those of B3LYP depend slightly on the Coulomb interaction but remain similar to the orbital gap. The BNL RSH and HF *off-site* excitations are not correlated with the orbital gap however, and instead the excitation energies are higher than the orbital gap due to the effect of Coulomb interaction.

APPENDIX D

Supporting Information - Ab Initio Calculation of the Electronic Absorption of Functionalized Octahedral Silsesquioxanes via Time-Dependent Density Functional Theory with Range-Separated Hybrid Functionals

Methods	Bond Length (\AA)		Bond Angle (Degree)		
	O-Si	H-Si	O-Si-O	Si-O-Si	H-Si-O
B3LYP/6-311+G**	1.64	1.46	109.1	149.2	109.9
Experiment	1.62	1.45	109.6	147.5	109.5
Error	0.02	0.01	-0.5	1.7	-0.4

Table D.1: Comparison of optimized geometry with experiment

Molecule	Diagonal Si-Si Distance	
	Si-Si (vinyl connected)	Si-Si (no vinyl connected)
OHSQ	N/A	5.49
1Vinyl-OHSQ	5.507	5.488 (3)
2Vinyl-OHSQ ortho	5.499, 5.509	5.477,5.486
2Vinyl-OHSQ meta	5.501 (2)	5.483 (2)
2Vinyl-OHSQ para	5.525	5.481,5.482,5.487
OVSQ	5.501 (4)	N/A

Table D.2: Si-Si diagonal length comparison in vinyl-OHSQ models. The number in parenthesis is the degeneracy having the same length. (\AA)

Molecule	B3LYP			BNL		
	HOMO	LUMO	GAP	HOMO	LUMO	GAP
OHSQ	-8.65	-0.19	8.46	-11.76	1.06	12.82
Ethylene	-7.65	-0.30	7.35	-10.45	1.93	12.38
1Vinyl-OHSQ	-8.05	-0.98	7.07	-10.23	0.98	11.21
2Vinyl-OHSQ para	-8.00	-0.95	7.05	-10.15	0.98	11.13
2Vinyl-OHSQ meta	-8.00	-0.93	7.07	-10.18	0.98	11.16
2Vinyl-OHSQ ortho	-8.00	-0.95	7.05	-10.18	0.98	11.16
OVSQ	-7.70	-0.79	6.91	-9.82	1.09	10.91

Table D.3: HOMO and LUMO gap for model systems (OHSQ coupled with vinyl). BNL parameter: OHSQ $\gamma=0.47$ a.u.; ethylene $\gamma=0.40$ a.u.; vinyl-OHSQ $\gamma=0.30$ a.u. (eV)

Molecule	B3LYP		BNL		LRC		Exp[4]
	Energy	Strength	Energy	Strength	Energy	Strength	
Styrene	4.745	0.140	4.918	0.154	5.014	0.150	
Average	4.884	0.228	5.106	0.233	5.166	0.238	
CH ₃ -Styrene	4.620	0.217	4.775	0.217	4.897	0.237	
Average	4.819	0.221	5.033	0.221	5.105	0.215	
CH ₃ O-Styrene	4.719	0.438	4.904	0.438	5.001	0.452	
Average	4.411	0.239	4.523	0.196	4.702	0.214	
CH ₃ O-Styrene	4.739	0.220	4.921	0.302	5.026	0.290	
Average	4.575	0.459	4.722	0.498	4.864	0.504	
1 <i>R_s</i> -Styrenyl-OHSQ							
<i>R_s</i> =H	4.606	0.599	4.727	0.582	4.869	0.632	
Average	4.693	0.060	4.893	0.098	5.021	0.065	
<i>R_s</i> =CH ₃	4.614	0.659	4.751	0.680	4.883	0.697	4.769
Average	4.465	0.682	4.577	0.644	4.743	0.713	
<i>R_s</i> =CH ₃ O	4.662	0.039	4.841	0.101	4.980	0.068	
Average	4.475	0.721	4.613	0.745	4.764	0.781	4.679
<i>R_s</i> =CH ₃ O	4.244	0.649	4.327	0.577	4.552	0.668	
Average	4.638	0.084	4.742	0.217	4.922	0.148	
Average	4.289	0.733	4.440	0.794	4.619	0.816	4.509
Vinylstilbene	3.484	1.200	3.684	1.160	3.876	1.255	3.769
CH ₃ -Vinylstilbene	3.433	1.256	3.636	1.223	3.835	1.329	
CH ₃ O-Vinylstilbene	3.348	1.217	3.553	1.208	3.776	1.326	
NH ₂ -Vinylstilbene	3.252	1.189	3.484	1.226	3.710	1.352	
1 <i>R_v</i> -Vinylstilbene-OHSQ							
<i>R_v</i> =H	3.396	1.492	3.587	1.504	3.800	1.602	3.701
<i>R_v</i> =CH ₃	3.332	1.530	3.532	1.570	3.754	1.670	3.668
<i>R_v</i> =CH ₃ O	3.227	1.467	3.440	1.547	3.855	1.660	3.594
<i>R_v</i> =NH ₂	3.256	1.397	3.360	1.553	3.609	1.683	3.462

Table D.4: Comparison of B3LYP, BNL and LRC- ω PBEh absorption energies to experiment [4] for both 1*R_s*-Styrenyl-OHSQ (*R_s* = H, CH₃, CH₃O) and 1*R_v*-Vinylstilbene-OHSQ (*R_v* = H, CH₃, CH₃O, NH₂). For each styrene substituted OHSQ molecule, two absorption transitions are listed along with oscillator strength-weighted averaged energy and two-state summation of oscillator strength. BNL parameter $\gamma=0.27/0.24$ a.u. (*R_s*-styrene/1*R_s*-styrene-OHSQ), $\gamma=0.21/0.20$ a.u. (*R_v*-vinylstilbene/1*R_v*-vinylstilbene-OHSQ) (eV).

Molecule	B3LYP Ground State Energy			BNL Ground State Energy		
	GAS	PCM	Diff	GAS	PCM	Diff
Styrene	-8428.09	-8428.23	0.14	-8230.58	-8230.75	0.17
1Styrene-OHSQ	-96 155.60	-96 155.87	0.26	-94 786.82	-94 787.12	0.30
Vinylstilbene	-16 823.66	-16 823.93	0.27	-16 415.45	-16 415.77	0.32
1Vinylstilbene-OHSQ	-104 551.24	-104 551.62	0.38	-102 952.11	-102 952.55	0.44

Table D.5: Gas phase and PCM solvent model ground state energy comparison of Styrene, 1Styrene-OHSQ, Vinylstilbene, and 1Vinylstilbene-OHSQ. (eV).

λ_α or λ_β		
	Styrene	Vinylstilbene
	0.4969	0.4723
$R_{s,v}$	$1R_s$ -Styrenyl-OHSQ	$1R_v$ -Vinylstilbene-OHSQ
H	0.4937	0.4708
CH ₃	0.4904	0.4699
CH ₃ O	0.4797	0.4691
NH ₂	N/A	0.4690

Table D.6: Attachment/Detachment density analysis of the selected strong absorption of styrene, vinylstilbene, $1R_s$ -Styrenyl-OHSQ ($R_s = \text{H, CH}_3, \text{CH}_3\text{O}$) and $1R_v$ -Vinylstilbene-OHSQ ($R_v = \text{H, CH}_3, \text{CH}_3\text{O, NH}_2$).

Molecule	B3LYP			BNL			LRC		
	HOMO	LUMO	GAP	HOMO	LUMO	GAP	HOMO	LUMO	GAP
Styrene	-6.395	-1.361	5.034	-8.136	0.707	8.844	-8.354	0.408	8.762
1Styrene-OHSQ	-6.694	-1.850	4.844	-8.218	0.136	8.354	-8.653	-0.109	8.544
Me-styrene	-6.177	-1.252	4.925	-7.864	0.789	8.653	-8.109	0.490	8.599
Me-styrene-OHSQ	-6.476	-1.769	4.707	-7.946	0.218	8.163	-8.408	-0.027	8.381
CH3O-styrene	-5.851	-1.116	4.735	-7.456	0.925	8.381	-7.755	0.653	8.408
CH3O-styrene-OHSQ	-6.150	-1.633	4.517	-7.537	0.327	7.864	-8.055	0.082	8.137
Vinylstilbene	-5.714	-2.041	3.673	-6.912	-0.245	6.667	-7.510	-0.408	7.102
1Vinylstilbene-OHSQ	-5.905	-2.286	3.619	-7.020	-0.517	6.503	-7.701	-0.680	7.020
Me-Vinylstilbene	-5.605	-1.959	3.646	-6.776	-0.163	6.612	-7.401	-0.354	7.048
1Me-Vinylstilbene-OHSQ	-5.769	-2.231	3.537	-6.857	-0.463	6.395	-7.592	-0.626	6.966
MeO-Vinylstilbene	-5.442	-1.878	3.565	-6.585	-0.082	6.503	-7.238	-0.272	6.966
1MeO-Vinylstilbene-OHSQ	-5.605	-2.150	3.456	-6.639	-0.381	6.259	-7.401	-0.571	6.830
NH2-Vinylstilbene	-5.225	-1.796	3.429	-6.340	0.000	6.340	-7.020	-0.190	6.830
1NH2-Vinylstilbene-OHSQ	-5.388	-2.068	3.320	-6.422	-0.327	6.095	-7.156	-0.490	6.667
o-Br-Vinylstilbene	-5.823	-2.204	3.619	-7.020	-0.408	6.612			
p-Br-Vinylstilbene	-5.823	-2.177	3.434	-6.993	-0.381	6.612			
o-1Br-Vinylstilbene-OHSQ	-6.041	-2.395	3.646	-7.156	-0.626	6.531			
p-1Br-Vinylstilbene-OHSQ	-5.987	-2.422	3.565	-7.075	-0.653	6.422			
COOH-Vinylstilbene	-5.959	-2.476	3.483	-7.102	-0.626	6.476			
1COOH-Vinylstilbene-OHSQ	-6.150	-2.716	3.434	-7.211	-0.844	6.367			
m-NO2-Vinylstilbene	-6.109	-2.884	3.225	-7.265	-0.789	6.476			
p-NO2-Vinylstilbene	-6.204	-3.048	3.156	-7.320	-1.088	6.231			
m-1NO2-Vinylstilbene-OHSQ	-6.286	-2.966	3.320	-7.361	-0.925	6.435			
p-1NO2-Vinylstilbene-OHSQ	-6.367	-3.156	3.211	-7.429	-1.252	6.177			

Table D.7: HOMO and LUMO energies and band gaps of the R_s -Styrenyl-OHSQ, R_v -Vinylstilbene-OHSQ and R_w -Vinylstilbene-OHSQ series. (eV)

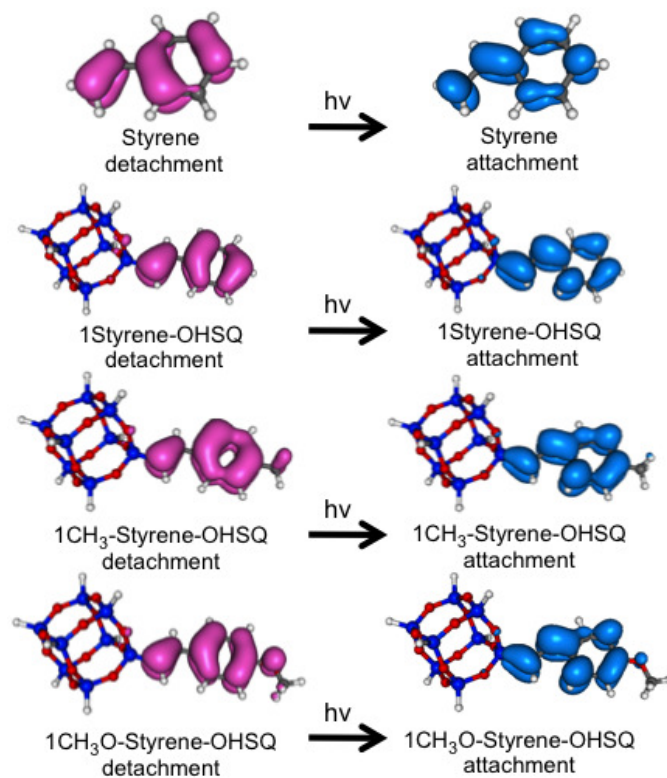


Figure D.1: Attachment/detachment densities of the transition with the strongest oscillator strength in first excitation band for Styrene, 1Styrenyl-OHSQ, 1CH₃-Styrenyl-OHSQ, and 1CH₃O-Styrenyl-OHSQ molecules. Attachment: blue; Detachment: pink.

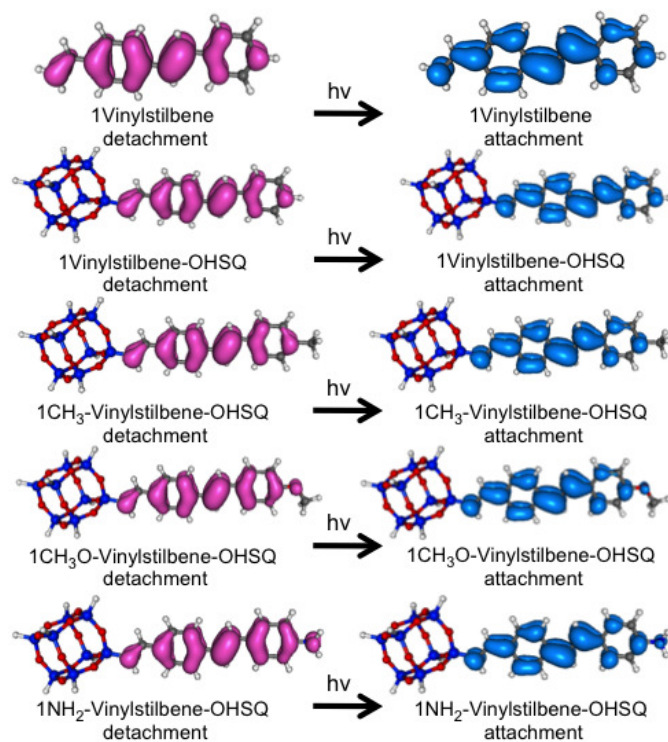


Figure D.2: Attachment/detachment densities of the absorbing transition for vinylstilbene and $R_{v,w}$ -Vinylstilbene-OHSQ molecules. Attachment: blue; Detachment: pink.

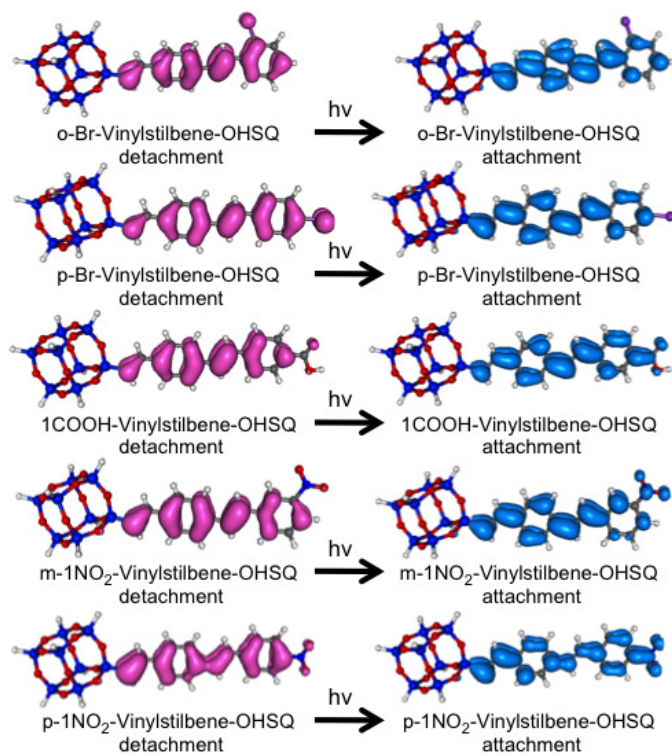


Figure D.3: Attachment/detachment densities of the absorbing transition for 1Br-Vinylstilbene-OHSQ, 1COOH-Vinylstilbene-OHSQ, and 1NO₂-Vinylstilbene-OHSQ molecules. Attachment: blue; Detachment: pink.

APPENDIX E

Supporting Information - Ethylene Absorption

The lowest frequency band in the high-resolution UV absorption spectrum appears at the 6.3-8.8 eV range and is assigned to transitions between the highest occupied orbital to the anti-bonding π^* orbital and 3s/3p/3d Rydberg orbitals.[180] Within this band, the first and second strongest absorption peaks are centered at 7.4 eV and 7.9 eV, respectively.[180] Our calculations yield the two corresponding excitation energies, where B3LYP features an energy split of 0.30 eV and BNL predicts a smaller energy split of 0.04 eV. In the B3LYP case, the HOMO-LUMO excitation corresponds to the relatively larger excitation energy and oscillator strength.

The 6-31+G* and 6-311+G** basis sets indicate convergence for the 1Vinyl-OHSQ and ethylene with the default γ parameter, 0.50 a.u. The small difference between the two ethylene excitation energies predicted by BNL when using the system-specific parameter, $\gamma=0.4$ a.u., is thought to be a basis set effect. Indeed, using this parameter value and the aug-cc-pVTZ basis set, we find the energy difference increases to 0.43 eV, with excitation energies 7.152 eV and 7.583 eV.

The BNL functional predicts the excitation ordering of the two absorbing states to be opposite that of B3LYP so that the HOMO-LUMO excitation is the lowest excited state, as shown in Table E.1. The same ordering also occurs at the BNL/aug-

Molecule	BNL		B3LYP	
	Energy	Strength	Energy	Strength
Ethylene	7.566	0.155	7.187	0.123
	7.601	0.371	7.481	0.338
1Vinyl-OHSQ	7.210	0.043	7.079	0.032
	7.230	0.453	7.105	0.448

Table E.1: Excitation energies of ethylene and 1Vinyl-OHSQ from Table 3.2, emphasizing the HOMO-LUMO excitation in boldface

Level of Theory	Energy
BNL/6-311+G**	7.566
	7.601
BNL/aug-cc-pVTZ	7.152
	7.583
HF/aug-cc-pVTZ	7.194
	7.464

Table E.2: Excitation energies of ethylene for different levels of theory, emphasizing the HOMO-LUMO excitation in boldface

cc-pVTZ level. It is shown in Table E.2 that the Hartree-Fock/aug-cc-pVTZ level of theory predicts the same excited state ordering as BNL.

APPENDIX F

Supporting Information - Ab Initio Study of the Emissive Charge-Transfer States of Solvated Chromophore-Functionalized Silsesquioxanes

State	TDA		TDDFT	
	B3LYP	BNL	B3LYP	BNL
$\pi - \pi^*$	4.03, 4.17	4.23, 4.35	3.82, 3.92	4.02, 4.12
CT1	5.81	6.85	5.81	6.84
CT2	3.73, 3.80	5.66, 5.71	3.73, 3.79	5.65, 5.70

Table F.1: Gas phase vertical electronic excitation energies (eV) for 2-stilbene-OHSQ at the solvated (within PCM) ground state geometry, as obtained via TD-DFT with the Tamm-Dancoff approximation with BNL and B3LYP functionals. (These energies correspond to Figure 3.12.) For comparison we provide the corresponding TD-DFT energies in the lower part of the table.

Geometry	Ground/PCM	CT/PCM		
1-stilbene-SQ/CT1:		$\lambda_g = 0.10$		
$\pi - \pi^*$	4.31	4.27		
CT1	6.85	6.78		
CDFT/CT1				
gas	3.13	3.01		
PCM	2.79	2.69		
Solvation	0.34	0.32		
Solvated CT1	6.51	6.46		
2-stilbene-SQ/CT2				
	state 1	state 2	state 1	state 2
		$\lambda_g =$	0.26	0.25
$\pi - \pi^*$	4.23	4.35	4.16	4.30
CT2	5.66	5.71	5.36	5.39
CDFT/CT2				
gas	5.77	5.76	5.50	5.47
PCM	4.32	4.30	4.05	4.00
Solvation	1.44	1.46	1.45	1.47
Solvated CT2	4.22	4.25	3.91	3.92

Table F.2: Electronic excitation energies (eV) of the charge transfer states at the ground and the corresponding excited state optimized geometry. Energies are relative to the ground state energy at the PCM optimized ground state geometry, whereas solvation energies are in absolute values. The geometry optimizations of solvated states are obtained with PCM and by constrained-DFT for CT states. Solvation energies are obtained from the difference between the C-DFT//PCM energy and the gas phase C-DFT energy *at the same molecular geometry*. The ground state gas phase reorganization energy is denoted by λ_g . (This table corresponds to Figure 3.14.)

Geometry	Ground/PCM	CT/PCM		
1-stilbene-SQ/CT1:		$\lambda_g = 0.14$		
$\pi - \pi^*$	4.31	4.26		
CT1	6.85	6.78		
CDFT/CT1				
gas	4.51	4.36		
PCM	3.93	3.81		
Solvation	0.58	0.55		
Solvated CT1	6.27	6.23		
2-stilbene-SQ/CT2				
	state 1	state 2	state 1	state 2
		$\lambda_g =$	0.28	0.27
$\pi - \pi^*$	4.23	4.35	4.16	4.30
CT2	5.66	5.71	5.35	5.39
CDFT/CT2				
gas	6.21	6.20	5.91	5.89
PCM	4.59	4.54	4.30	4.25
Solvation	1.62	1.66	1.61	1.64
Solvated CT2	4.04	4.05	3.74	3.75

Table F.3: The same information as in Table F.2, where the C-DFT optimization corresponds to a complete electron transfer. (This table corresponds to the CT1c and CT2c states in Figure 3.14.)

Structure	Energy (Hartree)
1-stilbene-OHSQ	-3764.194447
1-stilbene-OHSQ CT1c	-3764.18629
2-stilbene-OHSQ	-4303.728865
2-stilbene-OHSQ CT2c state 1	-4303.71862
2-stilbene-OHSQ CT2c state 2	-4303.718673

Table F.4: Ground state energy of ground and C-DFT B3LYP/PCM optimized structures

BIBLIOGRAPHY

BIBLIOGRAPHY

- [1] J. P. Perdew, R. G. Parr, M. Levy, and J. L. Balduz Jr. Density-Functional Theory for Fractional Particle Number: Derivative Discontinuities of the Energy. *Physical Review Letters*, 49(23):1691–1694, 1982.
- [2] Tamar Stein, Jochen Autschbach, Niranjan Govind, Leeor Kronik, and Roi Baer. Curvature and Frontier Orbital Energies in Density Functional Theory. *The Journal of Physical Chemistry Letters*, 3(24):3740–3744, December 2012.
- [3] Weitao Yang, Aron J Cohen, and Paula Mori-Sánchez. Derivative discontinuity, bandgap and lowest unoccupied molecular orbital in density functional theory. *The Journal of chemical physics*, 136:204111, 2012.
- [4] S. Sulaiman, a. Bhaskar, J. Zhang, R. Guda, T. Goodson, and Richard M. Laine. Molecules with Perfect Cubic Symmetry as Nanobuilding Blocks for 3-D Assemblies. Elaboration of Octavinylsilsesquioxane. Unusual Luminescence Shifts May Indicate Extended Conjugation Involving the Silsesquioxane Core. *Chemistry of Materials*, 20(17):5563–5573, September 2008.
- [5] International Energy Agency. *World Energy Outlook 2012: Executive Summary*. IEA Publications, Paris, France, 2012.
- [6] Oliver Morton. A new day dawning. *Nature*, 443(7):19–22, 2006.
- [7] Nicholas E. Jackson, Brett M. Savoie, Tobin J. Marks, Lin X. Chen, and Mark a. Ratner. The Next Breakthrough for Organic Photovoltaics ? *The Journal of Physical Chemistry Letters*, 6:77–84, 2015.
- [8] Veaceslav Coropceanu, Jerome Cornil, Demetrio A da Silva Filho, Yoann Olivier, Robert Silbey, and Jean-Luc Bredas. Charge Transport in Organic Semiconductors. *Chemical Reviews*, 107:926–952, 2007.
- [9] Serap Günes, Helmut Neugebauer, and Niyazi Serdar Sariciftci. Conjugated polymer-based organic solar cells. *Chemical Reviews*, 107(4):1324–38, April 2007.
- [10] S.R. Forrest and M.E. Thompson. Introduction: Organic electronics and optoelectronics. *Chemical Reviews*, 107(4):923–925, 2007.

- [11] Shih-chun Lo and Paul L Burn. Development of Dendrimers : Macromolecules for Use in Organic Light-Emitting Diodes and Solar Cells. *Chemical Reviews*, 107:1097–1116, 2007.
- [12] Andrew C. Grimsdale, Khai Leok Chan, Rainer E. Martin, Pawel G. Jokisz, and Andrew B. Holmes. Synthesis of light-emitting conjugated polymers for applications in electroluminescent devices. *Chemical Reviews*, 109:897–1091, 2009.
- [13] Anders Hagfeldt, Gerrit Boschloo, Licheng Sun, Lars Kloo, and Henrik Pettersson. Dye-sensitized solar cells. *Chemical Reviews*, 110:6595–6663, 2010.
- [14] Alexander W Hains, Ziqi Liang, Michael a Woodhouse, and Brian a Gregg. Molecular semiconductors in organic photovoltaic cells. *Chemical reviews*, 110(11):6689–735, November 2010.
- [15] J. J. M. Halls, C. a. Walsh, N. Greenham, C., E. a. Marseglia, R. Friend, H., S. C. Moratti, A. Holmes, and B. Efficient photodiodes from interpenetrating polymer networks. *Nature*, 376:498–500, 1995.
- [16] B Dandrade, S Datta, S Forrest, P Djurovich, E Polikarpov, and M Thompson. Relationship between the ionization and oxidation potentials of molecular organic semiconductors. *Organic Electronics*, 6(1):11–20, February 2005.
- [17] Peter I. Djurovich, Elizabeth I. Mayo, Stephen R. Forrest, and Mark E. Thompson. Measurement of the lowest unoccupied molecular orbital energies of molecular organic semiconductors. *Organic Electronics*, 10(3):515–520, May 2009.
- [18] Pabitra K. Nayak and N. Periasamy. Calculation of ionization potential of amorphous organic thin-films using solvation model and DFT. *Organic Electronics*, 10(3):532–535, May 2009.
- [19] Pabitra K. Nayak and N. Periasamy. Calculation of electron affinity, ionization potential, transport gap, optical band gap and exciton binding energy of organic solids using solvation model and DFT. *Organic Electronics*, 10(7):1396–1400, November 2009.
- [20] Mariachiara Pastore, Edoardo Mosconi, Filippo De Angelis, and Michael Gratzel. A Computational Investigation of Organic Dyes for Dye-Sensitized Solar Cells : Benchmark , Strategies , and Open Issues. *Journal of Physical Chemistry C*, 114:7205–7212, 2010.
- [21] P.E. Schwenn, P.L. Burn, and B.J. Powell. Calculation of solid state molecular ionisation energies and electron affinities for organic semiconductors. *Organic Electronics*, 12(2):394–403, February 2011.
- [22] Igor V. Kuvychko, James B. Whitaker, Bryon W. Larson, Travis C. Folsom, Natalia B. Shustova, Stanislav M. Avdoshenko, Yu-Sheng Chen, Hui Wen, Xue-Bin Wang, Lothar Dunsch, Alexey a. Popov, Olga V. Boltalina, and Steven H.

- Strauss. Substituent effects in a series of 1,7-C₆₀(RF)₂ compounds (RF = CF₃, C₂F₅, n-C₃F₇, i-C₃F₇, n-C₄F₉, s-C₄F₉, n-C₈F₁₇): electron affinities, reduction potentials and E(LUMO) values are not always correlated. *Chemical Science*, 3(5):1399, 2012.
- [23] Gregorio Garcia, Andres Garzon, Jose Manuel Granadino-Roldan, Monica Moral, Amparo Navarro, and Manuel Fernandez-Gomez. Optoelectronic and Charge Transport Properties of Oligomers Based on Phenylethynylene Units Linked to Thieno-acenes: A DFT Study. *The Journal of Physical Chemistry C*, 115:6922–6932, 2011.
- [24] Eric B. Isaacs, Sahar Sharifzadeh, Biwu Ma, and Jeffrey B. Neaton. Relating Trends in First-Principles Electronic Structure and Open-Circuit Voltage in Organic Photovoltaics. *The Journal of Physical Chemistry Letters*, 2(20):2531–2537, October 2011.
- [25] Bryan M Wong and Joseph G Cordaro. Electronic Properties of Vinylene-Linked Heterocyclic Conducting Polymers: Predictive Design and Rational Guidance from DFT Calculations. *The journal of physical chemistry. C, Nanomaterials and interfaces*, 115:18333–18341, 2011.
- [26] Noel M. OBoyle, Casey M. Campbell, and Geoffrey R. Hutchison. Computational Design and Selection of Optimal Organic Photovoltaic Materials. *The Journal of Physical Chemistry C*, 115(32):16200–16210, August 2011.
- [27] Graham E. Morse, Michael G. Helander, Jason Stanwick, Jennifer M. Sauks, Andrew S. Paton, Zheng-Hong Lu, and Timothy P. Bender. Experimentally Validated Model for the Prediction of the HOMO and LUMO Energy Levels of Boronsubphthalocyanines. *The Journal of Physical Chemistry C*, 115(23):11709–11718, June 2011.
- [28] Paul E Schwenn, Ke Gui, Yuliang Zhang, Paul L Burn, Paul Meredith, and Benjamin J Powell. Kinetics of charge transfer processes in organic solar cells: Implications for the design of acceptor molecules. *Organic Electronics*, 13(11):2538–2545, 2012.
- [29] Barry P. Rand, David Cheyng, Karolien Vasseur, Noel C. Giebink, Sébastien Mothy, Yuanping Yi, Veaceslav Coropceanu, David Beljonne, Jérôme Cornil, Jean-Luc Brédas, and Jan Genoe. The Impact of Molecular Orientation on the Photovoltaic Properties of a Phthalocyanine/Fullerene Heterojunction. *Advanced Functional Materials*, 22:2987–2995, July 2012.
- [30] Bong-Gi Kim, Chang-Gua Zhen, Eun Jeong Jeong, John Kieffer, and Jinsang Kim. Organic Dye Design Tools for Efficient Photocurrent Generation in Dye-Sensitized Solar Cells: Exciton Binding Energy and Electron Acceptors. *Advanced Functional Materials*, 22(8):1606–1612, February 2012.

- [31] Muhammet E Köse. Evaluation of acceptor strength in thiophene coupled donor-acceptor chromophores for optimal design of organic photovoltaic materials. *The journal of physical chemistry. A*, 116(51):12503–9, December 2012.
- [32] Pierre M Beaujuge, Hoi Nok Tsao, Michael Ryan Hansen, Chad M Amb, Chad Risko, Jegadesan Subbiah, Kaushik Roy Choudhury, Alexei Mavrinskiy, Wojciech Pisula, Jean-Luc Brédas, Franky So, Klaus Müllen, and John R Reynolds. Synthetic principles directing charge transport in low-band-gap dithienosilole-benzothiadiazole copolymers. *Journal of the American Chemical Society*, 134(21):8944–57, May 2012.
- [33] Massimo Ottonelli, Matteo Piccardo, Daniele Duce, Sergio Thea, and Giovanna Dellepiane. Tuning the photophysical properties of pyrene-based systems: a theoretical study. *The Journal of Physical Chemistry A*, 116(1):611–30, January 2012.
- [34] Shane R. Yost, Eric Hontz, Sina Yeganeh, and Troy Van Voorhis. Triplet vs Singlet Energy Transfer in Organic Semiconductors: The Tortoise and the Hare. *The Journal of Physical Chemistry C*, 116(33):17369–17377, August 2012.
- [35] Heidi Phillips, Eitan Geva, and Barry D. Dunietz. Calculating Off-Site Excitations in Symmetric Donor-Acceptor Systems via Time-Dependent Density Functional Theory with Range-Separated Density Functionals. *Journal of Chemical Theory and Computation*, 8(8):2661–2668, August 2012.
- [36] Heidi Phillips, Shaohui Zheng, Alexander Hyla, Richard Laine, Theodore Goodson, Eitan Geva, and Barry D Dunietz. Ab Initio Calculation of the Electronic Absorption of Functionalized Octahedral Silsesquioxanes via Time-Dependent Density Functional Theory with Range-Separated Hybrid Functionals. *The Journal of Physical Chemistry A*, 116(4):1137–45, February 2012.
- [37] Shaohui Zheng, Heidi Phillips, Eitan Geva, and Barry D. Dunietz. Ab Initio Study of the Emissive Charge-Transfer States of Solvated Chromophore-Functionalized Silsesquioxanes. *Journal of the American Chemical Society*, 134:6944–6947, 2012.
- [38] Shaohui Zheng, Eitan Geva, and Barry D Dunietz. Solvated Charge Transfer States of Functionalized Anthracene and Tetracyanoethylene Dimers: A Computational Study Based on a Range Separated Hybrid Functional and Charge Constrained Self-Consistent Field with Switching Gaussian Polarized Continuum Models. *Journal of Chemical Theory and Computation*, 9:1125–1131, 2013.
- [39] Johannes Hachmann, Roberto Olivares-Amaya, Adrian Jinich, Anthony L. Appleton, Martin a. Blood-Forsythe, László R. Seress, Carolina Román-Salgado, Kai Trepte, Sule Atahan-Evrenk, Süleyman Er, Supriya Shrestha, Rajib Mondal, Anatoliy Sokolov, Zhenan Bao, and Alán Aspuru-Guzik. Lead candidates for high-performance organic photovoltaics from high-throughput quan-

- tum chemistry the Harvard Clean Energy Project. *Energy & Environmental Science*, 2013.
- [40] Brett M Savoie, Nicholas E Jackson, Tobin J Marks, and Mark a Ratner. Reassessing the use of one-electron energetics in the design and characterization of organic photovoltaics. *Physical chemistry chemical physics : PCCP*, 15(13):4538–47, April 2013.
- [41] Askat E Jailaubekov, Adam P Willard, John R Tritsch, Wai-Lun Chan, Na Sai, Raluca Gearba, Loren G Kaake, Kenrick J Williams, Kevin Leung, Peter J Rossky, and X-Y Zhu. Hot charge-transfer excitons set the time limit for charge separation at donor/acceptor interfaces in organic photovoltaics. *Nature Materials*, 12(1):66–73, January 2013.
- [42] Nicolas Bérubé, Vincent Gosselin, Josiane Gaudreau, and Michel Côté. Designing Polymers for Photovoltaic Applications Using ab Initio Calculations. *The Journal of Physical Chemistry C*, 117(16):7964–7972, April 2013.
- [43] A Mabrouk, A Azazi, and K Alimi. Molecular Structure Property Engineering of Low-Band-Gap Copolymers , Based on Fluorene , for Efficient Bulk Heterojunction Solar Cells : A Density Functional Theory Study. *Polymer Engineering and Science*, 53(5):1040–1052, 2013.
- [44] Vu Thi Thu Huong, Huyen Thi Nguyen, Truong Ba Tai, and Minh Tho Nguyen. π -Conjugated Molecules Containing Naphtho[2,3- b]thiophene and Their Derivatives: Theoretical Design for Organic Semiconductors. *The Journal of Physical Chemistry C*, 117(19):10175–10184, May 2013.
- [45] Ilana Y. Kanal, Steven G. Owens, Jonathon S. Bechtel, and Geoffrey R. Hutchison. Efficient Computational Screening of Organic Polymer Photovoltaics. *The Journal of Physical Chemistry Letters*, 4(10):1613–1623, May 2013.
- [46] P. Hohenberg and W. Kohn. Inhomogeneous Electron Gas. *Physical Review*, 136:B864–B871, 1964.
- [47] W. Kohn and LJ Sham. Self-consistent equations including exchange and correlation effects. *Physical Review*, 140(4A):A1133–A1138, 1965.
- [48] E. Runge and EKV Gross. Density-Functional Theory for Time-Dependent Systems. *Physical Review Letters*, 52(12):997–1000, 1984.
- [49] Giovanni Onida, L. Reining, and A. Rubio. Electronic excitations : density-functional versus many-body Green s-function approaches. *Reviews of Modern Physics*, 74(2):601–659, 2002.
- [50] Kieron Burke, Jan Werschnik, and E K U Gross. Time-dependent density functional theory: past, present, and future. *The Journal of Chemical Physics*, 123(6):62206, August 2005.

- [51] Andreas Dreuw and Martin Head-Gordon. Single-reference ab initio methods for the calculation of excited states of large molecules. *Chemical reviews*, 105(11):4009–37, November 2005.
- [52] Mark E. Casida. Time-dependent density-functional theory for molecules and molecular solids. *Journal of Molecular Structure: THEOCHEM*, 914(1-3):3–18, November 2009.
- [53] Attila Szabo and Neil S. Ostlund. 1982.
- [54] Robert G. Parr and Weitao Yang. *Density Functional Theory for Atoms and Molecules*. Oxford Univeristy Press, New York, NY, 1989.
- [55] Mel Levy. Electron densities in search of Hamiltonians. *Physical Review A*, 26(3):1200–1208, 1982.
- [56] H. Englisch and R. Englisch. Hohenberg-Kohn theorem and non-V-representable densities. *Physica A: Statistical Mechanics and its Applications*, 121:253–268, 1983.
- [57] J. F. Janak. Proof that $dE/dn_i = \epsilon_i$ in density functional theory. *Physical Review B*, 18(12):7165–7168, 1978.
- [58] Robert G. Parr, Robert A Donnelly, Mel Levy, and William E. Palke. Electronegativity: The density functional viewpoint. *The Journal of Chemical Physics*, 68(8):3801, 1978.
- [59] J. P. Perdew and M. Levy. Physical Content of the Exact Kohn-Sham Orbital Energies: Band Gap and Derivative Discontinuities. *Physical Review Letters*, 51(20):1884–1887, 1983.
- [60] LJ Sham and M. Schluter. Density-Functional Theory of the Energy Gap. *Physical Review Letters*, 51(20):1888–1891, 1983.
- [61] Jp Perdew, K Burke, and M Ernzerhof. Generalized Gradient Approximation Made Simple. *Physical Review Letters*, 78(7):1396, October 1997.
- [62] Mark Casida. Correlated optimized effective-potential treatment of the derivative discontinuity and of the highest occupied Kohn-Sham eigenvalue: A Janak-type theorem for the optimized effective-potential model. *Physical Review B*, 59(7):4694–4698, February 1999.
- [63] D. P. Chong, O. V. Gritsenko, and E. J. Baerends. Interpretation of the Kohn-Sham orbital energies as approximate vertical ionization potentials. *The Journal of Chemical Physics*, 116(5):1760, 2002.
- [64] Andrew M Teale, Frank De Proft, and David J Tozer. Orbital energies and negative electron affinities from density functional theory: Insight from the integer discontinuity. *The Journal of Chemical Physics*, 129(4):044110, July 2008.

- [65] Myrta Grüning, Andrea Marini, and Angel Rubio. Effect of spatial nonlocality on the density functional band gap. *Physical Review B*, 74(16):161103, October 2006.
- [66] Leeor Kronik, Tamar Stein, Sivan Refaely-Abramson, and Roi Baer. Excitation Gaps of Finite-Sized Systems from Optimally Tuned Range-Separated Hybrid Functionals. *Journal of Chemical Theory and Computation*, 8(5):1515–1531, May 2012.
- [67] Espen Sagvolden and John Perdew. Discontinuity of the exchange-correlation potential: Support for assumptions used to find it. *Physical Review A*, 77(1):012517, January 2008.
- [68] Aron Cohen, Paula Mori-Sánchez, and Weitao Yang. Fractional charge perspective on the band gap in density-functional theory. *Physical Review B*, 77(11):1–6, March 2008.
- [69] Eli Kraisler and Leeor Kronik. Piecewise Linearity of Approximate Density Functionals Revisited: Implications for Frontier Orbital Energies. *Physical Review Letters*, 110(12):126403, March 2013.
- [70] Robert van Leeuwen. Mapping from Densities to Potentials in Time-Dependent Density-Functional Theory. *Physical Review Letters*, 82(3):3863–3866, 1999.
- [71] Giovanni Vignale. Real-time resolution of the causality paradox of time-dependent density-functional theory. *Physical Review A - Atomic, Molecular, and Optical Physics*, 77(January):1–9, 2008.
- [72] M a L Marques and E K U Gross. Time-dependent density functional theory. *Annual review of physical chemistry*, 55(2):427–455, 2004.
- [73] Mark E Casida. *Recent Advances in Density Functional Methods Part I*, chapter Time-dependent density-functional response theory for molecules. World Scientific, Singapore, 1995.
- [74] T Grabo. Molecular excitation energies from time-dependent density functional theory. *Journal of Molecular Structure: THEOCHEM*, 501-502:353–367, 2000.
- [75] D.J. Tozer, R.D. Amos, N.C. Handy, B.O. Roos, and L. Serrano-Andres. Does density functional theory contribute to the understanding of excited states of unsaturated organic compounds? *Molecular Physics*, 97(7):859–868, 1999.
- [76] Jürgen Fabian. Electronic excitation of sulfur-organic compounds - performance of time-dependent density functional theory. *Theoretical Chemistry Accounts: Theory, Computation, and Modeling (Theoretica Chimica Acta)*, 106(3):199–217, July 2001.

- [77] Meng-Sheng Liao, Yun Lu, and Steve Scheiner. Performance assessment of density-functional methods for study of charge-transfer complexes. *Journal of Computational Chemistry*, 24(5):623–31, April 2003.
- [78] RJ Magyar and S Tretiak. Dependence of spurious charge-transfer excited states on orbital exchange in TDDFT: Large molecules and clusters. *Journal of Chemical Theory and Computation*, 3:976–987, 2007.
- [79] Andreas Dreuw and Martin Head-Gordon. Failure of time-dependent density functional theory for long-range charge-transfer excited states: the zincbacteriochlorin-bacteriochlorin and bacteriochlorophyll-spheroidene complexes. *Journal of the American Chemical Society*, 126(12):4007–16, March 2004.
- [80] Andreas Dreuw, Jennifer L. Weisman, and Martin Head-Gordon. Long-range charge-transfer excited states in time-dependent density functional theory require non-local exchange. *The Journal of Chemical Physics*, 119(6):2943, 2003.
- [81] Wolfgang Hieringer and Andreas Görling. Reply to Comment on Failure of time-dependent density functional methods for excitations in spatially separated systems by Andreas Dreuw and Martin Head-Gordon. *Chemical Physics Letters*, 426(1-3):234–236, July 2006.
- [82] Andreas Dreuw and Martin Head-Gordon. Comment on: Failure of time-dependent density functional methods for excitations in spatially separated systems by Wolfgang Hieringer and Andreas Görling. *Chemical Physics Letters*, 426(1-3):231–233, July 2006.
- [83] Wolfgang Hieringer and Andreas Görling. Failure of time-dependent density functional methods for excitations in spatially separated systems. *Chemical Physics Letters*, 419(4-6):557–562, February 2006.
- [84] Ryan .M. Richard and John .M. Herbert. Time-Dependent Density-Functional Description of the 1La State in Polycyclic Aromatic Hydrocarbons: Charge-Transfer Character in Disguise? *Journal of Chemical Theory and Computation*, 7:1296–1306, 2011.
- [85] Natalia Kuritz, Tamar Stein, Roi Baer, and Leeor Kronik. Charge-Transfer-Like π - π^* Excitations in Time-Dependent Density Functional Theory: A Conundrum and Its Solution. *Journal of Chemical Theory and Computation*, 7:2408–2415, 2011.
- [86] Mary Kay Stein and Linda Kucan. Preface. In Mary Kay Stein and Linda Kucan, editors, *Instructional Explanations in the Disciplines*, pages 1–237. Springer, New York, NY, 2010.
- [87] David J. Tozer. Relationship between long-range charge-transfer excitation energy error and integer discontinuity in KohnSham theory. *The Journal of Chemical Physics*, 119(24):12697, 2003.

- [88] Stephan Kümmel and Leeor Kronik. Orbital-dependent density functionals: Theory and applications. *Reviews of Modern Physics*, 80(1):3–60, January 2008.
- [89] A Seidl, A Görling, P Vogl, J A Majewski, and M Levy. Generalized Kohn-Sham schemes and the band-gap problem. *Physical Review B*, 53(7):3764–3774, February 1996.
- [90] Roi Baer, Ester Livshits, and Ulrike Salzner. Tuned range-separated hybrids in density functional theory. *Annual Review of Physical Chemistry*, 61:85–109, March 2010.
- [91] So Hirata and Martin Head-Gordon. Time-dependent density functional theory within the TammDancoff approximation. *Chemical Physics Letters*, 314(3-4):291–299, December 1999.
- [92] S Hirata, M Head-Gordon, and R J Bartlett. Configuration interaction singles, time-dependent Hartree-Fock, and time-dependent density functional theory for the electronic excited states of extended systems. *Journal of Chemical Physics*, 111(1999):10774–10786, 1999.
- [93] So Hirata and Martin Head-Gordon. Time-dependent density functional theory for radicals An improved description of excited states with substantial double excitation character. *Chemical Physics Letters*, 302(26):375–382, 1999.
- [94] Thierry Leininger, Hermann Stoll, Hans-Joachim Werner, and Andreas Savin. Combining long-range configuration interaction with short-range density functionals. *Chemical Physics Letters*, 275(3-4):151–160, August 1997.
- [95] Hisayoshi Iikura, Takao Tsuneda, Takeshi Yanai, and Kimihiko Hirao. A long-range correction scheme for generalized-gradient-approximation exchange functionals. *The Journal of Chemical Physics*, 115(8):3540–3544, 2001.
- [96] Jochen Heyd, Gustavo E. Scuseria, and Matthias Ernzerhof. Hybrid functionals based on a screened Coulomb potential. *The Journal of Chemical Physics*, 118(18):8207, 2003.
- [97] Takeshi Yanai, David P. Tew, and Nicholas C. Handy. A new hybrid exchange-correlation functional using the Coulomb-attenuating method (CAM-B3LYP). *Chemical Physics Letters*, 393:51–57, 2004.
- [98] Yoshihiro Tawada, Takao Tsuneda, Susumu Yanagisawa, Takeshi Yanai, and Kimihiko Hirao. A long-range-corrected time-dependent density functional theory. *The Journal of Chemical Physics*, 120(18):8425–33, May 2004.
- [99] Julien Toulouse, Andreas Savin, and Heinz-Jrgen Flad. Short-range exchange-correlation energy of a uniform electron gas with modified electron-electron interaction. *International Journal of Quantum Chemistry*, 100(6):1047–1056, December 2004.

- [100] Michael J G Peach, Aron J Cohen, and David J Tozer. Influence of Coulomb-attenuation on exchange-correlation functional quality. *Physical Chemistry Chemical Physics : PCCP*, 8(39):4543–9, October 2006.
- [101] Oleg A Vydrov and Gustavo E Scuseria. Assessment of a long-range corrected hybrid functional. *The Journal of Chemical Physics*, 125(23):234109, December 2006.
- [102] Roi Baer and Daniel Neuhauser. Density Functional Theory with Correct Long-Range Asymptotic Behavior. *Physical Review Letters*, 94(4):043002, February 2005.
- [103] Ester Livshits and Roi Baer. A well-tempered density functional theory of electrons in molecules. *Physical Chemistry Chemical Physics : PCCP*, 9(23):2932–41, June 2007.
- [104] Thomas M Henderson, Benjamin G Janesko, and Gustavo E Scuseria. Generalized gradient approximation model exchange holes for range-separated hybrids. *The Journal of Chemical Physics*, 128(19):194105, May 2008.
- [105] Jeng-Da Chai and Martin Head-Gordon. Systematic optimization of long-range corrected hybrid density functionals. *The Journal of Chemical Physics*, 128(8):084106, February 2008.
- [106] Elon Weintraub, Thomas M. Henderson, and Gustavo E. Scuseria. Long-Range-Corrected Hybrids Based on a New Model Exchange Hole. *Journal of Chemical Theory and Computation*, 5:754–762, April 2009.
- [107] Myrta Grüning, Andrea Marini, and Angel Rubio. Density functionals from many-body perturbation theory: the band gap for semiconductors and insulators. *The Journal of chemical physics*, 124(15):154108, April 2006.
- [108] Sivan Refaely-Abramson, Roi Baer, and Leeor Kronik. Fundamental and excitation gaps in molecules of relevance for organic photovoltaics from an optimally tuned range-separated hybrid functional. *Physical Review B*, 84(7):075144, August 2011.
- [109] Takao Tsuneda, Jong-Won Song, Satoshi Suzuki, and Kimihiko Hirao. On Koopmans’ theorem in density functional theory. *The Journal of chemical physics*, 133(17):174101, November 2010.
- [110] Sivan Refaely-Abramson, Sahar Sharifzadeh, Niranjana Govind, Jochen Autschbach, Jeffrey B. Neaton, Roi Baer, and Leeor Kronik. Quasiparticle Spectra from a Nonempirical Optimally Tuned Range-Separated Hybrid Density Functional. *Physical Review Letters*, 109(22):226405, November 2012.
- [111] Sivan Refaely-Abramson, Sahar Sharifzadeh, Manish Jain, Roi Baer, Jeffrey B. Neaton, and Leeor Kronik. Gap renormalization of molecular crystals from density-functional theory. *Physical Review B*, 88(8):081204, August 2013.

- [112] Andreas Karolewski, Leeor Kronik, and Stephan Kümmel. Using optimally tuned range separated hybrid functionals in ground-state calculations: consequences and caveats. *The Journal of chemical physics*, 138(20):204115, May 2013.
- [113] Thomas Körzdörfer, John S Sears, Christopher Sutton, and Jean-Luc Brédas. Long-range corrected hybrid functionals for π -conjugated systems: dependence of the range-separation parameter on conjugation length. *The Journal of chemical physics*, 135(20):204107, November 2011.
- [114] Thomas Körzdörfer, Robert M. Parrish, Noa Marom, John S. Sears, C. David Sherrill, and Jean-Luc Brédas. Assessment of the performance of tuned range-separated hybrid density functionals in predicting accurate quasiparticle spectra. *Physical Review B*, 86(20):205110, November 2012.
- [115] Steffen Duham, Georg Heimel, Ingo Salzmann, Hendrik Glowatzki, Robert L Johnson, Antje Vollmer, Jürgen P Rabe, and Norbert Koch. Orientation-dependent ionization energies and interface dipoles in ordered molecular assemblies. *Nature materials*, 7(4):326–32, April 2008.
- [116] Yuki Matsuda, Jamil Tahir-Kheli, and William a. Goddard. Definitive Band Gaps for Single-Wall Carbon Nanotubes. *The Journal of Physical Chemistry Letters*, 1(19):2946–2950, October 2010.
- [117] Jeng-Da Chai and Po-Ta Chen. Restoration of the Derivative Discontinuity in Kohn-Sham Density Functional Theory: An Efficient Scheme for Energy Gap Correction. *Physical Review Letters*, 110(3):033002, January 2013.
- [118] Axel D. Becke. Density-functional thermochemistry. III. The role of exact exchange. *The Journal of Chemical Physics*, 98(7):5648, 1993.
- [119] Chengteh Lee, Weitao Yang, and Robert G Parr. Development of the Colle-Salvetti correlation-energy formula into a functional of the electron density. *Physical Review B*, 37(2):785–789, 1988.
- [120] S Vosko, L Wilk, and M Nusair. *Canadian Journal of Physics*, 58:1200–1211, 1980.
- [121] PJ Stephens, FJ Devlin, CF Chabalowski, and MJ Frisch. Ab Initio Calculation of Vibrational Absorption and Circular Dichroism Spectra Using Density Functional Force Fields. *The Journal of Physical Chemistry*, 98(45):11623–11627, 1994.
- [122] Yihan Shao, Zhengting Gan, Evgeny Epifanovsky, Andrew T.B. Gilbert, Michael Wormit, Joerg Kussmann, Adrian W. Lange, Andrew Behn, Jia Deng, Xintian Feng, Debashree Ghosh, Matthew Goldey, Paul R. Horn, Leif D. Jacobson, Ilya Kaliman, Rustam Z. Khaliullin, Tomasz Kuś, Arie Landau, Jie Liu, Emil I. Proynov, Young Min Rhee, Ryan M. Richard, Mary a.

Rohrdanz, Ryan P. Steele, Eric J. Sundstrom, H. Lee Woodcock, Paul M. Zimmerman, Dmitry Zuev, Ben Albrecht, Ethan Alguire, Brian Austin, Gregory J. O. Beran, Yves a. Bernard, Eric Berquist, Kai Brandhorst, Ksenia B. Bravaya, Shawn T. Brown, David Casanova, Chung-Min Chang, Yunqing Chen, Siu Hung Chien, Kristina D. Closser, Deborah L. Crittenden, Michael Diedenhofen, Robert a. DiStasio, Hainam Do, Anthony D. Dutoi, Richard G. Edgar, Shervin Fatehi, Laszlo Fusti-Molnar, An Ghysels, Anna Golubeva-Zadorozhnaya, Joseph Gomes, Magnus W.D. Hanson-Heine, Philipp H.P. Harbach, Andreas W. Hauser, Edward G. Hohenstein, Zachary C. Holden, Thomas-C. Jagau, Hyunjun Ji, Ben Kaduk, Kirill Khistyayev, Jaehoon Kim, Jihan Kim, Rollin a. King, Phil Klunzinger, Dmytro Kosenkov, Tim Kowalczyk, Caroline M. Krauter, Ka Un Lao, Adèle Laurent, Keith V. Lawler, Sergey V. Levchenko, Ching Yeh Lin, Fenglai Liu, Ester Livshits, Rohini C. Lochan, Arne Luenser, Prashant Manohar, Samuel F. Manzer, Shan-Ping Mao, Narbe Mardirossian, Aleksandr V. Marenich, Simon a. Maurer, Nicholas J. Mayhall, Eric Neuscamman, C. Melania Oana, Roberto Olivares-Amaya, Darragh P. O'Neill, John a. Parkhill, Trilisa M. Perrine, Roberto Peverati, Alexander Prociuk, Dirk R. Rehn, Edina Rosta, Nicholas J. Russ, Shaama M. Sharada, Sandeep Sharma, David W. Small, Alexander Sodt, Tamar Stein, David Stück, Yu-Chuan Su, Alex J.W. Thom, Takashi Tsuchimochi, Vitalii Vanovschi, Leslie Vogt, Oleg Vydrov, Tao Wang, Mark a. Watson, Jan Wenzel, Alec White, Christopher F. Williams, Jun Yang, Sina Yeganeh, Shane R. Yost, Zhi-Qiang You, Igor Ying Zhang, Xing Zhang, Yan Zhao, Bernard R. Brooks, Garnet K.L. Chan, Daniel M. Chipman, Christopher J. Cramer, William a. Goddard, Mark S. Gordon, Warren J. Hehre, Andreas Klamt, Henry F. Schaefer, Michael W. Schmidt, C. David Sherrill, Donald G. Truhlar, Arieh Warshel, Xin Xu, Alán Aspuru-Guzik, Roi Baer, Alexis T. Bell, Nicholas a. Besley, Jeng-Da Chai, Andreas Dreuw, Barry D. Dunietz, Thomas R. Furlani, Steven R. Gwaltney, Chao-Ping Hsu, Yousung Jung, Jing Kong, Daniel S. Lambrecht, WanZhen Liang, Christian Ochsenfeld, Vitaly a. Rassolov, Lyudmila V. Slipchenko, Joseph E. Subotnik, Troy Van Voorhis, John M. Herbert, Anna I. Krylov, Peter M.W. Gill, and Martin Head-Gordon. Advances in molecular quantum chemistry contained in the Q-Chem 4 program package. *Molecular Physics*, 113(2):1–32, September 2015.

- [123] Tom Ziegler, Arvi Rank, and Evert J Baerends. On the Calculation of Multiplet Energies by the Hartree-Fock-Slater Method. *Theoretica Chimica Acta*, 43:261–271, 1977.
- [124] Jacopo Tomasi, Benedetta Mennucci, and Roberto Cammi. Quantum mechanical continuum solvation models. *Chemical reviews*, 105(8):2999–3093, August 2005.
- [125] Adrian W Lange and John M Herbert. A smooth, nonsingular, and faithful discretization scheme for polarizable continuum models: the switching/Gaussian approach. *The Journal of chemical physics*, 133(24):244111, December 2010.

- [126] Adrian W. Lange and John M. Herbert. Symmetric versus asymmetric discretization of the integral equations in polarizable continuum solvation models. *Chemical Physics Letters*, 509(1-3):77–87, June 2011.
- [127] Helen R Eisenberg and Roi Baer. A new generalized Kohn-Sham method for fundamental band-gaps in solids. *Physical chemistry chemical physics : PCCP*, 11(22):4674–80, June 2009.
- [128] Daniel D. Eley, David J. Hazeldine, and T. Frank Palmer. Mass spectra, ionisation potentials and related properties of metal-free and transition metal phthalocyanines. *Journal of the Chemical Society, Faraday Transactions 2*, 69:1808–1814, 1973.
- [129] Fabrizio Evangelista, Vincenzo Carravetta, Giovanni Stefani, Branislav Jansik, Michele Alagia, Stefano Stranges, and Alessandro Ruocco. Electronic structure of copper phthalocyanine: an experimental and theoretical study of occupied and unoccupied levels. *The Journal of Chemical Physics*, 126(12):124709, March 2007.
- [130] Noa Marom, Xinguo Ren, Jonathan E. Moussa, James R. Chelikowsky, and Leeor Kronik. Electronic structure of copper phthalocyanine from $G_{0}W_{0}$ calculations. *Physical Review B*, 84(19):195143, November 2011.
- [131] J. Berkowitz. Photoelectron spectroscopy of phthalocyanine vapors. *The Journal of Chemical Physics*, 70(6):2819, 1979.
- [132] R M Laine, S Sulaiman, C Brick, M Roll, R Tamaki, M Z Asuncion, M Neurock, J-S Filhol, C-Y Lee, J Zhang, T Goodson, M Ronchi, M Pizzotti, S C Rand, and Y Li. Synthesis and photophysical properties of stilbeneoctasilsesquioxanes. Emission behavior coupled with theoretical modeling studies suggest a 3-D excited state involving the silica core. *Journal of the American Chemical Society*, 132(11):3708–22, March 2010.
- [133] Chang-Gua Zhen, Udo Becker, and John Kieffer. Tuning electronic properties of functionalized polyhedral oligomeric silsesquioxanes: a DFT and TDDFT study. *The Journal of Physical Chemistry A*, 113(35):9707–14, September 2009.
- [134] P. A. M. Dirac. *Proceedings of the Cambridge Philosophical Society*, 26:376, 1930.
- [135] Jp Perdew, K Burke, and M Ernzerhof. Generalized Gradient Approximation Made Simple. *Physical Review Letters*, 77(18):3865–3868, October 1996.
- [136] Tamar Stein, Leeor Kronik, and Roi Baer. Prediction of charge-transfer excitations in coumarin-based dyes using a range-separated functional tuned from first principles. *The Journal of Chemical Physics*, 131(24):244119, December 2009.

- [137] Tamar Stein, Leeor Kronik, and Roi Baer. Reliable prediction of charge transfer excitations in molecular complexes using time-dependent density functional theory. *Journal of the American Chemical Society*, 131(8):2818–20, March 2009.
- [138] Evgeny Epifanovsky, Igor Polyakov, Bella Grigorenko, Alexander Nemukhin, and Anna I Krylov. Quantum Chemical Benchmark Studies of the Electronic Properties of the Green Fluorescent Protein Chromophore . 1 . Electronically Excited and Ionized States of the Anionic Chromophore in the Gas Phase. *Journal of Chemical Theory and Computation*, 5:1895–1906, 2009.
- [139] Varetto. U. swiss national supercomputing centre: Manno, switzerland.
- [140] R.G. Pearson. Absolute Electronegativity and Hardness: Application to Inorganic Chemistry. *Inorganic Chemistry*, 27(4):734–740, 1988.
- [141] Martin Head-Gordon, Ana M. Grana, David Maurice, and Christopher A White. Analysis of Electronic Transitions as the Difference of Electron Attachment and Detachment Densities. *The Journal of Physical Chemistry*, 99(39):14261–14270, September 1995.
- [142] Donald W Scott. Thermal Rearrangement of Branched-Chain Methylpolysiloxanes. *Journal of the American Chemical Society*, 68:356–358, 1946.
- [143] Mg Voronkov and Vi Lavrent'yev. Polyhedral oligosilsesquioxanes and their homo derivatives. *Topics in Current Chemistry*, 102:199–236, 1982.
- [144] Ronald H. Baney, Maki Itoh, Akihito Sakakibara, and Toshio Suzuki. Silsesquioxanes. *chemical Reviews*, 95:1409–1430, 1995.
- [145] J Lichtenhan. *Silsesquioxane-Based Polymers*, volume 10. CRC Press, New York, 1996.
- [146] A. Provatas and J. G. Matison. *Trends Polym. Sci.*, 5:327–332, 1997.
- [147] Kai-Hua Xiang, Ravindra Pandey, Udo C. Pernisz, and Clive Freeman. Theoretical Study of Structural and Electronic Properties of H-Silsesquioxanes. *The Journal of Physical Chemistry B*, 102(44):8704–8711, October 1998.
- [148] Michiko Mattori, Koichi Mogi, Yoshiko Sakai, and Toshiyuki Isobe. Studies on the Trapping and Detrapping Transition States of Atomic Hydrogen in Octasilsesquioxane Using the Density Functional Theory B3LYP Method. *The Journal of Physical Chemistry A*, 104(46):10868–10872, November 2000.
- [149] P.J.a Ribeiro-Claro and a.M Amado. Effective core potential ab initio calculations on main group heptoxides and large silicate systems. *Journal of Molecular Structure: THEOCHEM*, 528(1-3):19–28, August 2000.
- [150] Wen-Dan Cheng, Kai-Hua Xiang, Ravindra Pandey, and Udo C. Pernisz. Calculations of Linear and Nonlinear Optical Properties of HSilsesquioxanes. *The Journal of Physical Chemistry B*, 104(29):6737–6742, July 2000.

- [151] Ruth Franco, Anil K. Kandalam, Ravindra Pandey, and Udo C. Pernisz. Theoretical Study of Structural and Electronic Properties of Methyl Silsesquioxanes. *The Journal of Physical Chemistry B*, 106(7):1709–1713, February 2002.
- [152] Tingting Lin, He Chaobin, and Yang Xiao. Theoretical Studies of Monosubstituted and Higher Phenyl-Substituted Octahydrosilsesquioxanes. *The Journal of Physical Chemistry B*, 107(50):13788–13792, December 2003.
- [153] Rob W.J.M. Hanssen, Rutger A. van Santen, and Hendrikus C.L. Abbenhuis. The Dynamic Status Quo of Polyhedral Silsesquioxane Coordination Chemistry. *European Journal of Inorganic Chemistry*, 2004(4):675–683, February 2004.
- [154] J Shen, W-D Cheng, D-S Wu, X-D Li, Y-Z Lan, H Zhang, Y-J Gong, F-F Li, and S-P Huang. Modeling of configurations and third-order nonlinear optical properties of methyl silsesquioxanes. *The Journal of chemical physics*, 122(20):204709, May 2005.
- [155] Ruben Y Kannan, Henryk J Salacinski, Peter E Butler, and Alexander M Seifalian. Polyhedral oligomeric silsesquioxane nanocomposites: the next generation material for biomedical applications. *Accounts of chemical research*, 38(11):879–84, November 2005.
- [156] Y. Xioa, S. Tripathy, and T. T. Lin and C. B. He. *Journal of Nanoscience and Nanotechnology*, 6:3882–3887, 2006.
- [157] Stanley E. Anderson, Connie Mitchell, Timothy S. Haddad, Ashwani Vij, Joseph J. Schwab, and Michael T. Bowers. Structural Characterization of POSS Siloxane Dimer and Trimer. *Chemistry of Materials*, 18(6):1490–1497, March 2006.
- [158] D Shieh, F Chen, and J Lin. Investigation of orientation and packing of H₈Si₈O₁₂ arrays on graphite by scanning tunneling microscopy. *Applied Surface Science*, 252(6):2171–2177, January 2006.
- [159] J A Tossell. ¹⁹F Calculation of and NMR Shifts and Stabilities of F - Encapsulating Silsesquioxanes. *Journal of Physical Chemistry C*, 111:3584–3590, 2007.
- [160] Hung-Chih Li, Cheng-Ying Lee, Clare McCabe, Alberto Striolo, and Matthew Neurock. Ab initio analysis of the structural properties of alkyl-substituted polyhedral oligomeric silsesquioxanes. *The journal of physical chemistry. A*, 111(18):3577–84, May 2007.
- [161] T. Kudo, M. Akasaka, and M. S. Gordon. Ab initio molecular orbital study of the insertion of H₂ into POSS compounds. *Theoretical Chemistry Accounts*, 120(1-3):155–166, May 2008.

- [162] Takako Kudo. Ab initio molecular orbital study of the insertion of H₂ into POSS compounds 2: the substituent effect and larger cages. *The journal of physical chemistry. A*, 113(44):12311–21, November 2009.
- [163] Delwar Hossain, Charles U Pittman, Svein Saebo, and Frank Hagelberg. Structures, Stabilities, and Electronic Properties of Endo- and Exohedral Complexes of T₁₀-Polyhedral Oligomeric Silsesquioxane Cages. *Journal of Physical Chemistry C*, 111:6199–6206, 2007.
- [164] Delwar Hossain, Steven R. Gwaltney, Charles U. Pittman, and Svein Saebo. Insertion of transition metal atoms and ions into the nanoscale dodecahedral silsesquioxane (T₁₂-POSS) cage: Structures, stabilities and electronic properties. *Chemical Physics Letters*, 467(4-6):348–353, 2009.
- [165] Delwar Hossain, Frank Hagelberg, Svein Saebo, and Charles U. Pittman. Structures, Stabilities and Electronic Properties of Endo- and Exohedral Dodecahedral Silsesquioxane (T₁₂-POSS) Nanosized Complexes with Atomic and Ionic Species. *Journal of Inorganic and Organometallic Polymers and Materials*, 20(3):424–444, May 2010.
- [166] David B Cordes, Paul D Lickiss, and Franck Rataboul. Recent developments in the chemistry of cubic polyhedral oligosilsesquioxanes. *Chemical reviews*, 110(4):2081–173, April 2010.
- [167] J. Zhou and J. Kieffer. Molecular Dynamics Simulations of Monofunctionalized Polyhedral Oligomeric Silsesquioxane C₆H₁₃(H₇Si₈O₁₂). *Journal of Physical Chemistry C*, 112(10):3473–3481, March 2008.
- [168] Khai Leok Chan, Prashant Sonar, and Alan Sellinger. Cubic silsesquioxanes for use in solution processable organic light emitting diodes (OLED). *Journal of Materials Chemistry*, 19(48):9103, 2009.
- [169] Richard M. Laine. Nanobuilding blocks based on the [OSiO_{1.5}]_x (x= 6, 8, 10) octasilsesquioxanes. *Journal of Materials Chemistry*, 15(35-36):3725, 2005.
- [170] Tom Ziegler and Mykhaylo Krykunov. On the calculation of charge transfer transitions with standard density functionals using constrained variational density functional theory. *The Journal of chemical physics*, 133(7):074104, August 2010.
- [171] Mary A Rohrdanz and John M Herbert. Simultaneous benchmarking of ground- and excited-state properties with long-range-corrected density functional theory. *The Journal of Chemical Physics*, 129(3):034107, July 2008.
- [172] Mary A Rohrdanz, Katie M Martins, and John M Herbert. A long-range-corrected density functional that performs well for both ground-state properties and time-dependent density functional theory excitation energies, including charge-transfer excited states. *The Journal of Chemical Physics*, 130(5):054112, February 2009.

- [173] Yihan Shao, Laszlo Fusti Molnar, Yousung Jung, Jörg Kussmann, Christian Ochsenfeld, Shawn T Brown, Andrew T B Gilbert, Lyudmila V Slipchenko, Sergey V Levchenko, Darragh P O'Neill, Robert a DiStasio, Rohini C Lochan, Tao Wang, Gregory J O Beran, Nicholas a Besley, John M Herbert, Ching Yeh Lin, Troy Van Voorhis, Siu Hung Chien, Alex Sodt, Ryan P Steele, Vitaly a Rassolov, Paul E Maslen, Prakashan P Korambath, Ross D Adamson, Brian Austin, Jon Baker, Edward F C Byrd, Holger Dachsel, Robert J Doerksen, Andreas Dreuw, Barry D Dunietz, Anthony D Dutoi, Thomas R Furlani, Steven R Gwaltney, Andreas Heyden, So Hirata, Chao-Ping Hsu, Gary Kedziora, Rustom Z Khalliulin, Phil Klunzinger, Aaron M Lee, Michael S Lee, Wanzhen Liang, Itay Lotan, Nikhil Nair, Baron Peters, Emil I Proynov, Piotr a Pieniazek, Young Min Rhee, Jim Ritchie, Edina Rosta, C David Sherrill, Andrew C Simmonett, Joseph E Subotnik, H Lee Woodcock, Weimin Zhang, Alexis T Bell, Arup K Chakraborty, Daniel M Chipman, Frerich J Keil, Arieh Warshel, Warren J Hehre, Henry F Schaefer, Jing Kong, Anna I Krylov, Peter M W Gill, and Martin Head-Gordon. Advances in methods and algorithms in a modern quantum chemistry program package. *Physical Chemistry Chemical Physics : PCCP*, 8(27):3172–91, July 2006.
- [174] E. Cancès, B. Mennucci, and J. Tomasi. A new integral equation formalism for the polarizable continuum model: Theoretical background and applications to isotropic and anisotropic dielectrics. *The Journal of Chemical Physics*, 107(8):3032, 1997.
- [175] Benedetta Mennucci and Jacopo Tomasi. Continuum solvation models: A new approach to the problem of solutes charge distribution and cavity boundaries. *The Journal of Chemical Physics*, 106(12):5151, 1997.
- [176] Jochen Autschbach and Shaohui Zheng. Density functional computations of 99 Ru chemical shifts : Relativistic effects , influence of the density functional , and study of solvent effects on fac [Ru (CO) 3 I 3] . *Magnetic Resonance in Chemistry*, 44:989–1007, 2006.
- [177] K. Larsson. *Ark. Kemi*, 16:215–219, 1960.
- [178] Murray Zelikoff and K. Watanabe. Absorption Coefficients of Ethylene in the Vacuum Ultraviolet. *Journal of the Optical Society of America*, 43(9):756, 1953.
- [179] G Cooper, T Olney, and C Brion. Absolute UV and Soft X-ray photoabsorption of ethylene by high resolution dipole (e, e) spectroscopy. *Chemical Physics*, 194(1):175–184, May 1995.
- [180] J. R. Platt, H. B. Klevens, and W. C. Price. Absorption Intensities of Ethylenes and Acetylenes in the Vacuum Ultraviolet. *The Journal of Chemical Physics*, 17(5):466–469, 1949.
- [181] M Z Asuncion and R M Laine. Fluoride rearrangement reactions of polyphenyl- and polyvinylsilsesquioxanes as a facile route to mixed functional phenyl, vinyl

- T10 and T12 silsesquioxanes. *Journal of the American Chemical Society*, 132(11):3723–36, March 2010.
- [182] Delwar Hossain, Charles U Pittman, Frank Hagelberg, and Svein Saebo. Endohedral and Exohedral Complexes of T 8 -Polyhedral Oligomeric Silsesquioxane (POSS) with Transition Metal Atoms and Ions. pages 16070–16077, 2008.
- [183] L Reynolds, J a Gardecki, S J V Frankland, M L Horng, and M Maroncelli. Dipole solvation in nondipolar solvents: Experimental studies of reorganization energies and solvation dynamics. *Journal of Physical Chemistry*, 100(95):10337–10354, 1996.
- [184] Abimbola Ogunsipe, David Maree, and Tebello Nyokong. Solvent effects on the photochemical and fluorescence properties of zinc phthalocyanine derivatives. *Journal of Molecular Structure*, 650:131–140, 2003.
- [185] Qin Wu and Troy Van Voorhis. Direct optimization method to study constrained systems within density-functional theory, August 2005.
- [186] Qin Wu and Troy Van Voorhis. Direct calculation of electron transfer parameters through constrained density functional theory. *The journal of physical chemistry. A*, 110(29):9212–8, July 2006.
- [187] Troy Van Voorhis, Tim Kowalczyk, Benjamin Kaduk, Lee-Ping Wang, Chiao-Lun Cheng, and Qin Wu. The diabatic picture of electron transfer, reaction barriers, and molecular dynamics. *Annual review of physical chemistry*, 61:149–170, 2010.
- [188] Benjamin Kaduk, Tim Kowalczyk, and Troy Van Voorhis. Constrained density functional theory. *Chemical reviews*, 112(1):321–70, January 2012.
- [189] Heidi Phillips, Alexander Prociuk, and Barry D Dunietz. Bias effects on the electronic spectrum of a molecular bridge. *The Journal of chemical physics*, 134(5):054708, February 2011.
- [190] Mark E Casida, Fabien Gutierrez, Jingang Guan, Florent-Xavier Gadea, and Dennis Salahub. Charge-transfer correction for improved time-dependent local density approximation excited-state potential energy curves: Analysis within the two-level model with illustration for H2 and LiH . *J. Chem. Phys.*, 113(2009):7062, 2000.
- [191] Chao-ping Hsu, So Hirata, and Martin Head-gordon. Excitation Energies from Time-Dependent Density Functional Theory for Linear Polyene Oligomers : Butadiene to Decapentaene. *Journal of Physical Chemistry A*, 105:451–458, 2001.
- [192] Stefan Grimme and Frank Neese. Double-hybrid density functional theory for excited electronic states of molecules. *Journal of Chemical Physics*, 127(2007), 2007.

- [193] Leonardo Bernasconi, Michiel Sprik, and Jürg Hutter. Time dependent density functional theory study of charge-transfer and intramolecular electronic excitations in acetone-water systems. *Journal of Chemical Physics*, 119(2003):12417–12431, 2003.
- [194] Harsha M Vaswani, Chao-Ping Hsu, Martin Head-Gordon, and Graham R Fleming. Quantum Chemical Evidence for an Intramolecular Charge-Transfer State in the Carotenoid Peridinin of Peridinin-Chlorophyll-Protein. *Journal of Physical Chemistry B*, 107:7940–7946, 2003.
- [195] J.P. Perdew and A. Zunger. Self-Interaction correction to density-functional approximations for many-electron systems. *Physical Review B*, 23(10):5048–5079, 1981.
- [196] G. Vignale and Walter Kohn. Current-dependent exchange-correlation potential for dynamical linear response theory. *Physical Review B*, 77(10):10, 1996.
- [197] E J Baerends and O V Gritsenko. A quantum chemical view of density functional theory. *Journal of Physical Chemistry A*, 101(30):5383–5403, 1997.
- [198] C. Toher, A. Filippetti, S. Sanvito, and K. Burke. Self-interaction errors in density functional calculations of electronic transport. *Phys. Rev. Lett.*, 95:146402, 2005.
- [199] M. Koentopp, K. Burke, and F. Evers. Zero-bias molecular electronics: Exchange-correlation correction’s to landauer formula. *Phys. Rev. B*, 73:121403(R), 2006.
- [200] Joseph C Furgal, Jae Hwan Jung, Theodore Goodson, and Richard M Laine. Analyzing Structure Photophysical Property Relationships for Isolated T 8 , T 10 , and T 12 Stilbenevinylsilsesquioxanes. *Journal of the American Chemical Society*, 135:12259–12269, 2013.
- [201] Jae Hwan Jung, Joseph C. Furgal, Theodore Goodson, Tomonobu Mizumo, Matthew Schwartz, Kathleen Chou, Jean François Vonnet, and Richard M. Laine. 3-D molecular mixtures of catalytically functionalized [vinylSiO 1.5] 10/[vinyl-SiO 1.5] 12. Photophysical characterization of second generation derivatives. *Chemistry of Materials*, 24:1883–1895, 2012.
- [202] L. A. Bumm, J. J. Arnold, M. T. Cygan, T. D. Dunbar, T. P. Burgin, L. II Jones, D. L. Allara, J. M. Tour, and P. S. Weiss. Are single molecular wires conducting? *Science*, 271:1705–1707, 1996.
- [203] M. A. Reed, C. Zhou, C. J. Muller, T. P. Burgin, and J. M. Tour. Conductance of a molecular junction. *Science*, 278:252–254, 1997.
- [204] B. C. Stipe, M. A. Rezaei, and W. Ho. Single-molecule vibrational spectroscopy and microscopy. *Science*, 280:1732–1735, 1998.

- [205] J. Chen, M. A. Reed, A. M. Rawlett, and J. M. Tour. Large on-off ratios and negative differential resistance in a molecular electronic device. *Science*, 286:1550–1552, 1999.
- [206] C. P. Collier, E. W. Wong, M. Belohradsky, F. M. Raymo, J. F. Stoddart, P. J. Kuekes, R. S. Williams, and J. R. Heath. Electronically configurable molecular-based logic gates. *Science*, 285:391–394, 1999.
- [207] Hongkun Park, J. Park, Andrew K. L. Lim, Erik H. Anderson, A. Paul Alivisatos, and Paul L. McEuen. Nanomechanical oscillations in a single-c60 transistor. *Nature*, 407:57–60, 2000.
- [208] C. P. Collier, G. Mattersteig, E. W. Wong, Y. Luo, K. Beverly, J. Sampaio, F. M. Raymo, J. F. Stoddart, and J. R. Heath. A [2]catenane-based solid state electronically reconfigurable switch. *Science*, 289:1172–1175, 2000.
- [209] P. G. Collins, M. S. Arnold, and P. Avouris. Engineering carbon nanotubes and nanotube circuits using electrical breakdown. *Science*, 292:706–709, 2001.
- [210] R. Erik Holmlin, Rainer Haag, Michael L. Chabinyk, Rustem F. Ismagilov, Adam E. Cohen, Andreas Terfort, Maria Anita Rampi, and George M. Whitesides. Electron transport through thin organic films in metal-insulator-metal junctions based on self-assembled monolayers. *J. Am. Chem. Soc.*, 123:5075–5085, 2001.
- [211] X. D. Cui, A. Primak, X. Zarate, J. Tomfohr, O. F. Sankey, A. L. Moore, T. A. Moore, D. Gust, G. Harris, and S. M. Lindsay. Reproducible measurement of single-molecule conductivity. *Science*, 294:571–574, 2001.
- [212] A. Nitzan. Electron transmission through molecules and molecular interfaces. *Annu. Rev. Phys. Chem.*, 52:681, 2001.
- [213] J. M. Tour, A. M. Rawlett, M. Kozaki, Y. X. Yao, R. C. Jagessar, S. M. Dirk, D. W. Price, M. A. Reed, C. W. Zhou, J. Chen, W. Y. Wang, and I. Campbell. Synthesis and preliminary testing of molecular wires and devices. *Chem.-Eur. J.*, 7:5118–5134, 2001.
- [214] J. Reichert, R. Ochs, D. Beckmann, H. B. Weber, M. Mayor, and H. v. Löhneysen. Driving current through single organic molecules. *Phys. Rev. Lett.*, 88:176804, 2002.
- [215] James G. Kushmerick, David B. Holt, Steven K. Pollack, Mark A. Ratner, John C. Yang, Terence L. Schull, Jawad Naciri, Martin H. Moore, and Ranganathan Shashidhar. Effect of bond-length alternation in molecular wires. *J. Am. Chem. Soc.*, 124:10654–10655, 2002.

- [216] Jeremiah K. N. Mbindyo, Thomas E. Mallouk, James B. Mattzela, Irena Kratochvilova, Baharak Razavi, Thomas N. Jackson, and Theresa S. Mayer. Template synthesis of metal nanowires containing monolayer molecular junctions. *jacs*, 124:4020–4026, 2002.
- [217] F. R. F. Fan, J. P. Yang, L. T. Cai, D. W. Price, S. M. Dirk, D. V. Kosynkin, Y. X. Yao, A. M. Rawlett, J. M. Tour, and A. J. Bard. Charge transport through self-assembled monolayers of compounds of interest in molecular electronics. *J. Am. Chem. Soc.*, 124:5550–5560, 2002.
- [218] J. Park, A. N. Pasupathy, J. I. Goldsmith, C. Chang, Y. Yaish, J. R. Petta, M. Rinkoski, J. P. Sethna, H. D. Abruna, P. L. McEuen, and D. C. Ralph. Coulomb blockade and the kondo effect in single-atom transistors. *Nature*, 417:722–725, 2002.
- [219] W. J. Liang, M. P. Shores, M. Bockrath, J. R. Long, and H. Park. Kondo resonance in a single-molecule transistor. *Nature*, 417:725–729, 2002.
- [220] Y. Luo, C. P. Collier, J. O. Jeppesen, K. A. Nielsen, E. Delonno, G. Ho, J. Perkins, H. R. Tseng, T. Yamamoto, J. F. Stoddart, and J. R. Heath. Two-dimensional molecular electronics circuits. *ChemPhysChem*, 3:519, 2002.
- [221] D. M. Adams, L. Brus, C. E. D. Chidsey, S. Creager, C. Creutz, C. R. Kagan, P. V. Kamat, M. Lieberman, S. Lindsay, R. A. Marcus, R. M. Metzger, M. E. Michel-Beyerle, J. R. Miller, M. D. Newton, D. R. Rolison, O. Sankey, K. S. Schanze, J. Yardley, and X. Y. Zhu. Charge transfer on the nanoscale: Current status. *J. Phys. Chem. B*, 107:6668–6697, 2003.
- [222] G. V. Nazin, X. H. Qiu, and W. Ho. Visualization and spectroscopy of a metal-molecule-metal bridge. *Science*, 302:77–81, 2003.
- [223] B. Q. Xu and N. Tao. Measurement of single-molecule resistance by repeated formation of molecular junctions. *Science*, 301:1221–1223, 2003.
- [224] J.G. Kushmerick, J. Lazorcik, C.H. Patterson, R. Shashidhar, D.S. Seferos, and G.C. Bazan. Vibronic contributions to charge transport across molecular junctions. *Nano. Lett.*, 4:639–642, 2004.
- [225] X. Xiao, B. Q. Xu, and N. Tao. Measurement of single molecule conductance: Benzenedithiol and benzenedimethanethiol. *Nano. Lett.*, 4:267–271, 2004.
- [226] X. Xiao, B. Q. Xu, and N. Tao. Changes in the conductance of single peptide molecules upon metal-ion binding. *Angew. Chem. Int. Ed.*, 45:6148–6152, 2004.
- [227] N.P. Guisinger, M.E. Greene, R. Basu, A.S. Baluch, and M.C. Hersam. Room temperature negative differential resistance through individual organic molecules on silicon surfaces. *Nano. Lett.*, 4:55–59, 2004.

- [228] R. L. McCreery. Molecular electronic junctions. *Chem. Mater.*, pages 4477–4496, 2004.
- [229] F.-R.F. Fan, Y. Yao, L. Cai, L. Cheng, J.M. Tour, and A.J. Bard. Structure-dependent charge transport and storage in self-assembled monolayers of compounds of interest in molecular electronics: Effects of tip material, head-group, and surface concentration. *Journal of the American Chemical Society*, 126(12):4035–4042, 2004.
- [230] Paul G. Piva, Gino A. DiLabio, Jason L. Pitters, Janik Zikovsky, Moh’d Rezeq, Stanislav Dogel, Werner A. Hofer, and Robert A. Wolkow. Field regulation of single-molecule conductivity by a charged surface atom. *Nature*, 435:658–661, 2005.
- [231] B. Q. Xu, X. Y. Xiao, X. Yang, L. Zang, and N. J. Tao. Large gate modulation in the current of a room temperature single molecule transistor. *J. Am. Chem. Soc.*, 127(8):2386–2387, 2005.
- [232] K. Kitagawa, T. Morita, and S. Kimura. Molecular rectification of a helical peptide with a redox group in the metal-molecule-metal junction. *J. Phys. Chem. B*, 109:13906–13911, 2005.
- [233] Xuefeng Guo, Joshua P. Small, Jennifer E. Klare, Yiliang Wang, Meninder S. Purewal, Iris W. Tam, Byung Hee Hong, Robert Caldwell, Limin Huang, Stephen O’Brien, Jiaming Yan, Ronald Breslow, Shalom J. Wind, James Hone, Philip Kim, and Colin Nuckolls. Covalently bridging gaps in single-walled carbon nanotubes with conducting molecules. *Science*, 311:356–359, 2006.
- [234] D. Natelson, L. H. Yu, J. W. Ciszek, and Z. K. Tour J. M. Keane. Single-molecule transistors: Electron transfer in the solid state. *Chem. Phys*, 324:267–275, 2006.
- [235] Z. K. Keane, J. W. Ciszek, J. M. Tour, and D. Natelson. Three-terminal devices to examine single-molecule conductance switching. *Nano. Lett.*, 6:1518–1521, 2006.
- [236] Victor V. Zhirnov and Ralph K. Cavin. Molecular electronics: Chemistry of molecules or physics of contacts? *Nat. Mater.*, 5:11–12, 2006.
- [237] J. Tang, Y. Wang, C. Nuckolls, and S. J. Wind. Chemically responsive molecular transistors fabricated by self-aligned lithography and chemical self-assembly. *J. Vac. Sci. Technol. B.*, 24(6):3227–3229, 2006.
- [238] Jin Yao Tang, Yi Liang Wang, Jennifer E. Klare, George S. Tulevski, Shalom J. Wind, and Colin Nuckolls. Encoding molecular wire formation within nanoscale sockets. *Angew. Chem. Int. Ed.*, 46:3892–3895, 2007.

- [239] L. Venkataraman, Y. S. Park, A. C. Whalley, C. Nuckolls, M. S. Hybertsen, and M. L. Steigerwald. Electronics and chemistry: Varying single-molecule junction conductance using chemical substituents. *Nano. Lett.*, 7(2):502–506, 2007.
- [240] F. Chen, J. Hihath, Z. Huang, X. Li, and N. J. Tao. Measurement of single-molecule conductance. *Annu. Rev. Phys. Chem.*, 58:535–564, 2007.
- [241] Xiaodong Chen, You-Moon Jeon, Jae-Won Jang, Lidong Qin, Fengwei Huo, Wei Wei, and Chad A. Mirkin. On-wire lithography-generated molecule-based transport junctions: A new testbed for molecular electronics. *J. Am. Chem. Soc.*, 130:8166–8188, 2008.
- [242] Geoffrey J. Ashwell, Piotr Wierzchowiec, Laurie J. Phillips, Christopher J. Collins, Joanna Gigon, Benjamin J. Robinson, Christopher M. Finch, Ian R. Grace, Colin J. Lambert, Philip D. Buckle, Kym Ford, Barry J. Wood, and Ian R. Gentle. Functional molecular wires. *Phys. Chem. Chem. Phys.*, 10(14):1859–1866, 2008.
- [243] L. P. Kouwenhoven, S. Jauhar, J. Orenstein, P. L. McEuen, Y. Nagamune, J. Motohisa, and H. Sakaki. Observation of photon-assisted tunneling through a quantum dot. *Phys. Rev. Lett.*, 73:3443–3446, 1994.
- [244] N. C. van der Vaart, S. F. Godijn, Y. V. Nazarov, C. J. P. M. Harmans, J. E. Mooij, L. W. Molenkamp, and C. T. Foxon. Resonant tunneling through two discrete energy states. *Phys. Rev. Lett.*, 74(23):4702–4705, Jun 1995.
- [245] B. J. Keay, S. Zeuner, S. J. Allen, K. D. Maranowski, A. C. Gossard, U. Bhattacharya, and M. J. W. Rodwell. Dynamic localization, absolute negative conductance, and stimulated, multiphoton emission in sequential resonant tunneling semiconductor superlattices. *Phys. Rev. Lett.*, 75(22):4102–4105, Nov 1995.
- [246] T. H. Oosterkamp, L. P. Kouwenhoven, A. E. A. Koolen, N. C. van der Vaart, and C. J. P. M. Harmans. Photon sidebands of the ground state and first excited state of a quantum dot. *Phys. Rev. Lett.*, 78(8):1536–1539, 1997.
- [247] Rosa López, Ramón Aguado, Gloria Platero, and Carlos Tejedor. Kondo effect in ac transport through quantum dots. *Phys. Rev. Lett.*, 81:4688–4691, 1998.
- [248] P. W. Brouwer. Scattering approach to parametric pumping. *Phys. Rev. B*, 58(16):R10135–R10138, 1998.
- [249] T. H. Oosterkamp, T. Fujisawa, W. G. van der Wiel, K. Ishibashi, R. V. Hijman, S. Tarucha, and L. P. Kouwenhoven. Microwave spectroscopy of a quantum-dot molecule. *Nature*, 395:873–876, 1998.
- [250] M. Switkes, C. M. Marcus, K. Campman, and A. C. Gossard. An Adiabatic Quantum Electron Pump. *Science*, 283:1905–1908, 1999.

- [251] F. Zhou, B. Spivak, and B. Altshuler. Mesoscopic mechanism of adiabatic charge transport. *Phys. Rev. Lett.*, 82(3):608–611, 1999.
- [252] Peter Nordlander, Michael Pustilnik, Yigal Meir, Ned S. Wingreen, and David C. Langreth. How long does it take for the kondo effect to develop? *Phys. Rev. Lett.*, 83(4):808–811, Jul 1999.
- [253] G. Platero and R. Aguado. Photon-assisted transport in semiconductor nanostructures. *Phys. Reports*, 395:1–157, 2004.
- [254] James E. Murphy, Matthew C. Beard, and Arthur J. Nozik. Time-resolved photoconductivity of pbse nanocrystal arrays. *J. Phys. Chem. B*, 110:25455–25461, 2006.
- [255] Z. Zhong, N. M. Gabor, J. E. Sharping, A. L. Gaeta, and P. L. MCEuen. Terahertz time-domain measurement of ballistic electron resonance in a single-walled carbon nanotube. *Nat. Nanotechnol.*, 3:201, 2008.
- [256] W. Ho. Single-molecule chemistry. *The Journal of Chemical Physics*, 117(24):11033–11061, 2002.
- [257] W. Wang, T. Lee, I. Kretzschmar, and M. A. Reed. Inelastic electron tunneling spectroscopy of an alkanedithiol self-assembled monolayer. *Nano. Lett.*, 4:643, 2004.
- [258] Yoram Selzer, Lintao Cai, Marco A. Cabassi, Yuxing Yao, James M. Tour, Theresa S. Mayer, and David L. Allara. Effect of local environment on molecular conduction: Isolated molecule versus self-assembled monolayer. *Nano. Lett.*, 5:61, 2005.
- [259] M. Galperin, M.A. Ratner, and A. Nitzan. Inelastic electron tunneling spectroscopy in molecular junctions: Peaks and dips. *J. Chem. Phys.*, 121:11965–11979, 2004.
- [260] N. Sergueev, D. Roubtsov, and Hong Guo. Ab initio analysis of electron-phonon coupling in molecular devices. *Phys. Rev. Lett.*, 95(14):146803, Sep 2005.
- [261] C. Hartle, R. Abd Benesch and M. Thoss. Vibrational nonequilibrium effects in the conductances of single molecules with multiple electronic states. *Phys. Rev. Lett.*, 102:146801, 2009.
- [262] D. A. Ryndyk, M. Hartung, and G. Cuniberti. Nonequilibrium molecular vibrons: An approach based on the nonequilibrium green function technique and the self-consistent born approximation. *Phys. Rev. B*, 73(4):045420, Jan 2006.
- [263] M. Galperin, M. A. Ratner, and A. Nitzan. Molecular transport junctions: vibrational effects. *Journal of Physics: Condensed Matter*, 19(10):103201 (81pp), 2007.

- [264] Aletha M. Nowak and Richard L. McCreery. In situ raman spectroscopy of bias-induced structural changes in nitroazobenzene molecular electronic junctions. *J. Am. Chem. Soc.*, 126(50):16621–16631, 2004.
- [265] Aletha M. Nowak and Richard L. McCreery. Characterization of carbon/nitroazobenzene/titanium molecular electronic junctions with photoelectron and raman spectroscopy. *Analytical Chemistry*, 76(4):1089–1097, 2004.
- [266] Andrew P. Bonifas and Richard L. McCreery. In-situ optical absorbance spectroscopy of molecular layers in carbon based molecular electronic devices. *Chemistry of Materials*, 20(12):3849–3856, 2008.
- [267] D. R. Ward, N. J. Halas, J. W. Ciszek, J. M. Tour, Y. Wu, P. Nordlander, and D Natelson. Simultaneous measurements of electronic conduction and raman response in molecular junctions. *Nano. Lett.*, 8:919–924, 2008.
- [268] D. R. Ward, G. D. Scott, Z. K. Keane, N. J. Halas, and D Natelson. Electronic and optical properties of electromigrated molecular junctions. *J. Phys.: Condens. Matter*, 20(37):374118, 2008.
- [269] H. Basch, R. Cohen, and M. A. Ratner. Interface geometry and molecular junction conductance: Geometric fluctuation and stochastic switching. *Nano. Lett.*, 5:1668–1675, 2005.
- [270] T. Perrine and B. D. Dunietz. Single-molecule field-effect transistors: A computational study of the effects of contact geometry and gating-field orientation on conductance-switching properties. *Phys. Rev. B*, 75:195319, 2007.
- [271] G. Stefanucci and C. O. Almbladh. Time-dependent partition free approach in resonant tunneling systems. *Phys. Rev. B*, 69:195318–195334, 2004.
- [272] S. Kurth, G. Stefanucci, C. O. Almbladh, A. Rubio, and E. K. U. Gross. Time-dependent quantum transport: A practical scheme using density functional theory. *Phys. Rev. B*, 72:035308, 2005.
- [273] N. Bushong, N. Sai, and M. Di Ventra. Approach to steady-state transport in nanoscale conductors. *Nano. Lett.*, 5:2569, 2005.
- [274] J. Maciejko, J. Wang, and H. Guo. Time-dependent quantum transport far from equilibrium: An exact non linear response theory. *Phys. Rev. B*, 74:085324, 2006.
- [275] D. Hou, Y. He, X. Liu, J. Kang, J. Chen, and R. Han. Time-dependent transport: Time domain recursively solving negf technique. *Physica E*, 31:191, 2006.
- [276] Na Sai, Neil Bushong, Ryan Hatcher, and Massimiliano Di Ventra. Microscopic current dynamics in nanoscale junctions. *Phys. Rev. B*, 75(11):115410, 2007.

- [277] A. Prociuk and B. D. Dunietz. Time-dependent current through electronic channel models using a mixed time-frequency solution of the equations of motion. *Phys. Rev. B*, 78:165112, 2008.
- [278] G. Stefanucci, S. Kurth, A. Rubio, and E. K. U. Gross. Time-dependent approach to electron pumping in open quantum systems. *Phys. Rev. B*, 77:075339, 2008.
- [279] L. P. Kouwenhoven, S. Jauhar, K. McCormick, D. Dixon, P. L. McEuen, Yu. V. Nazarov, N. C. van der Vaart, and C. T. Foxon. Photon-assisted tunneling through a quantum dot. *Phys. Rev. B*, 50:2019–2022, 1994.
- [280] T. H. Stoof and Yu. V. Nazarov. Time-dependent resonant tunneling via two discrete states. *Phys. Rev. B*, 53(3):1050–1053, Jan 1996.
- [281] C. A. Stafford and Ned S. Wingreen. Resonant photon-assisted tunneling through a double quantum dot: An electron pump from spatial rabi oscillations. *Phys. Rev. Lett.*, 76:1916–1919, 1996.
- [282] Ph. Brune, C. Bruder, and H. Schoeller. Photon-assisted transport through ultrasmall quantum dots: Influence of intradot transitions. *Phys. Rev. B*, 56(8):4730–4736, Aug 1997.
- [283] Morten Holm Pedersen and Markus Büttiker. Scattering theory of photon-assisted electron transport. *Phys. Rev. B*, 58(19):12993–13006, Nov 1998.
- [284] Baigeng Wang, Jian Wang, and Hong Guo. Current partition: A nonequilibrium green’s function approach. *Phys. Rev. Lett.*, 82(2):398–401, Jan 1999.
- [285] M. Moskalets and M. Büttiker. Adiabatic quantum pump in the presence of external ac voltages. *Phys. Rev. B*, 69:205316, 2004.
- [286] Liliana Arrachea. Symmetry and environment effects on rectification mechanisms in quantum pumps. *Phys. Rev. B*, 72:121306, 2005.
- [287] B. H. Wu and J. C. Cao. Interference of conductance and shot noise properties of photon-assisted transport through a t-shaped double quantum dot. *Phys. Rev. B*, 73(20):205318, 2006.
- [288] A. Agarwal and D. Sen. Nonadiabatic charge pumping in a one-dimensional system of noninteracting electrons by an oscillating potential. *Physical Review B (Condensed Matter and Materials Physics)*, 76(23):235316, 2007.
- [289] L. Arrachea, Carlos Naon, and Mariano Salvay. Quantum pump effect in one-dimensional systems of dirac fermions. *Phys. Rev. B*, 76:165401, 2007.
- [290] R. Baer and D. Neuhauser. Ab initio electrical conductance of a molecular wire. *Int. J. Quant. Chem.*, 91:524–532, 2003.

- [291] R. Baer, T. Seidman, S. Ilani, and D. Neuhauser. Ab initio study of the alternating current impedance of a molecular junction. *J. Chem. Phys.*, 120:3387–3396, 2004.
- [292] R. Baer and D. Neuhauser. Real-time linear response for time-dependent density-functional theory. *J. Chem. Phys.*, 121:9803–9807, 2004.
- [293] Kieron Burke, Roberto Car, and Ralph Gebauer. Density functional theory of the electrical conductivity of molecular devices. *Phys. Rev. Lett.*, 94:146803, 2005.
- [294] D. Neuhauser and R. Baer. Efficient linear-response method circumventing the exchange-correlation kernel: Theory for molecular conductance under finite bias. *J. Chem. Phys.*, 123:204105, 2005.
- [295] X. Qian, J. Ju Li, X. Lin, and S. Yip. Time-dependent density functional theory with ultrasoft pseudopotentials: Real-time electron propagation across a molecular junction. *Phys. Rev. B*, 73:035408, 2006.
- [296] X. Zheng, F. Wang, C. Y. Yam, Y. Mo, and G. Chen. Time-dependent density-functional theory for open systems. *Phys. Rev. B*, 75:195127, 2007.
- [297] S. A. Gurvitz and Ya. S. Prager. Microscopic derivation of rate equations for quantum transport. *Phys. Rev. B*, 53(23):15932–15943, Jun 1996.
- [298] Jörg Lehmann, Sigmund Kohler, Peter Hänggi, and Abraham Nitzan. Molecular wires acting as coherent quantum ratchets. *Phys. Rev. Lett.*, 88(22):228305, May 2002.
- [299] Jorg Lehmann, Sigmund Kohler, Peter Hanggi, and Abraham Nitzan. Rectification of laser-induced electronic transport through molecules. *The Journal of Chemical Physics*, 118(7):3283–3293, 2003.
- [300] Luis E. F. Foa Torres. Mono-parametric quantum charge pumping: Interplay between spatial interference and photon-assisted tunneling. *Phys. Rev. B*, 72:245339, 2005.
- [301] U Harbola, M. Esposito, and S. Mukamel. Quantum master equation for electron transport through quantum dots and single molecules. *Phys. Rev. B*, 74:235309, 2006.
- [302] M. Moskalets and M. Büttiker. Floquet scattering theory of quantum pumps. *Phys. Rev. B*, 66(20):205320, Nov 2002.
- [303] M. Moskalets and M. Büttiker. Floquet scattering theory for current and heat noise in large amplitude adiabatic pumps. *Phys. Rev. B*, 70:245305, 2004.
- [304] Antti-Pekka Jauho, Ned S. Wingreen, and Yigal Meir. Time-dependent transport in interacting and noninteracting resonant-tunneling systems. *Phys. Rev. B*, 50(8):5528–5544, Aug 1994.

- [305] J. Q. You, Chi-Hang Lam, and H. Z. Zheng. Landauer-büttiker formula for time-dependent transport through resonant-tunneling structures: A nonequilibrium green's function approach. *Phys. Rev. B*, 62(3):1978–1983, Jul 2000.
- [306] Yu Zhu, Joseph Maciejko, Tao Ji, Hong Guo, and Jian Wang. Time-dependent quantum transport: Direct analysis in the time domain. *Phys. Rev. B*, 71(7):075317, 2005.
- [307] Liliana Arrachea and Michael Moskalets. Relation between scattering-matrix and keldysh formalisms for quantum transport driven by time-periodic fields. *Phys. Rev. B*, 74(24):245322, 2006.
- [308] Liliana Arrachea, Alfredo Levy Yeyati, and Alvaro Martin-Rodero. Nonadiabatic features of electron pumping through a quantum dot in the kondo regime. *Physical Review B (Condensed Matter and Materials Physics)*, 77(16):165326, 2008.
- [309] G. Baym. Conservation laws and correlation functions. *Physical Review*, 124:287, 1961.
- [310] G. Baym. Self-consistent approximations in many-body systems. *Physical Review*, 127:1391, 1962.
- [311] L. P. Kadanoff and G. Baym. *Quantum Statistical Mechanics*. Benjamin and Cummings, New York, 1962.
- [312] D. C. Langerth. *Linear and Non-linear Electron Transport in Solids*. Plenum Press, New-York, 1976.
- [313] M. Bonitz. *Quantum Kinetic Theory*. Teubner, Stuttgart, 1998.
- [314] M. Cini. Time-dependent approach to electron transport through junctions: General theory and simple applications. *Phys. Rev. B*, 22:5887, 1980.
- [315] M. P. López Sancho, J. M. López Sancho, and J. Rubio. Quick iterative scheme for the calculation of transfer matrices - application to mo(100). *J. Phys. F:Met. Phys.*, 14:1205–1215, 1984.
- [316] M. P. López Sancho, J. M. López Sancho, and J. Rubio. Highly convergent schemes for the calculation of bulk and surface green function. *J. Phys. F: Met. Phys.*, 15:851–858, 1985.
- [317] A. Prociuk, H. Phillips, and B. D. Dunietz. Modeling transient aspects of coherehce-driven electron transport. *J. Phys.: Conf. Ser.*, 220:012008, 2010.
- [318] A. L. Fetter and J. D. Walecka. *Quantum Statistical Mechanics*. Dover, 2003.

- [319] A. Prociuk and B. D. Dunietz. *Atomic and Molecular Systems, Dynamics, Spectroscopy, Clusters, and Nanostructures*, volume 20 of *Progress in Theoretical Chemistry and Physics*, chapter On the electronic spectra of a molecular bridge under non-equilibrium electric potential conditions, pages 265–277. Springer, Netherlands, 2009.
- [320] Allan R. Burkett and Susan B. Dunkle. Technical writing in the undergraduate curriculum. *Journal of Chemical Education*, 60(6):469, June 1983.
- [321] National Research Council. *Reaching students: What research says about effective instruction in undergraduate science and engineering*. National Academies Press, Washington, DC, 2015.
- [322] David P Ausubel. A subsumtion theory of meaningful verbal learning and retention. *The Journal of General Psychology*, 66:213–224, 1962.
- [323] Christina Stefani and Georgios Tsaparlis. Students’ levels of explanations, models, and misconceptions in basic quantum chemistry: A phenomenographic study. *Journal of Research in Science Teaching*, 46(5):520–536, May 2009.
- [324] Larry D. Kirkpatrick and Adele S. Pittendrigh. A writing teacher in the physics classroom. *The Physics Teacher*, 22:159–164, 1984.
- [325] Naola VanOrden. Is writing an effective way to learn chemical concepts? Classroom-based research. *Journal of Chemical Education*, 67(7):583, July 1990.
- [326] H. Beall. In-class writing in general chemistry: A tool for increasing comprehension and communication. *Journal of Chemical Education*, 68(2):148, February 1991.
- [327] Melanie M. Cooper. Writing: An approach for large-enrollment chemistry courses. *Journal of Chemical Education*, 70(6):476, June 1993.
- [328] Shawn M. Glynn and K. Denise Muth. Reading and writing to learn science: Achieving scientific literacy. *Journal of Research in Science Teaching*, 31(9):1057–1073, November 1994.
- [329] Lé Onard P. Rivard. A review of writing to learn in science: Implications for practice and research. *Journal of Research in Science Teaching*, 31(9):969–983, November 1994.
- [330] Brian P Coppola and Douglas S Daniels. The role of written and verbal expression in learning. Promoting and improving communication skills for students in an undergraduate chemistry program. *Language and Learning across the Disciplines*, 1(3):67–86, 1996.
- [331] Vaughan Prain, Brian Hand, and Susan Kay. Writing for learning in physics. *The Physics Teacher*, 35(1):40, 1997.

- [332] Francis M. Rossi. Writing in an advanced undergraduate chemistry course: An assignment exploring the development of scientific ideas. *Journal of Chemical Education*, 74(4):395, April 1997.
- [333] Perry Klein. Reopening inquiry into cognitive processes in writing-to-learn. *Educational Psychology Review*, 11(3):203–270, 1999.
- [334] Martin P. Farrell. Physics , writing and attainment. *Physics Education*, 36:40–43, 2001.
- [335] Ivan A Shibley Jr, Louis M Milakofsky, and Cynthia L Nicotera. Incorporating a substantial writing assignment into organic chemistry: Library Research, peer review, and assessment. *Journal of Chemical Education*, 78(1):9–12, 2001.
- [336] K. A. Burke, Brian M. Hand, Jason R. Pooch, and Thomas J. Greenbowe. Using the science writing heuristic: Training chemistry teaching assistants. *Journal of College Science Teaching*, 35(1):36–41, 2005.
- [337] John Stewart and Shawn Ballard. Effect of written presentation on performance in introductory physics. *Physical Review Special Topics - Physics Education Research*, 6:020120, 2010.
- [338] Anne V Vazquez, Kaitlin McLoughlin, Melanie Sabbagh, Adam C Runkle, Jeffrey Simon, Brian P Coppola, and Samuel Pazicni. Writing-to-teach: A new pedagogical approach to elicit explanative writing from undergraduate chemistry students. *Journal of Chemical Education*, 89:1025–1031, 2012.
- [339] R Mayer. The promise of multimedia learning: using the same instructional design methods across different media. *Learning and Instruction*, 13(2):125–139, April 2003.
- [340] Brian Hand, Murat Gunel, and Cuneyt Ulu. Sequencing embedded multimodal representations in a writing to learn approach to the teaching of electricity. *Journal of Research in Science Teaching*, 46(3):225–247, March 2009.
- [341] Cheryl L Moy, Jonas R Locke, Brian P Coppola, and Anne J McNeil. Improving science education and understanding through editing wikipedia. *Journal of Chemical Education*, 87(11):1159–1162, 2010.
- [342] Mona Wells and Robert Clougherty. Use of wikis in chemistry instruction for problem-based learning assignments: An example in instrumental analysis. *Journal of Chemical Education*, 85(10):1446, October 2008.
- [343] Michael J Evans and Jeffrey S Moore. A collaborative, wiki-based organic chemistry project incorporating free chemistry software on the web. *Journal of Chemical Education*, 88:764–768, 2011.

- [344] Mark J W Lee, Catherine McLoughlin, and Anthony Chan. Talk the talk: Learner-generated podcasts as catalysts for knowledge creation. *British Journal of Educational Technology*, 39(3):501–521, 2008.
- [345] Sean Dowling. Using blogs to share learner-generated content. *The Electronic Journal for English as a Second Language*, 17(2):1–22, 2013.
- [346] Marlene Scardamalia and Carl Bereiter. Knowledge building, 2003.
- [347] Elaine B Coleman, Ann L Brown, and Inna D Rivkin. The effect of instructional explanations on learning from scientific texts. *The Journal of the Learning Sciences*, 6(4):347–365, 1997.
- [348] Elaine Coleman. Using explanatory knowledge during collaborative problem solving in science. *Journal of the Learning Sciences*, 7(3):387–427, July 1998.
- [349] Georgios Tsaparlis. Atomic orbitals, molecular orbitals and related concepts: Conceptual difficulties among chemistry students. *Research in Science Education*, 27(2):271–287, 1997.
- [350] Samuel Pazicni and Christopher F Bauer. Characterizing illusions of competence in introductory chemistry students. *Chemistry Education Research and Practice*, 15(1):24–34, 2014.
- [351] Stephen J Krause, Dale R Baker, Adam R Carberry, Milo Koretsky, Bill Jay Brooks, Debra Gilbuena, and Cindy Waters. Just-in-Time-Teaching with Interactive Frequent Formative Feedback (JiT- TIFFF or JTF) for Cyber Learning in Core Materials Courses. 2013.
- [352] George Gopen and Judith Swan. The science of scientific writing. *American Scientist*, 78:550–558, 1990.
- [353] John L Koprowski. Sharpening the craft of scientific writing: A peer review strategy to improve student writing. *Journal of College Science Teaching*, 1997.
- [354] Scott Freeman and John W. Parks. How accurate is peer grading? *Cell Biology Education - Life Sciences Education*, 9:323–332, 2010.
- [355] Daniel C. Edelson. Design research: What we learn when we engage in design. *Journal of the Learning Sciences*, 11(1):105–121, January 2002.
- [356] Philip Bell. On the theoretical breadth of design-based research in education. *Educational Psychologist*, 39(4):243–253, 2004.
- [357] Allan Collins, Diana Joseph, and Katerine Bielaczyc. Design research: Theoretical and methodological issues. *Journal of the Learning Sciences*, 13(1):15–42, 2004.

- [358] Brian P Coppola, Seyhan N Ege, and Richard G Lawton. The university of michigan undergraduate chemistry curriculum 2. Instructional strategies and assessment. *Journal of Chemical Education*, 74(1):84–94, 1997.
- [359] Seyhan N. Ege, Brian P. Coppola, and Richard G. Lawton. The university of michigan undergraduate chemistry curriculum 1. Philosophy, curriculum, and the nature of change. *Journal of Chemical Education*, 74(1):74–83, January 1997.
- [360] Amy C Gottfried, Ryan D Sweeder, Jeffrey M Bartolin, Jessica A Hessler, Benjamin P Reynolds, Ian C Stewart, Brian P Coppola, and Mark M Banaszak Holl. Design and implementation of a studio-based general chemistry course. *Journal of Chemical Education*, 84(2):265–270, 2007.
- [361] Jacqueline Cossentino. Importing artistry: Further lessons from the design studio. *Reflective Practice : International and Multidisciplinary Perspectives*, 3(1):39–52, 2002.
- [362] Jean Lave. Introduction: Situationally specific practice. *Anthropology & Education Quarterly*, 16(3):171–176, 1985.
- [363] Jean Lave. Situating learning in communities of practice. In Lauren B. Resnick, John M. Levine, and Stephanie D. Teasley, editors, *Perspectives on socially shared cognition*, chapter 4, pages 63–82. American Psychological Association, Washington, DC, US, 1991.
- [364] John Seely Brown, Allan Collins, and Paul Duguid. Situated cognition the culture of learning. *Educational Researcher*, 18(1):32–42, 1989.
- [365] John A. Bargh and Yaacov Schul. On the cognitive benefits of teaching. *Journal of Educational Psychology*, 72(5):593–604, 1980.
- [366] L. S. Fuchs, D. Fuchs, J. Bentz, N. B. Phillips, and C. L. Hamlett. The nature of student interactions during peer tutoring with and without prior training and experience. *American Educational Research Journal*, 31(1):75–103, 1994.
- [367] Kwangsu Cho and Charles MacArthur. Student revision with peer and expert reviewing. *Learning and Instruction*, 20(4):328–338, August 2010.
- [368] Rod D. Roscoe and Michelene T H Chi. Tutor learning: The role of explaining and responding to questions. *Instructional Science*, 36:321–350, 2008.
- [369] Logan Fiorella and Richard E. Mayer. The relative benefits of learning by teaching and teaching expectancy. *Contemporary Educational Psychology*, 38(4):281–288, October 2013.
- [370] Brian P. Coppola and Jason K. Pontrello. Using errors to teach through a two-staged, structured review: Peer-reviewed quizzes and Whats Wrong With Me?. *Journal of Chemical Education*, page 140821100714003, 2014.

- [371] S. B. Merriam. *Qualitative research: A guide to design and implementation*. Jossey-Bass, San Francisco, 2009.
- [372] K Anders Ericsson. The influence of experience and deliberate practice on the development of superior expert performance. In K. A. Ericsson, N. Charness, R. R. Hoffman, and P. J. Feltovich, editors, *The Cambridge Handbook of Expertise and Expert Performance*, pages 685–705. Cambridge University Press, New York, NY, 2006.
- [373] Victor Sampson, Jonathon Grooms, and Joi Phelps Walker. Argument-driven inquiry as a way to help students learn how to participate in scientific argumentation and craft written arguments: An exploratory study. *Science Education*, 95(2):217 – 257, 2010.
- [374] Alison King. Transactive peer tutoring: Distributing cognition and metacognition. *Educational Psychology Review*, 10(1):57–74, 1998.